NASA/CR—2004-212984

Jet Noise Modeling for Supersonic Business Jet Application

James R. Stone, Eugene A. Krejsa, and Bruce J. Clark
Modern Technologies Corporation, Middleburg Heights, Ohio

March 2004

The NASA STI Program Office . . . in Profile

Since its founding, NASA has been dedicated to the advancement of aeronautics and space science. The NASA Scientific and Technical Information (STI) Program Office plays a key part in helping NASA maintain this important role.

The NASA STI Program Office is operated by Langley Research Center, the Lead Center for NASA's scientific and technical information. The NASA STI Program Office provides access to the NASA STI Database, the largest collection of aeronautical and space science STI in the world. The Program Office is also NASA's institutional mechanism for disseminating the results of its research and development activities. These results are published by NASA in the NASA STI Report Series, which includes the following report types:

- TECHNICAL PUBLICATION. Reports of completed research or a major significant phase of research that present the results of NASA programs and include extensive data or theoretical analysis. Includes compilations of significant scientific and technical data and information deemed to be of continuing reference value. NASA's counterpart of peer-reviewed formal professional papers but has less stringent limitations on manuscript length and extent of graphic presentations.

- TECHNICAL MEMORANDUM. Scientific and technical findings that are preliminary or of specialized interest, e.g., quick release reports, working papers, and bibliographies that contain minimal annotation. Does not contain extensive analysis.

- CONTRACTOR REPORT. Scientific and technical findings by NASA-sponsored contractors and grantees.

- CONFERENCE PUBLICATION. Collected papers from scientific and technical conferences, symposia, seminars, or other meetings sponsored or cosponsored by NASA.

- SPECIAL PUBLICATION. Scientific, technical, or historical information from NASA programs, projects, and missions, often concerned with subjects having substantial public interest.

- TECHNICAL TRANSLATION. English-language translations of foreign scientific and technical material pertinent to NASA's mission.

Specialized services that complement the STI Program Office's diverse offerings include creating custom thesauri, building customized databases, organizing and publishing research results . . . even providing videos.

For more information about the NASA STI Program Office, see the following:

- Access the NASA STI Program Home Page at ***http://www.sti.nasa.gov***

- E-mail your question via the Internet to help@sti.nasa.gov

- Fax your question to the NASA Access Help Desk at 301–621–0134

- Telephone the NASA Access Help Desk at 301–621–0390

- Write to:
  NASA Access Help Desk
  NASA Center for AeroSpace Information
  7121 Standard Drive
  Hanover, MD 21076

NASA/CR—2004-212984

Jet Noise Modeling for Supersonic Business Jet Application

James R. Stone, Eugene A. Krejsa, and Bruce J. Clark
Modern Technologies Corporation, Middleburg Heights, Ohio

Prepared under Contract NAS3–00178, Task Order 9

National Aeronautics and
Space Administration

Glenn Research Center

March 2004

This report is a formal draft or working paper, intended to solicit comments and ideas from a technical peer group.

This report contains preliminary findings, subject to revision as analysis proceeds.

Available from

NASA Center for Aerospace Information
7121 Standard Drive
Hanover, MD 21076

National Technical Information Service
5285 Port Royal Road
Springfield, VA 22100

Available electronically at http://gltrs.grc.nasa.gov

JET NOISE MODELING FOR SUPERSONIC BUSINESS JET APPLICATION

James R. Stone, Eugene A. Krejsa, and Bruce J. Clark,
Modern Technologies Corporation
Middleburg Heights, Ohio 44130

SUMMARY

This document describes the development of an improved predictive model for coannular jet noise, including noise suppression modifications applicable to small supersonic-cruise aircraft such as the Supersonic Business Jet (SBJ), for NASA Langley Research Center (LaRC). For such aircraft a wide range of propulsion and integration options are under consideration. Thus there is a need for very versatile design tools, including a noise prediction model. The approach used is similar to that used with great success by the Modern Technologies Corporation (MTC) in developing a noise prediction model for two-dimensional mixer ejector (2DME) nozzles under the High Speed Research Program and in developing a more recent model for coannular nozzles over a wide range of conditions. If highly suppressed configurations are ultimately required, the 2DME model is expected to provide reasonable prediction for these smaller scales, although this has not been demonstrated. It is considered likely that more modest suppression approaches, such as dual stream nozzles featuring chevron or chute suppressors, perhaps in conjunction with inverted velocity profiles (IVP), will be sufficient for the SBJ.

The methodology recently developed by MTC for NASA for coannular nozzles with and without mixing enhancement chevrons is extended to a wider range of supersonic jet conditions and a wider range of suppressor geometries. Published data from a variety of test facilities, each with its own unique problems and limitations are utilized to establish the validity of the new methodology over a wide range of conditions including the effects of simulated flight. The baseline procedure is developed by updating our recently reported model developed for NASA Glenn Research Center (GRC). The chevron nozzle relations developed therein are generalized to apply to dual stream nozzles with generalized suppressor exit configurations, and comparisons with inner-stream petal nozzles and outer-stream chute nozzles are shown to demonstrate the validity of the model. Inner-stream, outer-stream and plug/downstream shock noises are included in the model, including the effects of convergent-divergent (C–D) terminations for both streams, whether suppressed or unsuppressed, and plug tip geometry.

The improved finalized model is incorporated into the *Footprint/Radius (FOOTPR)* code and a user's guide is provided. MTC will also support the adaptation of this code for incorporation in the NASA LaRC *Aircraft Noise Prediction Program (ANOPP).*

NOMENCLATURE

2DME	Two-dimensional mixer ejector nozzle
A	Nozzle exit area, m^2
ANOPP	Aircraft Noise Prediction Program
BPR	Bypass ratio
C	Noise component coefficient, dB
c	Sonic velocity, m/s
C-D	Convergent-divergent
D	Characteristic diameter, m
F	Empirical factor in shock noise relation, dB/deg
f	1/3-Octave-band center frequency, Hz
FAA	Federal Aviation Administration
FOOTPR	NASA GRC's Fortran code for noise prediction
GRC	NASA Glenn Research Center
IVP	Inverted velocity profile
k	Convection coefficient
L	Length (axial distance), m
LaRC	NASA Langley Research Center
LSF	Linear scale factor, full-scale dimension divided by model-scale dimension
M	Mach number
MTC	Modern Technologies Corporation
N	Slope of component noise versus effective velocity
NASA	National Aeronautics and Space Administration
n_c	Convection velocity coefficient
OASPL	Overall sound pressure level, dB re 20 μPa
P	Total pressure, Pa
PR	Perimeter ratio (suppressed divided by unsuppressed)
R	Source-to-observer distance, m
RMS	Root-mean-square average
r_{pt}	Plug tip radius, m
S	Strouhal number, dimensionless
SBJ	Supersonic business jet
SPL	1/3-Octave-band sound pressure level, dB re 20 μPa
SST	Supersonic transport aircraft
T	Total temperature, ^oK
UOL	Overall sound pressure level uncorrected for refraction, dB re 20 μPa
V	Characteristic velocity, m/s
V_e	Effective velocity for noise generation, m/s
$V_{I/O}$	Higher of inner stream or outer stream velocity, m/s
X_C	Empirical length scaling factor, m
X_s	Axial source location relative to outer stream nozzle exit, m
β	Shock strength
Δ	Difference in variable
θ	Directivity angle (Fig. 2), deg (thet on some figures)
θ′	Effective directivity angle, accounting for refraction, deg

θ_F	Empirical angle scaling factor
θ_M	Mach angle, deg
ρ	Fully-expanded jet density, kg/m^3
ω	Density exponent

Subscripts	(Note that on some figures subscripts appear as regular text)
1	Inner boundary
2	Outer boundary
amb	Ambient conditions
c	Convection
component	Noise component
cor	Corrected for source location
D	Downstream of plug
d	Design value
EE	Experimental/extracted
eff	Effective value, including perimeter ratio effect
ex	Exit of nozzle
exp	Experimental value
f	Flight (or simulated flight)
h	Hydraulic
I	Inner stream
ISA	International Standard Atmosphere
M	Merged mixing noise
mix	Isentropic mixed flow
Norm	Normalized
O	Outer stream
P	Inner stream plug separation
Pred	Predicted
Pred(f)	Finalized prediction
sh	Shock
T	Total

INTRODUCTION

For a balanced approach to aircraft and propulsion system design, noise must be considered from the outset. Commercial aircraft have stringent noise certification requirements, and military aircraft must be designed to minimize the adverse impacts of noise on flight-line personnel as well as on the communities near military installations. Therefore, the system designer needs a versatile noise prediction tool that can be used in system studies, and the National Aeronautics and Space Administration (NASA) *Footprint/Radius (FOOTPR)* code was originally developed to serve this purpose (ref. 1). The problems involved in the design of exhaust nozzles for supersonic transport (SST) aircraft are extremely complicated. Exhaust system aerodynamic performance at takeoff and supersonic cruise is extremely important, and performance at subsonic cruise may also be important, depending on the mission. Thus, as reviewed by Stitt (ref. 2), from an aerodynamic viewpoint alone, there are conflicting design requirements to be met while also maintaining low nozzle weight and minimum complexity. Further complications occur when noise considerations are important, as they are for all civil aircraft. For an SST of any size, jet noise is likely to be critical at takeoff and power cutback. The SST exhaust noise problem is further complicated by the contribution of shock-cell/turbulence interaction noise, which is simply termed "shock noise" herein. Shock noise is generally important at takeoff and can also be a significant contributor at cutback. For relatively small supersonic-cruise aircraft such as the supersonic business jet (SBJ) a wide range of propulsion and integration options are under consideration. Thus there is a need for very versatile design tools, including a noise prediction model.

NASA uses state-of-the-art system noise prediction codes to analytically calculate the noise levels of aircraft. Federal Aviation Administration (FAA) certification noise levels, airport-vicinity noise footprints, climbout, and en route noise levels all may be calculated with these computer models using a variety of noise metrics. These analysis tools (namely the NASA Langley Research Center (LaRC) *Aircraft Noise Prediction Program (ANOPP)* (ref. 3) and NASA Glenn Research Center (GRC) *FOOTPR* (ref. 1) codes) compute spectral, one-third octave band sound pressure levels from several aircraft noise sources for both static and in-flight conditions. The source noise models are generally semi-empirical, using real physical scaling laws that are calibrated with measured test data. The coded prediction structure is flexible enough that new methods may easily be added to the system. A new source noise model that more accurately predicts supersonic jet noise and that incorporates new noise suppression features for dual-stream nozzles is the focus of this report.

The Modern Technologies Corporation (MTC) has used the *FOOTPR* framework in developing new models for NASA and the industry, including the two-dimensional mixer ejector (2DME) noise model (e.g., ref. 4) and the recent high bypass ratio (BPR) nozzle model including chevron effects (refs. 5–7). The starting point for the present task is the model developed in the previous task (ref. 7) with additional improvements developed later (ref. 8). The methodology reported herein applies seamlessly to coannular nozzles of whatever geometric configuration or aero/thermodynamic conditions and includes all the appropriate noise generation mechanisms present in such complex systems. The approach used in developing this model might be called "hybrid experimental/empirical," but relevant elements of theory are utilized to the extent considered practical.

The approach MTC has employed in these tasks is to use an initial predictive model based on analogy to relatively simple semi-empirical expressions derived mainly from the theory of Lighthill (refs. 9–10) for circular jets. We assume that even for complex geometries subsonic jet noise will correlate in a manner analogous to the classical model (also taking into account the theoretical developments of Ffowcs-Williams (ref. 11) and Goldstein and Howes (ref. 12)), if the proper characteristic velocity and characteristic length can be established. For supersonic jet cases, we assume that the subsonic mixing noise relations may be extrapolated and that the additional shock/turbulence interaction noise can be correlated with a model similar to that of Harper-Bourne and Fisher (ref. 13), again assuming that characteristic velocity and characteristic length can be established. These initial models are used to estimate the relative contributions of each noise component at each frequency and angle, and the resulting corrections are applied to the experimental data, yielding what we refer to as "experimental/extracted" spectra at each angle. These experimental/extracted results are then correlated empirically to yield more accurate models than those originally used. Repeating this process starting with the already improved models further improves the ultimate accuracy of the final predictive model; sometimes several iterations are worthwhile. (This iterative process is an example of Bayesian logic, as discussed in ref. 7.)

A persistent problem in developing predictive models is in obtaining good quality experimental data. Noise generated in the experimental facility upstream of the test nozzle: valves, elbows, obstructions, and especially the combustor can contribute significant noise, and much of this noise is of a broadband nature, easily confused with jet noise. Muffling of these sources is costly in terms of size as well as expense, and it is particularly difficult in flight simulation facilities, where compactness of hardware is very important, as discussed by Viswanathan (ref. 14). Another feature of our approach is that all the analyses are conducted with lossless, rather than Standard Day spectra, as is often done in industry. We feel that it is important to isolate the effects of as many physical processes as practical.

Free-jet flight simulation facilities are very useful, and can provide meaningful data so long as that data can be analytically transformed to the flight frame of reference. The different methodologies used by NASA and industry to perform this transformation produce very different results, especially in the rear quadrant; this compelled us to rely largely on static data to develop our model, but we showed reasonable agreement with simulated flight data when these transformation issues are considered (refs. 6–8).

Based on recent analyses and past experience (ref. 15), seven potential source mechanisms must be assessed and preliminary models are available: merged mixing noise (the lowest frequency component), outer shear layer mixing noise (mid-to-high frequency), inner stream mixing noise (modeled as shear layer, but contributes over a broad frequency range in some cases), inner-stream plug separation noise (high-frequency), outer-stream shock noise (mid-to-high frequency), and inner-stream shock noise (mid-to-high frequency); downstream merged (beyond plug tip) shock noise (mid-to-high frequency) (ref. 16) also contributes under some specific circumstances.

PREDICTIVE MODEL

The general dual-stream nozzle geometry and the mixing noise generation regions modeled are illustrated in figure 1. Inner stream flow separation from the plug was also found to be a significant source. (ref. 6–8) When the exhaust conditions of either or both streams are supersonic, shock noise becomes significant, and we use an updated model structurally similar to that currently in *FOOTPR* (ref. 15).

Source Locations

Experimental jet noise measurements are typically made at a distance far enough from the nozzle to be in the far field of any individual noise source region, but not far enough away to treat the entire exhaust plume as a point source at the center of the nozzle exit plane, as is usually assumed in determining the directivity angle. The prediction procedures must take this difference into account. A simple method is used (ref. 6–8) herein to approximate these source location effects for the different sources. The geometric relations for noise sources downstream of the nozzle exit plane are given in figure 2. The relationship of the actual (corrected) source-to-observer distance, R_{cor}, to its apparent value, R, for a source at distance, X_s, downstream of the exit plane is as follows:

$$(R_{cor}/R)^2 = 1 + (X_s/R)^2 + 2\,(X_s/R)\cos\theta \tag{1}$$

The relationship of the corrected angle, θ_{cor}, to its apparent value, θ, is then

$$\theta_{cor} = \sin^{-1}[(R/R_{cor})\sin\theta] \tag{1a}$$

$$\Delta\theta = \theta_{cor} - \theta \tag{1b}$$

$$\Delta SPL = -20\log(R_{cor}/R) \tag{1c}$$

In reality the noise received at any point in the far field comes from multiple locations within the source region as a function of frequency, but reasonably accurate predictions can be made with a simple model wherein the source location variation with frequency is assumed to be less important than the variation with angle. Essentially the model accounts for the location, for each component, from which the peak of the noise spectrum at that angle appears to radiate. These corrections differ for each component, because the source positions are different. The simplification of assuming no change in source location as a function of frequency at each far field angle is generally adequate because each component contributes only over a limited frequency range; however, it is quite feasible to introduce frequency dependence if needed, as it might very well be to deal with airframe installation effects. Such an approach was used for ejector internal sources in reference 4. These source locations must be accounted for in the correction for free jet shear layer effects (ref. 17), as shown in references 7 and 8.

Mixing Noise Components

Any jet mixing noise source region is treated as a round jet of appropriate nozzle exit area at the appropriate conditions. Similar reasoning is used for all the mixing noise components. For a general mixing region the overall level, uncorrected for refraction, UOL, is given by the following:

$$UOL = C + 10 \log [(\rho_{amb}/\rho_{ISA})^2 (c_{amb}/c_{ISA})^4] + 10 \log (A/R^2) + 10\, \omega \log (\rho/\rho_{amb}) + N \log (V_e/c_{amb}) - 5\, k \log [(1 + M_c \cos \theta_{cor})^2 + 0.04\, M_c^2] \quad (2)$$

Where C is the coefficient and N the velocity slope, both determined experimentally and then correlated, A is the appropriate nozzle exit area, and ρ is the fully-expanded jet density for that region. The convection coefficient k has been taken as 3 in our past work based on the theory of Goldstein and Howes (ref. 12); whereas according to Ffowcs Williams (ref. 11) it should be 5; our current model uses k = 4. Note that the Doppler term, $-10 \log [1 - M_f \cos \theta]$ has been eliminated; this results from comparisons with the data of reference 18. The repeatability and consistency of those data is such that it can be deduced that better agreement between static and simulated flight data is obtained if this term is eliminated. The simulated flight transformation includes a Doppler correction, so it appears that the relations presented herein do model the flight situation, but this should be validated by comparison with actual flight data. Note that angle of attack effects are not yet included. The effective velocity for noise generation, V_e, is in most cases calculated as follows:

$$V_e = V [1 - M_f (c_{amb}/V)]^{1/2} \quad (2a)$$

Where V is the characteristic velocity for this region. This expression has evolved from earlier relations wherein jet noise was assumed to vary with relative jet velocity to a relatively high power, typically 5th or 6th, times absolute jet velocity to a somewhat lesser power, typically 2nd or 3rd, preserving the overall 8th power expected (refs. 9–10). Most of our earlier relations (e.g., ref. 15) split the velocity effect as 2/3 relative and 1/3 absolute; the current even split is somewhat more conservative, yielding a smaller in-flight reduction of jet noise than the earlier relations.

The effect of jet temperature or density on noise has also been a matter of contention, and is rather complicated even for a single subsonic static round jet. It is generally accepted that in the case of the hot jet the noise generated is due to two source terms: quadrupole and dipole, with the dipole term contributing more strongly as jet temperature increases (or as density decreases) and as jet velocity is reduced. Thus for cold jets the 8th power velocity effect is observed even to low velocity, while for hot jets at low velocity the jet velocity dependence reduces to a 5th or 6th power. Although such behavior can be explained on a theoretical basis, in an experiment it is difficult to separate this relative increase in noise with increasing temperature at low velocity from the contamination from upstream noise sources. This problem has long been recognized (ref. 19) and must still be considered (ref. 6). The approach to quantifying this effect, as suggested by Ahuja and Bushell (ref. 19), has been to assume that the density effect on noise can be correlated by a variable exponent ω as a function of velocity, i.e., OASPL $\propto 10\, \omega \log (\rho/\rho_{amb})$, where ω is tabulated as a function of nondimensionalized jet velocity, V/c_{amb}. In our

work (e.g., refs. 4 and 15) we have used a simple algebraic expression for this density exponent, as follows:

$$\omega = 3\,(V_e/c_{amb})^{3.5}/[0.6 + (V_e/c_{amb})^{3.5}] - 1 \tag{2b}$$

However, in our most recent work (refs. 7–8) we considered other approaches where ω is might be constant for some source regions. The resulting expressions are different for the different components.

The convective Mach number, M_c, is calculated from the following relation:

$$M_c = n_c\,[(V/c_{amb}) - M_f] \tag{2c}$$

In our recent work (refs. 7–8) initially n_c was assumed constant at 0.62, as has been assumed in many early models. We found that using a variable n_c was quite helpful. Such variations could be related to flow-acoustic interaction, or "flow shielding." These considerations are explored more thoroughly by Gliebe, et al (ref. 20).

The effect of refraction is incorporated in the spectral directivity relations in an empirical manner, but crudely in the direction suggested by theory. The relative sound pressure level, SPL – UOL, is correlated as a function of the effective directivity angle, θ', and the logarithmic Strouhal number, log S, where the Strouhal number is calculated as follows:

$$S = (f\,D/V_e)\,(T/T_{amb})^{0.4\,(1\,+\,\cos\,\theta')} \tag{3}$$

Where D is the characteristic diameter, typically $(4A/\pi)^{0.5}$ and T is the region total temperature. Analogously to the level relation (eq. (2)), the Doppler factor, $[1 - M_f \cos\,\theta]$, is no longer included. The effective angle, to account for refraction effects, is calculated as follows:

$$\theta' = \theta_{cor}\,(V/c_{amb})^{0.1} \tag{3b}$$

It is by use of this effective directivity angle that, in a very simple and approximate way, refraction is accounted for. It is assumed that the spectra for widely differing jet velocities are similar at this adjusted angle rather than at the same geometric angle. This approach, in conjunction with the analytically modeled convection effect in eq. (2), correlates the variation of SPL with frequency and angle rather well, as shown later herein. The resulting spectral directivity tables are developed iteratively as further discussed later in this report.

The source location for a mixing region noise, X_s, is as follows:

$$X_s = [L + (X_C + \theta/\theta_F)\,D]/LSF \tag{4}$$

L is this displacement of the start of the mixing region from the fan nozzle exit plane, while X_C and θ_F are empirical length and angle scaling factors. LSF is the linear scale factor, full-scale dimension divided by model-scale dimension. The uncorrected angle, θ, is used here to start the correction process in closed form. Even though the experimental data are scaled to the correct

size for comparisons, the linear scale factor is used in conjunction with the experiment geometry to correct the predictions for the effect of source location.

Shock Noise Components

The relationships used to predict any shock noise component $OASPL_{sh,}$ for $M \geq 1.0$, is as follows:

$$OASPL_{sh} = C_{sh} + 10 \log [(\rho_{amb}/\rho_{ISA})^2(c_{amb}/c_{ISA})^4] + 10 \log (A/R^2) + 10 \log \{\beta^4/(1 + \beta^4)\} - 40 \log (1 - M_f \cos \theta) - F (\theta - \theta_M) \quad (5)$$

Where β is the shock strength and the ambient property and area/distance terms also used in the internal mixing noise relations have the same meaning. The shock strength parameter β is calculated as follows:

$$\beta = [(M^2 - M_d{}^2)^2 + 0.01\, M_d/(1 - D_1/D_2)]^{1/4} \quad (5a)$$

Where M is the particular stream Mach number expanded to ambient conditions and M_d is the design Mach number. D_1 is the inner diameter and D_2 is the outer diameter for the stream under consideration; the term $0.01\, M_d/(1 - D_1/D_2)$ is included to prevent a singularity at $M = M_d$. The intercept C_{sh} may be dependent on geometry. The Mach angle is denoted by θ_M, calculated as follows:

$$\theta_M = 180 - \sin^{-1} (1/M) \qquad \text{(in degrees)} \quad (5b)$$

(Note on terminology: θ_M will always have an additional subscript; otherwise the subscript M on other variables refers to the merged region.) The term $F (\theta - \theta_M)$ is calculated as follows:

$$\left.\begin{aligned} F (\theta - \theta_M) &= 0.0 \quad \text{for } \theta < \theta_M \\ F (\theta - \theta_M) &= 0.75 (\theta - \theta_M) \text{for } \theta \geq \theta_M \end{aligned}\right\} \quad (5c)$$

Spectral directivity effects are calculated next. The relative sound pressure level, $SPL_{sh} - OASPL_{sh}$, is given in tabular form as a function of the directivity angle θ and the logarithmic Strouhal number $\log S_{sh}$. The Strouhal number is calculated as follows:

$$S_{sh} = [f\beta D_h/(0.7V)] (1 - M_f \cos \theta)\{[1 + (0.7\, V/c_{amb}) \cos \theta]^2 + 0.04 (0.7\, V/c_{amb})^2\}^{1/2} \quad (6)$$

It may very well be that the tables eventually developed will be different for under-expanded and over-expanded cases, but at present this is not the case.

The source location for shock noise, $X_{s,sh}$, is as follows:

$$X_{s,sh} = [L + 2\, D_h (M^2 - 1)^{1/2}]/LSF \quad (7)$$

COMPONENT EXTRACTION EXAMPLES

The process of component noise separation and coefficient adjustment is illustrated in the following examples. Examples are shown for a wide enough range of situations to give the reader an appreciation of the power of this approach and the issues that must be addressed in its application. The experimental/extracted component SPLs are obtained from the following relation for each component: $SPL_{component,EE} = SPL_{exp} - (SPL_{T,Pred} - SPL_{component,Pred})$.

Shock-Free External-Plug Coannular Nozzle

A static case from reference 18 for a mixed jet velocity near the low end of interest for SBJ applications is shown in figure 3 at four far-field locations: forward quadrant, θ = 60 deg (fig. 3(a)), θ = 90 deg (fig. 3(b)), θ = 120 deg (fig. 3(c)), and near the peak noise angle in aft quadrant at θ = 150 deg (fig. 3(d)). The measured noise spectra ($SPL_{T,exp}$) are shown by the heavy solid line (unsmoothed); the merged noise spectra ($SPL_{M,EE}$) are indicated by the ○ symbols connected by the dashed curve, the outer shear layer noise spectra ($SPL_{O,EE}$) are indicated by the □ symbols connected by the dotted curve, the inner stream noise spectra ($SPL_{I,EE}$) are indicated by the ◇ symbols connected by the dot-dash curve; and inner stream plug separation noise ($SPL_{P,EE}$) is indicated by the △ symbols connected by the double-dot-dash curve. Data are not usually plotted if $SPL_{component,EE} - SPL_{T,exp} \leq -10.0$ dB, since such data are not meaningful; where such low values are shown, it is simply to show that the particular component does not contribute significantly at that angle. Comparisons are only meaningful for the dominant component at each frequency and angle. It should be noted that regardless of whether or not component levels are plotted, using this method of extraction, the antilogarithmic sum of the components always equals the total SPL, whether experimental or predicted. Comparing the plots at the four angles shows that the various components have different directivity effects.

The magnitude of the correction applied to the experimental data can be seen by comparing the extracted component spectra with the total. At all angles for this test case the merged mixing noise is dominant over most of the spectrum, but the outer shear layer does contribute at high frequency. For other cases the other noise components can also become important, depending on test conditions and geometry. Where the extracted component SPL is within 4.0 dB of the total, the data are correlated in normalized spectral form, as discussed later herein. The values of the corrected effective directivity angles for each noise component are noted on these figures: for merged mixing noise, θ'_M = thet′M (on figure); for outer shear layer mixing noise, θ'_O = thet′O (on figure); for inner stream mixing, θ'_I = thet′I (on figure); and for plug separation noise, θ'_P = thet′P (on figure). Since for this particular case for all these components, the $(V_e/c)^{0.1}$ is close to 1.00, $\theta_{component} \cong \theta'_{component}$, and the magnitude of the correction due to source location can be seen.

Once the noise spectra have been broken down into their components, the experimental/extracted components can be compared with prediction, as shown in figure 4, for the same case as in figure 3. The same symbols are used for each component as in figure 3, but now the

corresponding curves are the predicted values. The coefficients for the various components, C_M, C_O, etc., are adjusted to minimize the average error (experimental minus predicted) at all angles where the data are considered valid, over the frequency range where that component is most important. The adjusted values of the component coefficients are shown on each such figure. (Note that as the coefficients change relative to each other, the correction $SPL_{compnent,EE} - SPL_{T,exp}$ as a function of frequency and angle, also changes. Reasonably good agreement between experimental/extracted and predicted spectra can be seen at all angles, but areas of potential improvement can be seen.

Coplanar Nozzle With Both Streams Supersonic

Shock noise is often relatively easy to identify, at least near its peak frequency, as shown for a very high mixed jet velocity case from reference 21. Component noise separation is shown in figure 5 at three far-field locations: forward quadrant, $\theta = 46$ deg (fig. 5(a)), sideline, $\theta = 95$ deg (fig. 5(b)), and near the peak noise angle in aft quadrant at $\theta = 139$ deg (fig. 5(c)). The total experimental noise and the mixing noise components are identified as in figure 3, but there is no plug to produce separation noise. Outer stream shock noise is indicated by the $\times$ symbols connected by the lighter solid line, while the inner stream shock noise is shown by the + symbols connected by the dotted line. Outer stream shock noise is the dominant component in the forward quadrant (fig. 5(a)) except at low frequency, where merged mixing noise controls; the contribution of the other components appear to be marginal. At the higher angles merged mixing noise dominates up to the middle frequency range. At $\theta = 95$ deg (fig. 5(b)) the contributions of all the other sources are too close to separate with confidence, but at $\theta = 139$ deg (fig. 5(c)) the shock noises are predicted to be low enough that significant spectral ranges are seen for inner stream mixing noise at middle-to-high frequency and for outer shear layer mixing noise at the highest frequencies. Comparisons of the component levels with the adjusted predictions are shown in figure 6. As illustrated in figure 6(a) the errors associated with not predicting the peak frequency are much greater than for the mixing noises, which have less sharply peaked spectra.

Shock-Free External-Plug Nozzle With Core and Fan Chevrons

A case from reference 18 for a mixed jet velocity near the low end of interest for SBJ applications is shown in figure 7 at four far-field locations: forward quadrant, $\theta = 60$ deg (fig. 7(a)), $\theta = 90$ deg (fig. 7(b)), $\theta = 120$ deg (fig. 7(c)), and near the peak noise angle in aft quadrant at $\theta = 150$ deg (fig. 7(d)). The conditions are essentially the same as for the unsuppressed case in figure 3 except that this is a simulated flight case at $M_f = 0.28$. By comparison with figure 3, it can be seen that the higher frequency components are relatively stronger contributors here. Comparisons of the component spectra with the adjusted predictions are shown in figure 8. In the forward quadrant (fig. 8(a)) the agreement is not quite as good as for the unsuppressed static case at low frequency, and at very high frequency the agreement gets worse with increasing angle, primarily related to the plug separation noise component (figs. 8 (b)–(c)). These issues will be discussed further a later section of this report.

Coannular Plug Nozzle With Both Streams Supersonic

For coannular plug nozzles with both streams supersonic the strongest shocks often appear downstream of the plug tip (ref. 22), as shown at $\theta = 50$ deg, where shock noise is very evident, in figures 9 and 10; the peak frequency is significantly lower than would be predicted for either stream independently. Because of this difference in peak frequency, it is somewhat arbitrarily assumed that the coefficient for outer stream shock noise is 30 dB less than for the plug/downstream shock noise: $C_{O,sh} = C_{D,sh} - 30.0$. The contributions of components other than merged mixing noise and plug/downstream shock noise are relatively small and cannot be unambiguously determined. The extraction process is shown in figure 9, and the comparisons with prediction in figure 10. The agreement is rather good for the two significant noise components.

Coannular Plug Nozzle With Both Streams Supersonic and Convergent-Divergent Terminations

Convergent–divergent (C–D) terminations on coannular nozzles are useful in reducing shock noise, but they no not eliminate it since even at the nominal design point shocks are not completely absent (ref. 22). Component extraction and comparison at $\theta = 50$ deg are shown in figures 11 and 12, respectively for conditions essentially the same as for the convergent termination case shown in figures 9 and 10. The dominant plug/downstream shock noise is reduced by 3 to 4 dB, but the situation is somewhat complicated by what appears to be the presence of a feedback, or "screech" tone at about half the broadband shock noise peak frequency. Such tones are relatively common in model testing, but are not usually observed for nozzles of this type at full scale.

Coannular Plug Nozzle With Both Streams Supersonic and Convergent–Divergent Terminations and Sharp-Tipped Plug

Plug/downstream shock noise can be further reduced if the generally-used truncated plug is replaced by a sharp-tipped plug since it is the downstream shock structure that is important and it is sensitive to tip termination, with the sharp tip providing more complete expansion. Component extraction and comparison at $\theta = 50$ deg are shown in figures 13 and 14, respectively for conditions essentially the same as for the truncated-plug cases shown in figures 9 to 12. Further reduction in broadband plug/downstream shock noise can be seen on the order of 3 dB, but the "screech" tone is not significantly affected, so its relative contribution is greater. If the screech-dominated bands are eliminated, the agreement of component levels with prediction is quite good.

Coannular Plug Nozzle With Outer Stream Suppressor

The unsuppressed inverted velocity ratio (IVP) coannular nozzle offers some acoustic benefits for potential SBJ applications, but it may very well be that additional suppression will be required, and a number of concepts have been investigated. One such concept is the incorporation of mixing-enhancement chutes in the outer stream (ref. 23). Component extraction and comparison for this configuration at high power are shown in figures 15 and 16 for θ = 60, 90 and 120 deg in parts (a), (b) and (c) respectively. Because of the segmentation of the outer flow it appears that the plug/downstream (relatively low frequency) shock noise is not significant but that outer stream (relatively high frequency) shock noise is. At all angles merged mixing noise dominates the low to middle frequency range. The outer stream shock noise dominates the high frequencies at θ = 60 and 90 deg, while at θ = 120 deg its contribution is marginal and only at the highest frequencies. Outer shear layer mixing noise appears to be the dominant high frequency component at θ = 120 deg, while the inner stream mixing noise may contribute in the middle frequency range, particularly at θ = 90 deg. The merged mixing noise and outer stream shock noise models show rather good agreement between experimental/extracted and adjusted prediction levels, while the outer shear layer and inner stream mixing components are more difficult to clearly identify and assess.

COMPONENT CORRELATIONS

The same extraction and coefficient adjustment approach demonstrated in the foregoing section was applied to a more extensive set of data from references 18 and 21 to 24. This includes reevaluation of representative cases previously analyzed in reference 8 to assure that the changes made to the predictive model to cover a wider range of conditions and geometries do not degrade the agreement demonstrated in the earlier comparisons. The baseline (unsuppressed) configurations are considered first, with the expectation that the changes will be minor for the relatively dominant merged mixing and outer shear layer mixing noise components and that some further improvements and/or simplifications may be found for the less dominant components. New correlations for the coefficients are developed in this section.

For all the components, adjusted spectral directivity relations are developed, although these changes for most components are relatively small with respect to the relations of references 8. These tables are given for merged mixing noise in table I, for outer shear layer mixing noise in table II, for inner stream mixing noise in table III, for inner stream plug separation noise in table IV, for plug/downstream shock noise in table V, for outer stream shock noise in table VI, and for inner stream shock noise in table VII.

Note that the effects of nozzle exit mixing enhancement modification are correlated only in terms of influence on levels and not the spectra, so simple “delta” correlations are all that is justified, at present, to represent the observed reductions in merged noise at the expense of small increases in the higher frequency components. However, there is some evidence of small spectral and directivity effects, particularly on merged mixing noise, and an approach to modifying the relations is discussed. As in the previous model (ref. 8), it is assumed, for correlation purposes, that the effects of outer nozzle chevrons is additive to that for inner nozzle chevrons. The

previous relations obtained in reference 8 for chevron effects, with chevron length and angle as correlating parameters, has been recast in terms of perimeter ratio, where the perimeter ratio for each stream is defined as the ratio of the total flow perimeter for that stream divided by the total flow perimeter for the unsuppressed annular passage.

Merged Mixing Noise

In reference 7 several different assumptions regarding the density exponent ω_M were investigated. Because of the range of test conditions included there was a significant range of temperature and velocity, so the method of correlating density effects was quite significant. Considered were $\omega_M = 0.0$, 1.0 and 2.0, as well as the variable ω_M (from eq. (2b)). To get a good correlation using any of the constant ω_M approaches requires a three-segment approach (three regions having different slopes versus velocity), while for the variable ω_M formulation, for up to log $(V_{e,M}/c_{amb}) = 0.10$ (low supersonic) the slope is constant at 90, and as expected at higher supersonic conditions the slope decreases. Since there is a velocity effect included in the ω_M formulation, the small deviation from the 80 slope of Lighthill (refs. 9–10) is quite reasonable. Since the other approaches yield a more complicated velocity relation, the variable exponent approach was selected. It was also found that inner nozzle extension L_I had an influence as a function of velocity ratio, increasing as $5 \log [1 + (V_O/V_I)^2 (L_I/D_{2,I})]$. Based on these considerations, the normalized baseline (unsuppressed) merged mixing noise overall level is defined as follows:

$$\begin{aligned} UOL_{M,Norm} = UOL_M &- 10 \log [(\rho_{amb}/\rho_{ISA})^2 (c_{amb}/c_{ISA})^4] - 10 \log (A_M/R^2) \\ &-10\, \omega_M \log (\rho_M/\rho_{amb}) + 20 \log [(1 + M_{c,M} \cos \theta_{M,cor})^2 + 0.04\, M_{c,M}{}^2] \\ &-5 \log [1 + (V_O/V_I)^2 (L_I/D_{2,I})] \end{aligned} \tag{8}$$

Where, as explained in reference 8:

$$\omega_M = 3 (V_{e,M}/c_{amb})^{3.5}/[0.6 + (V_{e,M}/c_{amb})^{3.5}] - 1 \tag{8a}$$

$$V_{e,M} = V_{mix} [1 - M_f (c_{amb}/V_{mix})]^{1/2} \tag{8b}$$

$$M_{c,M} = n_{c,M} [(V_{mix}/c_{amb}) - M_f] \tag{8c}$$

$$n_{c,M} = 0.4/(1 + 1.5 \{V_O/V_I\}^4) + 0.3 \tag{8d}$$

Values of this normalized merged mixing noise level are plotted against the nondimensionalized effective merged jet velocity parameter log $(V_{e,M}/c_{amb})$ in figure 17. Results for several unsuppressed configurations are shown in figure 17(a). The same two-segment relation as developed in reference 8 is compared with this sampling of baseline data, and most of the data agree rather well. The low value for the "lo V_O" case is not surprising since the outer stream velocity is unrealistically low and is only shown to verify reasonable limiting behavior. The reference 8 relation appears valid (with a slight change in terminology), as follows:

$$\left.\begin{aligned} UOL_{M,Norm} &= 141.5 + 90 \log (V_{e,M}/c_{amb}) \quad \text{for } \log (V_{e,M}/c_{amb}) \le 0.10 \\ UOL_{M,Norm} &= 145.0 + 55 \log (V_{e,M}/c_{amb}) \quad \text{for } \log (V_{e,M}/c_{amb}) > 0.10 \end{aligned}\right\} \tag{9}$$

As mentioned briefly in the foregoing, the relation obtained in reference 8 for chevron effects, with nozzle area ratio, chevron length and chevron angle as correlating parameters, has been recast in terms of perimeter ratios and nozzle bypass ratio, where the perimeter ratio for each stream is defined as the ratio of the total flow perimeter for that stream divided by the total flow perimeter for the unsuppressed annular passage. The resulting relation is as follows:

$$\Delta UOL_M = -45 [\log (PR_I PR_O)]/(1+BPR) \tag{9a}$$

Data for the suppressed configurations is compared with this relation in figure 17(b), where $UOL_{M,Norm} + 45 [\log (PR_I PR_O)]/(1 + BPR)$ is plotted against $\log (V_{e,M}/c_{amb})$. It can be seen that the current relations (eqs. (9)–(9a)) agree reasonably well, actually somewhat better for suppressed than the baseline cases, with the experimental data.

The relative sound pressure level, $SPL_M - UOL_M$, is correlated as a function of the effective directivity angle, θ'_M, and the logarithmic Strouhal number, $\log S_M$, where the Strouhal number is calculated as follows:

$$S_M = (f D_M/V_{e,M}) (T_{mix}/T_{amb})^{0.4 (1 + \cos \theta'_M)} \tag{10}$$

Where D_M is the equivalent diameter based on total fan plus core area and T_{mix} is the mass-averaged total temperature, calculated as follows:

$$T_{mix} = (\rho_I A_I V_I T_I + \rho_O A_O V_O T_O)/(\rho_I A_I V_I + \rho_O A_O V_O) \tag{10a}$$

The effective angle, to account for refraction effects, is calculated as follows:

$$\theta'_M = \theta_{cor,M} (V_{mix}/c_{amb})^{0.1} \tag{10b}$$

It is by use of this effective directivity angle that in a very simple and approximate way refraction is accounted for. It is assumed that the spectra for widely differing jet velocities are similar at this adjusted angle rather than at the same geometric angle. This approach, in conjunction with the analytically modeled convection effect in eq. (8), correlates the variation of SPL with frequency and angle rather well, as shown herein.

An alternative method of correlating the effects of mixing enhancement modifications on noise was briefly considered. It was found feasible to correlate the effects as a change in the effective merged velocity, which would also mean that there would be effects on the convection term based on a change in $M_{c,M}$ and in the refraction effect through θ'_M. The relation for the effective merged velocity would be approximately $V_{mix,eff} = V_{mix}(PR_I PR_O)^{-0.06}$. This appears feasible for the chevron configurations at $V_{mix}/c_{amb} \cong 1.0$, but more comparisons at higher V_{mix} data (and more time) are needed to see if the resulting change in convection effect gives a better correlation than just correlating ΔUOL vs. $PR_I PR_O$. So far it's inconclusive in terms of level and

only weakly supported by spectral directivity; therefore the simple delta correlation is retained at present.

The source location for merged region noise, $X_{s,M}$, is calculated from eq. (4) modified for this component specifically, including the effect of the mixing enhancement modifications, as follows:

$$X_{s,M} = [L_I + (4 + \theta/30)\, D_M\, (PR_I PR_O)^{-0.25}]/LSF \tag{11}$$

Note that the uncorrected angle, θ, is used here to start the correction process (eqs. (1) – (1c)) in closed form.

Spectral directivity comparisons are shown in figure 18 for some of the suppressed configurations. Comparisons for unsuppressed configurations are shown in references 7 and 8, and since the changes in spectral directivity correlations are so minor, they are not repeated herein. Comparisons are shown at four ranges of directivity angle, $\theta'_M \cong 60$, 90, 120 and 150 deg in figures 18 (a)–(d), respectively. There is some evidence of a lower peak frequency and somewhat higher peak level in the forward quadrant (fig. 18 (a)), but this problem is not present at higher angles and is not present at the high mixed jet velocities likely to be of interest for supersonic cruise applications. At $\theta'_M \cong 90$ and 120 deg (figs. 18 (b)–(c)) the agreement is excellent. Even at $\theta'_M \cong 150$ deg where the effects of angle and source location are very strong, the agreement is quite good considering the wide range of configurations, mixed jet velocity and free jet Mach number.

Outer Shear Layer Mixing Noise

There is not enough independent variation of outer stream velocity and temperature in the experimental data to really determine the best approach to correlating density effects. Therefore, as in reference 8, since the variable ω_M relation was found appropriate for merged mixing noise, the analogous assumption is made here, and the variable ω_O is calculated from eq. (2b). Based on these considerations, the normalized baseline (unsuppressed) outer shear layer mixing noise overall level is defined as follows:

$$\begin{aligned} UOL_{O,Norm} = UOL_O &- 10 \log [(\rho_{amb}/\rho_{ISA})^2\, (c_{amb}/c_{ISA})^4] - 10 \log (A_O/R^2) \\ &- 10\, \omega_O \log (\rho_O/\rho_{amb}) + 20 \log [(1 + M_{c,O} \cos \theta_{O,cor})^2 + 0.04\, M_{c,O}{}^2] \end{aligned} \tag{12}$$

Where, as explained in reference 8:

$$\omega_O = 3\, (V_{e,O}/c_{amb})^{3.5}/[0.6 + (V_{e,O}/c_{amb})^{3.5}] - 1 \tag{12a}$$

$$V_{e,O} = V_O\, [1 - M_f\, (c_{amb}/V_O)]^{1/2} \tag{12b}$$

$$M_{c,O} = n_{c,O}\, [(V_O/c_{amb}) - M_f] \tag{12c}$$

$$n_{c,O} = 0.3/(1 + \{V_O/V_I\}^2) + 0.35 \quad (12d)$$

Results for several unsuppressed configurations are shown in figure 19(a). For a wide range of configurations and test conditions, the relatively simple correlation of reference 8 agrees well, as follows:

$$UOL_{O,Norm} = 133.0 + 75 \log (V_{e,O}/c_{amb}) \quad (13)$$

The effects of mixing enhancement chevrons on the inner and outer nozzle exits are to increase outer shear layer noise slightly. For the effect of chevrons or other nozzle exit mixing enhancement modifications:

$$\Delta UOL_O = 3.37 \log (PR_I PR_O) \quad (13a)$$

Data for the suppressed configurations is compared with this relation in figure 19(b), where $UOL_{O,Norm} - 3.37 \log (PR_I PR_O)$ is plotted against $\log (V_{e,O}/c_{amb})$. It can be seen that the current relations (eqs. (13)–(13a)) agree reasonably well with the experimental data.

The relative sound pressure level, $SPL_O - UOL_O$, is correlated as a function of the effective directivity angle θ'_O and the logarithmic Strouhal number $\log S_O$, where the Strouhal number is calculated as follows:

$$S_O = (f D_{2,O}/V_{e,O}) (T_O/T_{amb})^{0.4 (1 + \cos \theta'_O)} \quad (14)$$

Where $D_{2,O}$ is the fan (outer stream) nozzle outer diameter and T_O is the fan (outer stream) total temperature. The effective angle, to account for refraction effects, is calculated as follows:

$$\theta'_O = \theta_{cor,O} (V_O/c_{amb})^{0.1} \quad (14a)$$

These spectral directivity tables are developed iteratively as discussed later in this report.

No effect of the mixing devices is expected on the location for outer shear layer noise, $X_{s,O}$, calculated as follows:

$$X_{s,O} = (\theta/45) D_{2,O}/LSF \quad (15)$$

Again, note that the uncorrected angle, θ, is used here to start the correction process in closed form.

Spectral directivity comparisons are shown in figure 20 for some of the suppressed configurations. Comparisons for unsuppressed configurations are shown in references 7 and 8, and since the changes in spectral directivity correlations are so minor, they are not repeated herein. Comparisons are shown at four ranges of directivity angle, $\theta'_O \cong 70$, 100, 130 and 160 deg in figures 20 (a)–(d), respectively. Since other components always contribute significantly where outer shear layer noise is the strongest source, there is more scatter than for merged mixing noise, but in general the agreement is fairly good except at the aft-most angles

(fig. 20 (d)) where merged noise is always dominant in terms of both OASPL and Perceived Noise Level.

Inner Stream Mixing Noise

A significant change from the early model (ref. 7) was made here in reference 8; it was found that much better agreement is obtained if the characteristic velocity $V_{I/O}$ is taken to be the larger of V_O and V_I, and that the overall level correlates reasonably well with $\omega_I = 0.0$. Our original attempts to correlate this component used a velocity difference term, $|V_O - V_I|$, but it was found that this component was present even as the difference term approached zero, so the more complicated form gradually evolved (refs. 7–8). It is interesting to note that in developing a prediction procedure for conventional velocity profile coannular nozzles, Fisher, et al (refs. 25–26) found that a term dependent on V_I was needed. Based on these considerations, the normalized baseline (unsuppressed) outer shear layer mixing noise overall level (fig. 21) is defined as follows:

$$UOL_{I,Norm} = UOL_I - 10 \log [(\rho_{amb}/\rho_{ISA})^2 (c_{amb}/c_{ISA})^4] - 10 \log (A_I/R^2) + 20 \log [(1 + M_{c,I} \cos \theta_{I,cor})^2 + 0.04 M_{c,I}^2] \quad (16)$$

Where:

$$V_{I/O} = MAX (V_O, V_I) \quad (16a)$$

$$V_{e,I} = V_{I/O} [1 - M_f (c_{amb}/V_{I/O})]^{1/2} \quad (16b)$$

$$M_{c,I} = n_{c,I} [(V_{I/O}/c_{amb}) - M_f] \quad (16c)$$

$$n_{c,I} = 0.3/(1 + 0.5 \{V_O/V_I\}^2) + 0.3 \quad (16d)$$

It was found in reference 8 that the overall level correlates reasonably well with $N_I = 75$ with an additional two-segment BPR effect. In the current analysis, with what is thought to be a better breakdown of the various components, this BPR effect is no longer seen. Even though there is significant scatter in the component coefficients, since this component is dominant only for a few limited cases, the corresponding total levels do not disagree nearly so much with prediction. A relatively simple correlation results, as can be seen in figure 21(a):

$$UOL_{I,Norm} = 129.0 + 75 \log (V_{e,I}/c_{amb}) \quad (17)$$

The effects of mixing enhancement chevrons on the inner and outer nozzle exits are to decrease inner stream mixing noise. Since this component is often difficult to isolate, for the present it is approximated that the effects are the same as for merged mixing noise, as follows:

$$\Delta UOL_I = -45 [\log (PR_I PR_O)]/(1+BPR) \quad (17a)$$

Data for the suppressed configurations is compared with this relation in figure 21(b), where $UOL_{I,Norm} + 45\ [\log (PR_I PR_O)]/(1+BPR)$ is plotted against $\log (V_{e,I}/c_{amb})$. It can be seen that the current relations (eqs. (17) – (17a)) agree reasonably well with the experimental data. Any further effects of mixing enhancement on this component are not significant for the configurations and cycle conditions tested, where this component is not a major contributor. Additional testing would be required to quantify any further effects.

The relative sound pressure level, $SPL_I - UOL_I$, is correlated as a function of the effective directivity angle θ'_I and the logarithmic Strouhal number $\log S_I$, where the Strouhal number is calculated as follows:

$$S_I = (f\ D_{2,I}/V_{e,I})\ (T_I/T_O)^{0.4\ (1\ +\ \cos\ \theta'_I)} \tag{18}$$

Where $D_{2,I}$ is the inner stream nozzle outer diameter and T_I is the core (inner stream) total temperature. The effective angle, to account for refraction effects, is calculated as follows:

$$\theta'_I = \theta_{cor,I}\ (V_{e,I}/c_{amb})^{0.1} \tag{18a}$$

The spectral directivity comparisons for the suppressed configurations are not shown since the spectral range is very limited in most cases and the scatter relatively large. Comparisons for unsuppressed configurations are shown in references 7 and 8, and since the changes in spectral directivity correlations are so minor, they are not repeated herein.

No effect of the mixing devices is expected on the location for source location for inner stream mixing noise, $X_{s,I}$, calculated as follows:

$$X_{s,I} = [L_I + (\theta/45)\ D_{h,I}]/LSF \tag{19}$$

Again, note that the uncorrected angle, θ, is used here to start the correction process in closed form.

Inner Stream Plug Separation Noise

This component appears strongly only for high bypass ratio and low mixed jet velocity, and therefore is not likely to be a significant problem for a small supersonic cruise aircraft, but it is included since it is a marginal contributor for some of the comparisons shown herein. There is also a concern as to whether the high frequency noise is really due to flow separation from the plug or whether it might be due to upstream sources such as valve noise; the fact that the component coefficients required to correlate the experimental data are about 10 dB less for the LaRC facility (ref. 27) than for the GRC facility (ref. 18) supports this notion.

Current model—Comparisons strongly indicate that better correlation is obtained for $\omega_P = 2.0$. Therefore, the normalized baseline (unsuppressed) outer shear layer mixing noise overall level is defined as follows:

$$UOL_{P,Norm} = UOL_P - 10 \log [(\rho_{amb}/\rho_{ISA})^2 (c_{amb}/c_{ISA})^4] - 10 \log (A_I/R^2) - 20 \log (\rho_I/\rho_O) + 20 \log [(1 + M_{c,P} \cos \theta_{P,cor})^2 + 0.04 M_{c,P}^2] + 50 \log (1 + L_P/D_{2,I}) \quad (20)$$

Where L_P is the plug length (beyond the inner nozzle exit) and

$$M_{c,P} = 0.62 [(V_{e,P}/c_O) - M_f] \quad (20a)$$

The determination of the effective velocity, $V_{e,P}$, for this component is quite difficult, as discussed in more detail in references 5 and 6, and the following simple relation is currently employed:

$$V_{e,P} = V_I \quad (20b)$$

For the three unsuppressed configurations tested with plugs at GRC (ref. 18) the data shown in figure 22(a) agree reasonably well with the following simple correlation expression:

$$UOL_{P,Norm} = 158.0 + 50 \log (V_{e,P}/c_O) \quad (21)$$

Behavior of this sort would be consistent with plug separation noise, which Olsen and Karchmer (ref. 28) found to be potentially significant for plug nozzles. The effects of mixing enhancement devices, chevrons in these configurations, on the inner and outer nozzle exits are to increase outer shear layer noise. The correlations are based partially on more extensive comparisons (ref. 6). The effect of the nozzle mixing enhancement modifications is shown in figure 22(b); it appears that any effects are on the same order as the data scatter, so with all the uncertainties regarding this component, the predictive model now includes no effect of the mixing enhancement devices on level or spectra.

The relative sound pressure level, $SPL_P - UOL_P$, is correlated as a function of the effective directivity angle θ'_P and the logarithmic Strouhal number $\log S_P$, where the Strouhal number is calculated as follows:

$$S_P = (2 f r_{pt}/V_{e,P}) (T_I/T_O)^{0.4 (1 + \cos \theta'_P)} \quad (22)$$

Where r_{pt} is the inner stream nozzle plug tip radius and T_I is the core (inner stream) total temperature. The effective angle, to account for refraction effects, is calculated as follows:

$$\theta'_P = \theta_{cor,P} (V_{e,P}/c_{amb})^{0.1} \quad (22a)$$

The spectral directivity comparisons for the suppressed configurations are not shown since the spectral range is very limited in most cases and the scatter relatively large. Comparisons for unsuppressed configurations are shown in references 7 and 8, and since the changes in spectral directivity correlations are so minor, they are not repeated herein.

No effect of the mixing devices is expected on the source location. The source location for inner stream plug separation noise, $X_{s,P}$, is as follows:

$$X_{s,P} = [L_I + L_P + 2\,(\theta/45)\,r_{pt}]/LSF \qquad (23)$$

Alternative model—As mentioned earlier, the evidence that this component is due to plug separation and correlates with plug separation parameters is clouded by the fact that error-prone high frequency data are involved. It is also troubling that the implied level coefficient C_P is significantly less for the cases from the LaRC facility (ref. 27) than those from the GRC facility (ref. 18). In particular, Strouhal-type scaling of the frequency spectra in terms of the plug separation parameter utilized herein is not very convincing. Therefore, we offer an alternative approach that is not currently included as an option in the predictive model.

In the process of adjusting the levels of the various noise components it became apparent that for some cases, the peak frequency of the predicted plug separation noise was too high when using the current model. An obvious example of this is shown in figure 23 (a). For this baseline static condition and angle, the predicted plug separation noise peaks at 16,000 Hz even though the data show evidence of a peak at 5000 Hz. To investigate this problem, the peak frequency was shifted by modifying the Strouhal number corresponding to 100 Hz. It was found that a fixed Strouhal number of 0.025 at f = 100 Hz worked for nearly all conditions examined. An example of this is shown in figure 23 (b), for the same conditions as figure 23 (a). In both figures 23 (a) and (b), the level of the plug separation noise was adjusted such that the predicted total spectra would agree with the data at this angle. The predicted levels of the other sources are the same for both figures. Other examples comparing the existing model and the model with the revised Strouhal number are shown in figures 24 and 25. For the last case shown, the predicted peak frequency, using the current model, agrees well with that inferred from the data. For this case the 100 Hz. Strouhal number equals 0.027 using the current model. Thus changing it to 0.025 provides little improvement. For the other cases presented, the modification to the Strouhal number results in a noticeable improvement in the prediction of this source.

To further investigate the characteristics of this source, the directivity and level of the source were analyzed. The levels of the plug separation noise were determined by subtracting the predicted mean square pressure of the other sources from the measured mean square pressure. These values were then used to calculate the dB levels of the plug separation source. In figure 26, the peak 1/3 octave level at 90 degrees is plotted against the log of the primary jet velocity. A curve fit to the data is also shown. The curve fit indicates that the levels correlate with primary velocity squared. No trend with free jet Mach number or configuration is obvious.

Examination of the data at angles other than 90 degrees reveals that a modification to the directivity of this source is also needed. With the exception of $M_f = 0.28$, for which there is some scatter, the data tend to follow a similar directivity pattern for each Mach number independent of configuration or flow condition. The only systematic variation is with free jet Mach number. The effect of increasing free jet Mach number is to increase the levels in the forward quadrant and to decrease the in the rear. The variation of directivity with simulated flight Mach number appears to be reasonably well predicted by subtracting 40 log $(1 - M_f \cos \theta)$ from the directivity at $M_f = 0$. This is typical of the effect associated with dynamic flight amplification and has traditionally been used to correlate the flight effect on internal noise sources.

A limited examination of peak frequency and spectra shape at angles other than 90 degrees indicated that there was little variation with geometry or condition. The peak frequency varied very little with angle, however some indication of a Doppler frequency shift was present. It also appeared that the current source spectral shape at 90 degrees could be used for all angles.

This alternate model for the plug separation source has only been applied to a limited number of test conditions and except for the examination of directivity was not evaluated in detail at angles other then 90 degrees. Further, application of the new model could result in some minor modifications to the other sources especially the high frequency portion of the outer mixing source spectra. Modifications to that source could result in changes to the inferred level of the plug separation source. Thus conclusions regarding the directivity and level variation with test conditions could change.

Although the alternate model for the plug separation noise appears to provide better agreement with data, it does little to clarify the mystery as to the actual source of this noise. In fact it may actually increase the uncertainty. The lack of variation of peak frequency with jet velocity would tend to infer that this is not a jet aerodynamic source. The low exponent correlation with jet velocity is also not consistent with jet aerodynamic sources, although little is known from past research regarding the dependence of separation noise on aerodynamic variables. The Doppler amplification effect on directivity would be consistent with an internal noise source. Thus this alternate model for this source appears to conflict with the conclusion that this source is due to separation on the plug, but does little to identify an alternative explanation.

Plug/Downstream Shock Noise

For the cases investigated to the present, it appears that this noise component only occurs when there is a plug present, both streams are supersonic with $P_O \geq P_I$, and there are no noise suppression modifications to the nozzle exit planes that might prevent this shock interaction process. Eq. (5) is made specific to this source, as follows:

$$OASPL_{D,sh} = C_{D,sh} + 10 \log [(\rho_{amb}/\rho_{ISA})^2 (c_{amb}/c_{ISA})^4] + 10 \log (A_M/R^2) + 10 \log \{\beta_D^4/(1 + \beta_D^4)\} - 40 \log (1 - M_f \cos \theta) - F (\theta - \theta_{M,D}) \quad (24)$$

Where A_M is the appropriate area, and

$$\beta_D = [(M_D^2 - M_{d,D}^2)^2 + 0.01 M_{d,D}/(1 - D_{1,I}/D_{2,O})]^{1/4} \quad (24a)$$

Where M_D is the Mach number based the mass-averaged specific heat ratio and the area-weighted pressure ratio, and $M_{d,D}$ is the design Mach number, calculated as follows:

$$M_{d,D} = (1 - 0.5\{1 - 2r_{pt}/D_{2,O,ex}\})(M_{d,I} + M_{d,O} BPR)/(1 + BPR) + 0.5\{1 - 2r_{pt}/D_{2,O,ex}\} M_D \quad (24b)$$

This formulation accounts for the reduction in shock strength due to both C–D exits and a sharp plug tip. $D_{1,I}$ is the inner diameter of the inner-stream nozzle and $D_{2,O}$ is the outer diameter of the outer-stream nozzle. The Mach angle is denoted by $\theta_{M,D}$, calculated as follows:

$$\theta_{M,D} = 180 - \sin^{-1}(1/M_D) \quad \text{(in degrees)} \tag{24c}$$

The term $F(\theta - \theta_{M,D})$ is calculated as follows:

$$\left.\begin{aligned} F(\theta - \theta_{M,D}) &= 0.0 \ \text{ for } \theta < \theta_{M,D} \\ F(\theta - \theta_{M,D}) &= 0.75(\theta - \theta_{M,D}) \ \text{ for } \theta \geq \theta_{M,D} \end{aligned}\right\} \tag{24d}$$

Where M_D is calculated from the mass-averaged specific heat ratio and the area-weighted pressure ratio, and the design Mach number M_d is $M_{d,D}$, as calculated above (eq. (24b)). The relation found appropriate for the coefficient $C_{D,Sh}$ is as follows:

$$C_{D,sh} = 164.5 - 50 \log [1 + (D_{1,I}/D_{2,O})^2] \tag{24e}$$

The Strouhal number is calculated from eq. (6) with the appropriate variables, as follows:

$$S_{D,sh} = [f\beta_D D_{h,D}/(0.7V_D)](1 - M_f \cos\theta)\{[1 + (0.7V_D/c_{amb})\cos\theta]^2 + 0.04(0.7V_D/c_{amb})^2\}^{1/2} \tag{25}$$

Where $D_{h,D}$ is the "total" hydraulic diameter, $4(A_{I,ex} + A_{O,ex})/[\pi(D_{1,I} + D_{2,O})]$, and V_D is calculated from M_D and the mass-averaged total temperature.

The source location for shock noise, $X_{s,D,sh}$, is taken to be as follows:

$$X_{s,D,sh} = [L_P + L_I + 2 D_M (M_D^2 - 1)^{1/2}]/LSF \tag{26}$$

Outer Stream Shock Noise

Outer stream shock noise is present only when plug/downstream shock noise is absent. To calculate outer stream shock noise, eq. (5) is made specific to this source, as follows:

$$OASPL_{O,sh} = C_{O,sh} + 10 \log [(\rho_{amb}/\rho_{ISA})^2 (c_{amb}/c_{ISA})^4] + 10 \log (A_O/R^2) + 10 \log \{\beta_O^4/(1 + \beta_O^4)\} - 40 \log (1 - M_f \cos\theta) - F(\theta - \theta_{M,O}) \tag{27}$$

Where the subscript O refers to the outer stream. The shock strength parameter β_O is calculated as follows:

$$\beta_O = [(M_O^2 - M_{d,O}^2)^2 + 0.01 M_{d,O}/(1 - D_{1,O,ex}/D_{2,O,ex})]^{1/4} \tag{27a}$$

Where M_O is the outer stream Mach number expanded to ambient conditions and $M_{d,O}$ is the outer stream nozzle design Mach number. $D_{1,O,ex}$ is the outer stream nozzle exit inner diameter and $D_{2,O,ex}$ is the outer stream nozzle exit outer diameter. The Mach angle is denoted by $\theta_{M,O}$, calculated as follows:

$$\theta_{M,O} = 180 - \sin^{-1}(1/M_O) \quad \text{(in degrees)} \tag{27b}$$

The term $F(\theta - \theta_{M,O})$ is calculated as follows:

$$\left.\begin{aligned} F(\theta - \theta_{M,O}) &= 0.0 && \text{for } \theta < \theta_{M,O} \\ F(\theta - \theta_{M,O}) &= 0.75(\theta - \theta_{M,O}) && \text{for } \theta \geq \theta_{M,O} \end{aligned}\right\} \quad (27c)$$

Results reported by Viswanathan (ref. 29) as this task neared completion indicate that outer stream shock noise may remain a significant contributor in the rear quadrant, so this term may need reevaluation in the future, but this is not surprising since this term was developed arbitrarily to give proper limiting behavior.

The relation found appropriate for the coefficient $C_{O,sh}$ is dependent on geometry and whether or not the inner stream is supersonic, as follows (as in ref. 8):

$$\left.\begin{aligned} C_{O,sh} &= 168.0 - 60 \log [1 + (D_{1,O,ex}/D_{2,O,ex})^2] && \text{for } M_I \geq 1.0 \\ C_{O,sh} &= 163.5 - 45 \log [1 + (D_{1,O,ex}/D_{2,O,ex})^2] && \text{for } M_I < 1.0 \end{aligned}\right\} \quad (27d)$$

The Strouhal number is calculated from eq. (6) modified and with the appropriate variables, as follows:

$$S_{O,sh} = [f\beta_O(D_{h,O}{}^{0.9} D_{eq,O}{}^{0.1})/(0.7V_O)](1 - M_f \cos\theta)\{[1 + (0.7\, V_O/c_{amb})\cos\theta]^2 + 0.04\,(0.7\, V_O/c_{amb})^2\}^{1/2} \quad (28)$$

The source location for shock noise, $X_{s,O,sh}$, is taken to be as follows:

$$X_{s,O,sh} = [2\, D_{h,O}\,(M_O{}^2 - 1)^{1/2}]/LSF \quad (29)$$

Inner Stream Shock Noise

To calculate inner stream shock noise, eq. (5) is made specific to this source, as follows:

$$OASPL_{I,sh} = C_{I,sh} + 10 \log [(\rho_{amb}/\rho_{ISA})^2 (c_{amb}/c_{ISA})^4] + 10 \log (A_I/R^2) + 10 \log \{\beta_I{}^4/(1 + \beta_I{}^4)\} - 40 \log (1 - M_f \cos\theta) - F(\theta - \theta_{M,I}) \quad (30)$$

Where the subscript I refers to the inner stream. The shock strength parameter β_I is calculated as follows:

$$\beta_I = [(M_I{}^2 - M_{d,I}{}^2)^2 + 0.01\, M_{d,I}/(1 - D_{1,I,ex}/D_{2,I,ex})]^{1/4} \quad (30a)$$

Where M_I is the inner stream Mach number expanded to ambient conditions and $M_{d,I}$ is the inner stream nozzle design Mach number. $D_{1,I,ex}$ is the inner stream nozzle exit inner diameter and $D_{2,I,ex}$ is the inner stream nozzle exit outer diameter. The Mach angle is denoted by $\theta_{M,I}$, calculated as follows:

$$\theta_{M,I} = 180 - \sin^{-1}(1/M_I) \qquad \text{(in degrees)} \tag{30b}$$

The term $F(\theta - \theta_{M,I})$ is calculated as follows:

$$\left.\begin{aligned} F(\theta - \theta_{M,I}) &= 0.0 && \text{for } \theta < \theta_{M,I} \\ F(\theta - \theta_{M,I}) &= 0.75(\theta - \theta_{M,I}) && \text{for } \theta \geq \theta_{M,I} \end{aligned}\right\} \tag{30c}$$

Inner stream shock noise is shown to correlate reasonably well with a constant coefficient for the plugless configurations (ref. 21). Previous experience indicates that nozzle diameter ratio is a factor, so the relation recommended is as follows:

$$C_{I,sh} = 158.0 - 50 \log\left[1 + (D_{1,I,ex}/D_{2,I,ex})^2\right] \tag{30d}$$

The Strouhal number is calculated from eq. (6) modified and with the appropriate variables, as follows:

$$S_{I,sh} = [f\beta_I D_{h,I}/(0.7V_I)](1 - M_f \cos\theta)\{[1 + (0.7V_I/c_{amb})\cos\theta]^2 + 0.04(0.7V_O/c_{amb})^2\}^{1/2} \tag{31}$$

The source location for shock noise, $X_{s,O,sh}$, is taken to be as follows:

$$X_{s,I,sh} = [L_I + 2\,D_{h,I}(M_I^2 - 1)^{1/2}]/LSF \tag{32}$$

Comparisons With Finalized Model

A number of comparisons are presented for a wide range of geometries and test conditions to demonstrate the degree of agreement between the finalized model and experimental data. The conditions chosen are in or near the range of interest for SBJ application.

Baseline Cases

Baseline coannular nozzle comparisons are shown for high subsonic mixed velocity cases where there is no shock noise and other higher velocity cases where shock noise is present. The validity of the flight effects relations are also demonstrated with simulated flight data. First, for the relatively high bypass (BPR about 5) static case at high mixed velocity but shock-free conditions, $V_{mix}/c_{amb} = 1.09$, the experimental OASPL directivity data are compared with prediction in figure 27. The prediction is that merged mixing noise strongly dominates the OASPL. The agreement is very good except at the most aft angles, where the experimental data exhibit a sharper drop-off than the prediction; it is in this range where the source location can have a very strong influence. Even with this problem, the RMS error between experimental and predicted OASPL is 1.5 dB. Spectral comparisons for this case are shown in figure 28. The low-frequency noise is slightly under-predicted at $\theta = 60$ (fig. 28 (a)), and is over-predicted at very high frequency in all cases. Except for the highest frequencies, the agreement at $\theta = 90$ and

120 (figs. 28 (b)–(c)) is excellent. At $\theta = 150$ deg (fig. 28 (d)) the noise is somewhat over-predicted across the spectrum. Considering the data at all angles, $55 \le \theta \le 160$ deg, and from 50 Hz $\le f \le 4$ kHz the RMS error is 2.0 dB.

For essentially the same conditions, but in simulated flight at $M_f = 0.28$, the OASPL comparison is shown in figure 29. The agreement seen is very similar to that for the static case (fig. 27) and the RMS error is the same, 1.5 dB. However, the deviation that is again only significant at aft angles is different in sign; here the noise is under-predicted at aft angles and the experimental data do not exhibit the expected peak. We feel that although the changes we have introduced to correct the experimental data for the effect of source location on shear layer effects, these aspects of the problem, source distribution and shear layer transmission effects, deserve further attention. Spectral comparisons are shown in figure 30. Agreement is not quite as good as in the static case (fig. 28) at $\theta = 60$, 90 and 120 deg (figs. 30 (a)–(c)) across most of the spectra, but at high frequencies the agreement here is actually somewhat better, at least qualitatively, in that the predicted upturn is observed. At $\theta = 150$ (fig. 30 (d)) the agreement over most of the spectrum is much better that the static case, but again there is a significant over-prediction at high frequency. Considering the data at all angles, $55 \le \theta \le 165$ deg, and from 50 Hz $\le f \le 4$ kHz the RMS error is 1.6 dB, which is excellent for comparisons of this type.

A very high velocity IVP case with shock noise (from ref. 21) is considered in figure 31 with spectral comparisons at three angles, outer stream shock noise is predicted to be dominant at $\theta = 46$ and 95 deg (figs. 31 (a)–(b)), while at $\theta = 139$ deg merged mixing noise is predicted to dominate at low to middle frequencies, while inner stream and outer shear layer dominate the middle-to-high and highest frequency ranges, respectively. The agreement is quite good in all cases. Considering the full spectral range from 100 Hz $\le f \le 80$ kHz at these three angles, the RMS error is 2.0 dB, which is probably as good as can be expected for these data obtained over 20 years ago using a combination of ground-level and centerline-level microphones analytically corrected and "patched" through the middle frequency range to provide approximately free-field spectra.

The final baseline case is from General Electric's anechoic free-jet facility for a high velocity IVP coannular plug nozzle with both streams supersonic at $M_f = 0.0$ (ref. 24), under conditions where plug/downstream shock noise is expected to contribute significantly. An OASPL comparison is shown in figure 32. The agreement is qualitatively similar to that seen for the lower-velocity shock-free case in figure 27, and the RMS error is OASPL 1.4 dB. (Frequencies where screech tones are present or there are other obvious problems with the experimental data have been removed from the error calculation.) Spectral comparisons are shown in figure 33. At $\theta = 50$ deg (fig. 33 (a)) there is a very obvious screech tone affecting the 125 and 160 Hz bands; aside from this and a modest over-prediction of the plug/downstream shock noise, the agreement is rather good. The screech is not as evident at $\theta = 80$ deg (fig. 33 (b)), but otherwise the same observations are appropriate. At $\theta = 120$ deg (fig. 33 (c)), where there are no screech tones, the agreement is excellent. The agreement is also good up to 1 kHz at $\theta = 150$ deg (fig. 33 (d)) and is not too bad at higher frequency. For the full angular range, $40 \le \theta \le 80$ and $100 \le \theta \le 160$, editing out screech and high-frequency problems, for the range from $50 \le f \le 4$ kHz the RMS error is 2.1 dB.

Core Chevrons

The comparisons shown for the core chevron nozzle of reference 18 are all at the highest mixed jet velocity. The OASPL directivity comparison under static conditions is shown in figure 34 for V_{mix}/c_{amb} = 1.04, and the RMS error is OASPL 1.1 dB. Except for the sight under-prediction in the forward quadrant, the agreement is very good. Spectral comparisons are shown in figure 35. There is an under-prediction at low frequency, or perhaps an anomalous source with a relatively sharp peak, in the forward quadrant (θ = 60 deg, fig. 35 (a)), and there is weak evidence of this problem at (θ = 90 deg, fig. 35 (b)). At θ = 120 deg (fig. 35 (c)) the agreement is excellent, while at θ = 150 deg (fig. 35 (d)) the low frequency peak is predicted well, with middle and high frequency levels being somewhat over-predicted. Considering the data at all angles, $55 \le \theta \le 160$ deg, and from 50 Hz $\le f \le$ 4 kHz the RMS error is 2.2 dB.

For essentially the same conditions (V_{mix}/c_{amb} = 1.07), but in simulated flight at M_f = 0.28, OASPL directivity comparisons are shown in figure 36. The agreement seen is similar to that for the static case and the RMS error is slightly higher, 1.4 dB. As for the unsuppressed case (fig. 29) the deviation is most significant at aft angles, where the experimental data do not exhibit the expected peak. Spectral comparisons shown in figure 37 are qualitatively similar to those under static conditions (fig. 35); statistically the agreement is somewhat better, with an RMS error of 1.6 dB over the full angular range from $55 \le \theta \le 160$ deg and frequency 50 Hz $\le f \le$ 4 kHz.

Next, comparisons are shown for a slightly different configuration, a core petal internal-plug nozzle (ref. 27). These tests were conducted with the microphone array relatively closer to the model than in the GRC facility (ref. 18), so the importance of the source location models is increased. The OASPL directivity comparison at V_{mix}/c_{amb} = 0.975 and M_f = 0.10 is shown in figure 38. The experimental data show essentially a constant level in the forward quadrant, contrary to expectations and other test results; this could be related to modest levels of excess noise from the upstream fluid supply systems or the free jet itself. Spectral comparisons are shown in figure 39. In the forward quadrant at θ = 58 deg (fig. 39 (a)) the experimental data fall well above the prediction over the low and middle frequency range, but at θ = 92 deg (fig. 39 (b)) the discrepancy is small. For some conditions relatively sharp low frequency peaks can be seen in the forward quadrant, so for statistical comparisons low frequencies are eliminated (up to 800 Hz at θ = 48 deg, gradually reducing to include the full experimental range at θ = 102 deg). Under these restrictions, and with the rear quadrant agreement rather good, the RMS error in OASPL (fig. 38) is 1.8 dB. The spectral agreement is also good at θ = 122 and 157 deg (figs. 39 (c)–(d)), and the RMS error is 1.8 dB, again subject to the low frequency restrictions mentioned above. The agreement in the rear quadrant is particularly supportive of the general validity of the source location model.

Combined Core and Fan Chevrons

With the success demonstrated above in predicting the acoustic performance of core nozzle chevrons and petal suppressors, comparisons are next made with the combined core and fan

chevron configuration of reference 18, again at the highest mixed jet velocities reported but without shock noise. OASPL comparisons at static conditions are shown in figure 40; agreement is very good except for the under-prediction (or slightly contaminated experimental) data in the forward quadrant. Even with the forward quadrant disagreement, the RMS error is a very good 1.2 dB. The forward quadrant experimental spectrum (θ = 60 deg, fig. 41 (a)) exhibits a higher than predicted level and a lower than predicted peak frequency; this trend is essentially eliminated at θ = 90 deg (fig. 41 (b)). It is quite likely that the forward quadrant disagreement is due to some excess noise in the experimental data. The agreement is excellent at θ = 90 deg and 120 deg (figs. 41 (b)–(c)) and is still rather good, especially in the peak region, at θ = 150 deg (fig. 41 (d)). Over the full angular range from $55 \leq \theta \leq 160$ deg and frequency $50 \text{ Hz} \leq f \leq 4$ kHz, the RMS error is 2.1 dB.

The corresponding simulated flight comparisons for OASPL directivity are shown in figure 42. Much like the unsuppressed and core chevron comparisons, general agreement is fairly good, but the experimental data do not exhibit the expected peak. The RMS error in OASPL is 1.5 dB. Spectral comparisons are shown in figure 43. The forward quadrant (θ = 60 deg, fig. 43 (a)) agreement is a little better at low frequency but not as good at high frequency relative to the unsuppressed and core chevron cases. At θ = 90 deg (fig. 43 (b) the agreement is good, but the experimental spectrum is a little flatter than predicted; similar agreement is seen at θ = 120 and 150 deg (figs. 43 (c)–(d)). Over the full angular range from $55 \leq \theta \leq 165$ deg and frequency $50 \text{ Hz} \leq f \leq 4$ kHz, the RMS error is 2.1 dB.

20-Chute Outer Stream Suppressor

The final comparisons shown herein are for a 20-chute outer stream suppressor applied to an IVP coannular nozzle. Even though simulated flight data are available in reference 23, only static comparisons are shown at present, since the free jet to flight transformation procedure used therein did not account for source locations and used a different methodology also. In references 7 and 8 the methodology used in reference 23 and that of reference 17, both with source locations at the nozzle exit plane, were shown to give significantly different results. It would be valuable to reanalyze some of these data using the current approach, but is not possible within the current resource restraints.

Spectral comparisons are for takeoff power, $V_{mix}/c_{amb} = 2.19$, at θ = 60, 90 and 120 deg in figures 44 (a)–(c), respectively. In the forward quadrant (fig. 44 (a)) outer stream shock noise controls the OASPL and PNL, while merged mixing noise controls the lower frequency range; agreement between experiment and prediction is very good. At θ = 90 deg (fig. 44 (b)), the same two components are dominant, but outer shear layer noise may contribute marginally; again the agreement between experiment and prediction is very good. In the rear quadrant, at θ = 120 deg (fig. 44 (c)) merged mixing noise and outer shear layer mixing noise are predicted to be dominant, but the agreement is not as good as at the lower angles. Overall, for these three angles plus θ = 110 deg, the RMS error is 1.2 dB in OASPL and 1.8 dB in all SPLs.

Analogous comparisons for cutback power, V_{mix}/c_{amb} = 1.92, are shown in figure 45. The agreement at θ = 60 deg (fig. 45 (a)), where outer stream shock noise is dominant, is very good, as it was at higher power. At θ = 90 deg (fig. 45 (b)), where the mixing noise become more important, the agreement is not quite as good as at higher power. At θ = 120 deg (fig. 45 (c)) the agreement is similar to that seen at higher power. It appears that the component prediction causing the inaccuracy is the outer shear layer mixing noise. Overall, for these three angles plus θ = 110 deg, the RMS error is 0.5 dB in OASPL and 1.8 dB in all SPLs.

Concluding Remarks

The predictive tool developed herein for coannular nozzles with noise suppression features is shown to agree well with a wide range of experimental data for subsonic and supersonic exhaust conditions from several static and simulated flight model test facilities. This model should enable reasonably accurate jet noise prediction for the range of propulsion systems under consideration for supersonic business jet application. This capability includes devices providing moderate levels of jet noise suppression. For applications requiring more aggressive suppression approaches, the two-dimensional mixer ejector predictive model is available in NASA Langley's *Aircraft Noise Prediction Program (ANOPP)* and in NASA Glenn's *FOOTPR* code.

Further comparisons with experimental data from a wider range of sources and statistical evaluation of the predictive model would be valuable follow-on activities and would likely lead to further improvement. However, the most important follow-on activity would be to conduct comparisons with larger-scale flight data.

REFERENCES

1. Clark, B.J., "Computer Program to Predict Aircraft Noise Levels," NASA TP-1913, September 1981.
2. Stitt, L.E., "Exhaust Nozzles for Propulsion Systems with Emphasis on Supersonic Cruise Aircraft," NASA RP-1235, May 1990.
3. Zorumski, W.E., "Aircraft Noise Prediction Program Theoretical Manual," NASA TM-83199, Parts 1 and 2, February 1982.
4. Stone, J.R., and Clark, B.J., "Development of a Noise Prediction Code for 2-D Mixer Ejector Nozzle Systems, I – Effects of Principal Geometric Variables," Modern Technologies Corporation Report to General Electric Aircraft Engines, December 30, 1996.
5. Stone, J.R., Krejsa, E.A. and Clark, B.J., "Jet Noise Source Separation and Improved Correlation Using Separate Flow Nozzle Data," MTC Report to GE Aircraft Engines, June 15, 2001. (Correction of October 6, 2000 Report)
6. Stone, J.R., "Separate Flow Nozzle Jet Noise Source Separation and Correlation Extension to Enhanced Mixing Configurations," MTC Report to GE Aircraft Engines, June 22, 2001.
7. Stone, J.R., Krejsa, E.A. and Clark, B.J., "Jet Noise Modeling for Coannular Nozzles Including the Effects of Chevrons," NASA CR-2003-212522, September 2003.

8. Stone, J.R., Krejsa, E.A. and Clark, B.J., "Semi-Empirical Model for Coannular Nozzle Component Noise Extraction and Correlation Including the Effects of Noise Reduction Devices," AIAA–2003–1060, January 2003.
9. Lighthill, M.J., "On Sound Generated Aerodynamically. I. General Theory," Proc. Roy. Soc. (London), Ser. A, vol. 211, No. 1107, March 1952, pp. 564–587.
10. Lighthill, M.J., "On Sound Generated Aerodynamically. II. Turbulence as a Source of Sound," Proc. Roy. Soc. (London), Ser. A, vol. 222, No. 1148, February 1954, pp. 1–32.
11. Ffowcs Williams, J.E., "Some Thoughts on the Effects of Aircraft Motion and Eddy Convection on the Noise from Air Jets," USAA Report 155, Southampton University, Great Britain, 1960.
12. Goldstein, M.E. and Howes, W.L., "New Aspects of Subsonic Aerodynamic Noise Theory," NASA TN D-7158, 1973.
13. Harper-Bourne, M. and Fisher, M.J., "The Noise from Shock Waves in Supersonic Jets," Noise Mechanisms, AGARD Conference Proceedings No. 131, 1974, Paper No. 11.
14. Viswanathan, K., "Quality of Jet Noise Data: Issues, Implications and Needs," AIAA–2002–0365, January 2002.
15. Stone, J.R., Zola, C.L. and Clark, B.J., "An Improved Model for Conventional and Inverted-Velocity-Profile Coannular Jet Noise," AIAA–99–0078, January 1999.
16. Stone, J.R., "Supersonic Jet Shock Noise Reduction," AIAA Paper 84–2278, October 1984 (also NASA TM-83799).
17. Ahuja, K.K., Tester, B.J. and Tanna, H.K., "The Free Jet as a Simulator of Forward Velocity Effects on Jet Noise," NASA CR-3056, October 1978.
18. Janardan, B.A., Hoff, G.E., Barter, J.W., Martens, S., and Gliebe, P.R. (GEAE), and Mengle, V. and Dalton, W.N. (Allison Engine Co.), "AST Critical Propulsion and Noise Reduction Technologies for Future Commercial Subsonic Engines – Separate-Flow Exhaust System Noise Reduction Evaluation," Final Report: NAS3–27720, Area of Interest 14.3, General Electric Report R98AEB152, May 1998.
19. Ahuja, K.K. and Bushell, K.W., "An Experimental Study of Subsonic Jet noise and Comparison with Theory," J. Sound Vibration, Vol. 30, No. 3, 1973, pp.317–341.
20. Gliebe, P.R., Brausch, J.F., Majjigi, R.K., and Lee, R., "Jet Noise Suppression," in Aeroacoustics of Flight Vehicles: Theory and Practice, Volume 2: Noise Control, NASA RP-1258, Vol. 2 (WRDC TR 90-3052), August 1991, pp. 207–269.
21. Goodykoontz, J.H. and Stone, J.R., "Experimental Study of Coaxial Nozzle Exhaust Noise," AIAA Paper 79–0631, March 1979.
22. Janardan, B.A., Yamamoto, K., Majjigi, R.K., and Brausch, J.F., "Experimental Investigation of Shock-Cell Noise Reduction for Dual-Stream Nozzles in Simulated Flight," NASA CR-3846, November 1984.
23. Janardan, B.A., Majjigi, R.K., Brausch, J.F. and Knott, P.R., "Free-Jet Investigation of Mechanically Suppressed, High-Radius-Ratio Coannular Plug Model Nozzles," NASA CR-3596, May 1985 (Date for General Release May 1987).
24. Knott, P.R., Janardan, B.A., Majjigi, R.K., Bhutiani, P.K. and Vogt, P.G., "Free-Jet Acoustic Investigation of High-Radius-Ratio Coannular Plug Nozzles," NASA CR-3818, October 1984 (Date for General Release November 1, 1985).
25. Fisher, M.J., Preston, G.A. and Bryce, W.D., "A Modelling of the Noise from Simple Co-axial Jets," AIAA–93–4413, October 1993.

26. Fisher, M.J., Preston, G.A. and Mead, C.J., “A Modelling of the Noise from Simple Coaxial Jets, Part II – With Heated Primary Flow,” AIAA–96–1666, 1996.
27. Posey, J.W., Norum, T.D., Brown, M.G. and Bhat, T.R.S., “Jet Noise from Ultra-High Bypass Turbofan Engines,” 143rd Meeting of the Acoustical Society of America, Pittsburgh, PA, June 3–7, 2002.
28. Olsen, W. and Karchmer, A., “Lip Noise Generated by Flow Separation from Nozzle Surfaces,” AIAA–76–3, January 1976. (Also NASA TM X-71859)
29. Viswanathan, K., “Parametric Study of Noise from Dual-Stream Nozzles,” AIAA–2003–1198, January 28, 2003.

Table I - Spectral Directivity Relations for Merged Mixing Noise
(a) Corrected Effective Directivity Angle, $\theta'_{M,cor}$, from 0 to 100 deg

Frequency parameter,	Normalized sound pressure level, SPL_M-UOL_M, dB vs. corrected effective directivity angle										
	Corrected effective directivity angle, $\theta'_{M,cor}$, deg										
$\log S_M$	0	10	20	30	40	50	60	70	80	90	100
-3.6	-92.9	-92.9	-92.9	-92.9	-92.9	-92.9	-92.9	-92.9	-92.9	-92.9	-92.9
-2.2	-50.9	-50.9	-50.9	-50.9	-50.9	-50.9	-50.9	-50.9	-50.9	-50.9	-50.9
-2.1	-47.9	-47.9	-47.9	-47.9	-47.9	-47.9	-47.9	-47.9	-47.9	-47.9	-47.9
-2.0	-44.9	-44.9	-44.9	-44.9	-44.9	-44.9	-44.9	-44.9	-44.9	-44.9	-44.9
-1.9	-41.9	-41.9	-41.9	-41.9	-41.9	-41.9	-41.9	-41.9	-41.9	-41.9	-41.9
-1.8	-39.1	-39.1	-39.1	-39.1	-39.1	-39.1	-39.1	-39.1	-39.1	-39.1	-39.1
-1.7	-36.5	-36.5	-36.5	-36.5	-36.5	-36.5	-36.5	-36.5	-36.5	-36.5	-36.5
-1.6	-34.0	-34.0	-34.0	-34.0	-34.0	-34.0	-34.0	-34.0	-34.0	-34.0	-34.0
-1.5	-31.6	-31.6	-31.6	-31.6	-31.6	-31.6	-31.6	-31.6	-31.6	-31.6	-31.6
-1.4	-29.3	-29.3	-29.3	-29.3	-29.3	-29.3	-29.3	-29.3	-29.3	-29.3	-29.3
-1.3	-27.1	-27.1	-27.1	-27.1	-27.1	-27.1	-27.1	-27.1	-27.1	-27.1	-27.1
-1.2	-24.9	-24.9	-24.9	-24.9	-24.9	-24.9	-24.9	-24.9	-24.9	-24.9	-24.9
-1.1	-22.7	-22.7	-22.7	-22.7	-22.7	-22.7	-22.7	-22.7	-22.7	-22.7	-22.7
-1.0	-20.6	-20.6	-20.6	-20.6	-20.6	-20.6	-20.6	-20.6	-20.6	-20.6	-20.6
-0.9	-18.5	-18.5	-18.5	-18.5	-18.5	-18.5	-18.5	-18.5	-18.5	-18.5	-18.5
-0.8	-16.5	-16.5	-16.5	-16.5	-16.5	-16.5	-16.5	-16.5	-16.5	-16.5	-16.5
-0.7	-14.6	-14.6	-14.6	-14.6	-14.6	-14.6	-14.6	-14.6	-14.6	-14.6	-14.6
-0.6	-13.1	-13.1	-13.1	-13.1	-13.1	-13.1	-13.1	-13.1	-13.1	-13.1	-13.1
-0.5	-12.0	-12.0	-12.0	-12.0	-12.0	-12.0	-12.0	-12.0	-12.0	-12.0	-12.0
-0.4	-11.2	-11.2	-11.2	-11.2	-11.2	-11.2	-11.2	-11.2	-11.2	-11.2	-11.2
-0.3	-10.7	-10.7	-10.7	-10.7	-10.7	-10.7	-10.7	-10.7	-10.7	-10.7	-10.7
-0.2	-10.4	-10.4	-10.4	-10.4	-10.4	-10.4	-10.4	-10.4	-10.4	-10.4	-10.4
-0.1	**-10.2**	**-10.2**	**-10.2**	**-10.2**	**-10.2**	**-10.2**	**-10.2**	**-10.2**	**-10.2**	**-10.2**	**-10.2**
0.0	-10.4	-10.4	-10.4	-10.4	-10.4	-10.4	-10.4	-10.4	-10.4	-10.4	-10.4
0.1	-10.8	-10.8	-10.8	-10.8	-10.8	-10.8	-10.8	-10.8	-10.8	-10.8	-10.8
0.2	-11.4	-11.4	-11.4	-11.4	-11.4	-11.4	-11.4	-11.4	-11.4	-11.4	-11.4
0.3	-12.3	-12.3	-12.3	-12.3	-12.3	-12.3	-12.3	-12.3	-12.3	-12.3	-12.3
0.4	-13.5	-13.5	-13.5	-13.5	-13.5	-13.5	-13.5	-13.5	-13.5	-13.5	-13.5
0.5	-15.0	-15.0	-15.0	-15.0	-15.0	-15.0	-15.0	-15.0	-15.0	-15.0	-15.0
0.6	-16.6	-16.6	-16.6	-16.6	-16.6	-16.6	-16.6	-16.6	-16.6	-16.6	-16.6
0.7	-18.2	-18.2	-18.2	-18.2	-18.2	-18.2	-18.2	-18.2	-18.2	-18.2	-18.2
0.8	-19.8	-19.8	-19.8	-19.8	-19.8	-19.8	-19.8	-19.8	-19.8	-19.8	-19.8
0.9	-21.4	-21.4	-21.4	-21.4	-21.4	-21.4	-21.4	-21.4	-21.4	-21.4	-21.4
1.0	-23.0	-23.0	-23.0	-23.0	-23.0	-23.0	-23.0	-23.0	-23.0	-23.0	-23.0
1.1	-24.6	-24.6	-24.6	-24.6	-24.6	-24.6	-24.6	-24.6	-24.6	-24.6	-24.6
1.2	-26.2	-26.2	-26.2	-26.2	-26.2	-26.2	-26.2	-26.2	-26.2	-26.2	-26.2
1.3	-27.8	-27.8	-27.8	-27.8	-27.8	-27.8	-27.8	-27.8	-27.8	-27.8	-27.8
1.4	-29.4	-29.4	-29.4	-29.4	-29.4	-29.4	-29.4	-29.4	-29.4	-29.4	-29.4
1.5	-31.0	-31.0	-31.0	-31.0	-31.0	-31.0	-31.0	-31.0	-31.0	-31.0	-31.0
1.6	-32.6	-32.6	-32.6	-32.6	-32.6	-32.6	-32.6	-32.6	-32.6	-32.6	-32.6
1.7	-34.2	-34.2	-34.2	-34.2	-34.2	-34.2	-34.2	-34.2	-34.2	-34.2	-34.2
1.8	-35.8	-35.8	-35.8	-35.8	-35.8	-35.8	-35.8	-35.8	-35.8	-35.8	-35.8
1.9	-37.4	-37.4	-37.4	-37.4	-37.4	-37.4	-37.4	-37.4	-37.4	-37.4	-37.4
2.0	-39.0	-39.0	-39.0	-39.0	-39.0	-39.0	-39.0	-39.0	-39.0	-39.0	-39.0
3.6	-61.4	-61.4	-61.4	-61.4	-61.4	-61.4	-61.4	-61.4	-61.4	-61.4	-61.4
$OASPL_M$-UOL_M	0.0	0.0	0.0	0.0	0.0	0.0	0.0	0.0	0.0	0.0	0.0

Table I (Concluded) - Spectral Directivity Relations for Merged Mixing Noise
(b) Corrected Effective Directivity Angle, $\theta'_{M,cor}$, from 110 to 250 deg

Frequency parameter,	Normalized sound pressure level, SPL_M-UOL_M, dB vs. corrected effective directivity angle										
	Corrected effective directivity angle, $\theta'_{M,cor}$, deg										
log S_M	110	120	130	140	150	160	170	180	190	200	250
-3.6	-93.4	-91.3	-93.0	-88.4	-86.9	-88.9	-90.5	-94.5	-99.5	-104.5	-129.5
-2.2	-51.4	-49.3	-51.0	-46.4	-44.9	-46.9	-49.9	-53.9	-58.9	-63.9	-88.9
-2.1	-48.4	-46.3	-48.0	-43.4	-41.9	-43.9	-46.9	-50.9	-55.9	-60.9	-85.9
-2.0	-45.4	-43.3	-45.0	-40.4	-38.9	-40.9	-43.9	-47.9	-52.9	-57.9	-82.9
-1.9	-42.4	-40.3	-42.0	-37.4	-35.9	-37.9	-40.9	-44.9	-49.9	-54.9	-79.9
-1.8	-39.6	-37.6	-39.0	-34.4	-32.9	-34.9	-37.9	-41.9	-46.9	-51.9	-76.9
-1.7	-37.0	-35.0	-36.0	-31.4	-29.9	-31.9	-34.9	-38.9	-43.9	-48.9	-73.9
-1.6	-34.5	-32.5	-33.0	-28.4	-26.9	-28.9	-31.9	-35.9	-40.9	-45.9	-70.9
-1.5	-32.1	-30.1	-30.0	-25.4	-24.0	-26.0	-29.0	-33.0	-38.0	-43.0	-68.0
-1.4	-29.8	-27.8	-27.0	-22.5	-21.2	-23.2	-26.2	-30.2	-35.2	-40.2	-65.2
-1.3	-27.6	-25.5	-24.1	-19.7	-18.5	-20.5	-23.5	-27.5	-32.5	-37.5	-62.5
-1.2	-25.4	-23.2	-21.3	-17.0	-15.9	-17.9	-20.9	-24.9	-29.9	-34.9	-59.9
-1.1	-23.2	-21.0	-18.6	-14.4	-13.4	-15.4	-18.4	-22.4	-27.4	-32.4	-57.4
-1.0	-21.1	-18.9	-16.0	-11.9	-11.2	-13.2	-16.2	-20.2	-25.2	-30.2	-55.2
-0.9	-19.0	-16.9	-13.5	-9.7	-9.4	-11.4	-14.4	-18.4	-23.4	-28.4	-53.4
-0.8	-17.0	-15.0	-11.3	-7.9	-7.9	-9.9	-12.9	-16.9	-21.9	-26.9	-51.9
-0.7	-15.2	-13.4	-9.5	-6.4	-6.7	-8.7	-11.7	-15.7	-20.7	-25.7	-50.7
-0.6	-13.6	-11.9	-8.0	-5.2	-5.9	-7.9	-10.9	-14.9	-19.9	-24.9	-49.9
-0.5	-12.2	-10.6	-6.8	-4.4	**-5.5**	**-7.5**	**-10.5**	**-14.5**	**-19.5**	**-24.5**	**-49.5**
-0.4	-11.0	-9.7	-6.0	**-4.0**	-6.3	-8.3	-11.3	-15.3	-20.3	-25.3	-50.3
-0.3	-10.2	-9.0	**-5.6**	-4.8	-7.8	-9.8	-12.6	-16.6	-21.6	-26.6	-51.6
-0.2	-9.8	**-8.7**	-6.2	-6.3	-10.2	-12.2	-15.0	-19.0	-24.0	-29.0	-54.0
-0.1	**-9.5**	-9.1	-7.1	-8.3	-13.1	-15.1	-17.9	-21.9	-26.9	-31.9	-56.9
0.0	-9.8	-9.7	-8.3	-10.5	-16.0	-18.1	-20.9	-24.9	-29.9	-34.9	-59.9
0.1	-10.4	-10.4	-9.8	-12.7	-18.9	-21.1	-23.9	-27.9	-32.9	-37.9	-62.9
0.2	-11.1	-11.4	-11.4	-14.9	-21.8	-24.1	-26.9	-30.9	-35.9	-40.9	-65.9
0.3	-12.3	-12.5	-13.1	-17.1	-24.7	-27.1	-29.9	-33.9	-38.9	-43.9	-68.9
0.4	-13.6	-13.8	-15.1	-19.4	-27.6	-30.1	-32.9	-36.9	-41.9	-46.9	-71.9
0.5	-15.1	-15.4	-17.1	-21.7	-30.5	-33.1	-35.9	-39.9	-44.9	-49.9	-74.9
0.6	-16.7	-17.2	-19.2	-24.0	-33.4	-36.1	-38.9	-42.9	-47.9	-52.9	-77.9
0.7	-18.3	-19.1	-21.3	-26.3	-36.3	-39.1	-41.9	-45.9	-50.9	-55.9	-80.9
0.8	-19.9	-21.0	-23.4	-28.6	-39.2	-42.1	-44.9	-48.9	-53.9	-58.9	-83.9
0.9	-21.6	-22.9	-25.5	-30.9	-42.1	-45.1	-47.9	-51.9	-56.9	-61.9	-86.9
1.0	-23.3	-24.8	-27.6	-33.2	-45.0	-48.1	-50.9	-54.9	-59.9	-64.9	-89.9
1.1	-25.0	-26.7	-29.7	-35.5	-47.9	-51.1	-53.9	-57.9	-62.9	-67.9	-92.9
1.2	-26.7	-28.6	-31.8	-37.9	-50.8	-54.1	-56.9	-60.9	-65.9	-70.9	-95.9
1.3	-28.4	-30.5	-33.9	-40.3	-53.7	-57.1	-59.9	-63.9	-68.9	-73.9	-98.9
1.4	-30.1	-32.5	-36.0	-42.7	-56.6	-60.1	-62.9	-66.9	-71.9	-76.9	-101.9
1.5	-31.8	-34.5	-38.2	-45.1	-59.5	-63.1	-65.9	-69.9	-74.9	-79.9	-104.9
1.6	-33.5	-36.5	-40.4	-47.5	-62.4	-66.1	-68.9	-72.9	-77.9	-82.9	-107.9
1.7	-35.2	-38.5	-42.6	-49.9	-65.3	-69.1	-71.9	-75.9	-80.9	-85.9	-110.9
1.8	-37.0	-40.5	-44.8	-52.3	-68.2	-72.1	-74.9	-78.9	-83.9	-88.9	-113.9
1.9	-38.8	-42.5	-47.0	-54.7	-71.1	-75.1	-77.9	-81.9	-86.9	-91.9	-116.9
2.0	-40.6	-44.5	-49.2	-57.1	-74.0	-78.1	-80.9	-84.9	-89.9	-94.9	-119.9
3.6	-69.4	-72.5	-80.0	-90.7	-120.4	-126.1	-128.9	-132.9	-137.9	-142.9	-167.9
$OASPL_M$-UOL_M	0.2	0.9	3.2	4.2	2.6	0.6	-2.4	-6.4	-11.4	-16.4	-41.4

Table II - Spectral Directivity Relations for Outer Shear Layer Mixing Noise
(a) Corrected Effective Directivity Angle, $\theta'_{O,cor}$, from 0 to 100 deg

Frequency parameter,	Normalized sound pressure level, SPL_O-UOL_O, dB vs. corrected effective directivity angle Corrected effective directivity angle, $\theta'_{O,cor}$, deg										
log S_O	0	10	20	30	40	50	60	70	80	90	100
-3.6	-253.5	-253.5	-253.5	-253.5	-253.5	-253.5	-253.5	-253.5	-253.5	-253.8	-253.6
-2.2	-169.5	-169.5	-169.5	-169.5	-169.5	-169.5	-169.5	-169.5	-169.5	-169.8	-169.6
-2.1	-163.5	-163.5	-163.5	-163.5	-163.5	-163.5	-163.5	-163.5	-163.5	-163.8	-163.6
-2.0	-157.5	-157.5	-157.5	-157.5	-157.5	-157.5	-157.5	-157.5	-157.5	-157.8	-157.6
-1.9	-151.5	-151.5	-151.5	-151.5	-151.5	-151.5	-151.5	-151.5	-151.5	-151.8	-151.6
-1.8	-145.5	-145.5	-145.5	-145.5	-145.5	-145.5	-145.5	-145.5	-145.5	-145.8	-145.6
-1.7	-139.5	-139.5	-139.5	-139.5	-139.5	-139.5	-139.5	-139.5	-139.5	-139.8	-139.6
-1.6	-133.5	-133.5	-133.5	-133.5	-133.5	-133.5	-133.5	-133.5	-133.5	-133.8	-133.6
-1.5	-127.5	-127.5	-127.5	-127.5	-127.5	-127.5	-127.5	-127.5	-127.5	-127.8	-127.6
-1.4	-121.5	-121.5	-121.5	-121.5	-121.5	-121.5	-121.5	-121.5	-121.5	-121.8	-121.6
-1.3	-115.5	-115.5	-115.5	-115.5	-115.5	-115.5	-115.5	-115.5	-115.5	-115.8	-115.6
-1.2	-109.5	-109.5	-109.5	-109.5	-109.5	-109.5	-109.5	-109.5	-109.5	-109.8	-109.6
-1.1	-103.5	-103.5	-103.5	-103.5	-103.5	-103.5	-103.5	-103.5	-103.5	-103.8	-103.6
-1.0	-97.5	-97.5	-97.5	-97.5	-97.5	-97.5	-97.5	-97.5	-97.5	-97.8	-97.6
-0.9	-91.5	-91.5	-91.5	-91.5	-91.5	-91.5	-91.5	-91.5	-91.5	-91.8	-91.6
-0.8	-85.5	-85.5	-85.5	-85.5	-85.5	-85.5	-85.5	-85.5	-85.5	-85.8	-85.6
-0.7	-79.5	-79.5	-79.5	-79.5	-79.5	-79.5	-79.5	-79.5	-79.5	-79.8	-79.6
-0.6	-73.5	-73.5	-73.5	-73.5	-73.5	-73.5	-73.5	-73.5	-73.5	-73.8	-73.6
-0.5	-67.5	-67.5	-67.5	-67.5	-67.5	-67.5	-67.5	-67.5	-67.5	-67.8	-67.6
-0.4	-61.5	-61.5	-61.5	-61.5	-61.5	-61.5	-61.5	-61.5	-61.5	-61.8	-61.6
-0.3	-55.5	-55.5	-55.5	-55.5	-55.5	-55.5	-55.5	-55.5	-55.5	-55.8	-55.6
-0.2	-49.5	-49.5	-49.5	-49.5	-49.5	-49.5	-49.5	-49.5	-49.5	-49.8	-49.6
-0.1	-43.5	-43.5	-43.5	-43.5	-43.5	-43.5	-43.5	-43.5	-43.5	-43.8	-43.6
0.0	-37.6	-37.6	-37.6	-37.6	-37.6	-37.6	-37.6	-37.6	-37.6	-37.8	-37.6
0.1	-32.6	-32.6	-32.6	-32.6	-32.6	-32.6	-32.6	-32.6	-32.6	-32.8	-32.6
0.2	-28.1	-28.1	-28.1	-28.1	-28.1	-28.1	-28.1	-28.1	-28.1	-28.3	-28.1
0.3	-24.1	-24.1	-24.1	-24.1	-24.1	-24.1	-24.1	-24.1	-24.1	-24.3	-24.1
0.4	-20.6	-20.6	-20.6	-20.6	-20.6	-20.6	-20.6	-20.6	-20.6	-20.8	-20.6
0.5	-17.5	-17.5	-17.5	-17.5	-17.5	-17.5	-17.5	-17.5	-17.5	-17.6	-17.6
0.6	-15.0	-15.0	-15.0	-15.0	-15.0	-15.0	-15.0	-15.0	-15.0	-15.1	-15.1
0.7	-13.0	-13.0	-13.0	-13.0	-13.0	-13.0	-13.0	-13.0	-13.0	-13.1	-13.1
0.8	-11.5	-11.5	-11.5	-11.5	-11.5	-11.5	-11.5	-11.5	-11.5	-11.6	-11.6
0.9	-10.5	-10.5	-10.5	-10.5	-10.5	-10.5	-10.5	-10.5	-10.5	-10.6	-10.6
1.0	-9.8	-9.8	-9.8	-9.8	-9.8	-9.8	-9.8	-9.8	-9.8	-9.9	-9.9
1.1	**-9.5**	**-9.5**	**-9.5**	**-9.5**	**-9.5**	**-9.5**	**-9.5**	**-9.5**	**-9.5**	**-9.6**	**-9.6**
1.2	-9.7	-9.7	-9.7	-9.7	-9.7	-9.7	-9.7	-9.7	-9.7	-9.8	-9.8
1.3	-10.0	-10.0	-10.0	-10.0	-10.0	-10.0	-10.0	-10.0	-10.0	-10.1	-10.1
1.4	-10.4	-10.4	-10.4	-10.4	-10.4	-10.4	-10.4	-10.4	-10.4	-10.5	-10.6
1.5	-11.0	-11.0	-11.0	-11.0	-11.0	-11.0	-11.0	-11.0	-11.0	-11.1	-11.3
1.6	-11.7	-11.7	-11.7	-11.7	-11.7	-11.7	-11.7	-11.7	-11.7	-11.8	-12.2
1.7	-12.6	-12.6	-12.6	-12.6	-12.6	-12.6	-12.6	-12.6	-12.6	-12.7	-13.2
1.8	-13.6	-13.6	-13.6	-13.6	-13.6	-13.6	-13.6	-13.6	-13.6	-13.7	-14.2
1.9	-14.7	-14.7	-14.7	-14.7	-14.7	-14.7	-14.7	-14.7	-14.7	-14.8	-15.4
2.0	-15.8	-15.8	-15.8	-15.8	-15.8	-15.8	-15.8	-15.8	-15.8	-15.9	-16.6
3.6	-33.4	-33.4	-33.4	-33.4	-33.4	-33.4	-33.4	-33.4	-33.4	-33.5	-35.8
$OASPL_O$-UOL_O	0.2	0.2	0.2	0.2	0.2	0.2	0.2	0.2	0.2	0.0	0.0

Table II (Concluded) - Spectral Directivity Relations for Outer Shear Layer Mixing Noise
(b) Corrected Effective Directivity Angle, $\theta'_{O,cor}$, from 110 to 250 deg

Frequency parameter,	Normalized sound pressure level, SPL_O-UOL_O, dB vs. corrected effective directivity angle										
	Corrected effective directivity angle, $\theta'_{O,cor}$, deg										
log S_O	110	120	130	140	150	160	170	180	190	200	250
-3.6	-253.6	-255.1	-257.6	-254.0	-256.0	-258.0	-261.0	-265.0	-270.0	-305.0	-310.0
-2.2	-169.6	-171.1	-173.6	-170.0	-172.0	-174.0	-177.0	-181.0	-186.0	-221.0	-226.0
-2.1	-163.6	-165.1	-167.6	-164.0	-166.0	-168.0	-171.0	-175.0	-180.0	-215.0	-220.0
-2.0	-157.6	-159.1	-161.6	-158.0	-160.0	-162.0	-165.0	-169.0	-174.0	-209.0	-214.0
-1.9	-151.6	-153.1	-155.6	-152.0	-154.0	-156.0	-159.0	-163.0	-168.0	-203.0	-208.0
-1.8	-145.6	-147.1	-149.6	-146.0	-148.0	-150.0	-153.0	-157.0	-162.0	-197.0	-202.0
-1.7	-139.6	-141.1	-143.6	-140.0	-142.0	-144.0	-147.0	-151.0	-156.0	-191.0	-196.0
-1.6	-133.6	-135.1	-137.6	-134.0	-136.0	-138.0	-141.0	-145.0	-150.0	-185.0	-190.0
-1.5	-127.6	-129.1	-131.6	-128.0	-130.0	-132.0	-135.0	-139.0	-144.0	-179.0	-184.0
-1.4	-121.6	-123.1	-125.6	-122.0	-124.0	-126.0	-129.0	-133.0	-138.0	-173.0	-178.0
-1.3	-115.6	-117.1	-119.6	-116.0	-118.0	-120.0	-123.0	-127.0	-132.0	-167.0	-172.0
-1.2	-109.6	-111.1	-113.6	-110.0	-112.0	-114.0	-117.0	-121.0	-126.0	-161.0	-166.0
-1.1	-103.6	-105.1	-107.6	-104.0	-106.0	-108.0	-111.0	-115.0	-120.0	-155.0	-160.0
-1.0	-97.6	-99.1	-101.6	-98.0	-100.0	-102.0	-105.0	-109.0	-114.0	-149.0	-154.0
-0.9	-91.6	-93.1	-95.6	-92.0	-94.0	-96.0	-99.0	-103.0	-108.0	-143.0	-148.0
-0.8	-85.6	-87.1	-89.6	-86.0	-88.0	-90.0	-93.0	-97.0	-102.0	-137.0	-142.0
-0.7	-79.6	-81.1	-83.6	-80.0	-82.0	-84.0	-87.0	-91.0	-96.0	-131.0	-136.0
-0.6	-73.6	-75.1	-77.6	-74.0	-76.0	-78.0	-81.0	-85.0	-90.0	-125.0	-130.0
-0.5	-67.6	-69.1	-71.6	-68.0	-70.0	-72.0	-75.0	-79.0	-84.0	-119.0	-124.0
-0.4	-61.6	-63.1	-65.6	-62.0	-64.0	-66.0	-69.0	-73.0	-78.0	-113.0	-118.0
-0.3	-55.6	-57.1	-59.6	-56.0	-58.0	-60.0	-63.0	-67.0	-72.0	-107.0	-112.0
-0.2	-49.6	-51.1	-53.6	-50.0	-52.0	-54.0	-57.0	-61.0	-66.0	-101.0	-106.0
-0.1	-43.6	-45.1	-47.6	-44.0	-46.0	-48.0	-51.0	-55.0	-60.0	-95.0	-100.0
0.0	-37.6	-39.1	-41.6	-39.0	-41.0	-43.0	-46.0	-50.0	-55.0	-90.0	-95.0
0.1	-32.6	-34.1	-36.6	-34.5	-36.5	-38.5	-41.5	-45.5	-50.5	-85.5	-90.5
0.2	-28.1	-29.6	-32.1	-30.5	-32.5	-34.5	-37.5	-41.5	-46.5	-81.5	-86.5
0.3	-24.1	-25.6	-28.1	-27.0	-29.0	-31.0	-34.0	-38.0	-43.0	-78.0	-83.0
0.4	-20.6	-22.1	-24.6	-24.0	-26.0	-28.0	-31.0	-35.0	-40.0	-75.0	-80.0
0.5	-17.6	-19.1	-21.6	-21.5	-23.5	-25.5	-28.5	-32.5	-37.5	-72.5	-77.5
0.6	-15.1	-16.6	-19.1	-19.5	-21.5	-23.5	-26.5	-30.5	-35.5	-70.5	-75.5
0.7	-13.1	-14.6	-17.1	-18.0	-20.0	-22.0	-25.0	-29.0	-34.0	-69.0	-74.0
0.8	-11.6	-13.1	-15.6	-17.0	-19.0	-21.0	-24.0	-28.0	-33.0	-68.0	-73.0
0.9	-10.6	-12.1	-14.6	-16.3	-18.3	-20.3	-23.3	-27.3	-32.3	-67.3	-72.3
1.0	-9.9	-11.4	-13.9	**-16.0**	**-18.0**	**-20.0**	**-23.0**	**-27.0**	**-32.0**	**-67.0**	**-72.0**
1.1	**-9.6**	**-11.1**	**-13.6**	-16.3	-18.3	-20.3	-23.3	-27.3	-32.3	-67.3	-72.3
1.2	-9.8	-11.3	-13.8	-16.9	-18.9	-20.9	-23.9	-27.9	-32.9	-67.9	-72.9
1.3	-10.2	-11.8	-14.4	-17.8	-19.8	-21.8	-24.8	-28.8	-33.8	-68.8	-73.8
1.4	-10.8	-12.4	-15.1	-19.0	-21.0	-23.0	-26.0	-30.0	-35.0	-70.0	-75.0
1.5	-11.6	-13.2	-16.0	-20.4	-22.4	-24.4	-27.4	-31.4	-36.4	-71.4	-76.4
1.6	-12.7	-14.4	-17.2	-21.8	-23.8	-25.8	-28.8	-32.8	-37.8	-72.8	-77.8
1.7	-13.8	-14.9	-17.8	-23.2	-25.2	-27.2	-30.2	-34.2	-39.2	-74.2	-79.2
1.8	-15.0	-15.5	-18.5	-24.6	-26.6	-28.6	-31.6	-35.6	-40.6	-75.6	-80.6
1.9	-16.2	-16.3	-19.4	-26.0	-28.0	-30.0	-33.0	-37.0	-42.0	-77.0	-82.0
2.0	-17.4	-17.5	-20.6	-27.4	-29.4	-31.4	-34.4	-38.4	-43.4	-78.4	-83.4
3.6	-36.6	-38.3	-43.0	-49.8	-51.8	-53.8	-56.8	-60.8	-65.8	-100.8	-105.8
$OASPL_O$-UOL_O	-0.2	-1.7	-4.3	-6.8	-8.8	-10.8	-13.8	-17.8	-22.8	-57.8	-62.8

Table III - Spectral Directivity Relations for Inner Stream Mixing Noise
(a) Corrected Effective Directivity Angle, $\theta'_{I,cor}$, from 0 to 100 deg

Frequency parameter,	Normalized sound pressure level, SPL_I-UOL_I, dB vs. corrected effective directivity angle										
	Corrected effective directivity angle, $\theta'_{I,cor}$, deg										
$\log S_I$	0	10	20	30	40	50	60	70	80	90	100
-3.6	-206.0	-205.2	-204.6	-204.2	-204.0	-204.4	-204.8	-205.3	-205.8	-198.5	-194.0
-2.2	-122.0	-121.2	-120.6	-120.2	-120.0	-120.4	-120.8	-121.3	-121.8	-114.5	-110.0
-2.1	-116.0	-115.2	-114.6	-114.2	-114.0	-114.4	-114.8	-115.3	-115.8	-108.5	-104.0
-2.0	-110.0	-109.2	-108.6	-108.2	-108.0	-108.4	-108.8	-109.3	-109.8	-102.5	-98.0
-1.9	-104.0	-103.2	-102.6	-102.2	-102.0	-102.4	-102.8	-103.3	-103.8	-96.5	-92.0
-1.8	-98.0	-97.2	-96.6	-96.2	-96.0	-96.4	-96.8	-97.3	-97.8	-90.5	-86.0
-1.7	-92.0	-91.2	-90.6	-90.2	-90.0	-90.4	-90.8	-91.3	-91.8	-84.5	-80.0
-1.6	-86.0	-85.2	-84.6	-84.2	-84.0	-84.4	-84.8	-85.3	-85.8	-78.5	-74.0
-1.5	-80.0	-79.2	-78.6	-78.2	-78.0	-78.4	-78.8	-79.3	-79.8	-72.5	-68.0
-1.4	-74.0	-73.2	-72.6	-72.2	-72.0	-72.4	-72.8	-73.3	-73.8	-66.5	-62.0
-1.3	-68.0	-67.2	-66.6	-66.2	-66.0	-66.4	-66.8	-67.3	-67.8	-60.5	-56.0
-1.2	-62.0	-61.2	-60.6	-60.2	-60.0	-60.4	-60.8	-61.3	-61.8	-54.5	-50.0
-1.1	-56.0	-55.2	-54.6	-54.2	-54.0	-54.4	-54.8	-55.3	-55.8	-48.5	-44.0
-1.0	-50.0	-49.2	-48.6	-48.2	-48.0	-48.4	-48.8	-49.3	-49.8	-42.5	-38.0
-0.9	-44.0	-43.2	-42.6	-42.2	-42.0	-42.4	-42.8	-43.3	-43.8	-37.5	-33.0
-0.8	-38.0	-37.2	-36.6	-36.2	-36.0	-36.4	-36.8	-37.3	-37.8	-32.5	-28.5
-0.7	-33.0	-32.2	-31.6	-31.2	-31.0	-31.4	-31.8	-32.3	-32.8	-28.0	-24.5
-0.6	-28.5	-27.7	-27.1	-26.7	-26.5	-26.9	-27.3	-27.8	-28.3	-24.0	-21.0
-0.5	-24.5	-23.7	-23.1	-22.7	-22.5	-22.9	-23.3	-23.8	-24.3	-20.5	-18.0
-0.4	-21.0	-20.2	-19.6	-19.2	-19.0	-19.4	-19.8	-20.3	-20.8	-17.5	-15.5
-0.3	-18.0	-17.2	-16.6	-16.2	-16.0	-16.4	-16.8	-17.3	-17.8	-15.0	-13.5
-0.2	-15.5	-14.7	-14.1	-13.7	-13.5	-13.9	-14.3	-14.8	-15.3	-13.0	-12.0
-0.1	-13.5	-12.7	-12.1	-11.7	-11.5	-11.9	-12.3	-12.8	-13.3	-11.5	-11.0
0.0	-12.0	-11.2	-10.6	-10.2	-10.0	-10.4	-10.8	-11.3	-11.8	-10.5	-10.5
0.1	-11.0	-10.2	-9.6	-9.2	-9.0	-9.4	-9.8	-10.3	-10.8	-10.0	**-10.3**
0.2	-10.5	-9.7	-9.1	-8.7	-8.5	-8.9	-9.3	-9.8	-10.3	**-9.8**	-10.5
0.3	**-10.3**	**-9.5**	**-8.9**	**-8.5**	**-8.3**	**-8.7**	**-9.1**	**-9.6**	**-10.1**	-10.0	-10.9
0.4	-10.5	-9.7	-9.1	-8.7	-8.5	-8.9	-9.3	-9.8	-10.3	-10.4	-11.5
0.5	-10.9	-10.1	-9.5	-9.1	-8.9	-9.3	-9.7	-10.2	-10.7	-11.0	-12.7
0.6	-11.5	-10.7	-10.1	-9.7	-9.5	-9.9	-10.3	-10.8	-11.3	-12.2	-13.9
0.7	-12.7	-11.9	-11.3	-10.9	-10.7	-11.1	-11.5	-12.0	-12.5	-13.4	-15.1
0.8	-14.0	-13.2	-12.6	-12.2	-12.0	-12.4	-12.8	-13.2	-13.7	-14.6	-16.3
0.9	-15.4	-14.6	-14.0	-13.6	-13.4	-13.8	-14.1	-14.4	-14.9	-15.8	-17.5
1.0	-16.8	-16.0	-15.4	-15.0	-14.8	-15.2	-15.4	-15.6	-16.1	-17.0	-18.7
1.1	-18.2	-17.4	-16.8	-16.4	-16.2	-16.6	-16.7	-16.8	-17.3	-18.2	-19.9
1.2	-19.6	-18.8	-18.2	-17.8	-17.6	-18.0	-18.0	-18.0	-18.5	-19.4	-21.1
1.3	-21.0	-20.2	-19.6	-19.2	-19.0	-19.4	-19.3	-19.2	-19.7	-20.6	-22.3
1.4	-22.4	-21.6	-21.0	-20.6	-20.4	-20.8	-20.6	-20.4	-20.9	-21.8	-23.5
1.5	-23.8	-23.0	-22.4	-22.0	-21.8	-22.2	-21.9	-21.6	-22.1	-23.0	-24.7
1.6	-25.2	-24.4	-23.8	-23.4	-23.2	-23.6	-23.2	-22.8	-23.3	-24.2	-25.9
1.7	-26.6	-25.8	-25.2	-24.8	-24.6	-25.0	-24.5	-24.0	-24.5	-25.4	-27.1
1.8	-28.0	-27.2	-26.6	-26.2	-26.0	-26.4	-25.8	-25.2	-25.7	-26.6	-28.3
1.9	-29.4	-28.6	-28.0	-27.6	-27.4	-27.8	-27.1	-26.4	-26.9	-27.8	-29.5
2.0	-30.8	-30.0	-29.4	-29.0	-28.8	-29.2	-28.4	-27.6	-28.1	-29.0	-30.7
3.6	-50.4	-49.6	-49.0	-48.6	-48.4	-48.8	-46.6	-44.4	-44.9	-45.8	-47.5
$OASPL_I$-UOL_I	-0.6	0.2	0.8	1.2	1.4	1.0	0.6	0.2	-0.3	0.0	-0.5

Table III (Concluded) - Spectral Directivity Relations for Inner Stream Mixing Noise
(b) Corrected Effective Directivity Angle, $\theta'_{I,cor}$, from 110 to 250 deg

Frequency parameter,	Normalized sound pressure level, SPL_I-UOL_I, dB vs. corrected effective directivity angle										
	Corrected effective directivity angle, $\theta'_{I,cor}$, deg										
$\log S_I$	110	120	130	140	150	160	170	180	190	200	250
-3.6	-194.3	-189.3	-184.3	-179.3	-174.3	-173.3	-171.5	-173.0	-174.0	-174.5	-195.0
-2.2	-110.3	-105.3	-100.3	-95.3	-90.3	-89.3	-87.5	-89.0	-90.0	-90.5	-111.0
-2.1	-104.3	-99.3	-94.3	-89.3	-84.3	-83.3	-81.5	-83.0	-84.0	-84.5	-105.0
-2.0	-98.3	-93.3	-88.3	-83.3	-78.3	-77.3	-75.5	-77.0	-78.0	-78.5	-99.0
-1.9	-92.3	-87.3	-82.3	-77.3	-72.3	-71.3	-69.5	-71.0	-72.0	-72.5	-93.0
-1.8	-86.3	-81.3	-76.3	-71.3	-66.3	-65.3	-63.5	-65.0	-66.0	-66.5	-87.0
-1.7	-80.3	-75.3	-70.3	-65.3	-60.3	-59.3	-57.5	-59.0	-60.0	-60.5	-81.0
-1.6	-74.3	-69.3	-64.3	-59.3	-54.3	-53.3	-53.0	-55.0	-56.5	-57.5	-75.0
-1.5	-68.3	-63.3	-58.3	-53.3	-48.3	-47.3	-48.5	-51.0	-53.0	-54.5	-73.5
-1.4	-62.3	-57.3	-52.3	-47.3	-42.3	-42.3	-44.0	-47.0	-49.5	-51.5	-72.0
-1.3	-56.3	-51.3	-46.3	-41.3	-37.3	-37.8	-40.0	-43.5	-46.5	-49.0	-70.5
-1.2	-50.3	-45.3	-40.3	-36.3	-32.8	-33.8	-36.5	-40.5	-44.0	-47.0	-69.5
-1.1	-44.3	-39.3	-35.3	-31.8	-28.8	-30.3	-33.5	-38.0	-42.0	-45.5	**-69.0**
-1.0	-38.3	-34.3	-30.8	-27.8	-25.3	-27.3	-31.0	-36.0	-40.5	-44.5	-69.3
-0.9	-33.3	-29.8	-26.8	-24.3	-22.3	-24.8	-29.0	-34.5	-39.5	**-44.0**	-70.1
-0.8	-28.8	-25.8	-23.3	-21.3	-19.8	-22.8	-27.5	-33.5	**-39.0**	-44.3	-71.3
-0.7	-24.8	-22.3	-20.3	-18.8	-17.8	-21.3	-26.5	**-33.0**	-39.3	-45.1	-72.8
-0.6	-21.3	-19.3	-17.8	-16.8	-16.3	-20.3	**-26.0**	-33.3	-40.1	-46.3	-74.6
-0.5	-18.3	-16.8	-15.8	-15.3	-15.3	**-19.8**	-26.3	-34.1	-41.3	-47.8	-76.4
-0.4	-15.8	-14.8	-14.3	-14.3	**-14.8**	-20.1	-27.1	-35.3	-42.8	-49.6	-78.2
-0.3	-13.8	-13.3	-13.3	**-13.8**	-15.1	-20.9	-28.3	-36.8	-44.6	-51.4	-80.0
-0.2	-12.3	-12.3	**-12.8**	-14.1	-15.9	-22.1	-29.8	-38.6	-46.4	-53.2	-81.8
-0.1	-11.3	**-11.8**	-13.1	-14.9	-17.1	-23.6	-31.6	-40.4	-48.2	-55.0	-83.6
0.0	**-10.8**	-12.1	-13.9	-16.1	-18.6	-25.4	-33.4	-42.2	-50.0	-56.8	-85.4
0.1	-11.1	-12.9	-15.0	-17.6	-20.4	-27.2	-35.2	-44.0	-51.8	-58.6	-87.2
0.2	-11.8	-14.0	-16.6	-19.4	-22.2	-29.0	-37.0	-45.8	-53.6	-60.4	-89.0
0.3	-12.8	-15.6	-18.2	-21.4	-24.0	-30.8	-38.8	-47.6	-55.4	-62.2	-90.8
0.4	-14.3	-17.3	-20.0	-23.4	-25.8	-32.6	-40.6	-49.4	-57.2	-64.0	-92.6
0.5	-15.8	-19.1	-21.9	-25.4	-27.6	-34.4	-42.4	-51.2	-59.0	-65.8	-94.4
0.6	-17.3	-20.9	-23.9	-27.4	-29.4	-36.2	-44.2	-53.0	-60.8	-67.6	-96.2
0.7	-18.8	-22.7	-25.9	-29.4	-31.2	-38.0	-46.0	-54.8	-62.6	-69.4	-98.0
0.8	-20.3	-24.5	-27.9	-31.4	-33.0	-39.8	-47.8	-56.6	-64.4	-71.2	-99.8
0.9	-21.8	-26.3	-29.9	-33.4	-34.8	-41.6	-49.6	-58.4	-66.2	-73.0	-101.6
1.0	-23.3	-28.1	-31.9	-35.4	-36.6	-43.4	-51.4	-60.2	-68.0	-74.8	-103.4
1.1	-24.8	-29.9	-33.9	-37.4	-38.4	-45.2	-53.2	-62.0	-69.8	-76.6	-105.2
1.2	-26.3	-31.7	-35.9	-39.4	-40.2	-47.0	-55.0	-63.8	-71.6	-78.4	-107.0
1.3	-27.8	-33.5	-37.9	-41.4	-42.0	-48.8	-56.8	-65.6	-73.4	-80.2	-108.8
1.4	-29.3	-35.3	-39.9	-43.4	-43.8	-50.6	-58.6	-67.4	-75.2	-82.0	-110.6
1.5	-30.8	-37.1	-41.9	-45.4	-45.6	-52.4	-60.4	-69.2	-77.0	-83.8	-112.4
1.6	-32.3	-38.9	-43.9	-47.4	-47.4	-54.2	-62.2	-71.0	-78.8	-85.6	-114.2
1.7	-33.8	-40.7	-45.9	-49.4	-49.2	-56.0	-64.0	-72.8	-80.6	-87.4	-116.0
1.8	-35.3	-42.5	-47.9	-51.4	-51.0	-57.8	-65.8	-74.6	-82.4	-89.2	-117.8
1.9	-36.8	-44.3	-49.9	-53.4	-52.8	-59.6	-67.6	-76.4	-84.2	-91.0	-119.6
2.0	-38.3	-46.1	-51.9	-55.4	-54.6	-61.4	-69.4	-78.2	-86.0	-92.8	-121.4
3.6	-59.3	-71.3	-79.9	-83.4	-79.8	-86.6	-94.6	-103.4	-111.2	-118.0	-146.6
$OASPL_I$-UOL_I	-2.0	-3.2	-4.2	-5.2	-6.2	-11.2	-17.4	-24.4	-30.4	-35.4	-60.4

Table IV - Spectral Directivity Relations for Inner Stream Plug Separation Noise
(a) Corrected Effective Directivity Angle, $\theta'_{P,cor}$, from 0 to 100 deg

Frequency parameter	Normalized sound pressure level, SPL_P-UOL_P, dB vs. corrected effective directivity angle										
	Corrected effective directivity angle, $\theta'_{P,cor}$, deg										
$\log S_P$	0	10	20	30	40	50	60	70	80	90	100
-3.6	-196.6	-184.7	-182.8	-180.9	-179.0	-177.1	-175.0	-172.9	-170.6	-169.5	-169.3
-2.2	-140.6	-128.7	-126.8	-124.9	-123.0	-121.1	-119.0	-116.9	-114.6	-113.5	-113.3
-2.1	-136.6	-124.7	-122.8	-120.9	-119.0	-117.1	-115.0	-112.9	-110.6	-109.5	-109.3
-2.0	-132.6	-120.7	-118.8	-116.9	-115.0	-113.1	-111.0	-108.9	-106.6	-105.5	-105.3
-1.9	-128.6	-116.7	-114.8	-112.9	-111.0	-109.1	-107.0	-104.9	-102.6	-101.5	-101.3
-1.8	-124.6	-112.7	-110.8	-108.9	-107.0	-105.1	-103.0	-100.9	-98.6	-97.5	-97.3
-1.7	-120.6	-108.7	-106.8	-104.9	-103.0	-101.1	-99.0	-96.9	-94.6	-93.5	-93.3
-1.6	-116.6	-104.7	-102.8	-100.9	-99.0	-97.1	-95.0	-92.9	-90.6	-89.5	-89.3
-1.5	-112.6	-100.7	-98.8	-96.9	-95.0	-93.1	-91.0	-88.9	-86.6	-85.5	-85.3
-1.4	-108.6	-96.7	-94.8	-92.9	-91.0	-89.1	-87.0	-84.9	-82.6	-81.5	-81.3
-1.3	-104.6	-92.7	-90.8	-88.9	-87.0	-85.1	-83.0	-80.9	-78.6	-77.5	-77.3
-1.2	-100.6	-88.7	-86.8	-84.9	-83.0	-81.1	-79.0	-76.9	-74.6	-73.5	-73.3
-1.1	-96.6	-84.7	-82.8	-80.9	-79.0	-77.1	-75.0	-72.9	-70.6	-69.5	-69.3
-1.0	-92.6	-80.7	-78.8	-76.9	-75.0	-73.1	-71.0	-68.9	-66.6	-65.5	-65.3
-0.9	-88.6	-76.7	-74.8	-72.9	-71.0	-69.1	-67.0	-64.9	-62.6	-61.5	-61.3
-0.8	-84.6	-72.7	-70.8	-68.9	-67.0	-65.1	-63.0	-60.9	-58.6	-57.5	-57.3
-0.7	-80.6	-68.7	-66.8	-64.9	-63.0	-61.1	-59.0	-56.9	-54.6	-53.5	-53.3
-0.6	-76.6	-64.7	-62.8	-60.9	-59.0	-57.1	-55.0	-52.9	-50.6	-49.5	-49.3
-0.5	-72.6	-60.7	-58.8	-56.9	-55.0	-53.1	-51.0	-48.9	-46.6	-45.5	-45.3
-0.4	-68.6	-56.7	-54.8	-52.9	-51.0	-49.1	-47.0	-44.9	-42.6	-41.5	-41.3
-0.3	-64.6	-52.7	-50.8	-48.9	-47.0	-45.1	-43.0	-40.9	-38.6	-37.5	-37.3
-0.2	-60.6	-48.7	-46.8	-44.9	-43.0	-41.1	-39.0	-36.9	-34.6	-33.5	-33.3
-0.1	-56.6	-44.7	-42.8	-40.9	-39.0	-37.1	-35.0	-32.9	-30.6	-29.5	-29.3
0.0	-52.6	-40.7	-38.8	-36.9	-35.0	-33.1	-31.0	-28.9	-26.6	-25.5	-25.3
0.1	-48.6	-36.7	-34.8	-32.9	-31.0	-29.1	-27.0	-24.9	-22.6	-21.5	-21.3
0.2	-44.6	-32.7	-30.8	-28.9	-27.0	-25.1	-23.0	-20.9	-18.6	-17.5	-17.3
0.3	-40.6	-28.7	-26.8	-24.9	-23.0	-21.1	-19.0	-16.9	-14.8	-14.0	-13.8
0.4	-37.4	-25.5	-23.6	-21.7	-19.8	-17.9	-15.9	-13.9	-11.8	-11.2	-11.2
0.5	-35.0	-23.1	-21.2	-19.3	-17.4	-15.5	-13.5	-11.6	-9.7	-9.4	-9.5
0.6	**-33.8**	**-21.9**	**-20.0**	**-18.1**	**-16.2**	**-14.3**	**-12.4**	**-10.5**	**-8.6**	**-8.4**	**-8.5**
0.7	-34.2	-22.3	-20.4	-18.5	-16.6	-14.7	-12.8	-10.9	-9.0	-8.8	-8.9
0.8	-34.8	-22.9	-21.0	-19.1	-17.2	-15.3	-13.4	-11.5	-9.6	-9.4	-9.5
0.9	-36.0	-24.1	-22.2	-20.3	-18.4	-16.5	-14.6	-12.7	-10.8	-10.6	-10.7
1.0	-37.2	-25.3	-23.4	-21.5	-19.6	-17.7	-15.8	-13.9	-12.0	-11.8	-11.9
1.1	-38.4	-26.5	-24.6	-22.7	-20.8	-18.9	-17.0	-15.1	-13.2	-13.0	-13.1
1.2	-39.6	-27.7	-25.8	-23.9	-22.0	-20.1	-18.2	-16.3	-14.4	-14.2	-14.3
1.3	-40.8	-28.9	-27.0	-25.1	-23.2	-21.3	-19.4	-17.5	-15.6	-15.4	-15.5
1.4	-42.0	-30.1	-28.2	-26.3	-24.4	-22.5	-20.6	-18.7	-16.8	-16.6	-16.7
1.5	-43.2	-31.3	-29.4	-27.5	-25.6	-23.7	-21.8	-19.9	-18.0	-17.8	-17.9
1.6	-44.4	-32.5	-30.6	-28.7	-26.8	-24.9	-23.0	-21.1	-19.2	-19.0	-19.1
1.7	-45.6	-33.7	-31.8	-29.9	-28.0	-26.1	-24.2	-22.3	-20.4	-20.2	-20.3
1.8	-46.8	-34.9	-33.0	-31.1	-29.2	-27.3	-25.4	-23.5	-21.6	-21.4	-21.5
1.9	-48.0	-36.1	-34.2	-32.3	-30.4	-28.5	-26.6	-24.7	-22.8	-22.6	-22.7
2.0	-49.2	-37.3	-35.4	-33.5	-31.6	-29.7	-27.8	-25.9	-24.0	-23.8	-23.9
3.6	-68.4	-56.5	-54.6	-52.7	-50.8	-48.9	-47.0	-45.1	-43.2	-43.0	-43.1
$OASPL_P$-UOL_P	-25.6	-13.7	-11.8	-9.9	-8.0	-6.1	-4.2	-2.3	-0.3	0.0	-0.1

Table IV (Concluded) - Spectral Directivity Relations for Inner Stream Plug Separation Noise
(b) Corrected Effective Directivity Angle, $\theta'_{P,cor}$, from 110 to 250 deg

Frequency	Normalized sound pressure level, SPL_P-UOL_P, dB vs. corrected effective directivity angle										
parameter	Corrected effective directivity angle, $\theta'_{P,cor}$, deg										
$\log S_P$	110	120	130	140	150	160	170	180	190	200	250
-3.6	-169.8	-170.5	-173.2	-176.7	-182.2	-182.8	-185.8	-188.8	-191.8	-194.8	-209.8
-2.2	-113.8	-114.5	-117.2	-120.7	-126.2	-126.8	-129.8	-132.8	-135.8	-138.8	-153.8
-2.1	-109.8	-110.5	-113.2	-116.7	-122.2	-122.8	-125.8	-128.8	-131.8	-134.8	-149.8
-2.0	-105.8	-106.5	-109.2	-112.7	-118.2	-118.8	-121.8	-124.8	-127.8	-130.8	-145.8
-1.9	-101.8	-102.5	-105.2	-108.7	-114.2	-114.8	-117.8	-120.8	-123.8	-126.8	-141.8
-1.8	-97.8	-98.5	-101.2	-104.7	-110.2	-110.8	-113.8	-116.8	-119.8	-122.8	-137.8
-1.7	-93.8	-94.5	-97.2	-100.7	-106.2	-106.8	-109.8	-112.8	-115.8	-118.8	-133.8
-1.6	-89.8	-90.5	-93.2	-96.7	-102.2	-102.8	-105.8	-108.8	-111.8	-114.8	-129.8
-1.5	-85.8	-86.5	-89.2	-92.7	-98.2	-98.8	-101.8	-104.8	-107.8	-110.8	-125.8
-1.4	-81.8	-82.5	-85.2	-88.7	-94.2	-94.8	-97.8	-100.8	-103.8	-106.8	-121.8
-1.3	-77.8	-78.5	-81.2	-84.7	-90.2	-90.8	-93.8	-96.8	-99.8	-102.8	-117.8
-1.2	-73.8	-74.5	-77.2	-80.7	-86.2	-86.8	-89.8	-92.8	-95.8	-98.8	-113.8
-1.1	-69.8	-70.5	-73.2	-76.7	-82.2	-82.8	-85.8	-88.8	-91.8	-94.8	-109.8
-1.0	-65.8	-66.5	-69.2	-72.7	-78.2	-78.8	-81.8	-84.8	-87.8	-90.8	-105.8
-0.9	-61.8	-62.5	-65.2	-68.7	-74.2	-74.8	-77.8	-80.8	-83.8	-86.8	-101.8
-0.8	-57.8	-58.5	-61.2	-64.7	-70.2	-70.8	-73.8	-76.8	-79.8	-82.8	-97.8
-0.7	-53.8	-54.5	-57.2	-60.7	-66.2	-66.8	-69.8	-72.8	-75.8	-78.8	-93.8
-0.6	-49.8	-50.5	-53.2	-56.7	-62.2	-62.8	-65.8	-68.8	-71.8	-74.8	-89.8
-0.5	-45.8	-46.5	-49.2	-52.7	-56.2	-56.8	-59.8	-62.8	-65.8	-68.8	-83.8
-0.4	-41.8	-42.5	-45.2	-48.7	-52.2	-52.8	-55.8	-58.8	-61.8	-64.8	-79.8
-0.3	-37.8	-38.5	-41.2	-44.7	-48.2	-48.8	-51.8	-54.8	-57.8	-60.8	-75.8
-0.2	-33.8	-34.5	-37.2	-40.7	-44.2	-44.8	-47.8	-50.8	-53.8	-56.8	-71.8
-0.1	-29.8	-30.5	-33.2	-36.7	-40.2	-40.8	-43.8	-46.8	-49.8	-52.8	-67.8
0.0	-25.8	-26.5	-29.2	-32.7	-36.2	-36.8	-39.8	-42.8	-45.8	-48.8	-63.8
0.1	-21.8	-22.5	-25.2	-28.7	-32.2	-33.6	-36.6	-39.6	-42.6	-45.6	-60.6
0.2	-17.8	-19.0	-21.7	-25.5	-29.0	-31.2	-34.2	-37.2	-40.2	-43.2	-58.2
0.3	-14.8	-16.4	-19.1	-23.1	-26.6	**-30.0**	**-33.0**	**-36.0**	**-39.0**	**-42.0**	**-57.0**
0.4	-12.6	-14.4	-17.1	**-21.9**	**-25.4**	-30.4	-33.4	-36.4	-39.4	-42.4	-57.4
0.5	-11.1	**-13.4**	**-16.1**	-22.3	-25.8	-31.0	-34.0	-37.0	-40.0	-43.0	-58.0
0.6	**-10.1**	-13.8	-16.5	-22.9	-26.4	-32.2	-35.2	-38.2	-41.2	-44.2	-59.2
0.7	-10.5	-14.4	-17.1	-24.1	-27.6	-33.4	-36.4	-39.4	-42.4	-45.4	-60.4
0.8	-11.1	-15.6	-18.3	-25.3	-28.8	-34.6	-37.6	-40.6	-43.6	-46.6	-61.6
0.9	-12.3	-16.8	-19.5	-26.5	-30.0	-35.8	-38.8	-41.8	-44.8	-47.8	-62.8
1.0	-13.5	-18.0	-20.7	-27.7	-31.2	-37.0	-40.0	-43.0	-46.0	-49.0	-64.0
1.1	-14.7	-19.2	-21.9	-28.9	-32.4	-38.2	-41.2	-44.2	-47.2	-50.2	-65.2
1.2	-15.9	-20.4	-23.1	-30.1	-33.6	-39.4	-42.4	-45.4	-48.4	-51.4	-66.4
1.3	-17.1	-21.6	-24.3	-31.3	-34.8	-40.6	-43.6	-46.6	-49.6	-52.6	-67.6
1.4	-18.3	-22.8	-25.5	-32.5	-36.0	-41.8	-44.8	-47.8	-50.8	-53.8	-68.8
1.5	-19.5	-24.0	-26.7	-33.7	-37.2	-43.0	-46.0	-49.0	-52.0	-55.0	-70.0
1.6	-20.7	-25.2	-27.9	-34.9	-38.4	-44.2	-47.2	-50.2	-53.2	-56.2	-71.2
1.7	-21.9	-26.4	-29.1	-36.1	-39.6	-45.4	-48.4	-51.4	-54.4	-57.4	-72.4
1.8	-23.1	-27.6	-30.3	-37.3	-40.8	-46.6	-49.6	-52.6	-55.6	-58.6	-73.6
1.9	-24.3	-28.8	-31.5	-38.5	-42.0	-47.8	-50.8	-53.8	-56.8	-59.8	-74.8
2.0	-25.5	-30.0	-32.7	-39.7	-43.2	-49.0	-52.0	-55.0	-58.0	-61.0	-76.0
3.6	-44.7	-49.2	-51.9	-58.9	-62.4	-68.2	-71.2	-74.2	-77.2	-80.2	-95.2
$OASPL_P$-UOL_P	-1.6	-5.0	-7.7	-13.7	-17.2	-21.8	-24.8	-27.8	-30.8	-33.8	-48.8

Table V - Spectral Directivity Relations for Plug/Downstream Shock Noise
(a) Corrected Directivity Angle, $\theta_{D.sh,cor}$, 0 to 90 deg

Frequency parameter	Normalized sound pressure level, $SPL_{D,sh}$-$UOL_{D,sh}$, dB vs. corrected directivity angle Corrected directivity angle, $\theta_{D,sh,cor}$, deg									
log $S_{D,sh}$	0	10	20	30	40	50	60	70	80	90
-3.6	-174.2	-173.0	-171.8	-170.6	-169.4	-168.2	-166.0	-165.3	-159.8	-159.6
-2.2	-104.2	-103.0	-101.8	-100.6	-99.4	-98.2	-96.0	-95.3	-89.8	-89.6
-2.1	-99.2	-98.0	-96.8	-95.6	-94.4	-93.2	-91.0	-90.3	-84.8	-84.6
-2.0	-94.2	-93.0	-91.8	-90.6	-89.4	-88.2	-86.0	-85.3	-79.8	-79.6
-1.9	-89.2	-88.0	-86.8	-85.6	-84.4	-83.2	-81.0	-80.3	-74.8	-74.6
-1.8	-84.2	-83.0	-81.8	-80.6	-79.4	-78.2	-76.0	-75.3	-69.8	-69.6
-1.7	-79.2	-78.0	-76.8	-75.6	-74.4	-73.2	-71.0	-70.3	-64.8	-64.6
-1.6	-74.2	-73.0	-71.8	-70.6	-69.4	-68.2	-66.0	-65.3	-59.8	-59.6
-1.5	-69.2	-68.0	-66.8	-65.6	-64.4	-63.2	-61.0	-60.3	-54.8	-54.6
-1.4	-64.2	-63.0	-61.8	-60.6	-59.4	-58.2	-56.0	-55.3	-49.8	-49.6
-1.3	-59.2	-58.0	-56.8	-55.6	-54.4	-53.2	-51.0	-50.3	-44.8	-44.6
-1.2	-54.2	-53.0	-51.8	-50.6	-49.4	-48.2	-46.0	-45.3	-39.8	-39.6
-1.1	-49.2	-48.0	-46.8	-45.6	-44.4	-43.2	-41.0	-40.3	-34.8	-34.6
-1.0	-44.2	-43.0	-41.8	-40.6	-39.4	-38.2	-36.0	-35.3	-29.8	-29.6
-0.9	-39.2	-38.0	-36.8	-35.6	-34.4	-33.2	-31.0	-30.3	-24.8	-24.6
-0.8	-34.2	-33.0	-31.8	-30.6	-29.4	-28.2	-26.0	-25.3	-19.8	-19.6
-0.7	-29.2	-28.0	-26.8	-25.6	-24.4	-23.2	-21.0	-20.3	-14.8	-14.6
-0.6	-24.2	-23.0	-21.8	-20.6	-19.4	-18.2	-16.0	-15.3	-9.8	-9.6
-0.5	-19.2	-18.0	-16.8	-15.6	-14.4	-13.2	-11.0	-10.3	**-7.3**	**-7.6**
-0.4	**-14.2**	**-13.0**	**-11.8**	**-10.6**	**-9.4**	**-8.2**	**-7.0**	**-7.3**	-9.3	-8.6
-0.3	-16.2	-15.0	-13.8	-12.6	-11.4	-10.2	-9.0	-9.3	-10.3	-9.6
-0.2	-18.2	-17.0	-15.8	-14.6	-13.4	-12.2	-11.0	-10.3	-11.3	-10.6
-0.1	-20.2	-19.0	-17.8	-16.6	-15.4	-14.2	-12.0	-11.3	-12.3	-11.6
0.0	-22.2	-21.0	-19.8	-18.6	-16.4	-15.2	-13.0	-12.3	-13.3	-12.6
0.1	-23.2	-22.0	-20.8	-19.6	-17.4	-16.2	-14.0	-13.3	-14.3	-13.6
0.2	-24.2	-23.0	-21.8	-20.6	-18.4	-17.2	-15.0	-14.3	-15.3	-14.6
0.3	-25.2	-24.0	-22.8	-21.6	-19.4	-18.2	-16.0	-15.3	-16.3	-15.6
0.4	-26.2	-25.0	-23.8	-22.6	-20.4	-19.2	-17.0	-16.3	-17.3	-16.6
0.5	-27.2	-26.0	-24.8	-23.6	-21.4	-20.2	-18.0	-17.3	-18.3	-17.6
0.6	-28.2	-27.0	-25.8	-24.6	-22.4	-21.2	-19.0	-18.3	-19.3	-18.6
0.7	-29.2	-28.0	-26.8	-25.6	-23.4	-22.2	-20.0	-19.3	-20.3	-19.6
0.8	-30.2	-29.0	-27.8	-26.6	-24.4	-23.2	-21.0	-20.3	-21.3	-20.6
0.9	-31.2	-30.0	-28.8	-27.6	-25.4	-24.2	-22.0	-21.3	-22.3	-21.6
1.0	-32.2	-31.0	-29.8	-28.6	-26.4	-25.2	-23.0	-22.3	-23.3	-22.6
1.1	-33.2	-32.0	-30.8	-29.6	-27.4	-26.2	-24.0	-23.3	-24.3	-23.6
1.2	-34.2	-33.0	-31.8	-30.6	-28.4	-27.2	-25.0	-24.3	-25.3	-24.6
1.3	-35.2	-34.0	-32.8	-31.6	-29.4	-28.2	-26.0	-25.3	-26.3	-25.6
1.4	-36.2	-35.0	-33.8	-32.6	-30.4	-29.2	-27.0	-26.3	-27.3	-26.6
1.5	-37.2	-36.0	-34.8	-33.6	-31.4	-30.2	-28.0	-27.3	-28.3	-27.6
1.6	-38.2	-37.0	-35.8	-34.6	-32.4	-31.2	-29.0	-28.3	-29.3	-28.6
1.7	-39.2	-38.0	-36.8	-35.6	-33.4	-32.2	-30.0	-29.3	-30.3	-29.6
1.8	-40.2	-39.0	-37.8	-36.6	-34.4	-33.2	-31.0	-30.3	-31.3	-30.6
1.9	-41.2	-40.0	-38.8	-37.6	-35.4	-34.2	-32.0	-31.3	-32.3	-31.6
2.0	-42.2	-41.0	-39.8	-38.6	-36.4	-35.2	-33.0	-32.3	-33.3	-32.6
3.6	-58.2	-57.0	-55.8	-54.6	-52.4	-51.2	-49.0	-48.3	-49.3	-48.6
$OASPL_{D,sh}$-$UOL_{D,sh}$	-8.8	-7.6	-6.4	-5.2	-3.7	-2.5	-0.8	-0.5	-0.4	0.0

Table V (Concluded) - Spectral Directivity Relations for Plug/Downstream Shock Noise
(b) Corrected Directivity Angle, $\theta_{D.sh,cor}$, 100 to 180 deg

Frequency parameter	Normalized sound pressure level, $SPL_{D,sh}$-$UOL_{D,sh}$, dB vs. corrected directivity angle, $\theta_{D,sh,cor}$, deg								
log $S_{D,sh}$	100	110	120	130	140	150	160	170	180
-3.6	-159.6	-159.6	-159.6	-159.6	-159.6	-159.6	-159.6	-159.6	-159.6
-2.2	-89.6	-89.6	-89.6	-89.6	-89.6	-89.6	-89.6	-89.6	-89.6
-2.1	-84.6	-84.6	-84.6	-84.6	-84.6	-84.6	-84.6	-84.6	-84.6
-2.0	-79.6	-79.6	-79.6	-79.6	-79.6	-79.6	-79.6	-79.6	-79.6
-1.9	-74.6	-74.6	-74.6	-74.6	-74.6	-74.6	-74.6	-74.6	-74.6
-1.8	-69.6	-69.6	-69.6	-69.6	-69.6	-69.6	-69.6	-69.6	-69.6
-1.7	-64.6	-64.6	-64.6	-64.6	-64.6	-64.6	-64.6	-64.6	-64.6
-1.6	-59.6	-59.6	-59.6	-59.6	-59.6	-59.6	-59.6	-59.6	-59.6
-1.5	-54.6	-54.6	-54.6	-54.6	-54.6	-54.6	-54.6	-54.6	-54.6
-1.4	-49.6	-49.6	-49.6	-49.6	-49.6	-49.6	-49.6	-49.6	-49.6
-1.3	-44.6	-44.6	-44.6	-44.6	-44.6	-44.6	-44.6	-44.6	-44.6
-1.2	-39.6	-39.6	-39.6	-39.6	-39.6	-39.6	-39.6	-39.6	-39.6
-1.1	-34.6	-34.6	-34.6	-34.6	-34.6	-34.6	-34.6	-34.6	-34.6
-1.0	-29.6	-29.6	-29.6	-29.6	-29.6	-29.6	-29.6	-29.6	-29.6
-0.9	-24.6	-24.6	-24.6	-24.6	-24.6	-24.6	-24.6	-24.6	-24.6
-0.8	-19.6	-19.6	-19.6	-19.6	-19.6	-19.6	-19.6	-19.6	-19.6
-0.7	-14.6	-14.6	-14.6	-14.6	-14.6	-14.6	-14.6	-14.6	-14.6
-0.6	-9.6	-9.6	-9.6	-9.6	-9.6	-9.6	-9.6	-9.6	-9.6
-0.5	**-7.6**	**-7.6**	**-7.6**	**-7.6**	**-7.6**	**-7.6**	**-7.6**	**-7.6**	**-7.6**
-0.4	-8.6	-8.6	-8.6	-8.6	-8.6	-8.6	-8.6	-8.6	-8.6
-0.3	-9.6	-9.6	-9.6	-9.6	-9.6	-9.6	-9.6	-9.6	-9.6
-0.2	-10.6	-10.6	-10.6	-10.6	-10.6	-10.6	-10.6	-10.6	-10.6
-0.1	-11.6	-11.6	-11.6	-11.6	-11.6	-11.6	-11.6	-11.6	-11.6
0.0	-12.6	-12.6	-12.6	-12.6	-12.6	-12.6	-12.6	-12.6	-12.6
0.1	-13.6	-13.6	-13.6	-13.6	-13.6	-13.6	-13.6	-13.6	-13.6
0.2	-14.6	-14.6	-14.6	-14.6	-14.6	-14.6	-14.6	-14.6	-14.6
0.3	-15.6	-15.6	-15.6	-15.6	-15.6	-15.6	-15.6	-15.6	-15.6
0.4	-16.6	-16.6	-16.6	-16.6	-16.6	-16.6	-16.6	-16.6	-16.6
0.5	-17.6	-17.6	-17.6	-17.6	-17.6	-17.6	-17.6	-17.6	-17.6
0.6	-18.6	-18.6	-18.6	-18.6	-18.6	-18.6	-18.6	-18.6	-18.6
0.7	-19.6	-19.6	-19.6	-19.6	-19.6	-19.6	-19.6	-19.6	-19.6
0.8	-20.6	-20.6	-20.6	-20.6	-20.6	-20.6	-20.6	-20.6	-20.6
0.9	-21.6	-21.6	-21.6	-21.6	-21.6	-21.6	-21.6	-21.6	-21.6
1.0	-22.6	-22.6	-22.6	-22.6	-22.6	-22.6	-22.6	-22.6	-22.6
1.1	-23.6	-23.6	-23.6	-23.6	-23.6	-23.6	-23.6	-23.6	-23.6
1.2	-24.6	-24.6	-24.6	-24.6	-24.6	-24.6	-24.6	-24.6	-24.6
1.3	-25.6	-25.6	-25.6	-25.6	-25.6	-25.6	-25.6	-25.6	-25.6
1.4	-26.6	-26.6	-26.6	-26.6	-26.6	-26.6	-26.6	-26.6	-26.6
1.5	-27.6	-27.6	-27.6	-27.6	-27.6	-27.6	-27.6	-27.6	-27.6
1.6	-28.6	-28.6	-28.6	-28.6	-28.6	-28.6	-28.6	-28.6	-28.6
1.7	-29.6	-29.6	-29.6	-29.6	-29.6	-29.6	-29.6	-29.6	-29.6
1.8	-30.6	-30.6	-30.6	-30.6	-30.6	-30.6	-30.6	-30.6	-30.6
1.9	-31.6	-31.6	-31.6	-31.6	-31.6	-31.6	-31.6	-31.6	-31.6
2.0	-32.6	-32.6	-32.6	-32.6	-32.6	-32.6	-32.6	-32.6	-32.6
3.6	-48.6	-48.6	-48.6	-48.6	-48.6	-48.6	-48.6	-48.6	-48.6
$OASPL_{D,sh}$-$UOL_{D,sh}$	0.0	0.0	0.0	0.0	0.0	0.0	0.0	0.0	0.0

Table VI - Spectral Directivity Relations for Outer Stream Shock Noise
(a) Corrected Directivity Angle, $\theta_{O.sh,cor}$, 0 to 90 deg

Frequency parameter	Normalized sound pressure level, $SPL_{O,sh}$-$UOL_{O,sh}$, dB vs. corrected directivity angle Corrected directivity angle, $\theta_{O,sh,cor}$, deg									
log $S_{O,sh}$	0	10	20	30	40	50	60	70	80	90
-3.6	-186.6	-184.6	-182.6	-180.6	-178.6	-176.6	-174.6	-174.6	-174.6	-174.6
-2.2	-116.6	-114.6	-112.6	-110.6	-108.6	-106.6	-104.6	-104.6	-104.6	-104.6
-2.1	-111.6	-109.6	-107.6	-105.6	-103.6	-101.6	-99.6	-99.6	-99.6	-99.6
-2.0	-106.6	-104.6	-102.6	-100.6	-98.6	-96.6	-94.6	-94.6	-94.6	-94.6
-1.9	-101.6	-99.6	-97.6	-95.6	-93.6	-91.6	-89.6	-89.6	-89.6	-89.6
-1.8	-96.6	-94.6	-92.6	-90.6	-88.6	-86.6	-84.6	-84.6	-84.6	-84.6
-1.7	-91.6	-89.6	-87.6	-85.6	-83.6	-81.6	-79.6	-79.6	-79.6	-79.6
-1.6	-86.6	-84.6	-82.6	-80.6	-78.6	-76.6	-74.6	-74.6	-74.6	-74.6
-1.5	-81.6	-79.6	-77.6	-75.6	-73.6	-71.6	-69.6	-69.6	-69.6	-69.6
-1.4	-76.6	-74.6	-72.6	-70.6	-68.6	-66.6	-64.6	-64.6	-64.6	-64.6
-1.3	-71.6	-69.6	-67.6	-65.6	-63.6	-61.6	-59.6	-59.6	-59.6	-59.6
-1.2	-66.6	-64.6	-62.6	-60.6	-58.6	-56.6	-54.6	-54.6	-54.6	-54.6
-1.1	-61.6	-59.6	-57.6	-55.6	-53.6	-51.6	-49.6	-49.6	-49.6	-49.6
-1.0	-56.6	-54.6	-52.6	-50.6	-48.6	-46.6	-44.6	-44.6	-44.6	-44.6
-0.9	-51.6	-49.6	-47.6	-45.6	-43.6	-41.6	-39.6	-39.6	-39.6	-39.6
-0.8	-46.6	-44.6	-42.6	-40.6	-38.6	-36.6	-34.6	-34.6	-34.6	-34.6
-0.7	-41.6	-39.6	-37.6	-35.6	-33.6	-31.6	-29.6	-29.6	-29.6	-29.6
-0.6	-36.6	-34.6	-32.6	-30.6	-28.6	-26.6	-24.6	-24.6	-24.6	-24.6
-0.5	-31.6	-29.6	-27.6	-25.6	-23.6	-21.6	-19.6	-19.6	-19.6	-19.6
-0.4	-26.6	-24.6	-22.6	-20.6	-18.6	-16.6	-14.6	-14.6	-14.6	-14.6
-0.3	-21.6	-19.6	-17.6	-15.6	-13.6	-11.6	-9.6	-9.6	-9.6	-9.6
-0.2	**-19.6**	**-17.6**	**-15.6**	**-13.6**	**-11.6**	**-9.6**	**-7.6**	**-7.6**	**-7.6**	**-7.6**
-0.1	-20.6	-18.6	-16.6	-14.6	-12.6	-10.6	-8.6	-8.6	-8.6	-8.6
0.0	-21.6	-19.6	-17.6	-15.6	-13.6	-11.6	-9.6	-9.6	-9.6	-9.6
0.1	-22.6	-20.6	-18.6	-16.6	-14.6	-12.6	-10.6	-10.6	-10.6	-10.6
0.2	-23.6	-21.6	-19.6	-17.6	-15.6	-13.6	-11.6	-11.6	-11.6	-11.6
0.3	-24.6	-22.6	-20.6	-18.6	-16.6	-14.6	-12.6	-12.6	-12.6	-12.6
0.4	-25.6	-23.6	-21.6	-19.6	-17.6	-15.6	-13.6	-13.6	-13.6	-13.6
0.5	-26.6	-24.6	-22.6	-20.6	-18.6	-16.6	-14.6	-14.6	-14.6	-14.6
0.6	-27.6	-25.6	-23.6	-21.6	-19.6	-17.6	-15.6	-15.6	-15.6	-15.6
0.7	-28.6	-26.6	-24.6	-22.6	-20.6	-18.6	-16.6	-16.6	-16.6	-16.6
0.8	-29.6	-27.6	-25.6	-23.6	-21.6	-19.6	-17.6	-17.6	-17.6	-17.6
0.9	-30.6	-28.6	-26.6	-24.6	-22.6	-20.6	-18.6	-18.6	-18.6	-18.6
1.0	-31.6	-29.6	-27.6	-25.6	-23.6	-21.6	-19.6	-19.6	-19.6	-19.6
1.1	-32.6	-30.6	-28.6	-26.6	-24.6	-22.6	-20.6	-20.6	-20.6	-20.6
1.2	-33.6	-31.6	-29.6	-27.6	-25.6	-23.6	-21.6	-21.6	-21.6	-21.6
1.3	-34.6	-32.6	-30.6	-28.6	-26.6	-24.6	-22.6	-22.6	-22.6	-22.6
1.4	-35.6	-33.6	-31.6	-29.6	-27.6	-25.6	-23.6	-23.6	-23.6	-23.6
1.5	-36.6	-34.6	-32.6	-30.6	-28.6	-26.6	-24.6	-24.6	-24.6	-24.6
1.6	-37.6	-35.6	-33.6	-31.6	-29.6	-27.6	-25.6	-25.6	-25.6	-25.6
1.7	-38.6	-36.6	-34.6	-32.6	-30.6	-28.6	-26.6	-26.6	-26.6	-26.6
1.8	-39.6	-37.6	-35.6	-33.6	-31.6	-29.6	-27.6	-27.6	-27.6	-27.6
1.9	-40.6	-38.6	-36.6	-34.6	-32.6	-30.6	-28.6	-28.6	-28.6	-28.6
2.0	-41.6	-39.6	-37.6	-35.6	-33.6	-31.6	-29.6	-29.6	-29.6	-29.6
3.6	-57.6	-55.6	-53.6	-51.6	-49.6	-47.6	-45.6	-45.6	-45.6	-45.6
$OASPL_{O,sh}$-$UOL_{O,sh}$	-12.0	-10.0	-8.0	-6.0	-4.0	-2.0	0.0	0.0	0.0	0.0

Table VI (Concluded) - Spectral Directivity Relations for Outer Stream Shock Noise
(b) Corrected Directivity Angle, $\theta_{O.sh,cor}$, 100 to 180 deg

Frequency parameter	Normalized sound pressure level, $SPL_{o,sh}$-$UOL_{o,sh}$, dB vs. corrected directivity angle								
	Corrected directivity angle, $\theta_{O,sh,cor}$, deg								
log $S_{O,sh}$	100	110	120	130	140	150	160	170	180
-3.6	-174.6	-174.6	-174.6	-174.6	-179.6	-179.6	-179.6	-179.6	-179.6
-2.2	-104.6	-104.6	-104.6	-104.6	-109.6	-109.6	-109.6	-109.6	-109.6
-2.1	-99.6	-99.6	-99.6	-99.6	-104.6	-104.6	-104.6	-104.6	-104.6
-2.0	-94.6	-94.6	-94.6	-94.6	-99.6	-99.6	-99.6	-99.6	-99.6
-1.9	-89.6	-89.6	-89.6	-89.6	-94.6	-94.6	-94.6	-94.6	-94.6
-1.8	-84.6	-84.6	-84.6	-84.6	-89.6	-89.6	-89.6	-89.6	-89.6
-1.7	-79.6	-79.6	-79.6	-79.6	-84.6	-84.6	-84.6	-84.6	-84.6
-1.6	-74.6	-74.6	-74.6	-74.6	-79.6	-79.6	-79.6	-79.6	-79.6
-1.5	-69.6	-69.6	-69.6	-69.6	-74.6	-74.6	-74.6	-74.6	-74.6
-1.4	-64.6	-64.6	-64.6	-64.6	-69.6	-69.6	-69.6	-69.6	-69.6
-1.3	-59.6	-59.6	-59.6	-59.6	-64.6	-64.6	-64.6	-64.6	-64.6
-1.2	-54.6	-54.6	-54.6	-54.6	-59.6	-59.6	-59.6	-59.6	-59.6
-1.1	-49.6	-49.6	-49.6	-49.6	-54.6	-54.6	-54.6	-54.6	-54.6
-1.0	-44.6	-44.6	-44.6	-44.6	-49.6	-49.6	-49.6	-49.6	-49.6
-0.9	-39.6	-39.6	-39.6	-39.6	-44.6	-44.6	-44.6	-44.6	-44.6
-0.8	-34.6	-34.6	-34.6	-34.6	-39.6	-39.6	-39.6	-39.6	-39.6
-0.7	-29.6	-29.6	-29.6	-29.6	-34.6	-34.6	-34.6	-34.6	-34.6
-0.6	-24.6	-24.6	-24.6	-24.6	-29.6	-29.6	-29.6	-29.6	-29.6
-0.5	-19.6	-19.6	-19.6	-19.6	-24.6	-24.6	-24.6	-24.6	-24.6
-0.4	-14.6	-14.6	-14.6	-14.6	-19.6	-19.6	-19.6	-19.6	-19.6
-0.3	-9.6	-9.6	-9.6	-9.6	-14.6	-14.6	-14.6	-14.6	-14.6
-0.2	**-7.6**	**-7.6**	**-7.6**	**-7.6**	-9.6	-9.6	-9.6	-9.6	-9.6
-0.1	-8.6	-8.6	-8.6	-8.6	**-7.6**	**-7.6**	**-7.6**	**-7.6**	**-7.6**
0.0	-9.6	-9.6	-9.6	-9.6	-8.6	-8.6	-8.6	-8.6	-8.6
0.1	-10.6	-10.6	-10.6	-10.6	-9.6	-9.6	-9.6	-9.6	-9.6
0.2	-11.6	-11.6	-11.6	-11.6	-10.6	-10.6	-10.6	-10.6	-10.6
0.3	-12.6	-12.6	-12.6	-12.6	-11.6	-11.6	-11.6	-11.6	-11.6
0.4	-13.6	-13.6	-13.6	-13.6	-12.6	-12.6	-12.6	-12.6	-12.6
0.5	-14.6	-14.6	-14.6	-14.6	-13.6	-13.6	-13.6	-13.6	-13.6
0.6	-15.6	-15.6	-15.6	-15.6	-14.6	-14.6	-14.6	-14.6	-14.6
0.7	-16.6	-16.6	-16.6	-16.6	-15.6	-15.6	-15.6	-15.6	-15.6
0.8	-17.6	-17.6	-17.6	-17.6	-16.6	-16.6	-16.6	-16.6	-16.6
0.9	-18.6	-18.6	-18.6	-18.6	-17.6	-17.6	-17.6	-17.6	-17.6
1.0	-19.6	-19.6	-19.6	-19.6	-18.6	-18.6	-18.6	-18.6	-18.6
1.1	-20.6	-20.6	-20.6	-20.6	-19.6	-19.6	-19.6	-19.6	-19.6
1.2	-21.6	-21.6	-21.6	-21.6	-20.6	-20.6	-20.6	-20.6	-20.6
1.3	-22.6	-22.6	-22.6	-22.6	-21.6	-21.6	-21.6	-21.6	-21.6
1.4	-23.6	-23.6	-23.6	-23.6	-22.6	-22.6	-22.6	-22.6	-22.6
1.5	-24.6	-24.6	-24.6	-24.6	-23.6	-23.6	-23.6	-23.6	-23.6
1.6	-25.6	-25.6	-25.6	-25.6	-24.6	-24.6	-24.6	-24.6	-24.6
1.7	-26.6	-26.6	-26.6	-26.6	-25.6	-25.6	-25.6	-25.6	-25.6
1.8	-27.6	-27.6	-27.6	-27.6	-26.6	-26.6	-26.6	-26.6	-26.6
1.9	-28.6	-28.6	-28.6	-28.6	-27.6	-27.6	-27.6	-27.6	-27.6
2.0	-29.6	-29.6	-29.6	-29.6	-28.6	-28.6	-28.6	-28.6	-28.6
3.6	-45.6	-45.6	-45.6	-45.6	-44.6	-44.6	-44.6	-44.6	-44.6
$OASPL_{O,sh}$-$UOL_{O,sh}$	0.0	0.0	0.0	0.0	0.0	0.0	0.0	0.0	0.0

Table VII - Spectral Directivity Relations for Inner Stream Shock Noise
(a) Corrected Directivity Angle, $\theta_{l.sh,cor}$, 0 to 90 deg

Frequency parameter	Normalized sound pressure level, $SPL_{l,sh}$-$UOL_{l,sh}$, dB vs. corrected directivity angle Corrected directivity angle, $\theta_{l,sh,cor}$, deg									
log $S_{l,sh}$	0	10	20	30	40	50	60	70	80	90
-3.6	-181.0	-181.0	-181.0	-181.0	-181.0	-181.5	-182.0	-182.5	-178.0	-178.4
-2.2	-111.0	-111.0	-111.0	-111.0	-111.0	-111.5	-112.0	-112.5	-108.0	-108.4
-2.1	-106.0	-106.0	-106.0	-106.0	-106.0	-106.5	-107.0	-107.5	-103.0	-103.4
-2.0	-101.0	-101.0	-101.0	-101.0	-101.0	-101.5	-102.0	-102.5	-98.0	-98.4
-1.9	-96.0	-96.0	-96.0	-96.0	-96.0	-96.5	-97.0	-97.5	-93.0	-93.4
-1.8	-91.0	-91.0	-91.0	-91.0	-91.0	-91.5	-92.0	-92.5	-88.0	-88.4
-1.7	-86.0	-86.0	-86.0	-86.0	-86.0	-86.5	-87.0	-87.5	-83.0	-83.4
-1.6	-81.0	-81.0	-81.0	-81.0	-81.0	-81.5	-82.0	-82.5	-78.0	-78.4
-1.5	-76.0	-76.0	-76.0	-76.0	-76.0	-76.5	-77.0	-77.5	-73.0	-73.4
-1.4	-71.0	-71.0	-71.0	-71.0	-71.0	-71.5	-72.0	-72.5	-68.0	-68.4
-1.3	-66.0	-66.0	-66.0	-66.0	-66.0	-66.5	-67.0	-67.5	-63.0	-63.4
-1.2	-61.0	-61.0	-61.0	-61.0	-61.0	-61.5	-62.0	-62.5	-58.0	-58.4
-1.1	-56.0	-56.0	-56.0	-56.0	-56.0	-56.5	-57.0	-57.5	-53.0	-53.4
-1.0	-51.0	-51.0	-51.0	-51.0	-51.0	-51.5	-52.0	-52.5	-48.0	-48.4
-0.9	-46.0	-46.0	-46.0	-46.0	-46.0	-46.5	-47.0	-47.5	-43.0	-43.4
-0.8	-41.0	-41.0	-41.0	-41.0	-41.0	-41.5	-42.0	-42.5	-38.0	-38.4
-0.7	-36.0	-36.0	-36.0	-36.0	-36.0	-36.5	-37.0	-37.5	-33.0	-33.4
-0.6	-31.0	-31.0	-31.0	-31.0	-31.0	-31.5	-32.0	-32.5	-28.0	-28.4
-0.5	-26.0	-26.0	-26.0	-26.0	-26.0	-26.5	-27.0	-27.5	-23.0	-23.4
-0.4	-21.0	-21.0	-21.0	-21.0	-21.0	-21.5	-22.0	-22.5	-18.0	-18.4
-0.3	-16.0	-16.0	-16.0	-16.0	-16.0	-16.5	-17.0	-17.5	-13.0	-13.4
-0.2	-11.0	-11.0	-11.0	-11.0	-11.0	-11.5	-12.0	-12.5	-8.0	-8.4
-0.1	-6.0	-6.0	-6.0	-6.0	-6.0	-6.5	-7.0	-7.5	**-6.0**	**-6.4**
0.0	**-4.0**	**-4.0**	**-4.0**	**-4.0**	**-4.0**	**-4.5**	**-5.0**	**-5.5**	-7.5	-7.9
0.1	-5.5	-5.5	-5.5	-5.5	-5.5	-6.0	-6.5	-7.0	-9.5	-9.4
0.2	-7.5	-7.5	-7.5	-7.5	-7.5	-8.0	-8.5	-9.0	-11.5	-10.9
0.3	-9.5	-9.5	-9.5	-9.5	-9.5	-10.0	-10.5	-11.0	-13.5	-12.4
0.4	-11.5	-11.5	-11.5	-11.5	-11.5	-12.0	-12.5	-13.0	-15.5	-13.9
0.5	-13.5	-13.5	-13.5	-13.5	-13.5	-14.0	-14.5	-15.0	-17.5	-15.4
0.6	-15.5	-15.5	-15.5	-15.5	-15.5	-16.0	-16.5	-17.0	-19.5	-16.9
0.7	-17.5	-17.5	-17.5	-17.5	-17.5	-18.0	-18.5	-19.0	-21.5	-18.4
0.8	-19.5	-19.5	-19.5	-19.5	-19.5	-20.0	-20.5	-21.0	-23.5	-19.9
0.9	-21.5	-21.5	-21.5	-21.5	-21.5	-22.0	-22.5	-23.0	-25.5	-21.4
1.0	-23.5	-23.5	-23.5	-23.5	-23.5	-24.0	-24.5	-25.0	-27.5	-22.9
1.1	-25.5	-25.5	-25.5	-25.5	-25.5	-26.0	-26.5	-27.0	-29.5	-24.4
1.2	-27.5	-27.5	-27.5	-27.5	-27.5	-28.0	-28.5	-29.0	-31.5	-25.9
1.3	-29.5	-29.5	-29.5	-29.5	-29.5	-30.0	-30.5	-31.0	-33.5	-27.4
1.4	-31.5	-31.5	-31.5	-31.5	-31.5	-32.0	-32.5	-33.0	-35.5	-28.9
1.5	-33.5	-33.5	-33.5	-33.5	-33.5	-34.0	-34.5	-35.0	-37.5	-30.4
1.6	-35.5	-35.5	-35.5	-35.5	-35.5	-36.0	-36.5	-37.0	-39.5	-31.9
1.7	-37.5	-37.5	-37.5	-37.5	-37.5	-38.0	-38.5	-39.0	-41.5	-33.4
1.8	-39.5	-39.5	-39.5	-39.5	-39.5	-40.0	-40.5	-41.0	-43.5	-34.9
1.9	-41.5	-41.5	-41.5	-41.5	-41.5	-42.0	-42.5	-43.0	-45.5	-36.4
2.0	-43.5	-43.5	-43.5	-43.5	-43.5	-44.0	-44.5	-45.0	-47.5	-37.9
3.6	-71.5	-71.5	-71.5	-71.5	-71.5	-72.0	-72.5	-73.0	-75.5	-65.9
$OASPL_{l,sh}$-$UOL_{l,sh}$	1.8	1.8	1.8	1.8	1.8	1.3	0.8	0.3	-0.2	0.0

Table VII (Concluded) - Spectral Directivity Relations for Inner Stream Shock Noise
(b) Corrected Directivity Angle, $\theta_{l.sh,cor}$, 100 to 180 deg

Frequency parameter	Normalized sound pressure level, SPL_{lsh}-$UOL_{l,sh}$, dB vs. corrected directivity angle								
	Corrected directivity angle, $\theta_{l,sh,cor}$, deg								
log $S_{l,sh}$	100	110	120	130	140	150	160	170	180
-3.6	-178.6	-178.8	-179.0	-179.2	-179.4	-179.6	-179.8	-180.0	-180.2
-2.2	-108.6	-108.8	-109.0	-109.2	-109.4	-109.6	-109.8	-110.0	-110.2
-2.1	-103.6	-103.8	-104.0	-104.2	-104.4	-104.6	-104.8	-105.0	-105.2
-2.0	-98.6	-98.8	-99.0	-99.2	-99.4	-99.6	-99.8	-100.0	-100.2
-1.9	-93.6	-93.8	-94.0	-94.2	-94.4	-94.6	-94.8	-95.0	-95.2
-1.8	-88.6	-88.8	-89.0	-89.2	-89.4	-89.6	-89.8	-90.0	-90.2
-1.7	-83.6	-83.8	-84.0	-84.2	-84.4	-84.6	-84.8	-85.0	-85.2
-1.6	-78.6	-78.8	-79.0	-79.2	-79.4	-79.6	-79.8	-80.0	-80.2
-1.5	-73.6	-73.8	-74.0	-74.2	-74.4	-74.6	-74.8	-75.0	-75.2
-1.4	-68.6	-68.8	-69.0	-69.2	-69.4	-69.6	-69.8	-70.0	-70.2
-1.3	-63.6	-63.8	-64.0	-64.2	-64.4	-64.6	-64.8	-65.0	-65.2
-1.2	-58.6	-58.8	-59.0	-59.2	-59.4	-59.6	-59.8	-60.0	-60.2
-1.1	-53.6	-53.8	-54.0	-54.2	-54.4	-54.6	-54.8	-55.0	-55.2
-1.0	-48.6	-48.8	-49.0	-49.2	-49.4	-49.6	-49.8	-50.0	-50.2
-0.9	-43.6	-43.8	-44.0	-44.2	-44.4	-44.6	-44.8	-45.0	-45.2
-0.8	-38.6	-38.8	-39.0	-39.2	-39.4	-39.6	-39.8	-40.0	-40.2
-0.7	-33.6	-33.8	-34.0	-34.2	-34.4	-34.6	-34.8	-35.0	-35.2
-0.6	-28.6	-28.8	-29.0	-29.2	-29.4	-29.6	-29.8	-30.0	-30.2
-0.5	-23.6	-23.8	-24.0	-24.2	-24.4	-24.6	-24.8	-25.0	-25.2
-0.4	-18.6	-18.8	-19.0	-19.2	-19.4	-19.6	-19.8	-20.0	-20.2
-0.3	-13.6	-13.8	-14.0	-14.2	-14.4	-14.6	-14.8	-15.0	-15.2
-0.2	-8.6	-8.8	-9.0	-9.2	-9.4	-9.6	-9.8	-10.0	-10.2
-0.1	**-6.6**	**-6.8**	**-7.0**	**-7.2**	**-7.4**	**-7.6**	**-7.8**	**-8.0**	**-8.2**
0.0	-8.1	-8.3	-8.5	-8.7	-8.9	-9.1	-9.3	-9.5	-9.7
0.1	-9.6	-9.8	-10.0	-10.2	-10.4	-10.6	-10.8	-11.0	-11.2
0.2	-11.1	-11.3	-11.5	-11.7	-11.9	-12.1	-12.3	-12.5	-12.7
0.3	-12.6	-12.8	-13.0	-13.2	-13.4	-13.6	-13.8	-14.0	-14.2
0.4	-14.1	-14.3	-14.5	-14.7	-14.9	-15.1	-15.3	-15.5	-15.7
0.5	-15.6	-15.8	-16.0	-16.2	-16.4	-16.6	-16.8	-17.0	-17.2
0.6	-17.1	-17.3	-17.5	-17.7	-17.9	-18.1	-18.3	-18.5	-18.7
0.7	-18.6	-18.8	-19.0	-19.2	-19.4	-19.6	-19.8	-20.0	-20.2
0.8	-20.1	-20.3	-20.5	-20.7	-20.9	-21.1	-21.3	-21.5	-21.7
0.9	-21.6	-21.8	-22.0	-22.2	-22.4	-22.6	-22.8	-23.0	-23.2
1.0	-23.1	-23.3	-23.5	-23.7	-23.9	-24.1	-24.3	-24.5	-24.7
1.1	-24.6	-24.8	-25.0	-25.2	-25.4	-25.6	-25.8	-26.0	-26.2
1.2	-26.1	-26.3	-26.5	-26.7	-26.9	-27.1	-27.3	-27.5	-27.7
1.3	-27.6	-27.8	-28.0	-28.2	-28.4	-28.6	-28.8	-29.0	-29.2
1.4	-29.1	-29.3	-29.5	-29.7	-29.9	-30.1	-30.3	-30.5	-30.7
1.5	-30.6	-30.8	-31.0	-31.2	-31.4	-31.6	-31.8	-32.0	-32.2
1.6	-32.1	-32.3	-32.5	-32.7	-32.9	-33.1	-33.3	-33.5	-33.7
1.7	-33.6	-33.8	-34.0	-34.2	-34.4	-34.6	-34.8	-35.0	-35.2
1.8	-35.1	-35.3	-35.5	-35.7	-35.9	-36.1	-36.3	-36.5	-36.7
1.9	-36.6	-36.8	-37.0	-37.2	-37.4	-37.6	-37.8	-38.0	-38.2
2.0	-38.1	-38.3	-38.5	-38.7	-38.9	-39.1	-39.3	-39.5	-39.7
3.6	-66.1	-66.3	-66.5	-66.7	-66.9	-67.1	-67.3	-67.5	-67.7
$OASPL_{l,sh}$-$UOL_{l,sh}$	-0.2	-0.4	-0.6	-0.8	-1.0	-1.2	-1.4	-1.6	-1.8

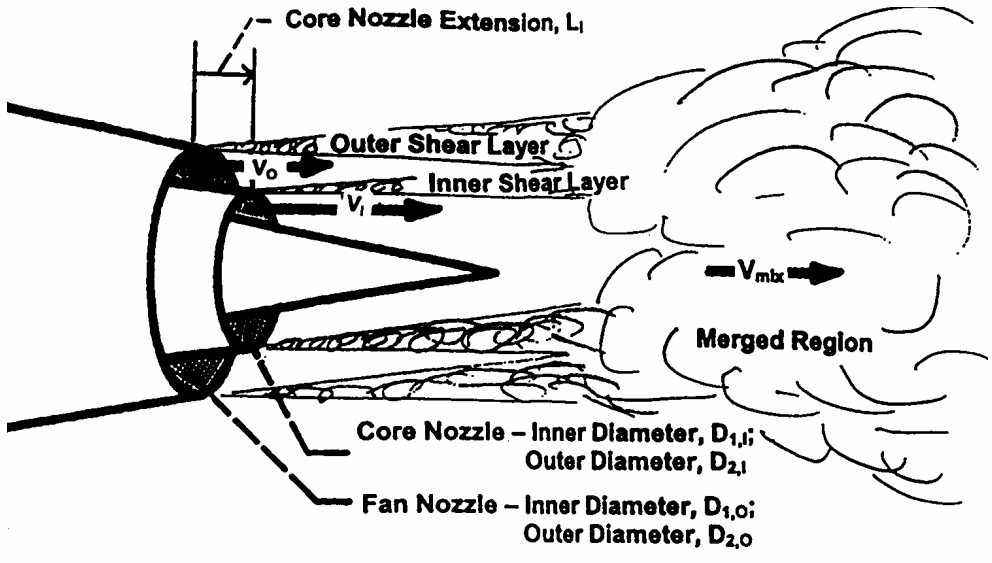

Figure 1.—Separate-Flow Coannular Plug Nozzle Geometry
and Mixing Noise Generation Regions.

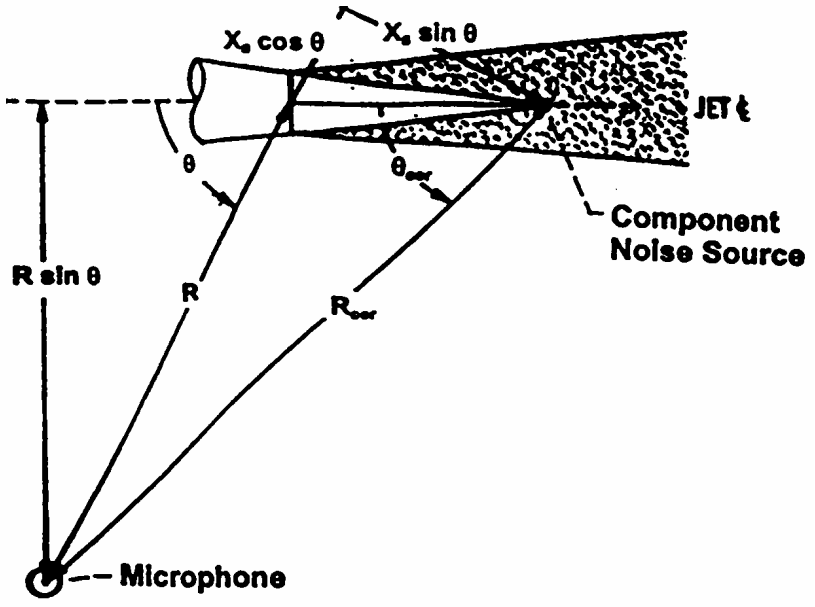

Figure 2.—Noise Source and Microphone Location Geometry.

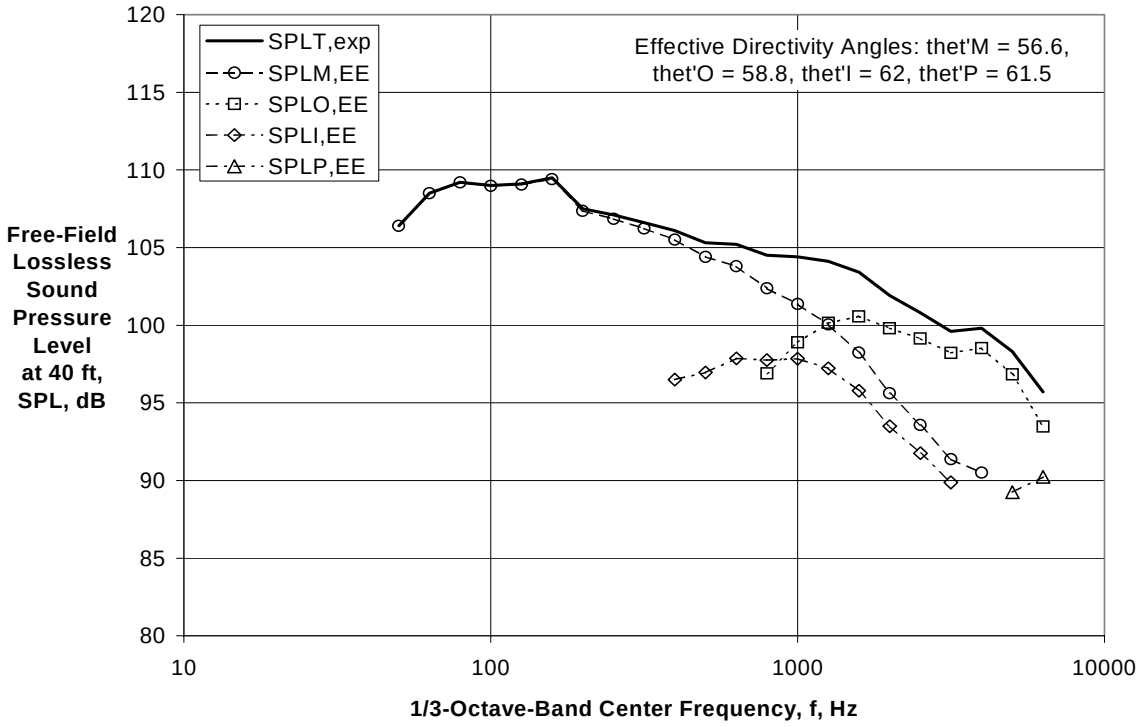

(a) Directivity Angle θ = 60 deg

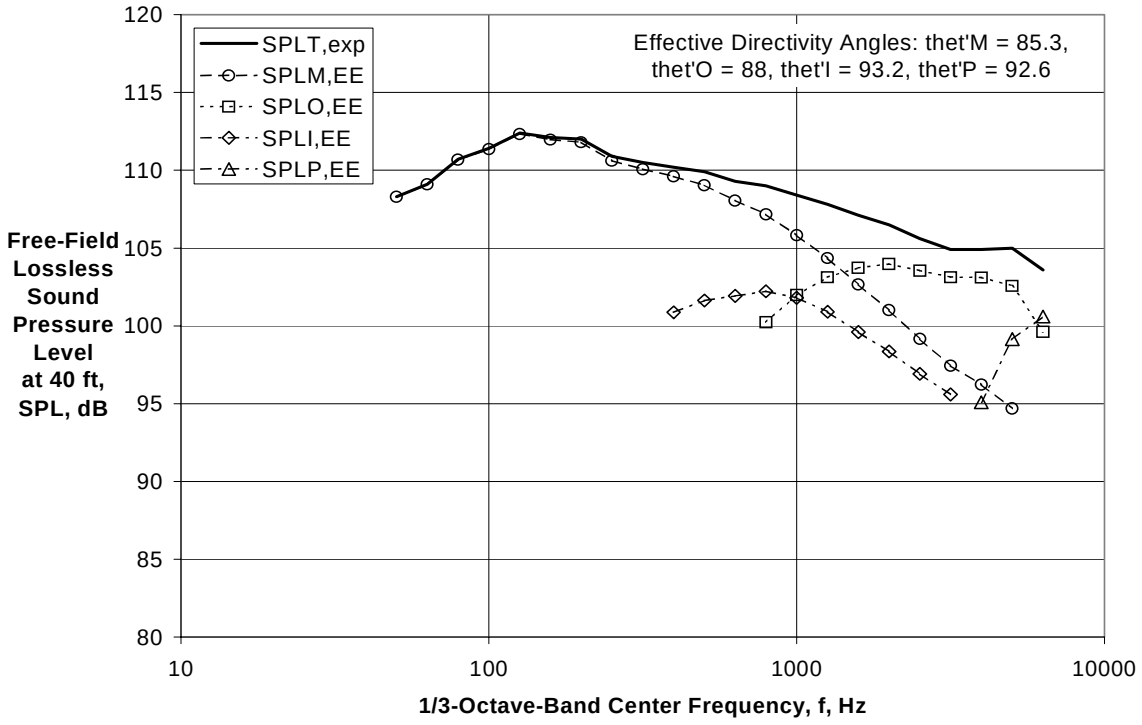

(b) Directivity Angle θ = 90 deg

Figure 3.—Component Spectral Extraction Using Experimental Coefficients for Baseline BPR ≅ 5 External Plug Nozzle at V_{mix}/c_{amb} = 1.09 and M_f = 0.0.

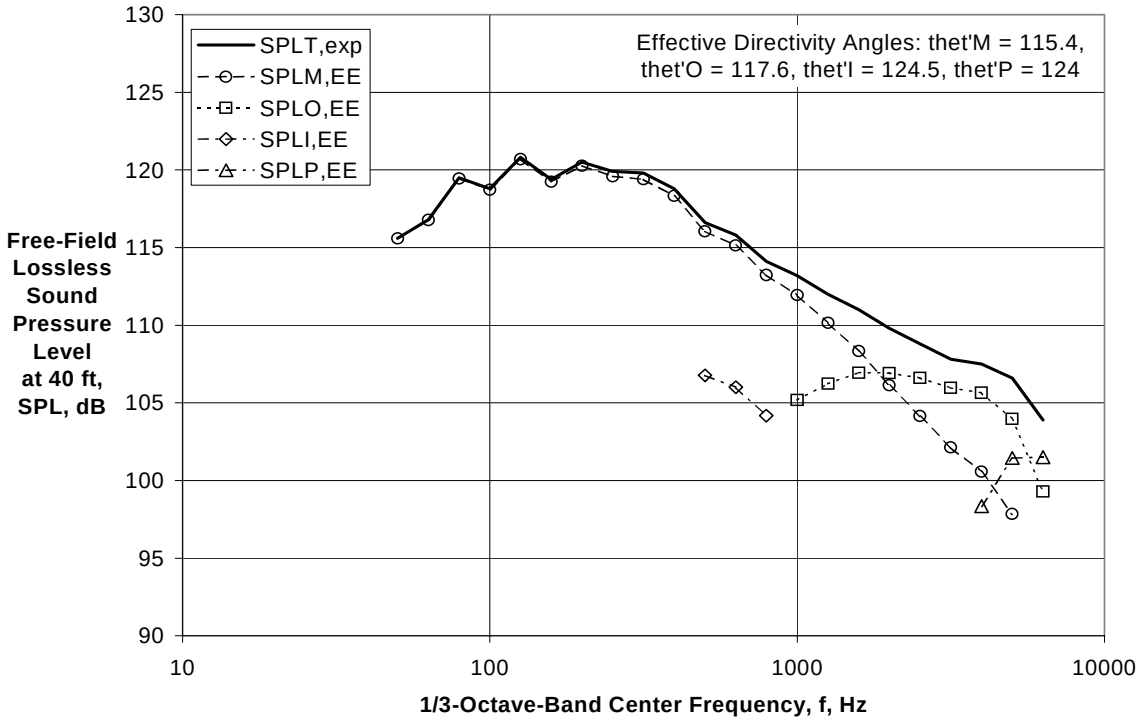

(c) Directivity Angle θ = 120 deg

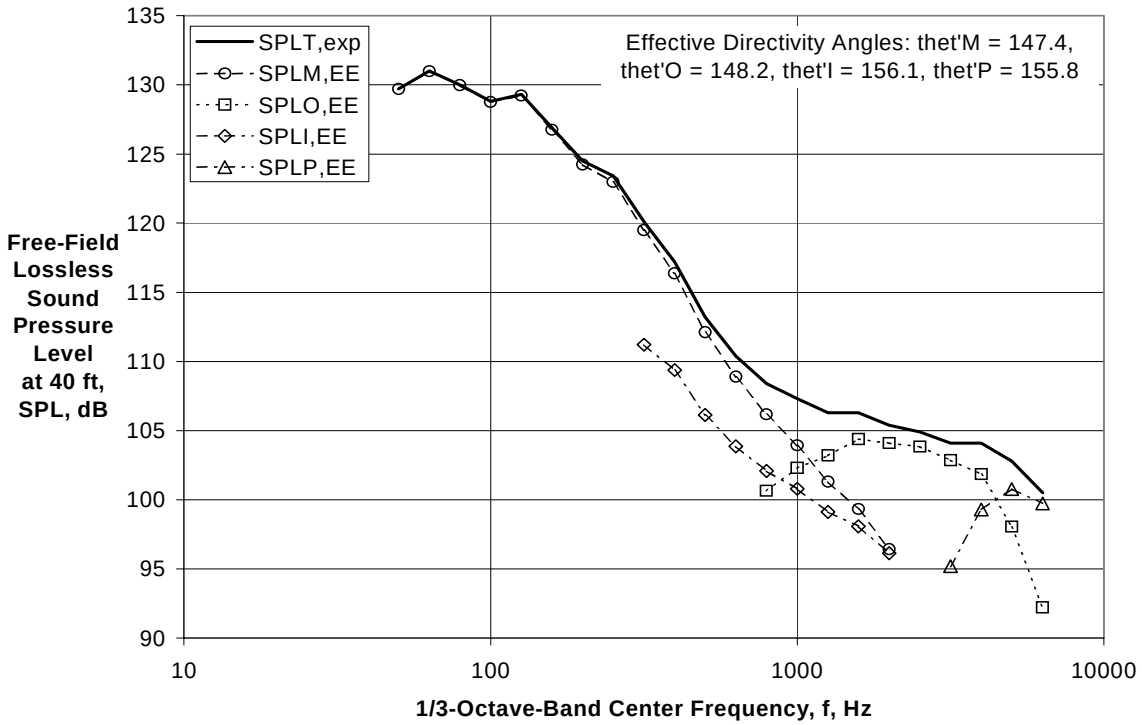

(d) Directivity Angle θ = 150 deg

Figure 3.—(Concluded) Component Spectral Extraction Using Experimental Coefficients for Baseline BPR ≅ 5 External Plug Nozzle at V_{mix}/c_{amb} = 1.09 and M_f = 0.0.

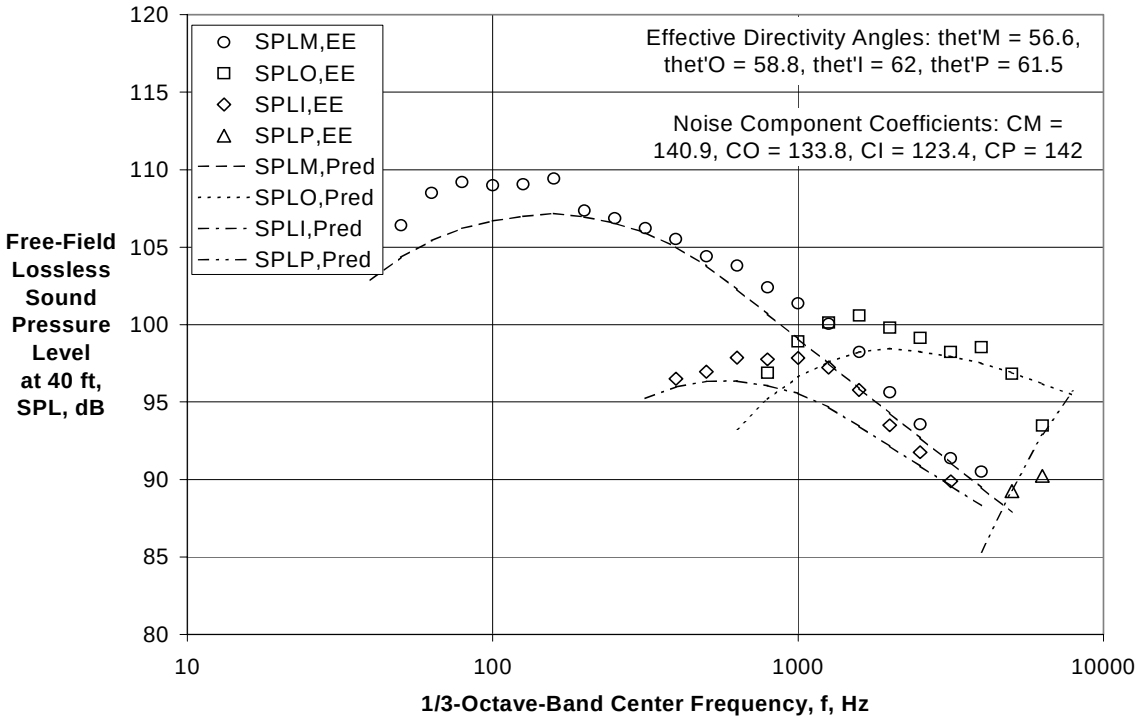

(a) Directivity Angle θ = 60 deg

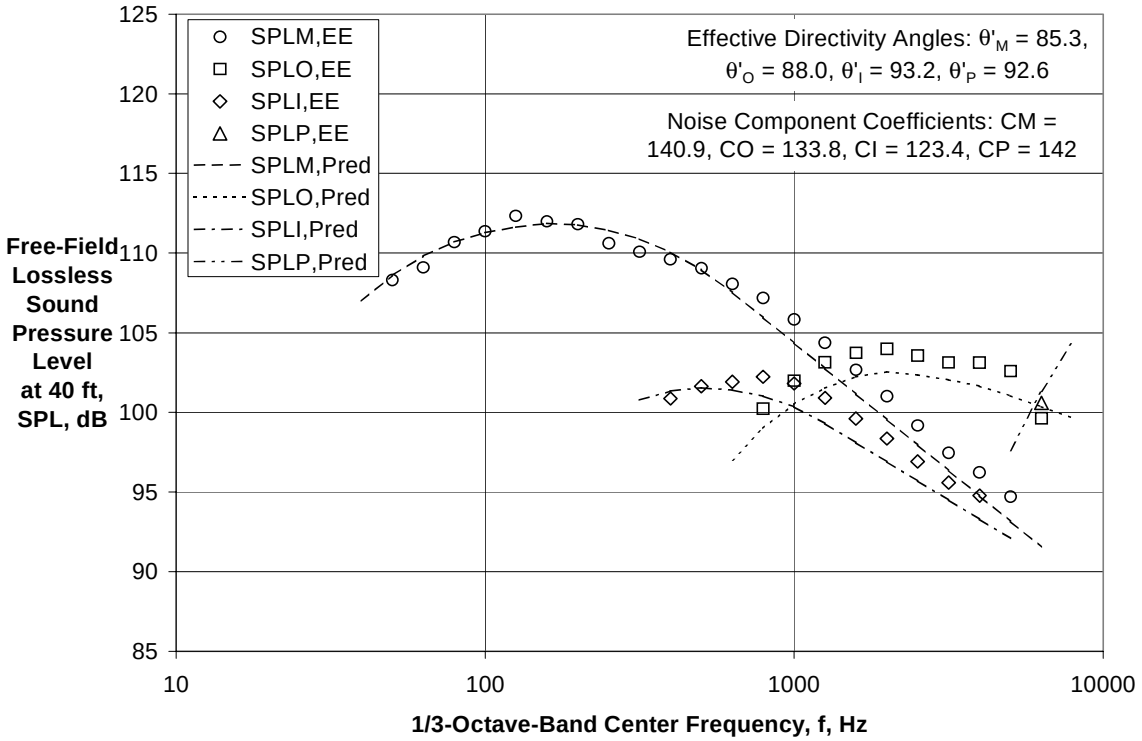

(b) Directivity Angle θ = 90 deg

Figure 4.—Comparison of Extracted and Predicted Component Spectra for Baseline BPR ≅ 5 External Plug Nozzle at V_{mix}/c_{amb} = 1.09 and M_f = 0.0.

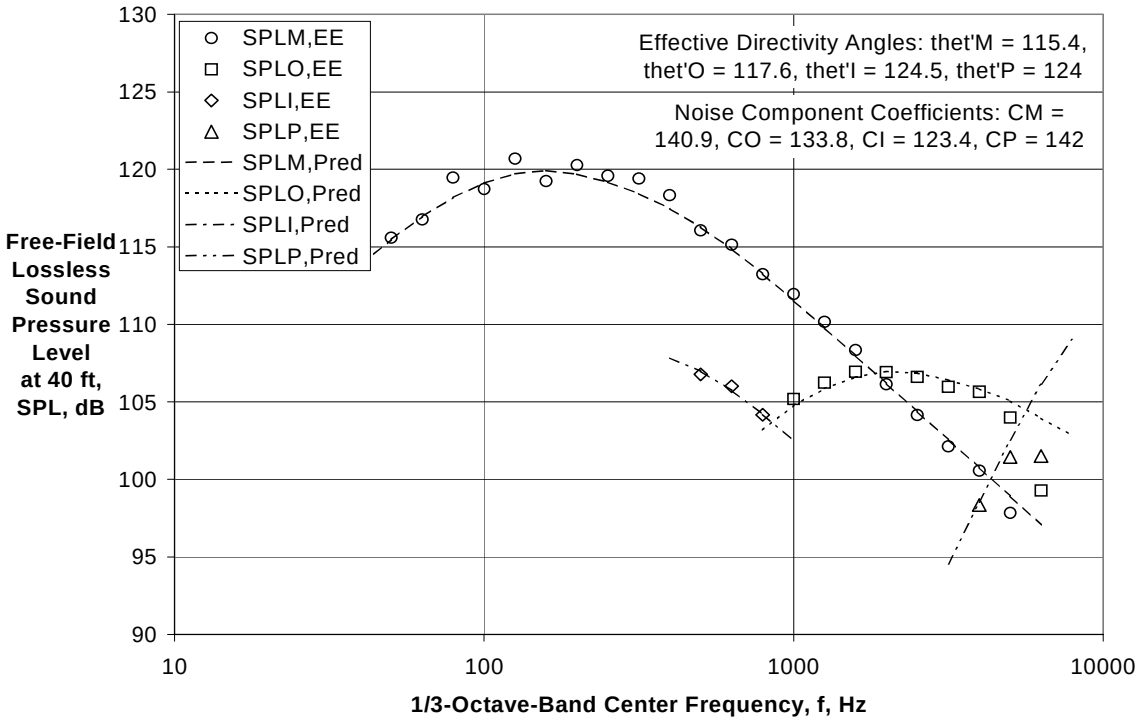

(c) Directivity Angle θ = 120 deg

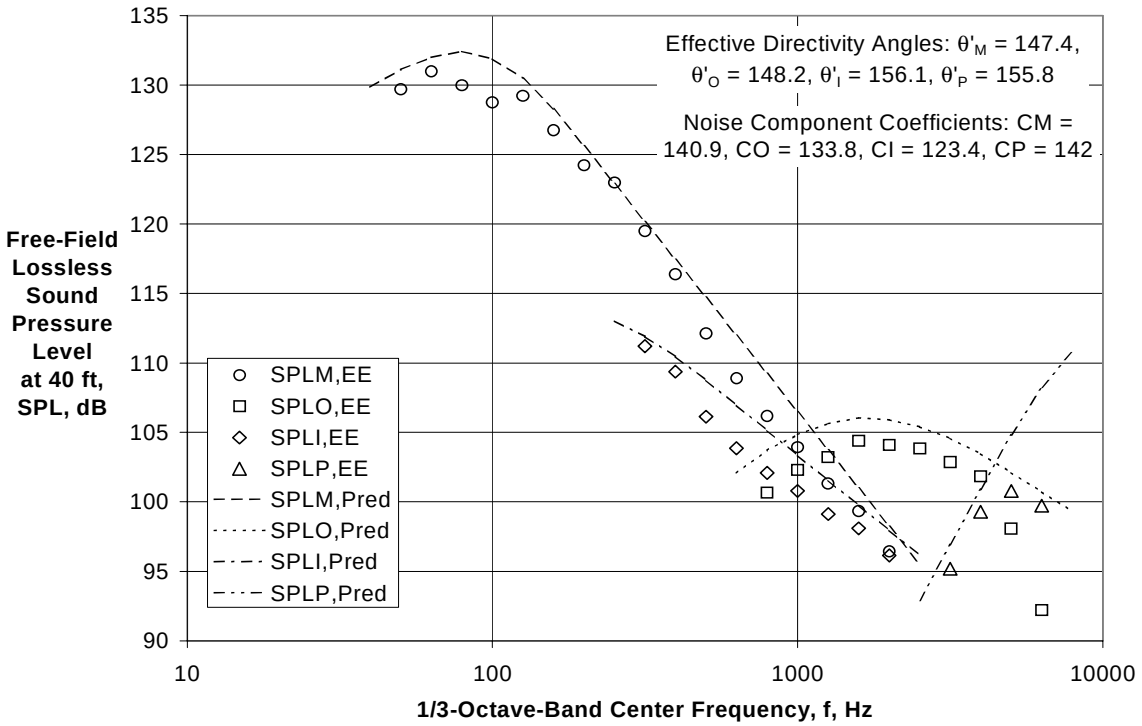

(d) Directivity Angle θ = 150 deg

Figure 4.—(Concluded) Comparison of Extracted and Predicted Component Spectra for Baseline BPR ≅ 5 External Plug Nozzle at V_{mix}/c_{amb} = 1.09 and M_f = 0.0.

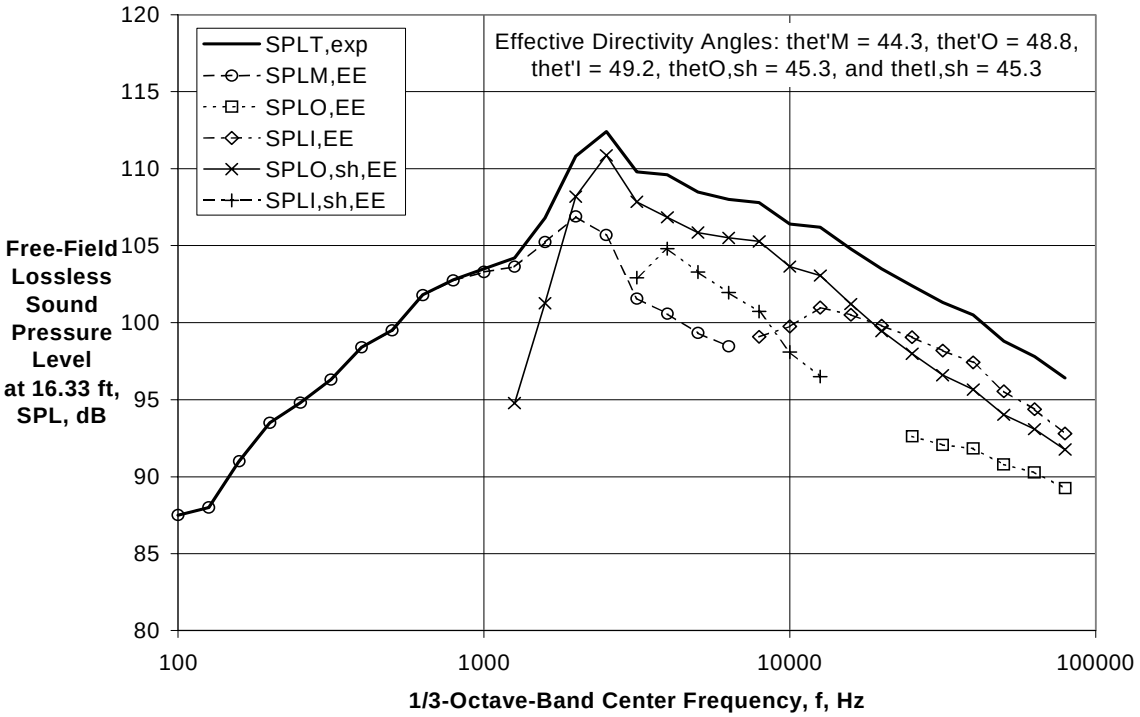

(a) Directivity Angle θ = 46 deg

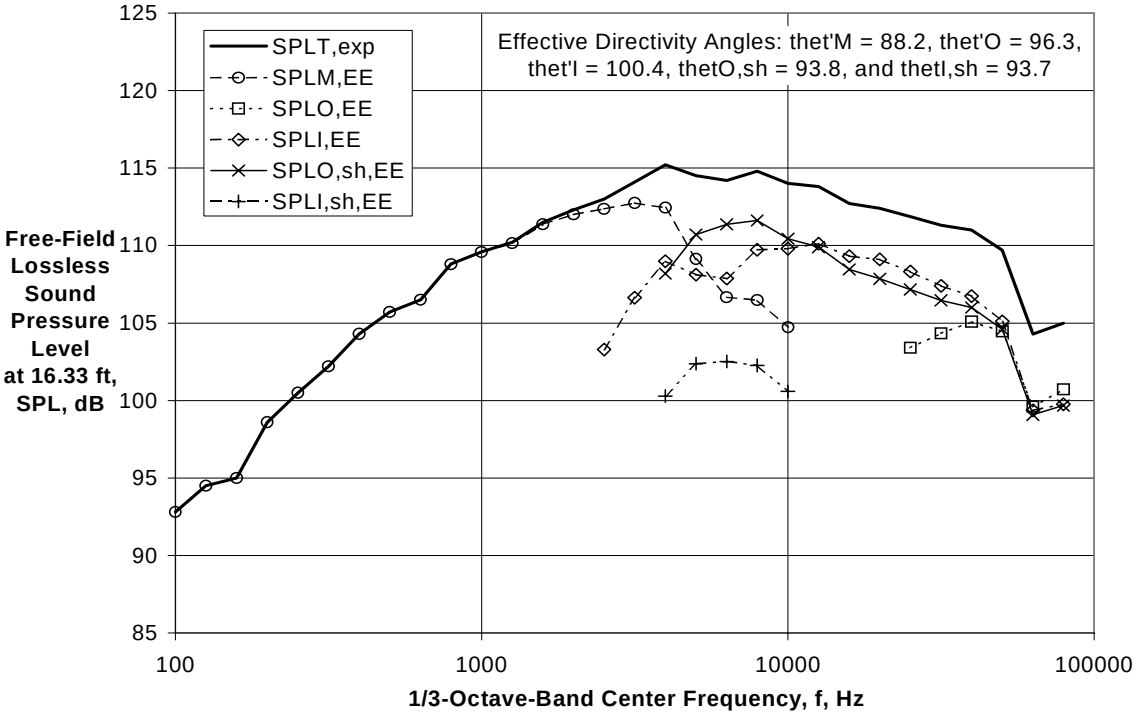

(b) Directivity Angle θ = 95 deg

Figure 5.—Component Spectral Extraction Using Experimental Coefficients for Baseline BPR ≅ 1 Plugless Coplanar Nozzle at V_{mix}/c_{amb} = 2.04 and M_f = 0.0.

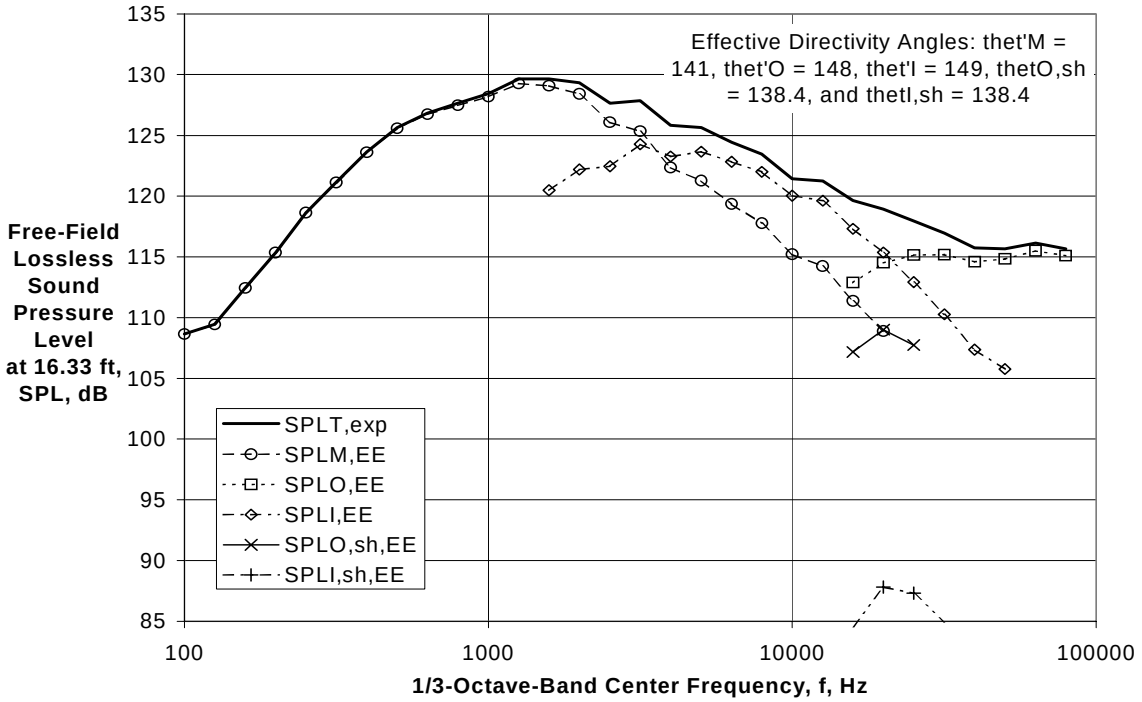

(c) Directivity Angle θ = 139 deg

Figure 5.—(Concluded) Component Spectral Extraction Using Experimental Coefficients for Baseline BPR ≅ 1 Plugless Coplanar Nozzle at V_{mix}/c_{amb} = 2.04 and M_f = 0.0.

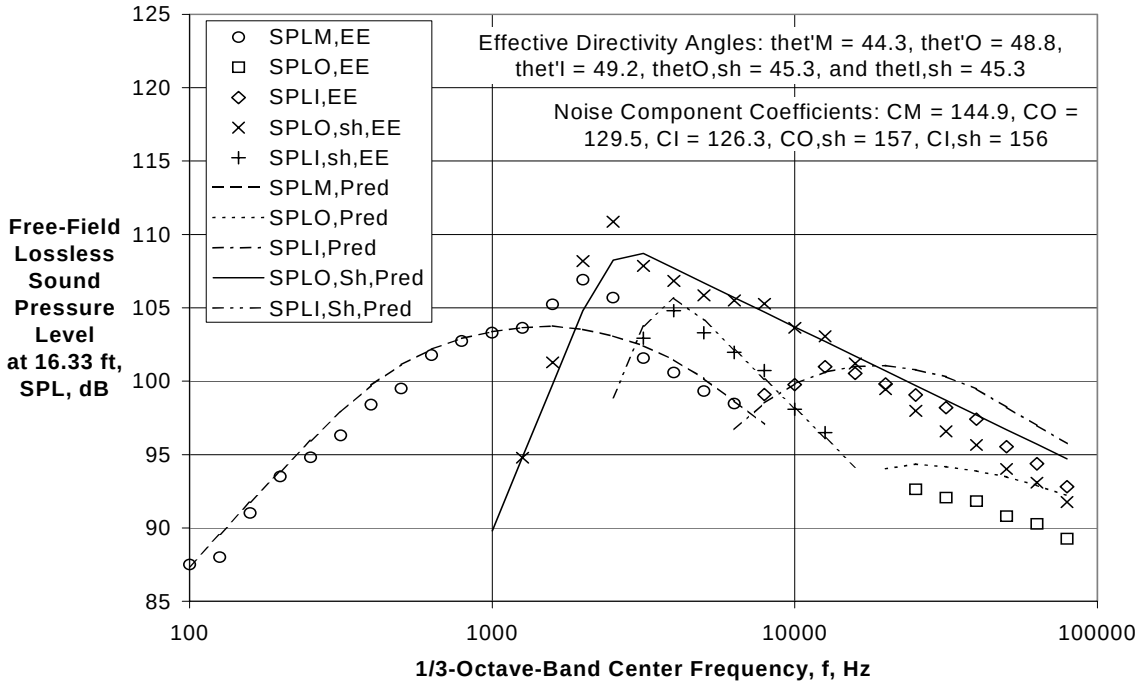

(a) Directivity Angle θ = 46 deg

Figure 6.—Comparison of Extracted and Predicted Component Spectra for Baseline BPR ≅ 1 Plugless Coplanar Nozzle at V_{mix}/c_{amb} = 2.04 and M_f = 0.0.

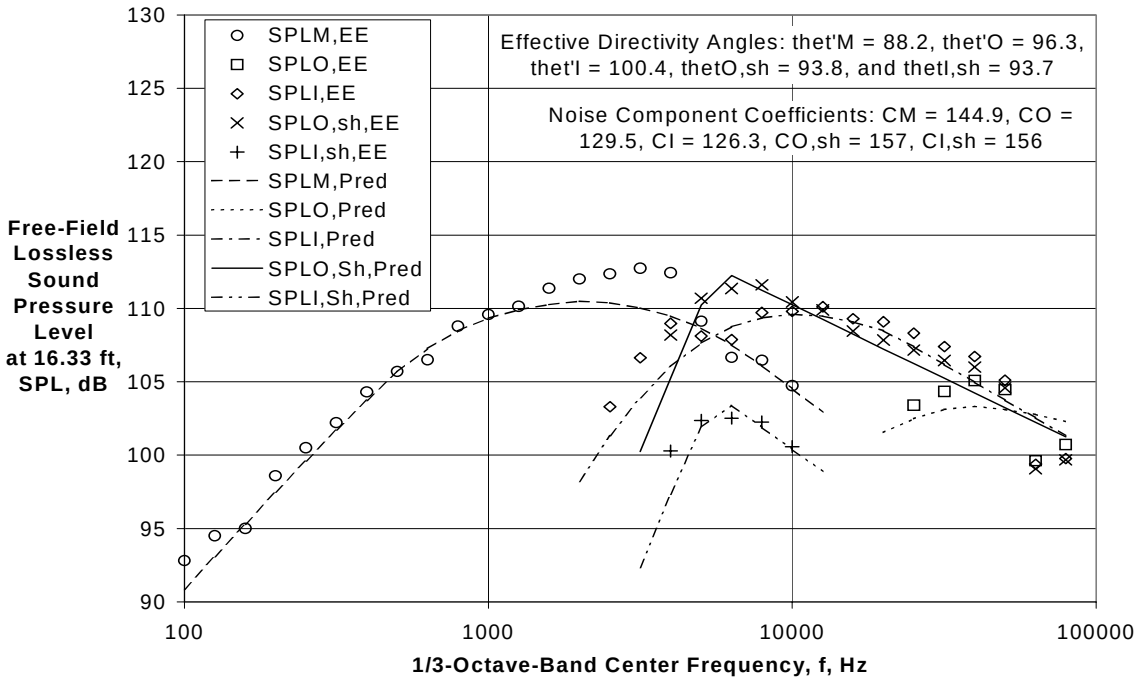

(a) Directivity Angle θ = 95 deg

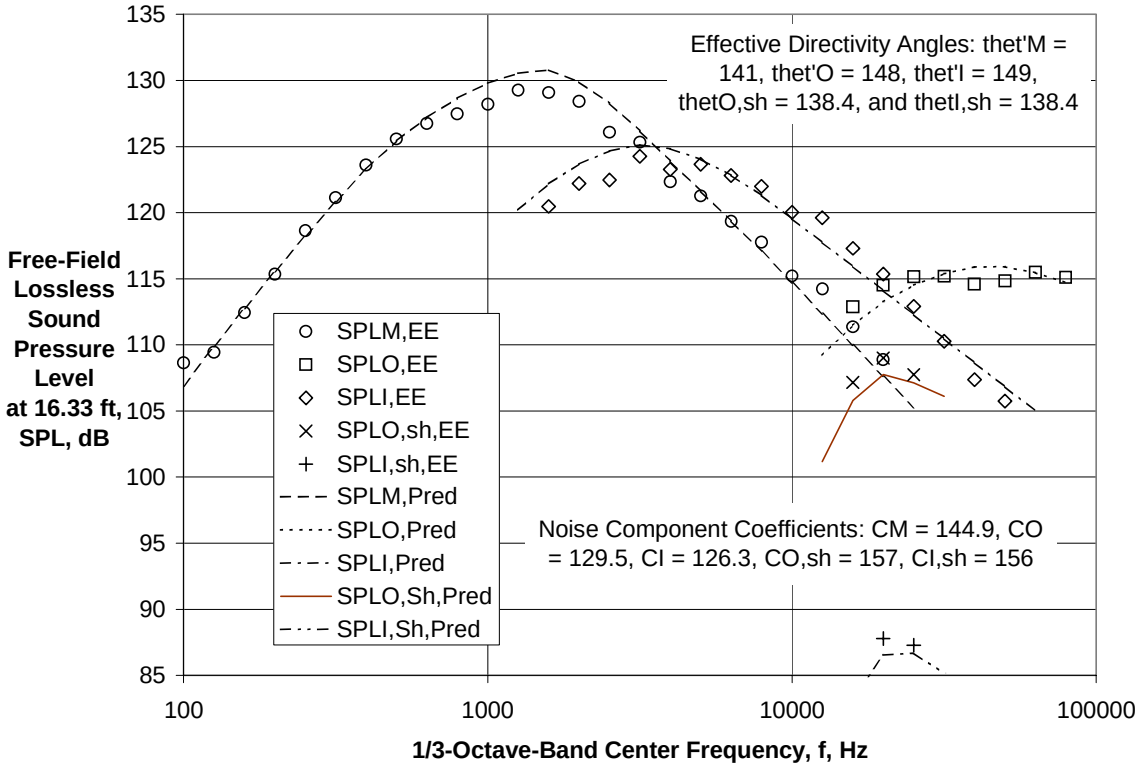

(c) Directivity Angle θ = 139 deg

Figure 6.—(Concluded) Comparison of Extracted and Predicted Component Spectra for Baseline BPR ≅ 1 Plugless Coplanar Nozzle at V_{mix}/c_{amb} = 2.04 and M_f = 0.0.

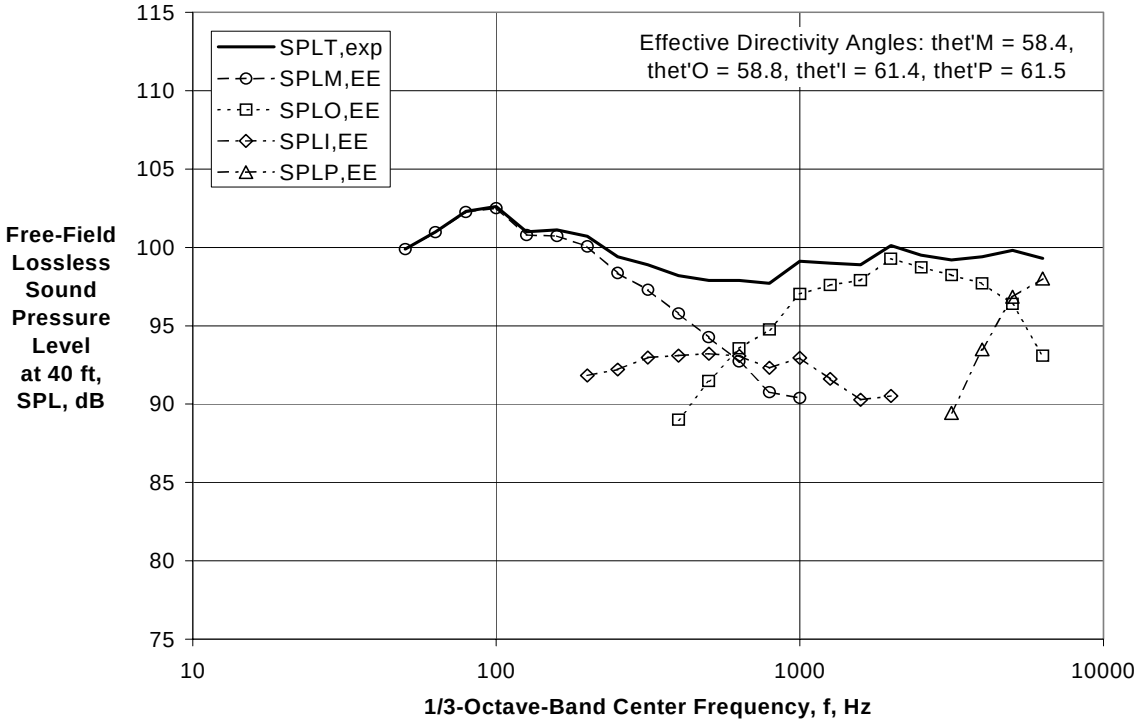

(a) Directivity Angle θ = 60 deg

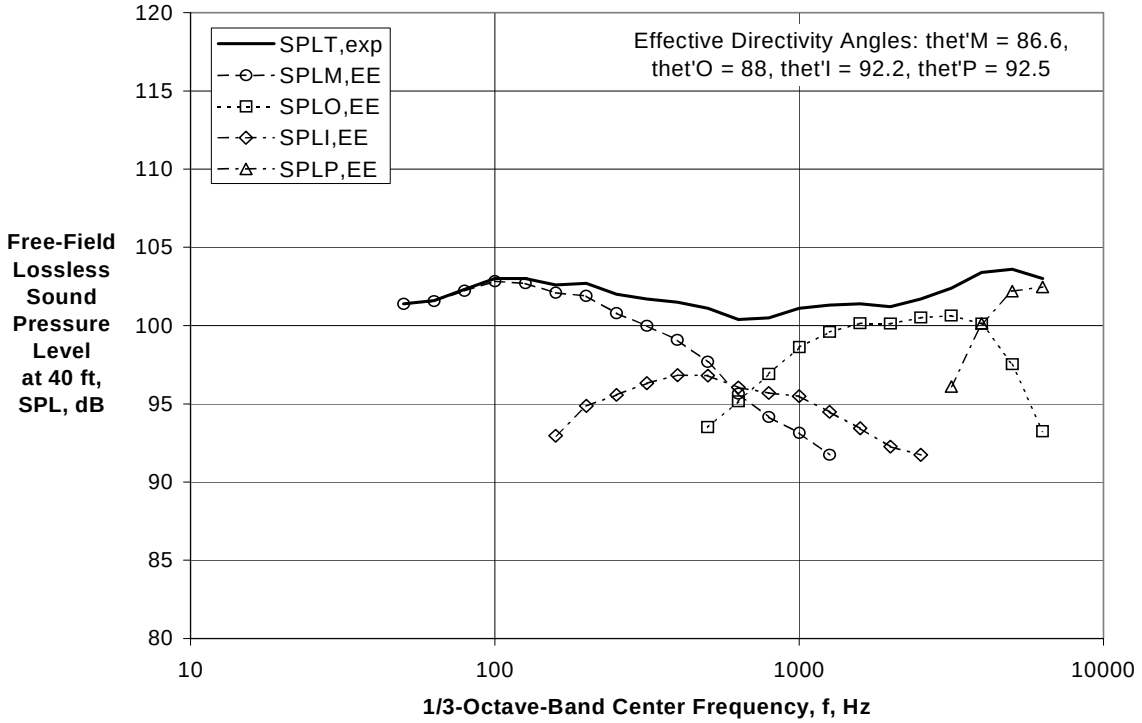

(b) Directivity Angle θ = 90 deg

Figure 7.—Component Spectral Extraction Using Experimental Coefficients for Core and Fan Chevrons on BPR ≅ 5 External Plug Nozzle at V_{mix}/c_{amb} = 1.09 and M_f = 0.28.

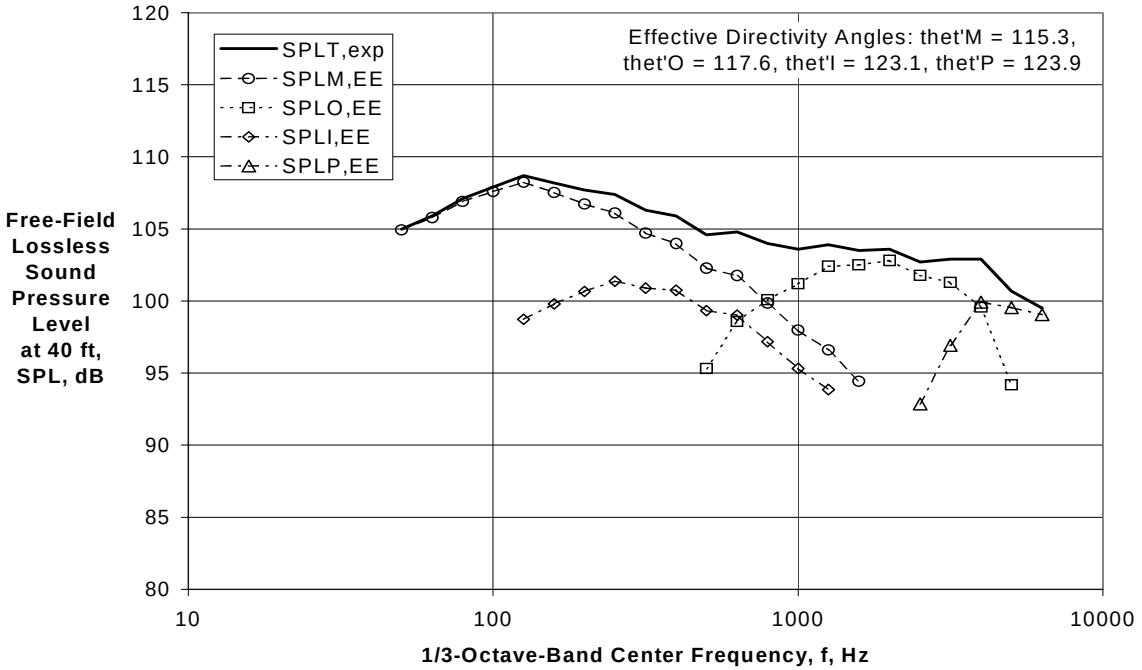

(c) Directivity Angle θ = 120 deg

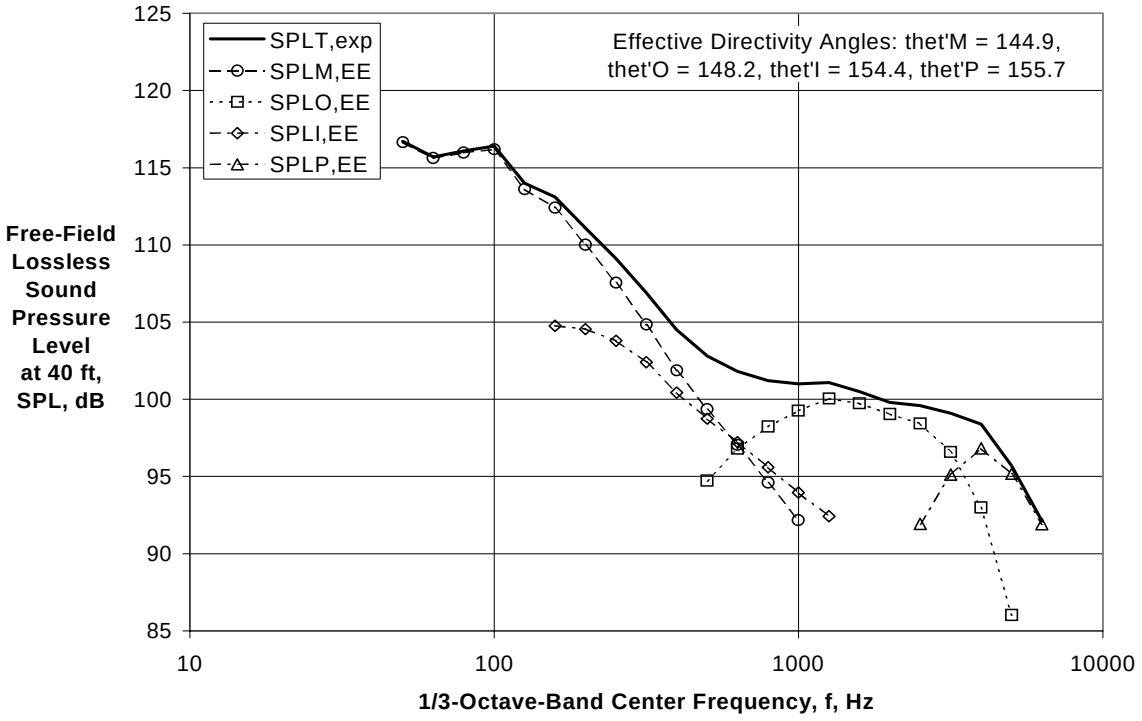

(d) Directivity Angle θ = 150 deg

Figure 7.—(Concluded) Component Spectral Extraction Using Experimental Coefficients for Core and Fan Chevrons on BPR ≅ 5 External Plug Nozzle at V_{mix}/c_{amb} = 1.09 and M_f = 0.28.

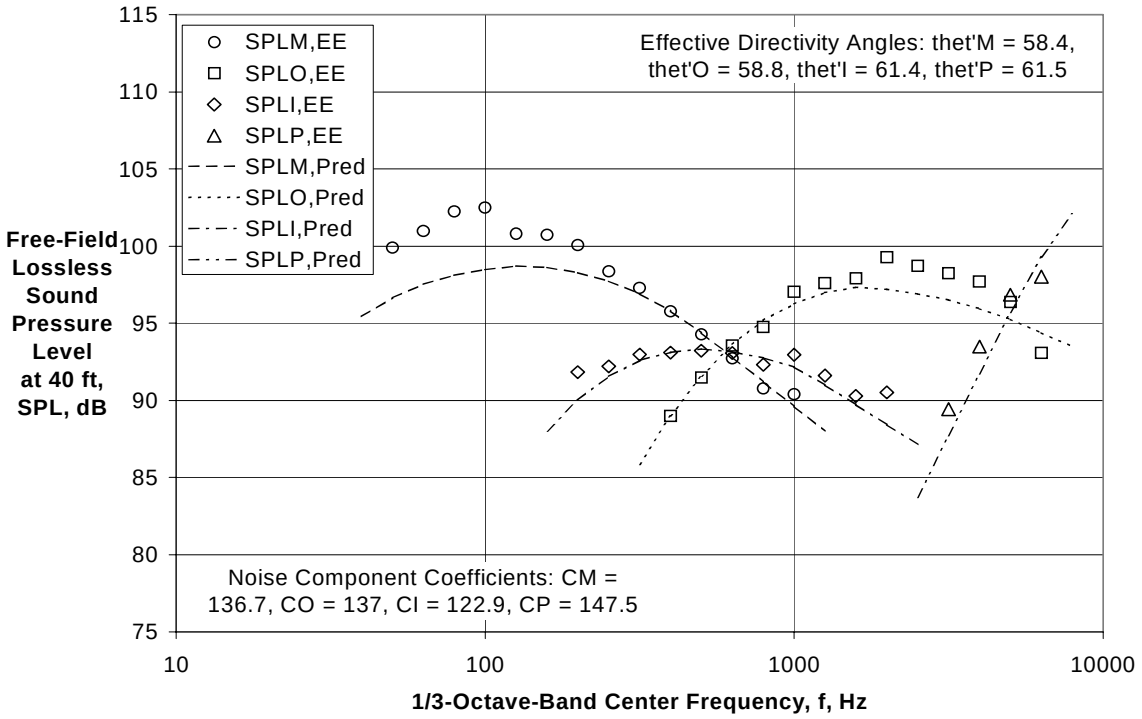

(a) Directivity Angle θ = 60 deg

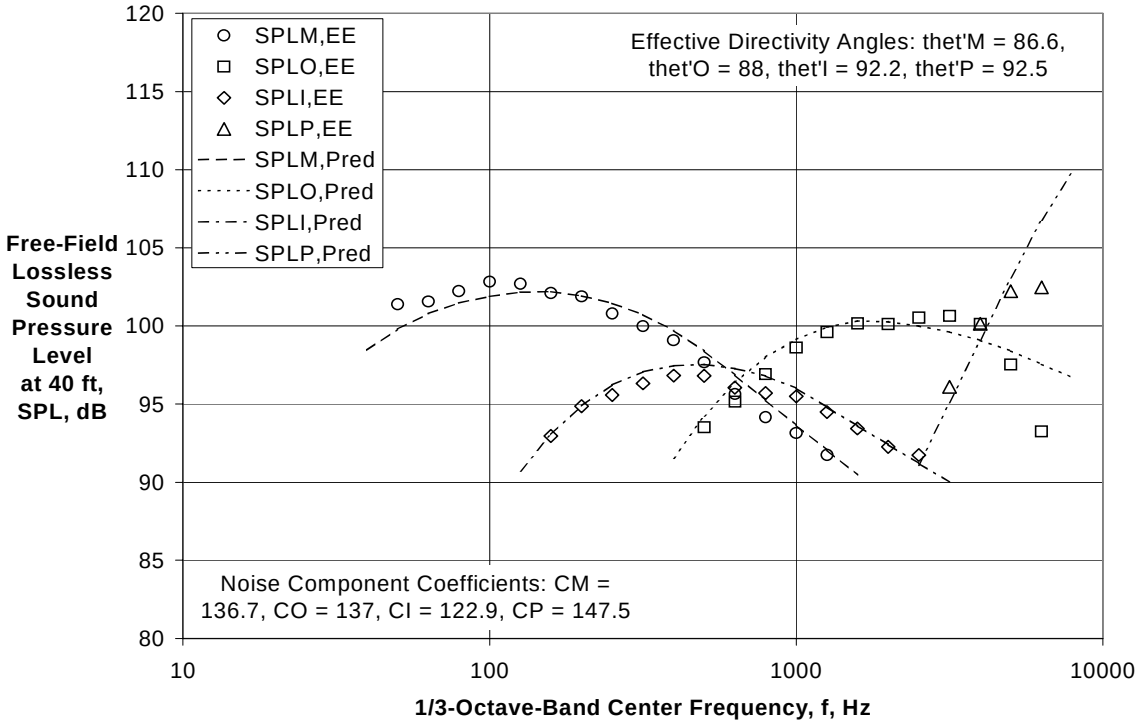

(b) Directivity Angle θ = 90 deg

Figure 8.—Comparison of Extracted and Predicted Component Spectra for Core and Fan Chevrons on BPR ≅ 5 External Plug Nozzle at V_{mix}/c_{amb} = 1.09 and M_f = 0.28.

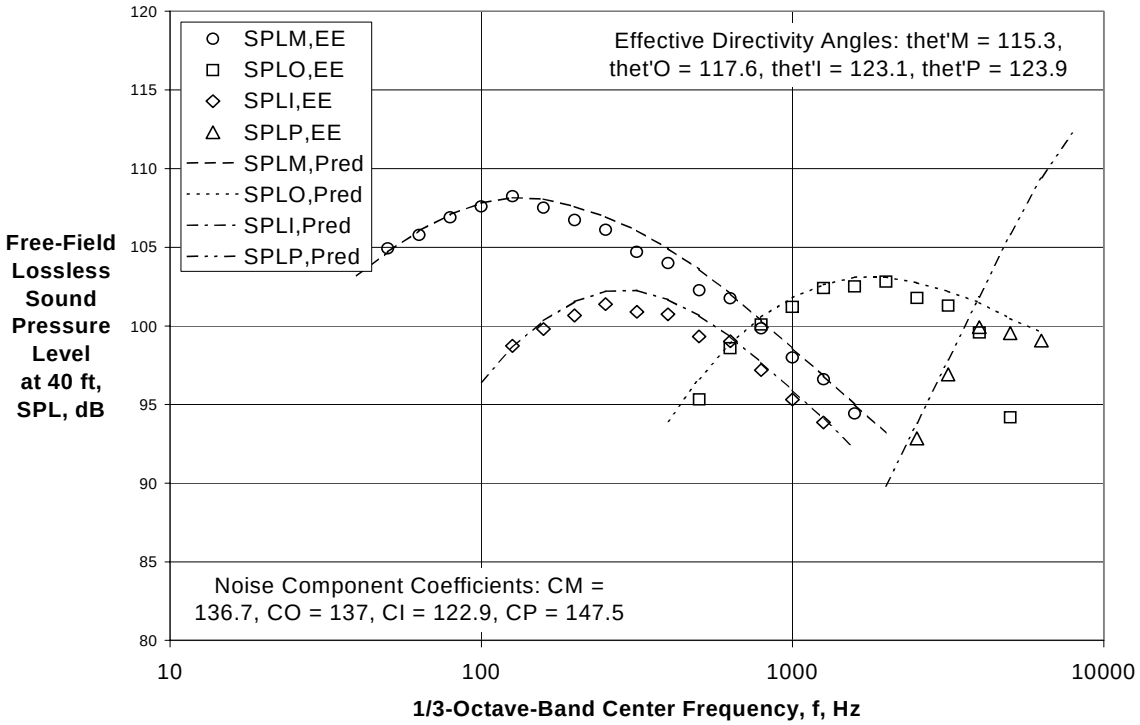

(c) Directivity Angle θ = 120 deg

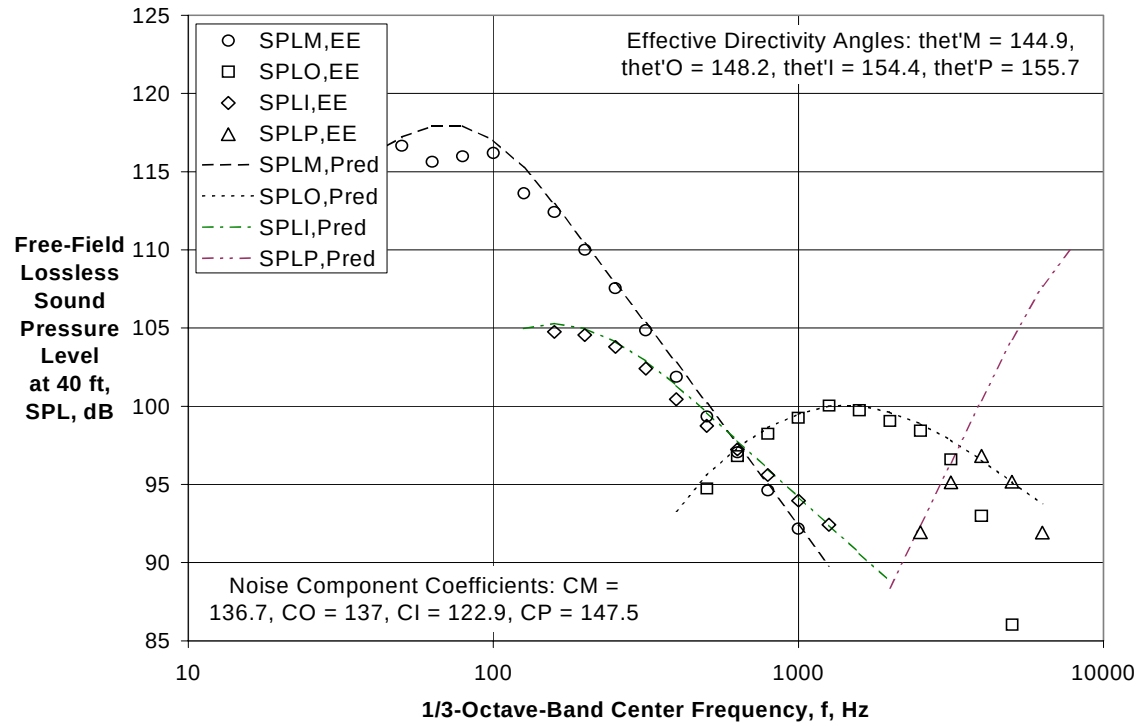

(d) Directivity Angle θ = 150 deg

Figure 8.— (Concluded) Comparison of Extracted and Predicted Component Spectra for Core and Fan Chevrons on BPR ≅ 5 External Plug Nozzle at V_{mix}/c_{amb} = 1.09 and M_f = 0.28.

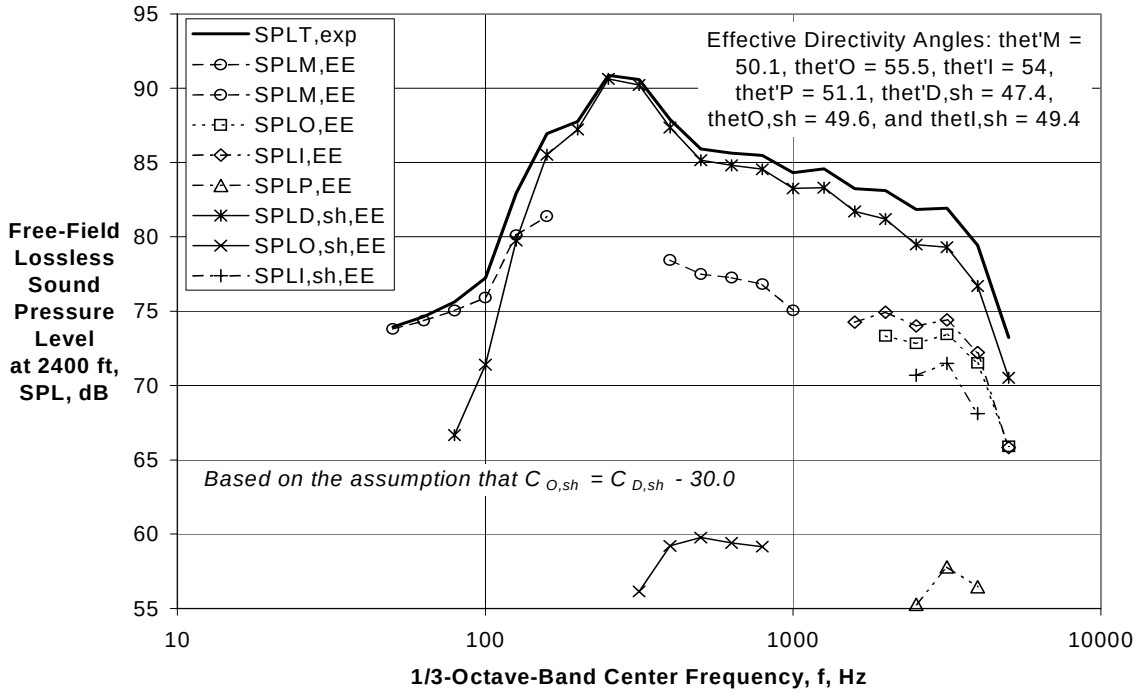

Figure 9.—Component Spectral Extraction Using Experimental Coefficients for BPR ≅ 4 External Plug Nozzle with Convergent Exits and Truncated Plug at θ = 50 deg, V_{mix}/c_{amb} = 2.06 and M_f = 0.0.

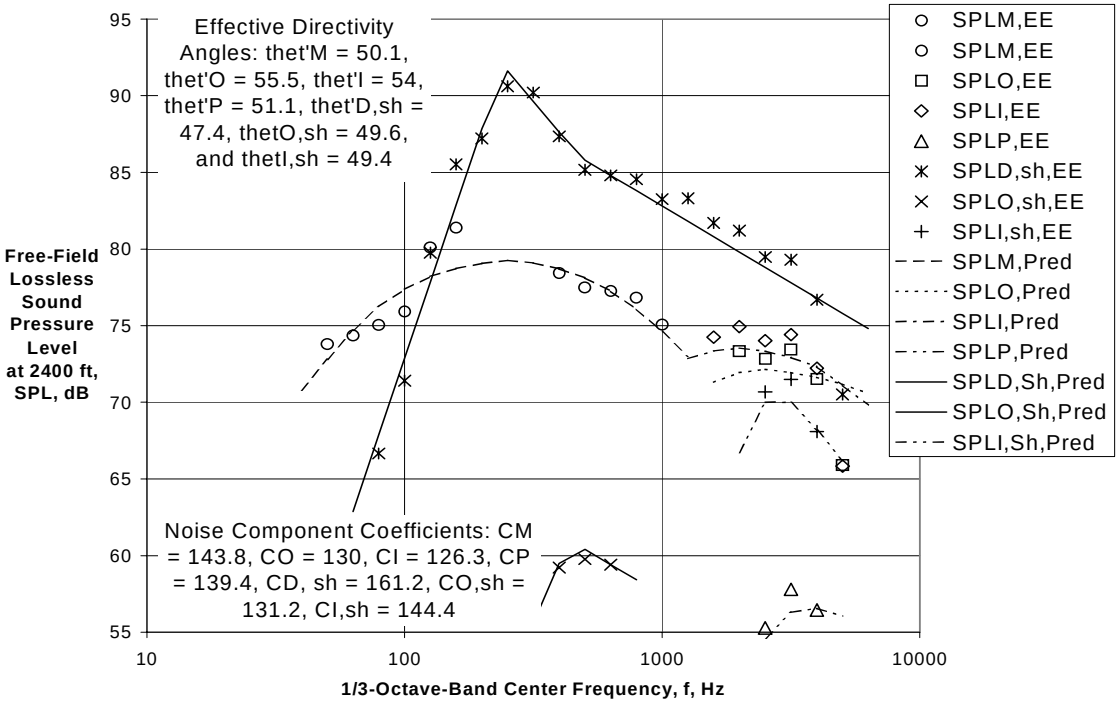

Figure 10.—Comparison of Extracted and Predicted Component Spectra for BPR ≅ 4 External Plug Nozzle with Convergent Exits and Truncated Plug at θ = 50 deg, V_{mix}/c_{amb} = 2.06 and M_f = 0.0.

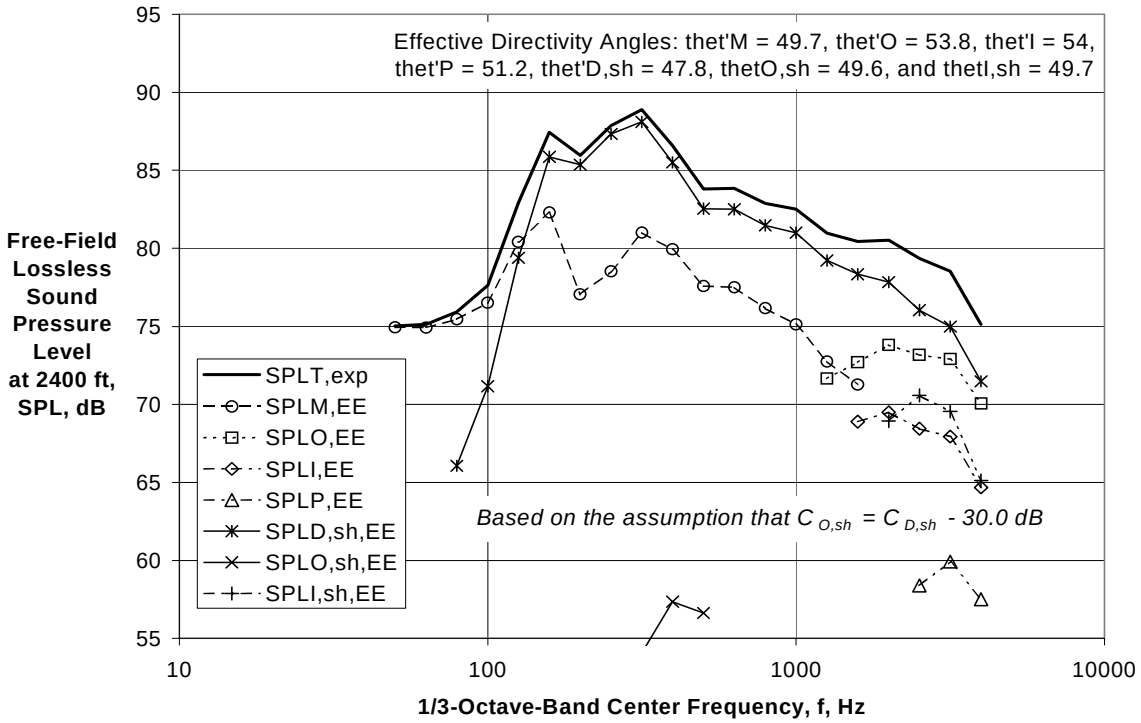

Figure 11.—Component Spectral Extraction Using Experimental Coefficients for BPR ≅ 4 External Plug Nozzle with Convergent-Divergent Exits and Truncated Plug at θ = 50 deg, V_{mix}/c_{amb} = 2.05 and M_f = 0.0.

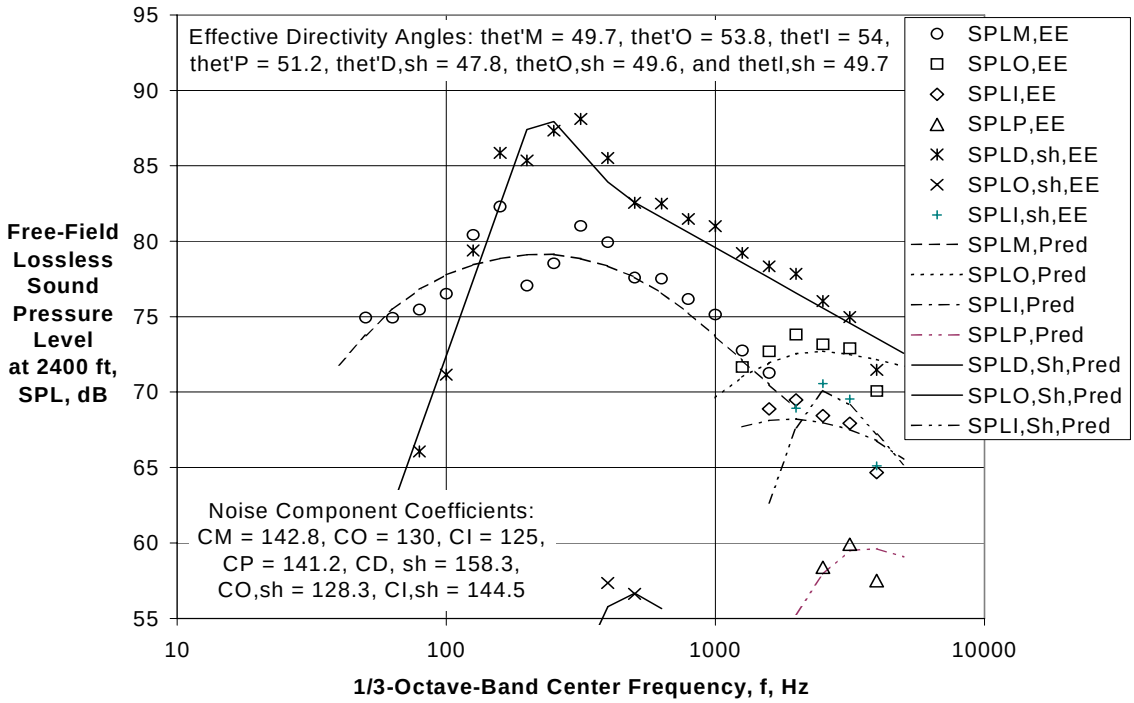

Figure 12.—Comparison of Extracted and Predicted Component Spectra for BPR ≅ 4 External Plug Nozzle with Convergent Exits and Truncated Plug at θ = 50 deg, V_{mix}/c_{amb} = 2.06 and M_f = 0.0.

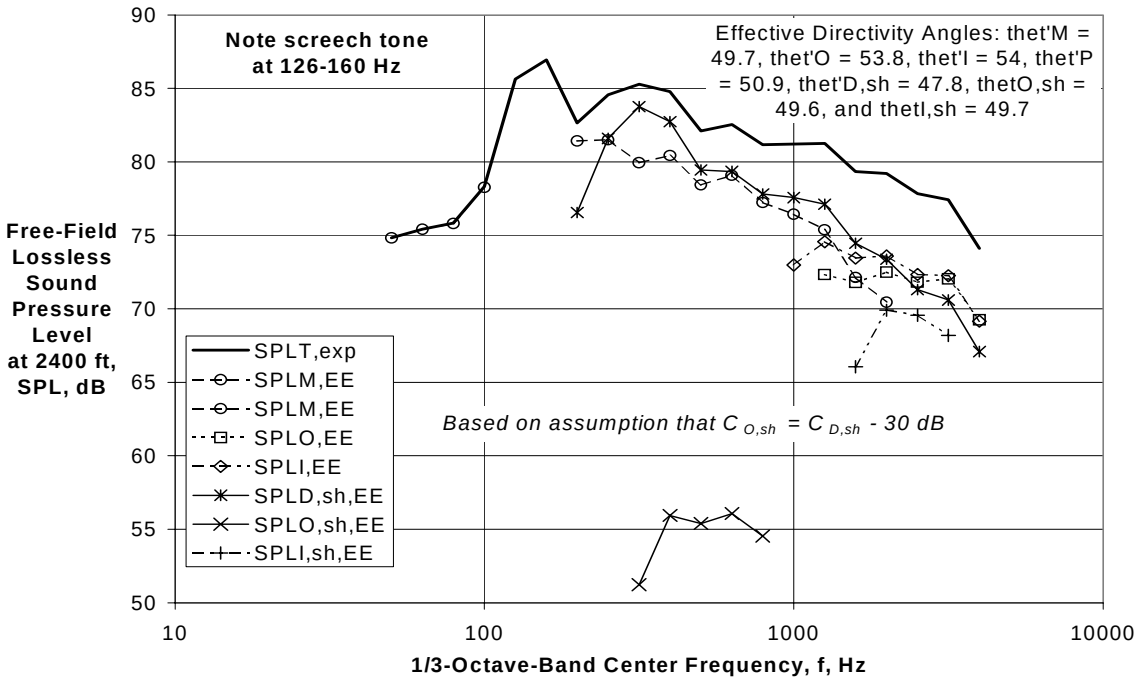

Figure 13.—Component Spectral Extraction Using Experimental Coefficients for BPR ≅ 4 External Plug Nozzle with Convergent-Divergent Exits and Sharp-Tipped Plug at θ = 50 deg, V_{mix}/c_{amb} = 2.05 and M_f = 0.0.

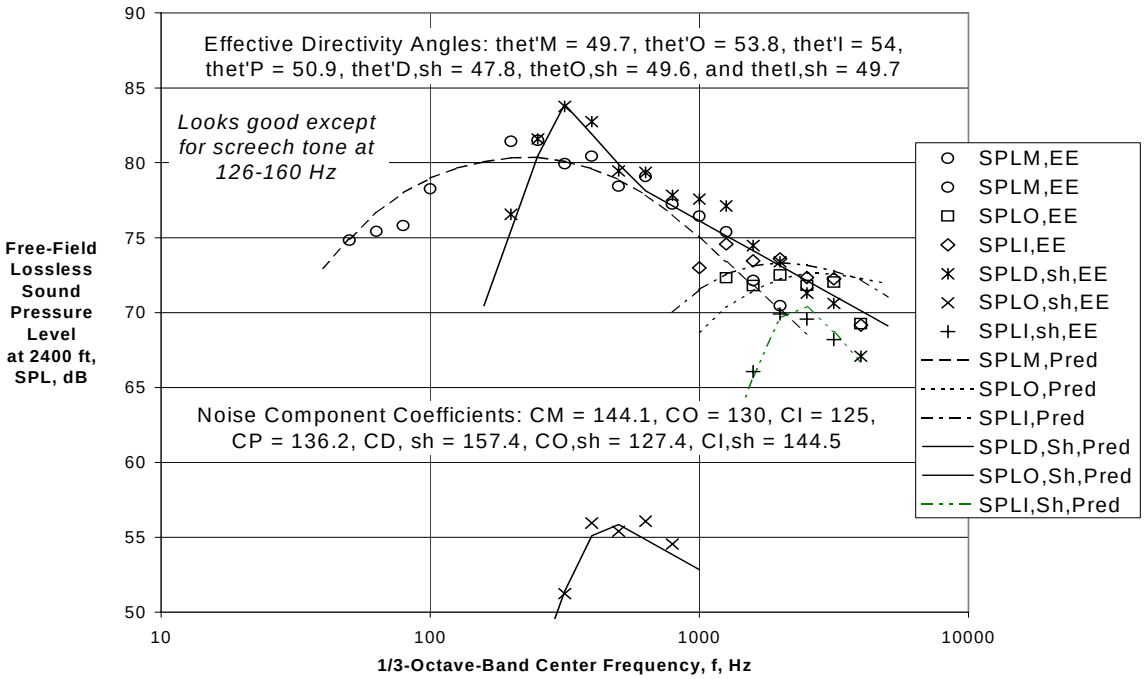

Figure 14.—Comparison of Extracted and Predicted Component Spectra for BPR ≅ 4 External Plug Nozzle with Convergent-Divergent Exits and Sharp-Tipped Plug at θ = 50 deg, V_{mix}/c_{amb} = 2.05 and M_f = 0.0.

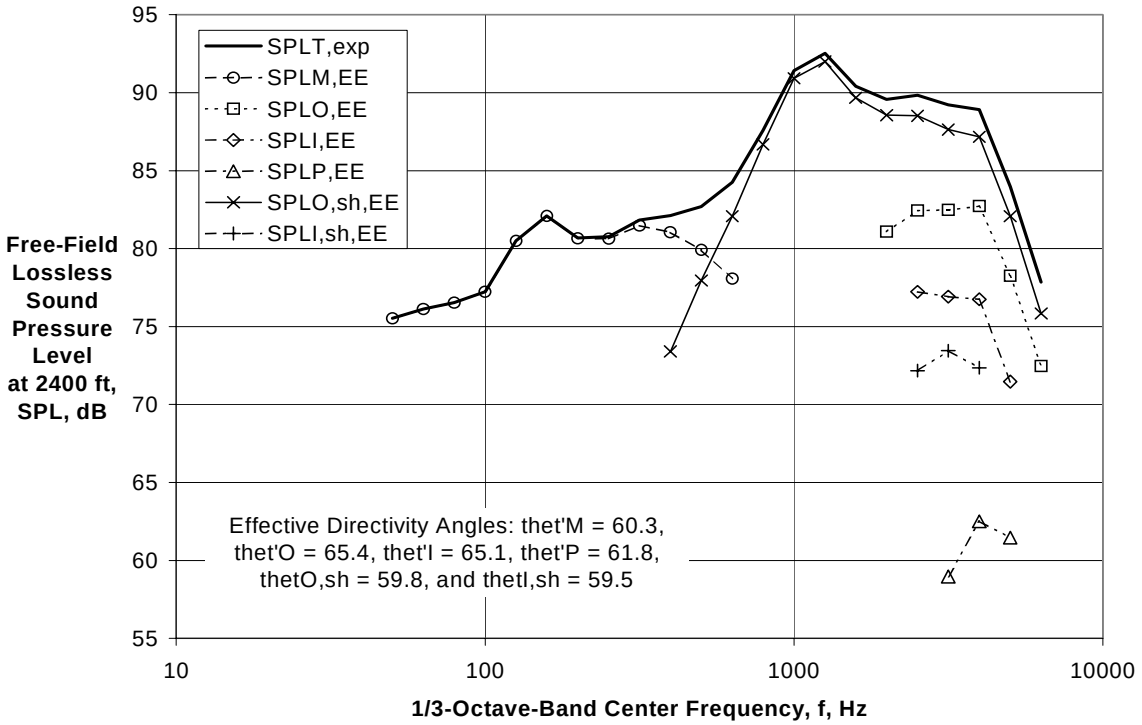

(a) Directivity Angle θ = 60 deg

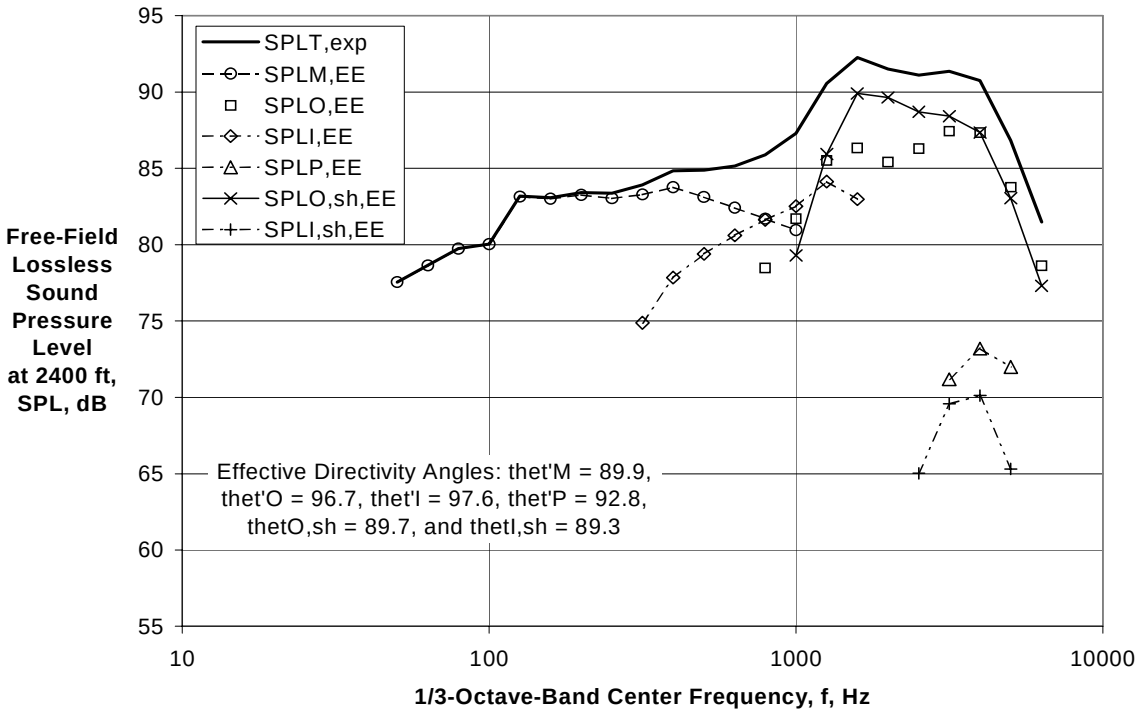

(b) Directivity Angle θ = 90 deg

Figure 15.—Component Spectral Extraction Using Experimental Coefficients for BPR ≅ 4 External Plug Nozzle with 20-Chute Outer Stream Suppressor at V_{mix}/c_{amb} = 2.19 and M_f = 0.0.

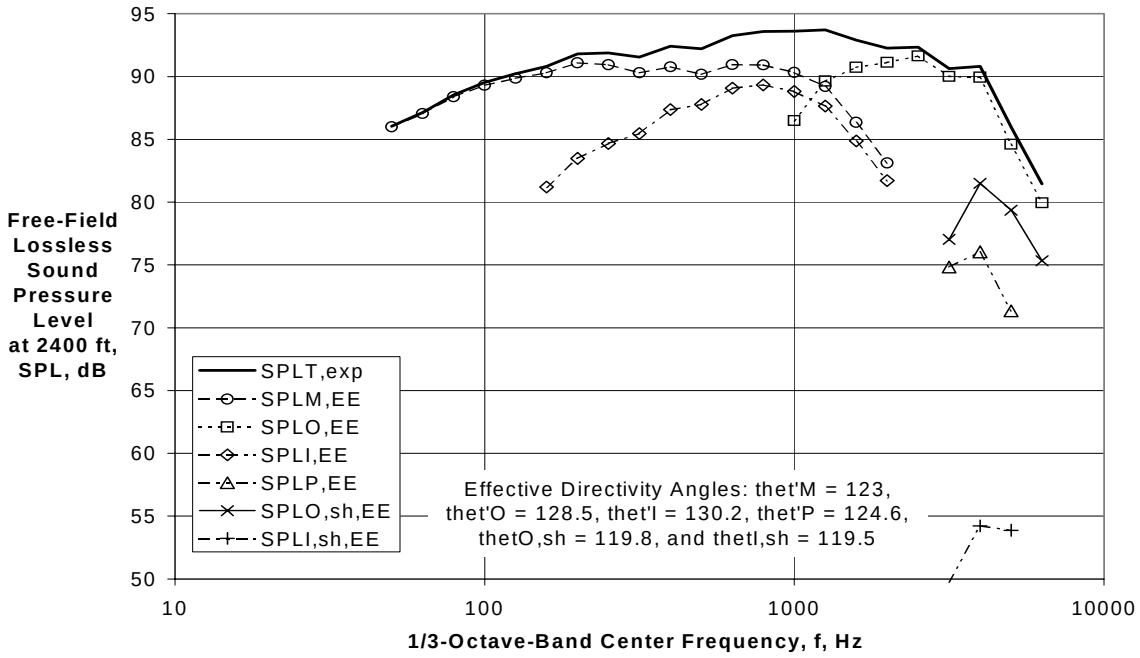

(c) Directivity Angle θ = 120 deg

Figure 15.—(Concluded) Component Spectral Extraction Using Experimental Coefficients for BPR ≅ 4 External Plug Nozzle with 20-Chute Outer Stream Suppressor at V_{mix}/c_{amb} = 2.19 and M_f = 0.0.

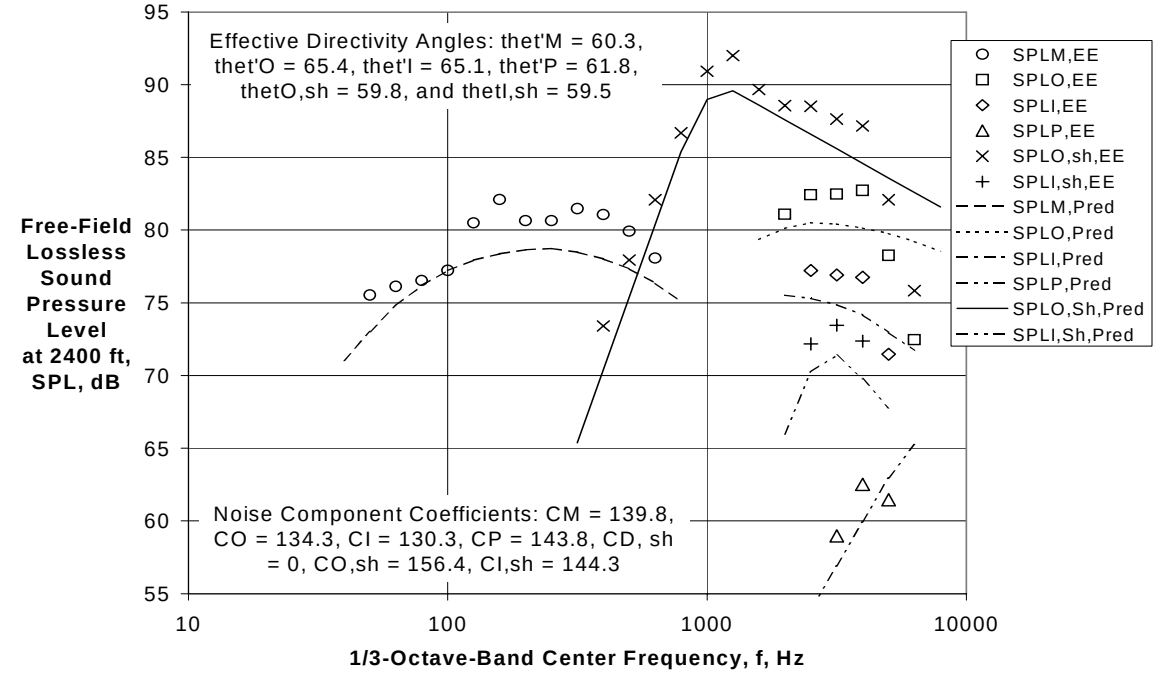

(a) Directivity Angle θ = 60 deg

Figure 16.—Comparison of Extracted and Predicted Component Spectra for BPR ≅ 4 External Plug Nozzle with 20-Chute Outer Stream Suppressor at V_{mix}/c_{amb} = 2.19 and M_f = 0.0.

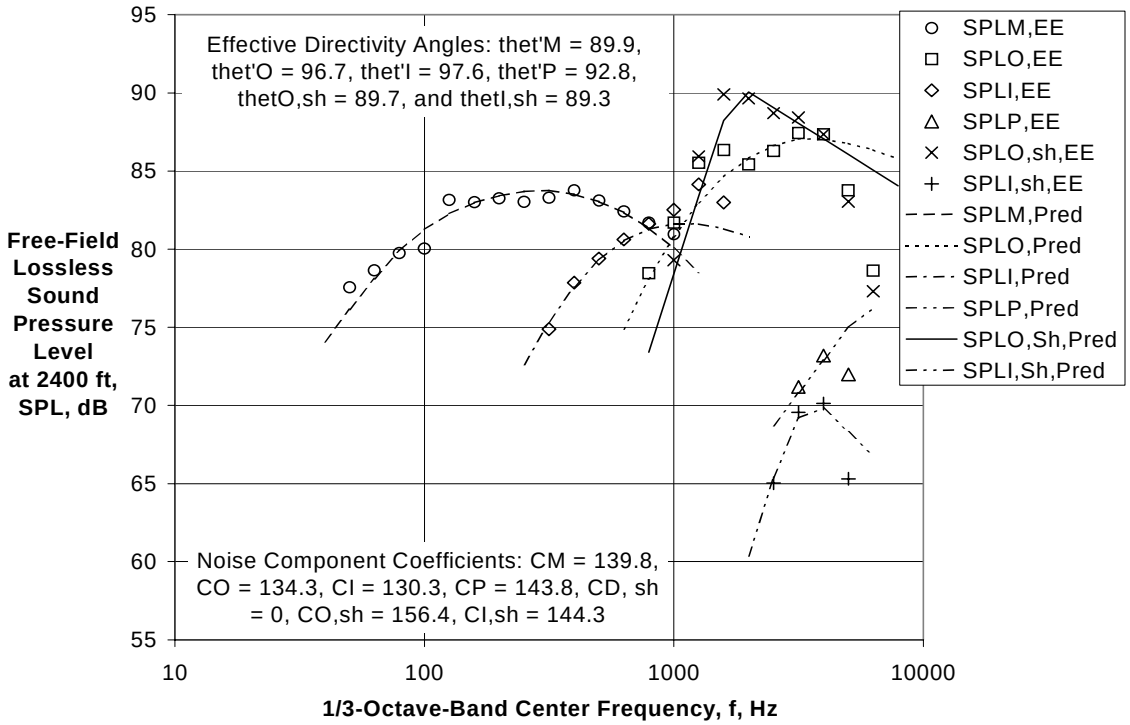

(b) Directivity Angle θ = 90 deg

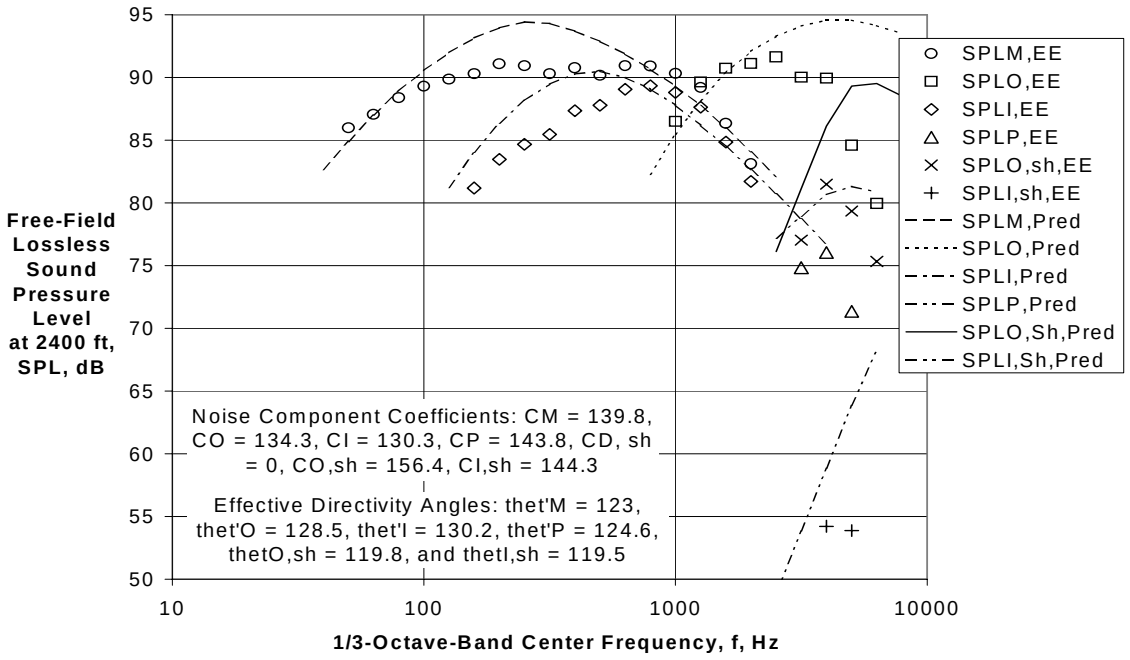

(c) Directivity Angle θ = 120 deg

Figure 16.—(Concluded)Comparison of Extracted and Predicted Component Spectra for BPR ≅ 4 External Plug Nozzle with 20-Chute Outer Stream Suppressor at V_{mix}/c_{amb} = 2.19 and M_f = 0.0.

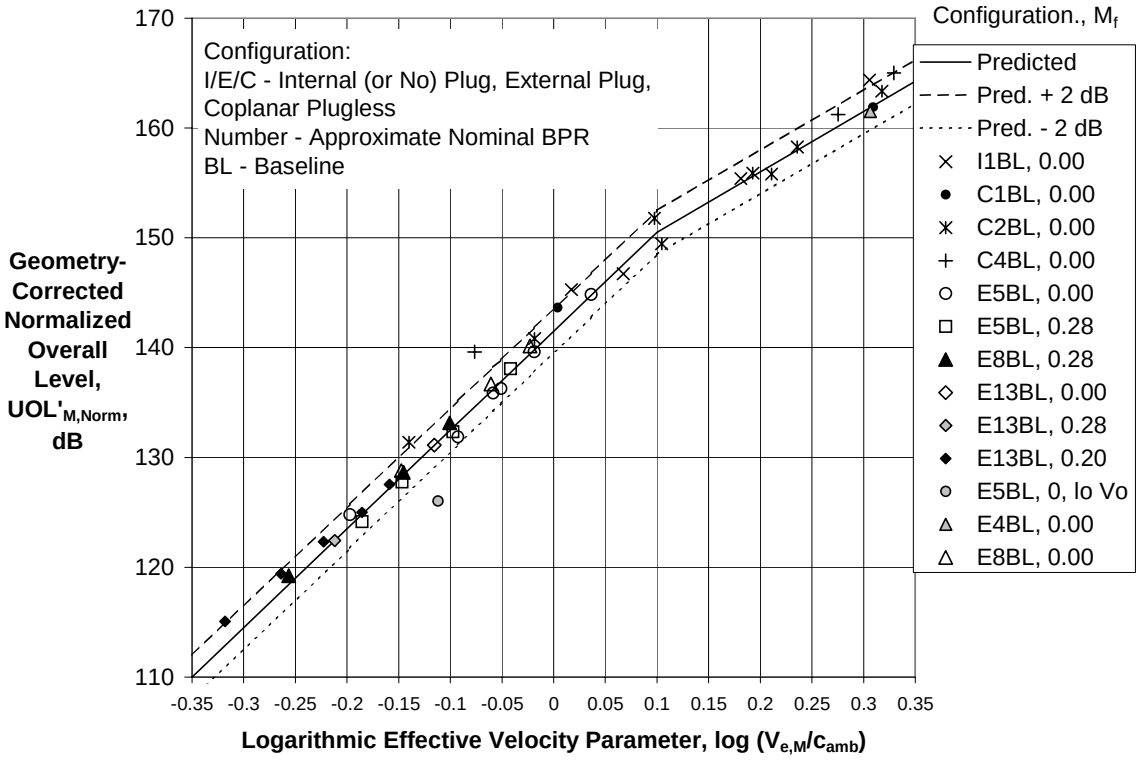

(a) Baseline Coannular Nozzles

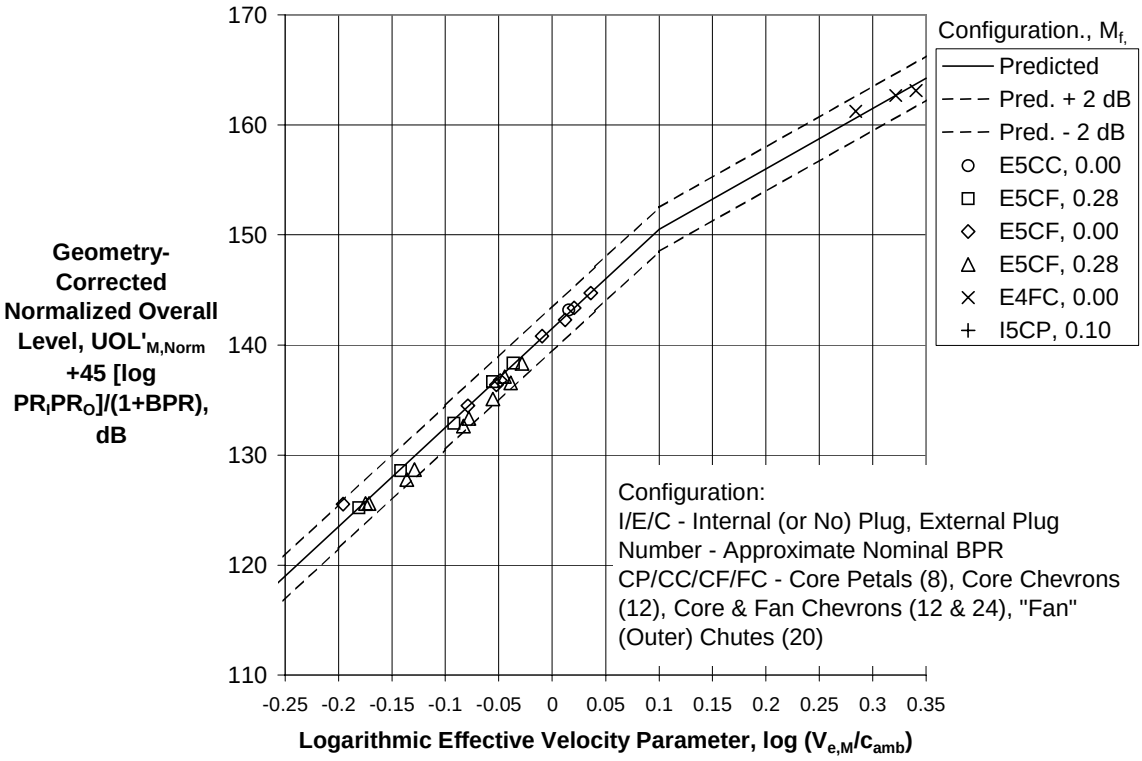

(b) Suppressed Coannular Nozzles

Figure 17.—Merged Mixing Noise Level Correlation

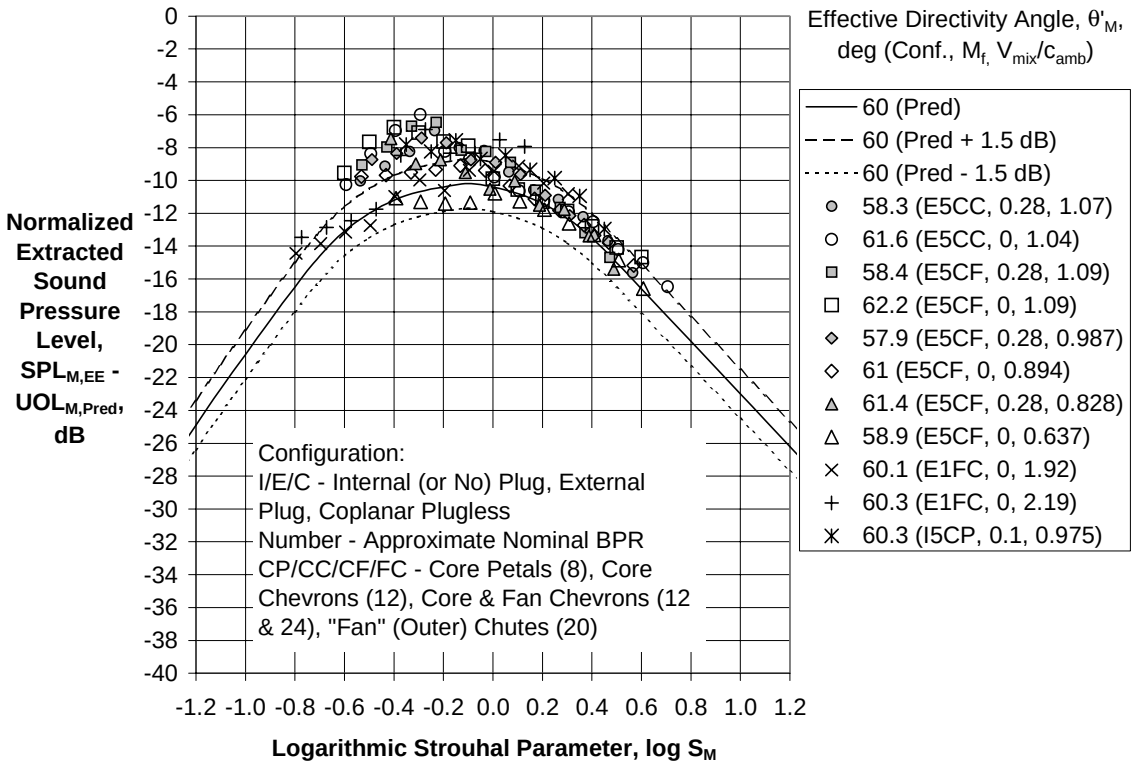

(a) Effective Directivity Angle $\theta'_M \cong 60$ deg

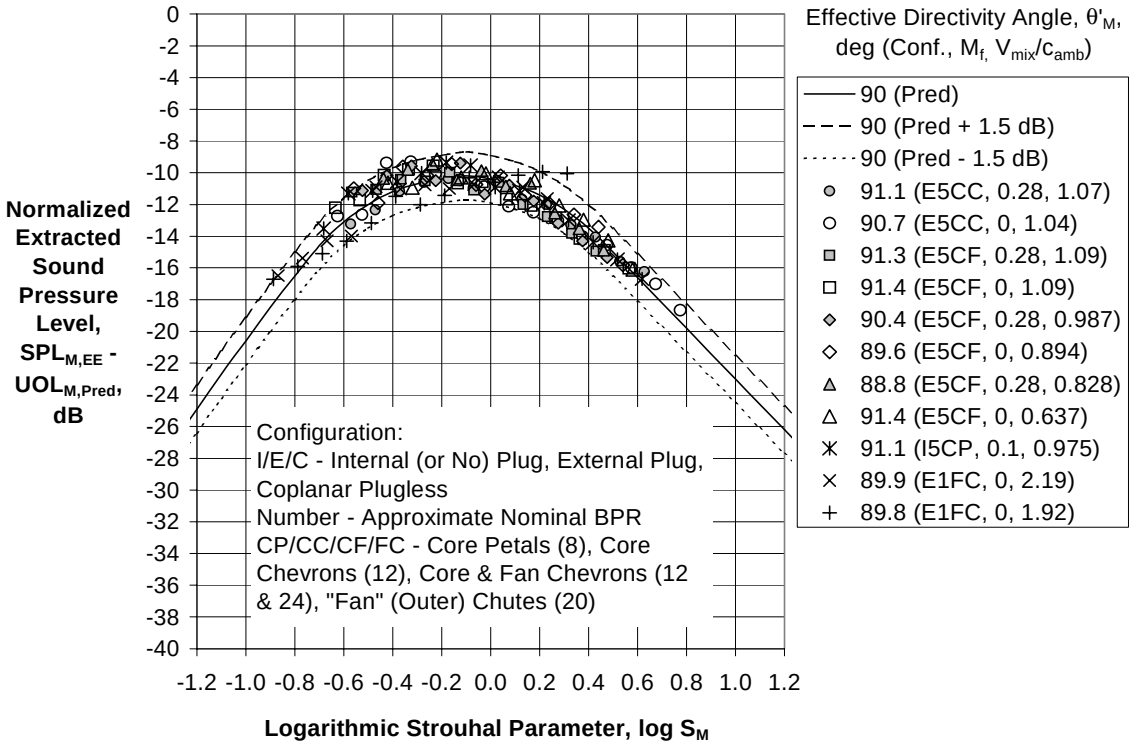

(b) Effective Directivity Angle $\theta'_M \cong 90$ deg

Figure 18.—Merged Mixing Noise Spectral Directivity Correlation for Suppressed Coannular Nozzles.

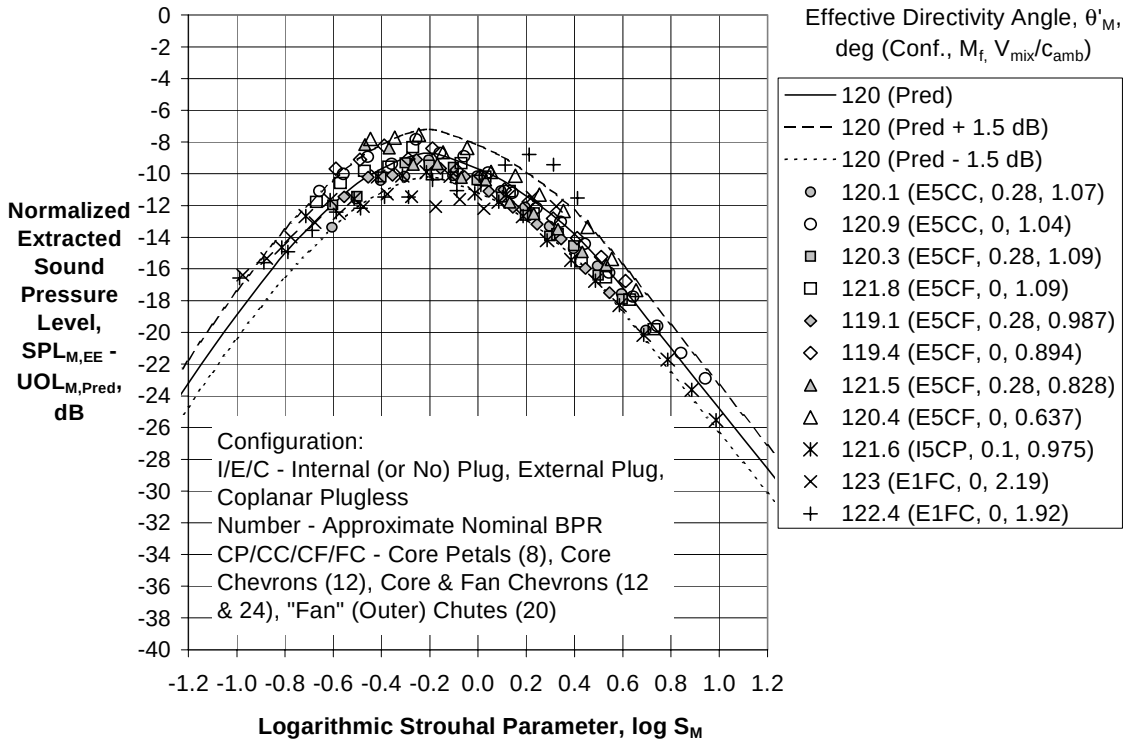

(c) Effective Directivity Angle $\theta'_M \cong 120$ deg

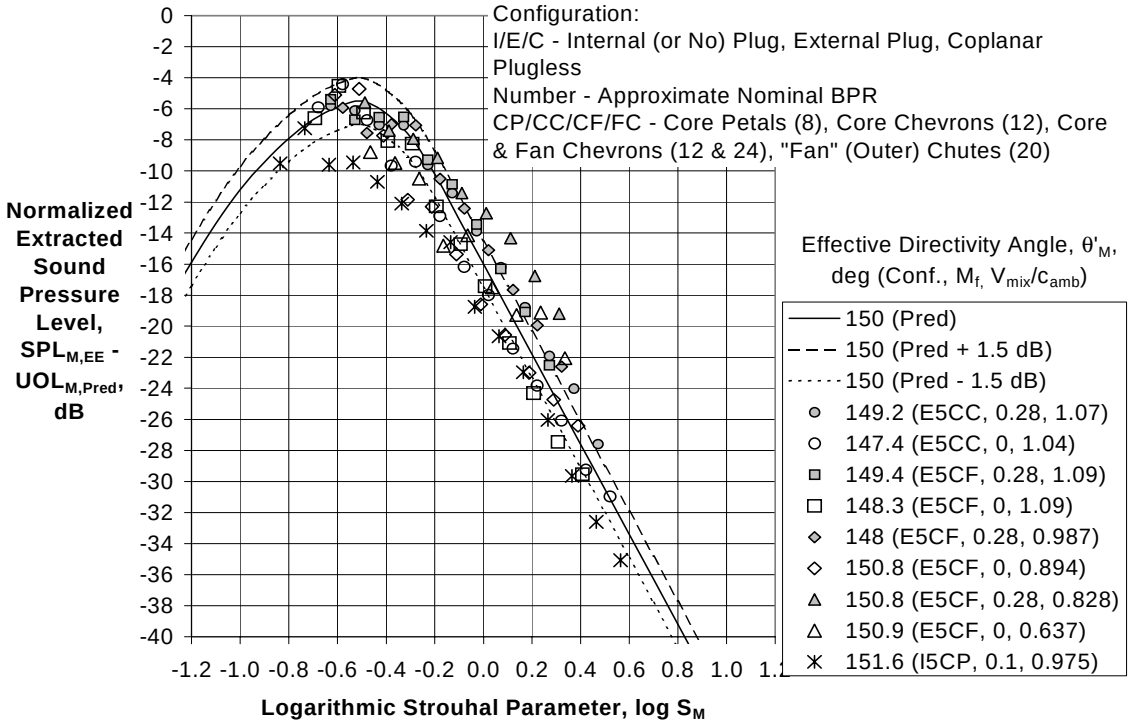

(d) Effective Directivity Angle $\theta'_M \cong 150$ deg

Figure 18.—(Concluded) Merged Mixing Noise Spectral Directivity Correlation for Suppressed Coannular Nozzles.

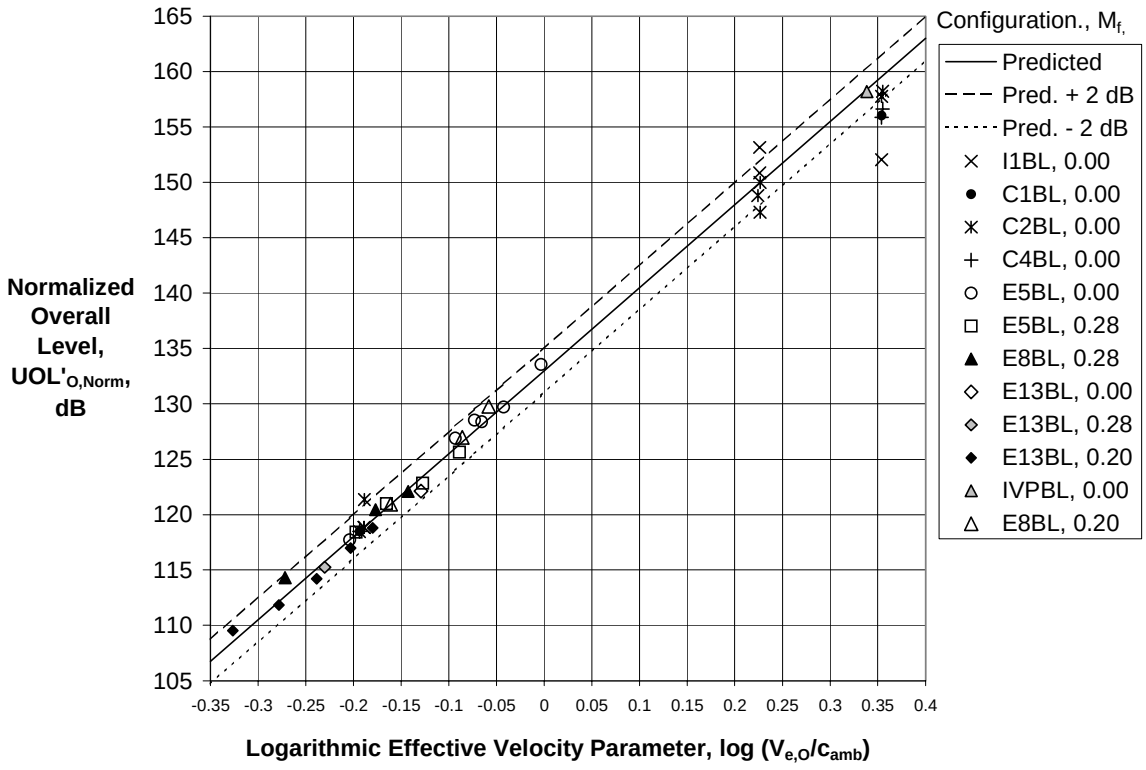

(a) Baseline Coannular Nozzles

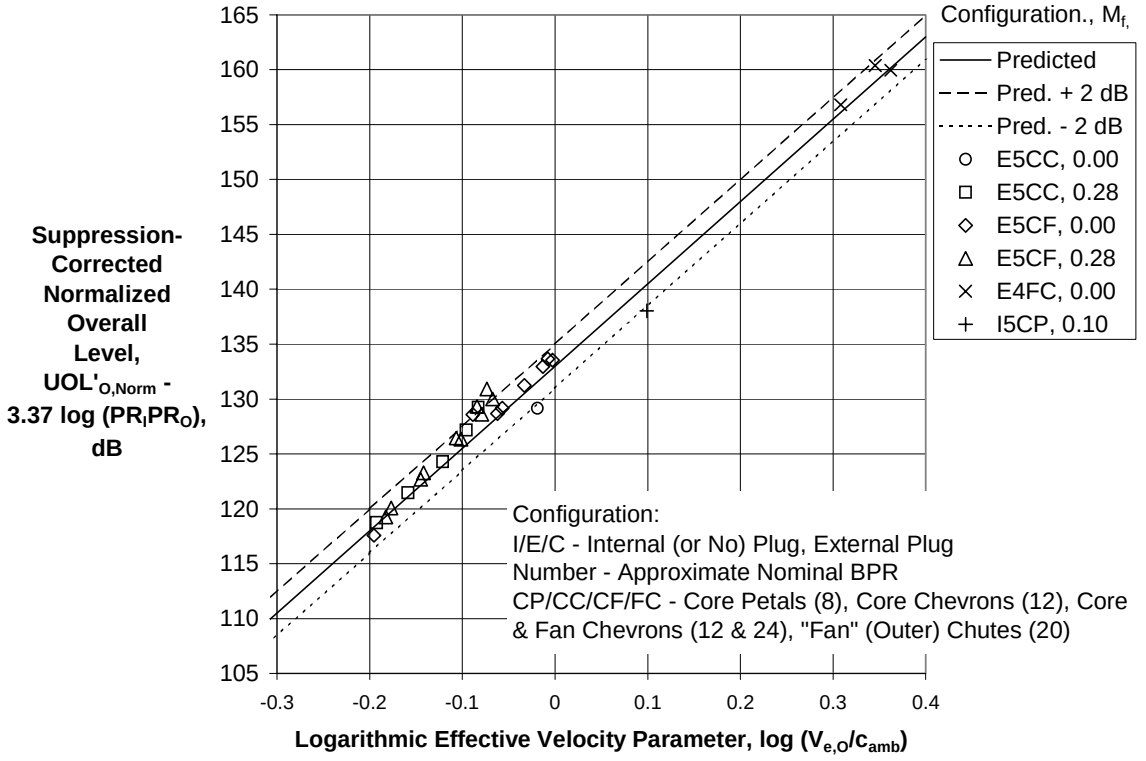

(b) Suppressed Coannular Nozzles

Figure 19.—Outer Shear Layer Mixing Noise Level Correlation.

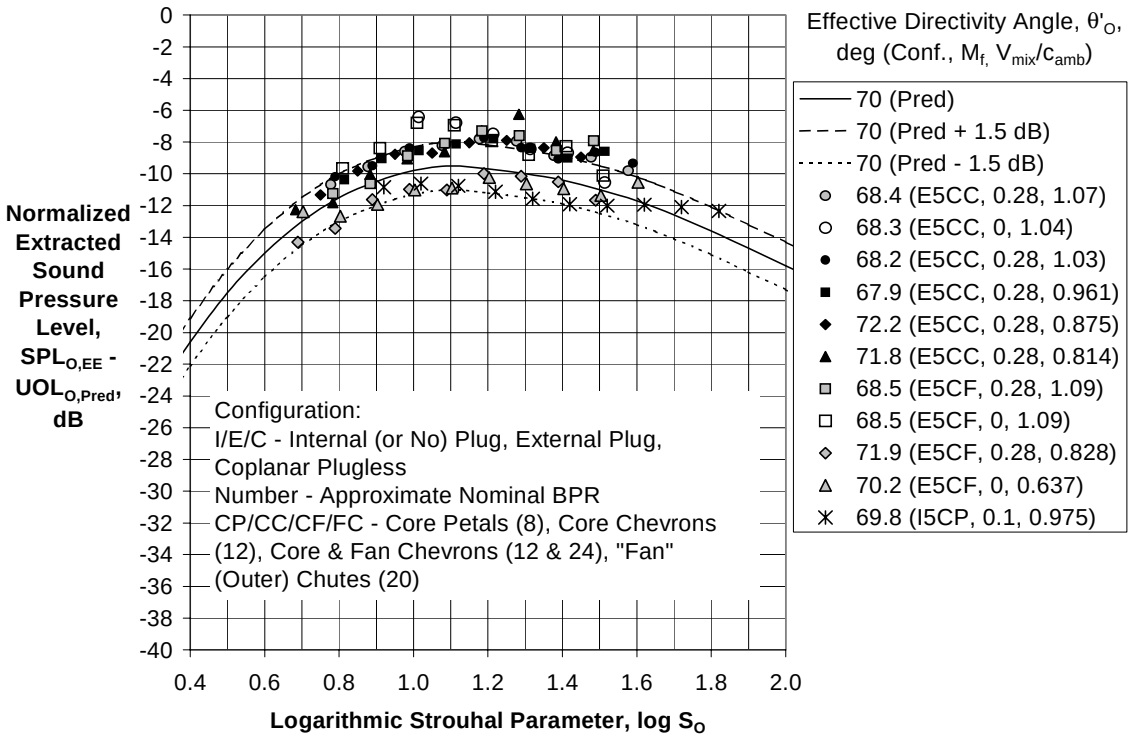

(a) Effective Directivity Angle, $\theta'_O \cong 70$ deg

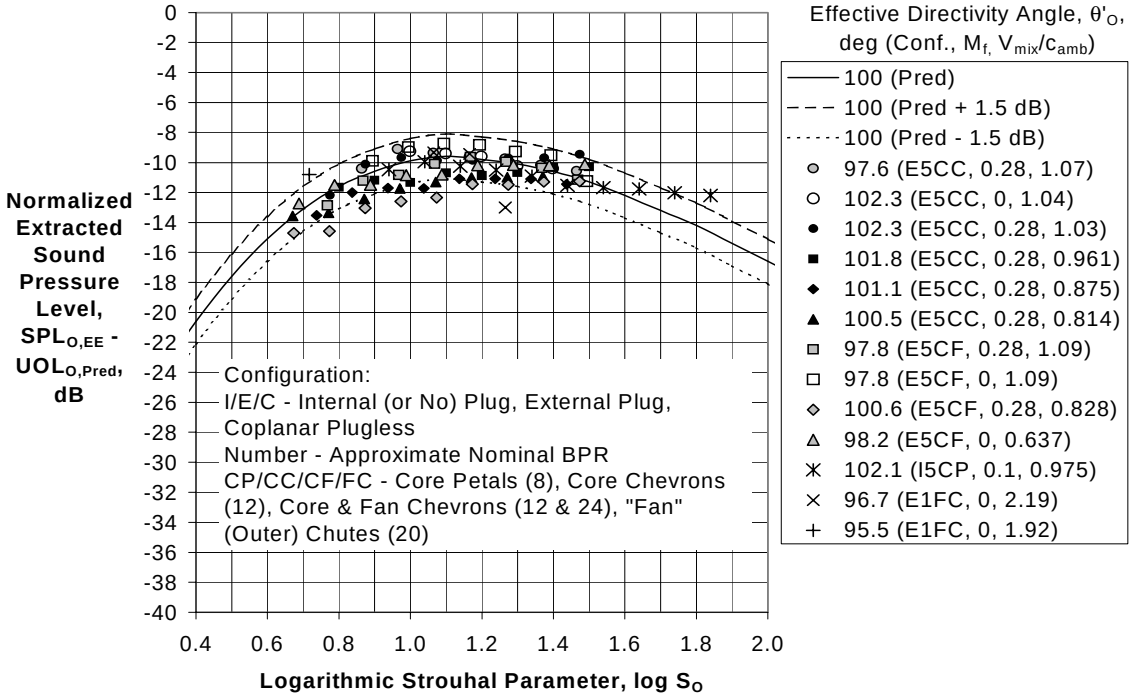

(b) Effective Directivity Angle, $\theta'_O \cong 100$ deg

Figure 20.—Outer Shear Layer Mixing Noise Spectral Directivity Correlation for Suppressed Coannular Nozzles.

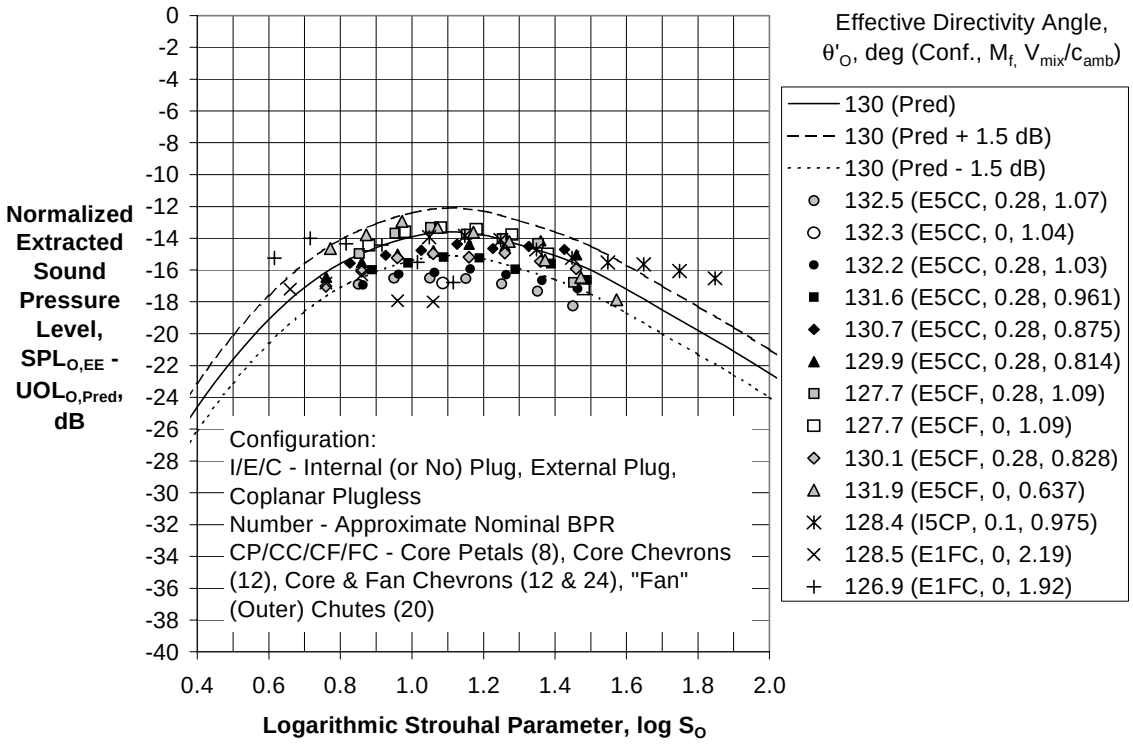

(c) Effective Directivity Angle, $\theta'_O \cong 130$ deg

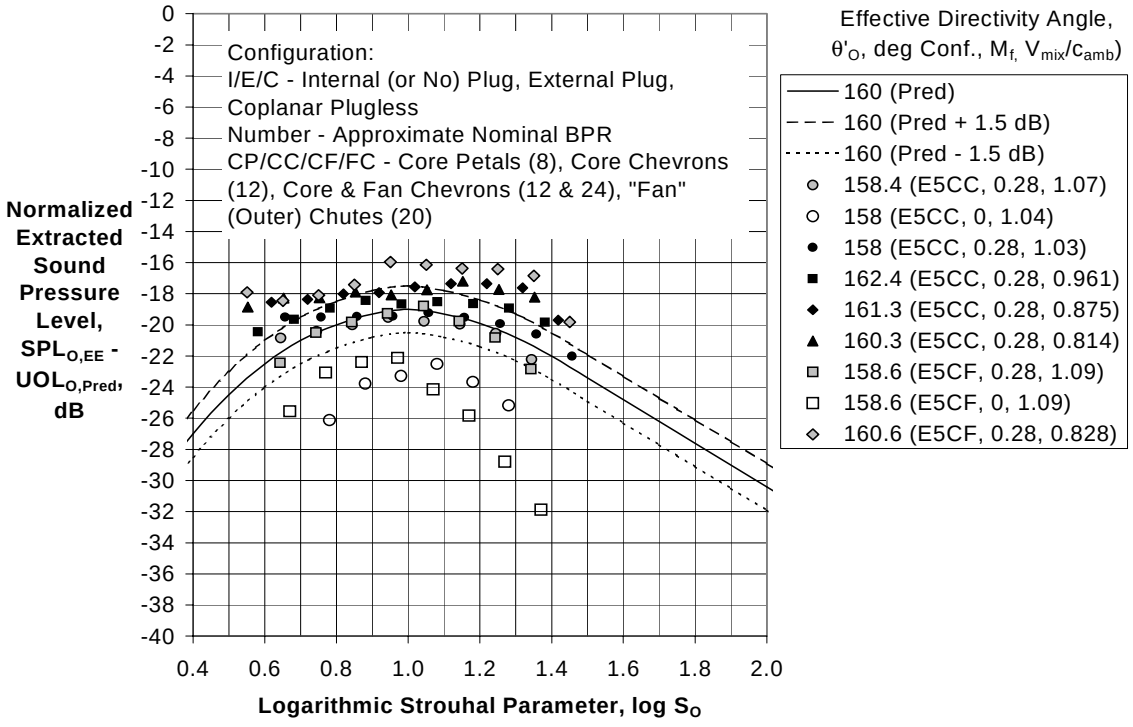

(d) Effective Directivity Angle, $\theta'_O \cong 160$ deg

Figure 20.—(Concluded) Outer Shear Layer Mixing Noise Spectral Directivity Correlation for Suppressed Coannular Nozzles.

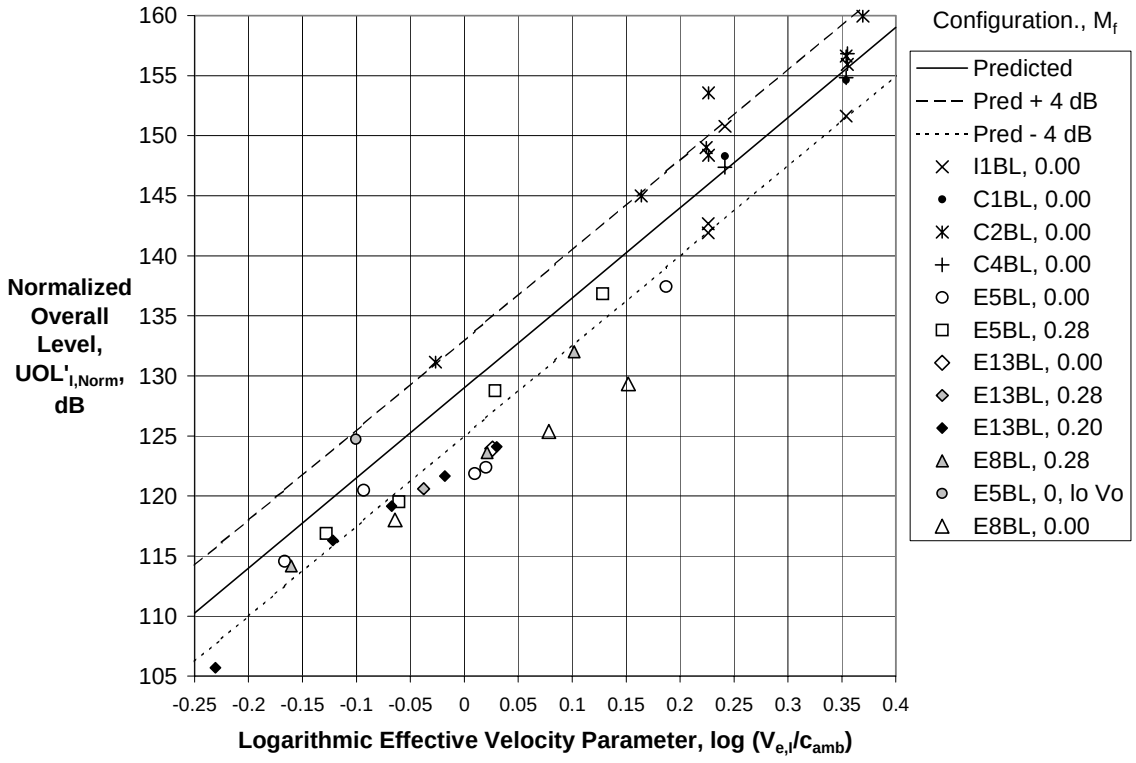

(a) Baseline Coannular Nozzles

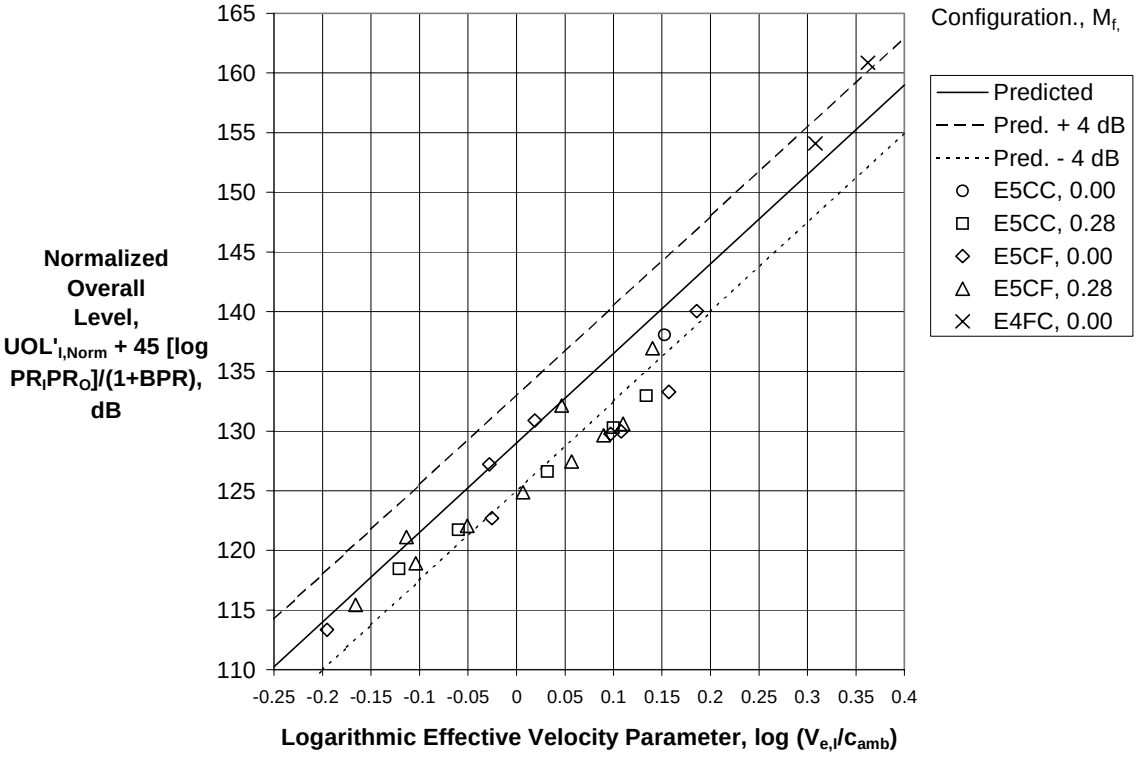

(b) Suppressed Coannular Nozzles

Figure 21.—Inner Stream Mixing Noise Level Correlation.

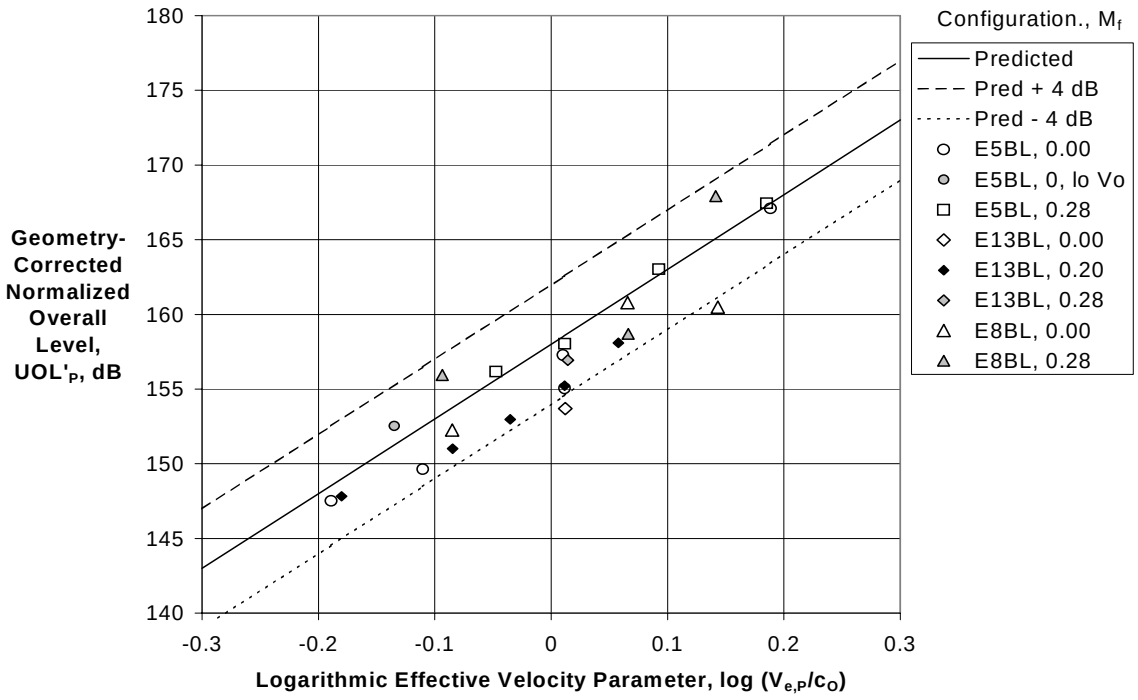

(a) Baseline Coannular Nozzles

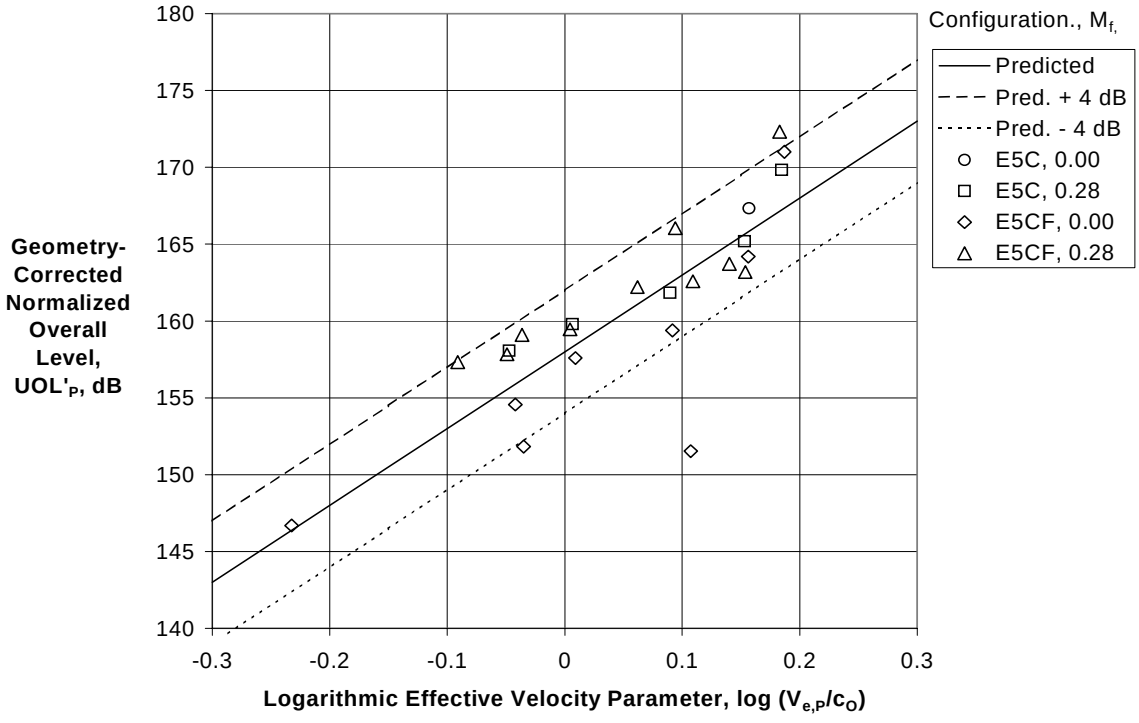

(b) Suppressed Coannular Nozzles

Figure 22.—Inner Stream Plug Separation Mixing Noise Level Correlation.

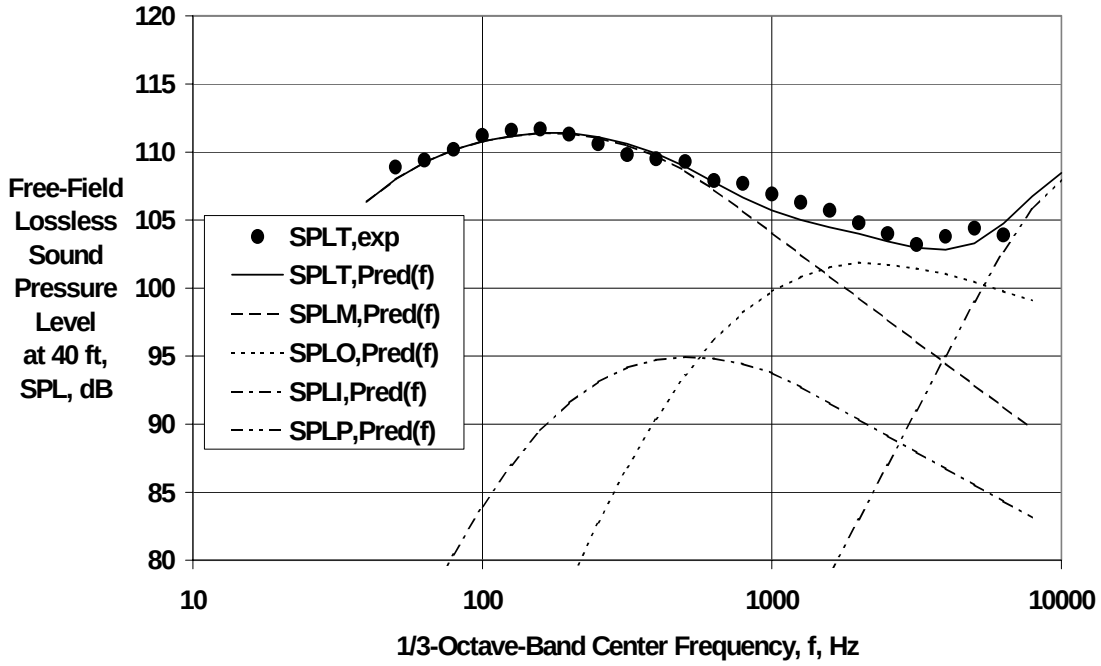

(a) Using Current Model

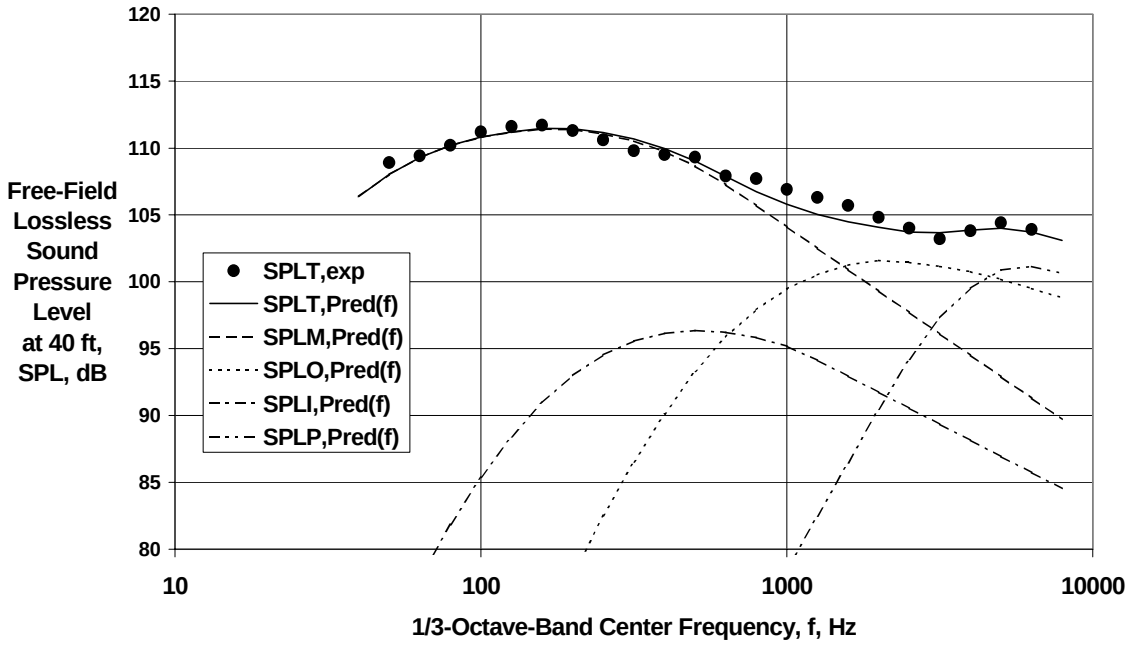

(b) With Revised Plug Separation Noise Model

Figure 23.—Comparison of Experimental and Predicted Spectra at θ = 90 deg for BPR ≅ 5 Baseline Nozzle at V_{mix}/c_{amb} = 1.07 and M_f = 0.0.

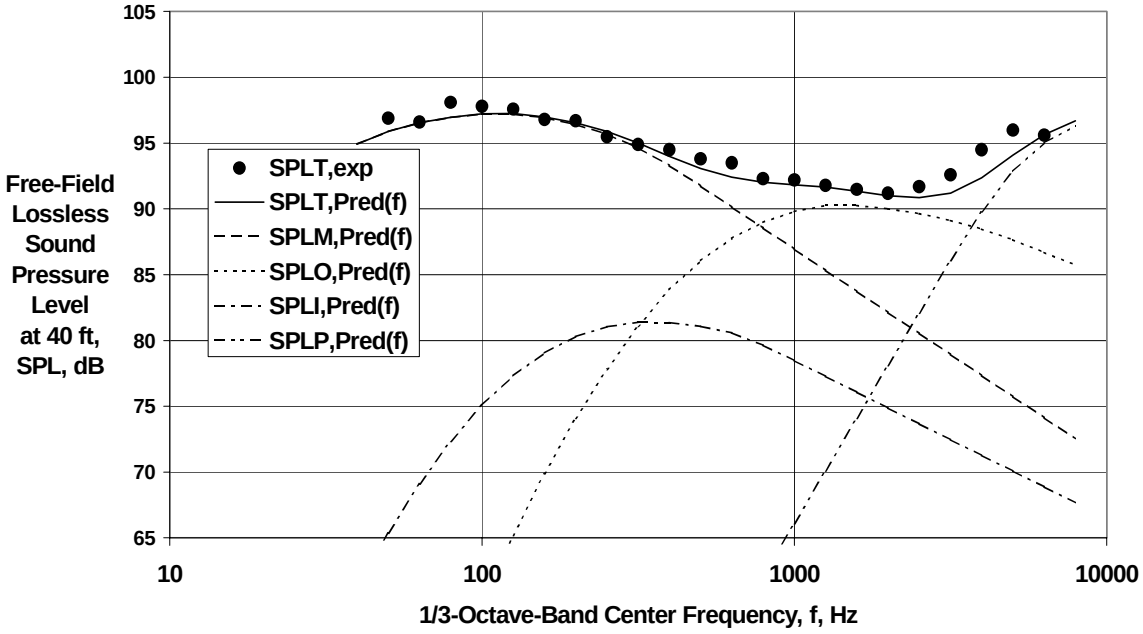

(a) Using Current Model

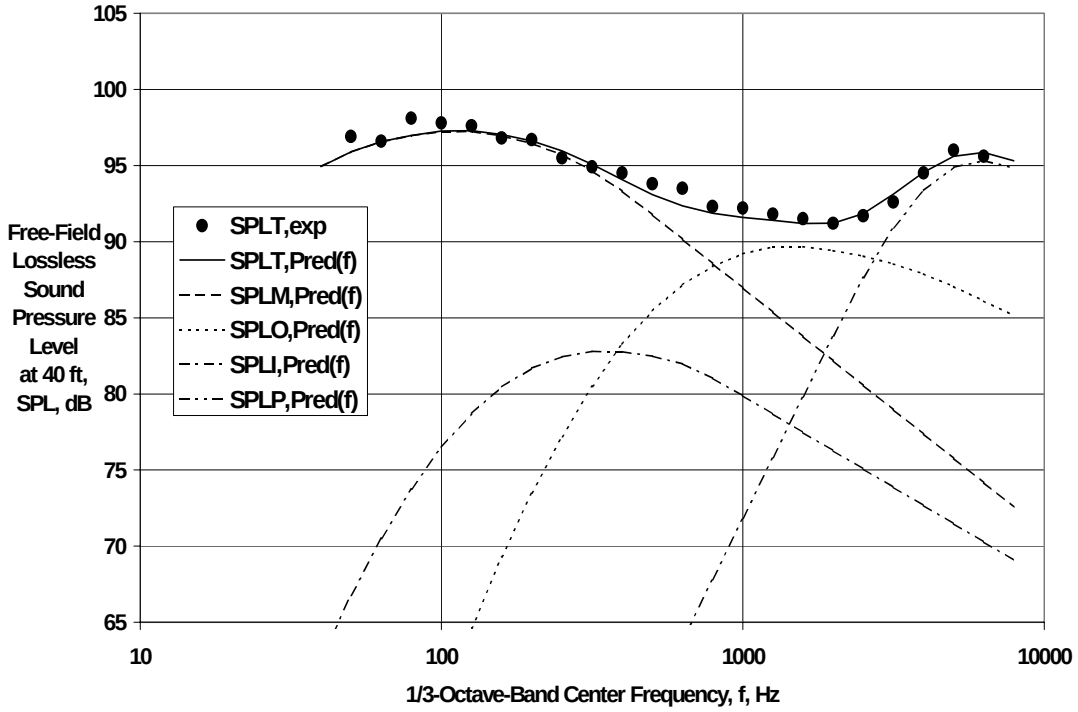

(b) Using Modified Plug Separation Noise Model

Figure 24.—Comparison of Experimental and Predicted Spectra at θ = 90 deg for BPR ≅ 8 Baseline Nozzle at V_{mix}/c_{amb} = 0.712 and M_f = 0.0.

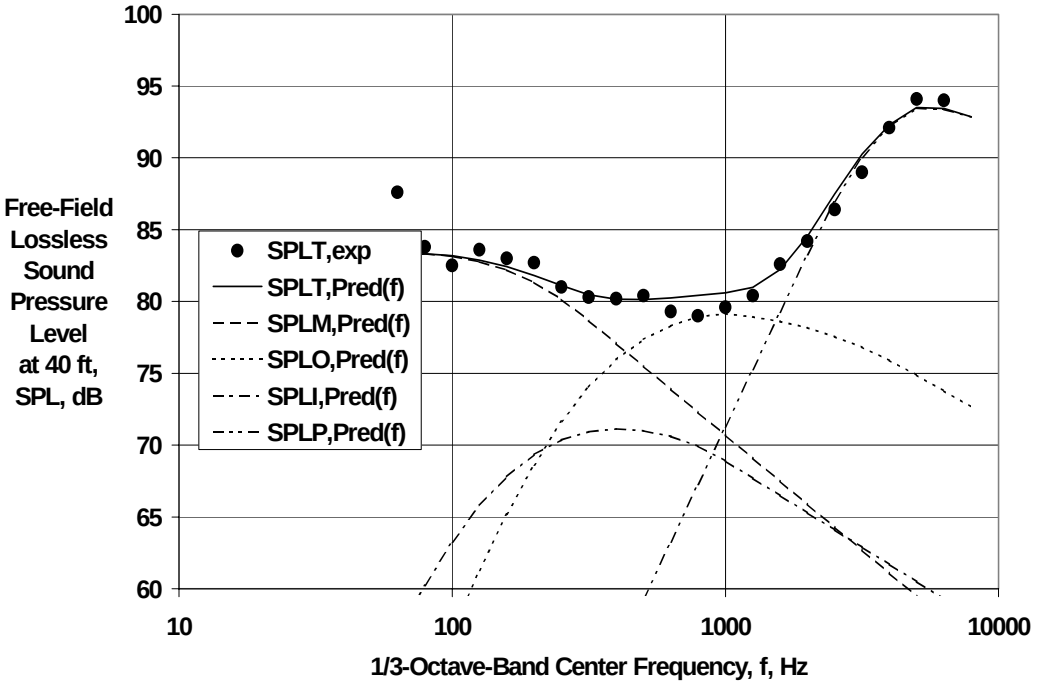

(a) Using Current Model

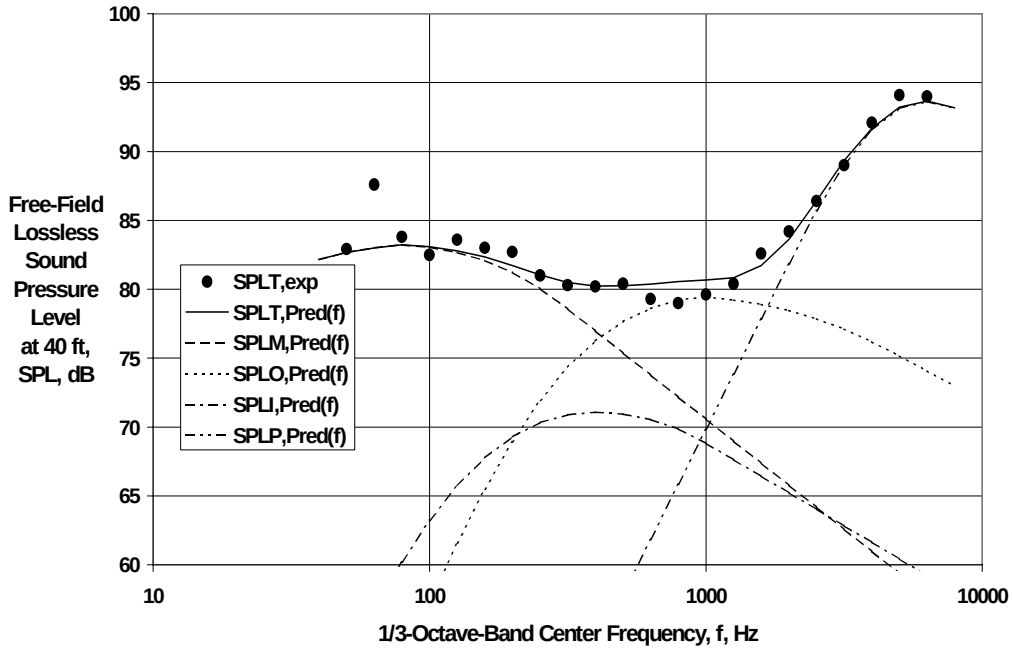

(b) Using Modified Plug Separation Noise Model

Figure 25.—Comparison of Experimental and Predicted Spectra at θ = 90 deg for BPR ≅ 13 Baseline Nozzle at V_{mix}/c_{amb} = 0.591 and M_f = 0.20.

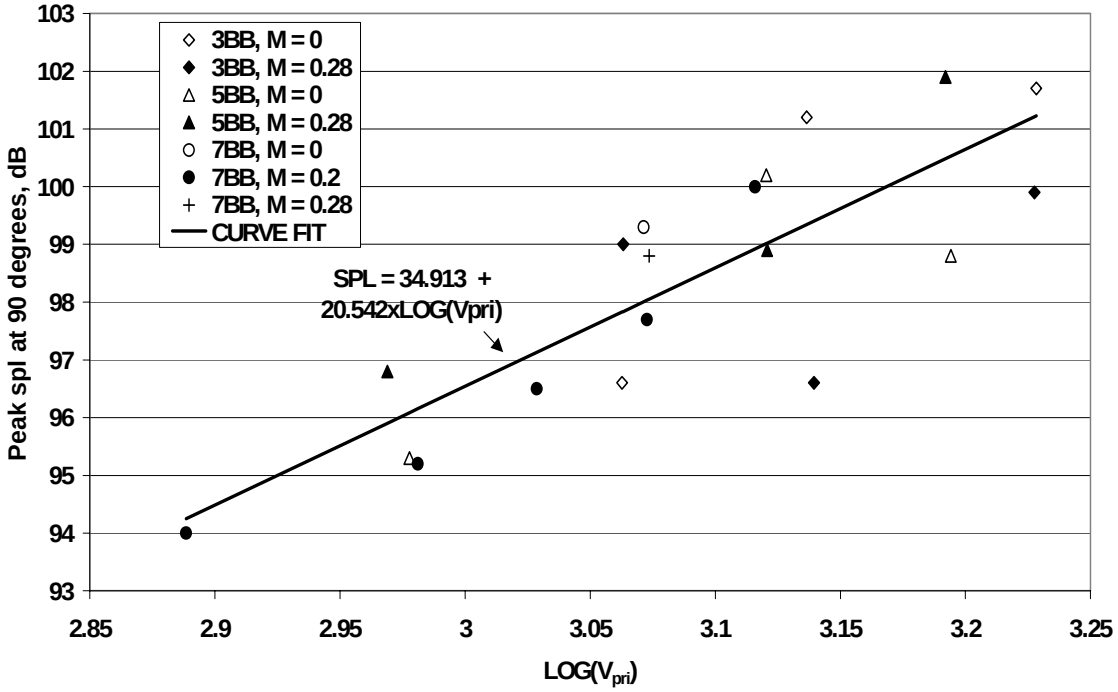

Figure 26.—Variation of Peak SPL at θ = 90 deg with Logarithm of Primary Velocity (Vpri = V_1)

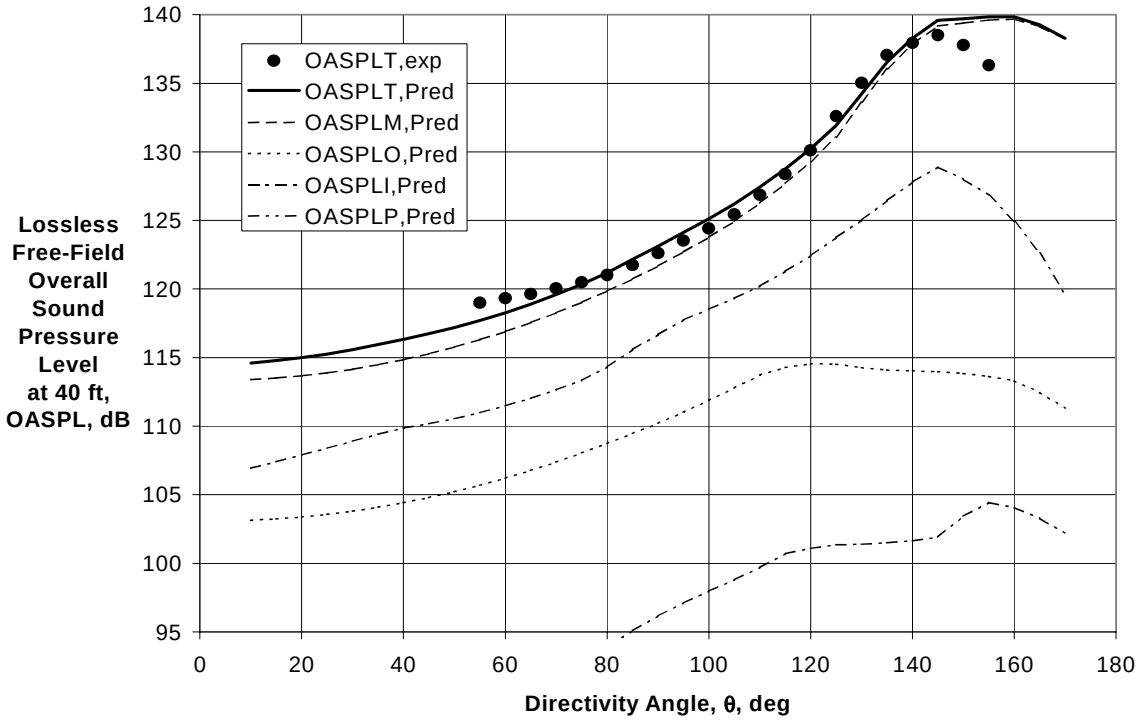

Figure 27.—Experimental and Predicted Directivities for Baseline BPR ≅ 5 External Plug Nozzle at V_{mix}/c_{amb} = 1.09 and M_f = 0.0.

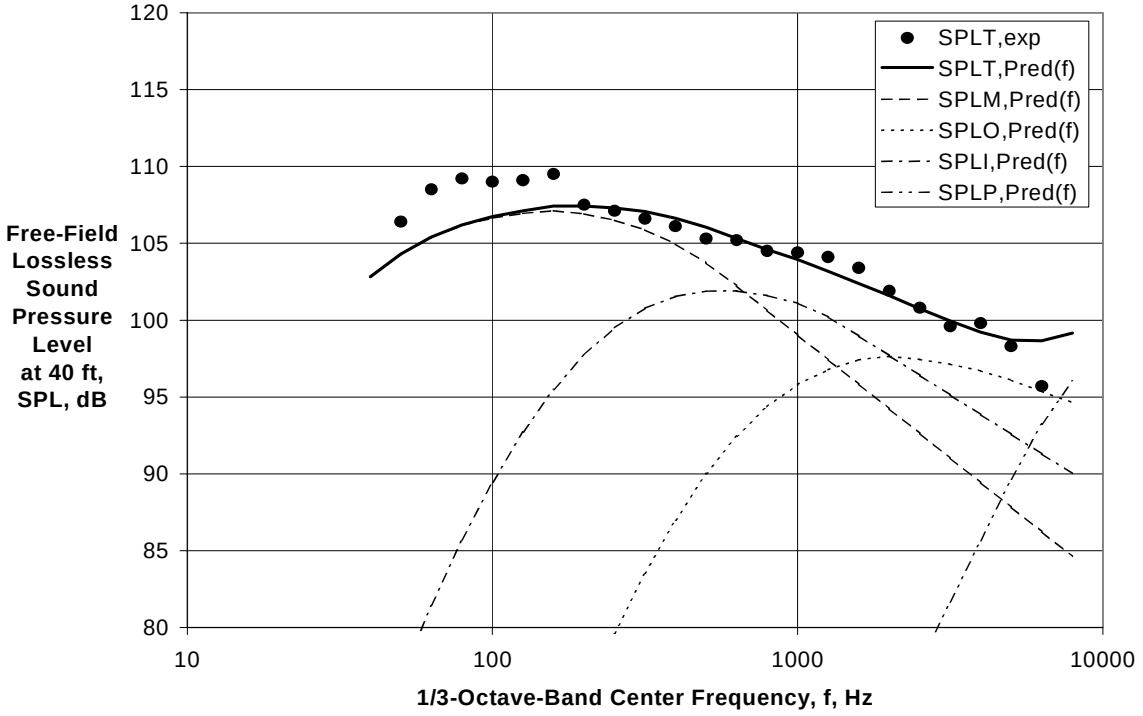

(a) Directivity Angle θ = 60 deg

Figure 28.—Experimental and Predicted Spectra for Baseline BPR ≅ 5 External Plug Nozzle at V_{mix}/c_{amb} = 1.09 and M_f = 0.0.

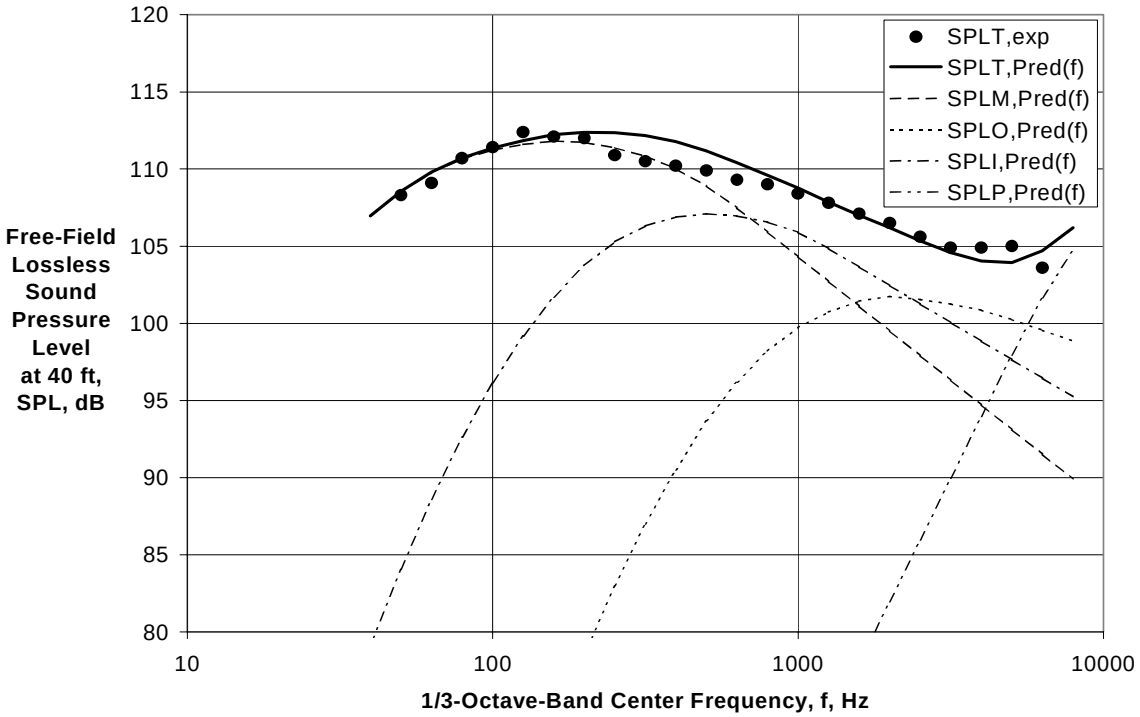

(b) Directivity Angle θ = 90 deg

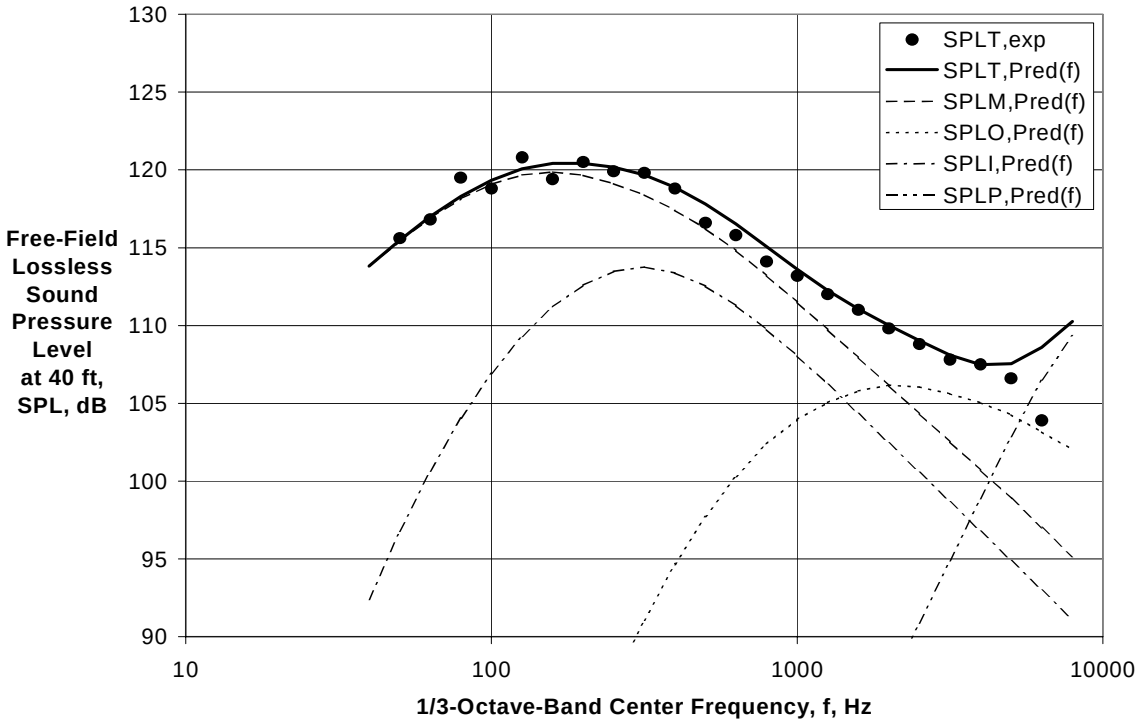

(c) Directivity Angle θ = 120 deg

Figure 28.—(Continued) Experimental and Predicted Spectra for Baseline BPR ≅ 5 External Plug Nozzle at V_{mix}/c_{amb} = 1.09 and M_f = 0.0.

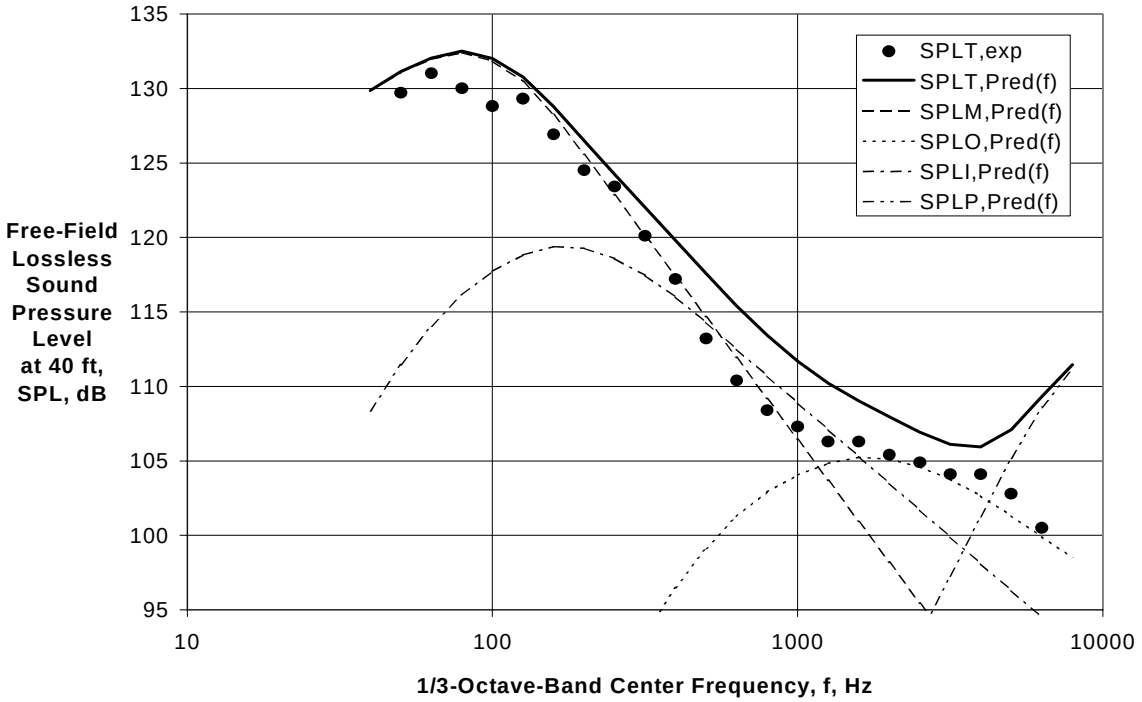

(d) Directivity Angle θ = 150 deg

Figure 28.—(Concluded) Experimental and Predicted Spectra for Baseline BPR ≅ 5 External Plug Nozzle at V_{mix}/c_{amb} = 1.09 and M_f = 0.0.

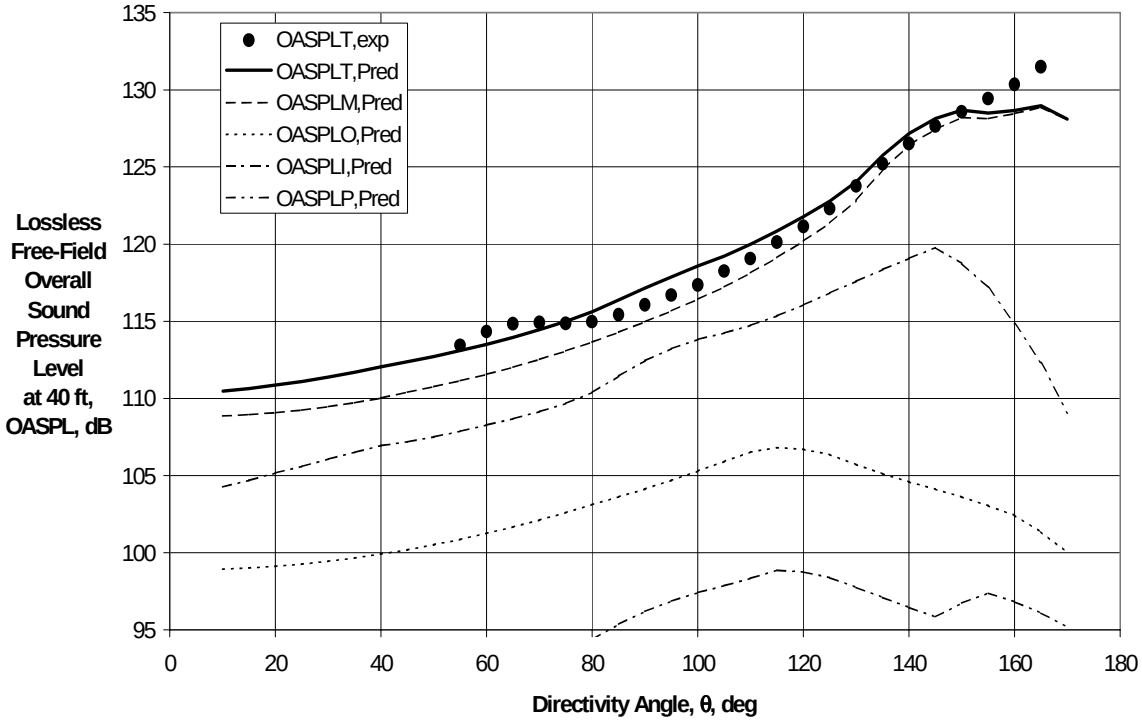

Figure 29.—Experimental and Predicted Directivities for Baseline BPR ≅ 5 External Plug Nozzle at V_{mix}/c_{amb} = 1.06 and M_f = 0.28.

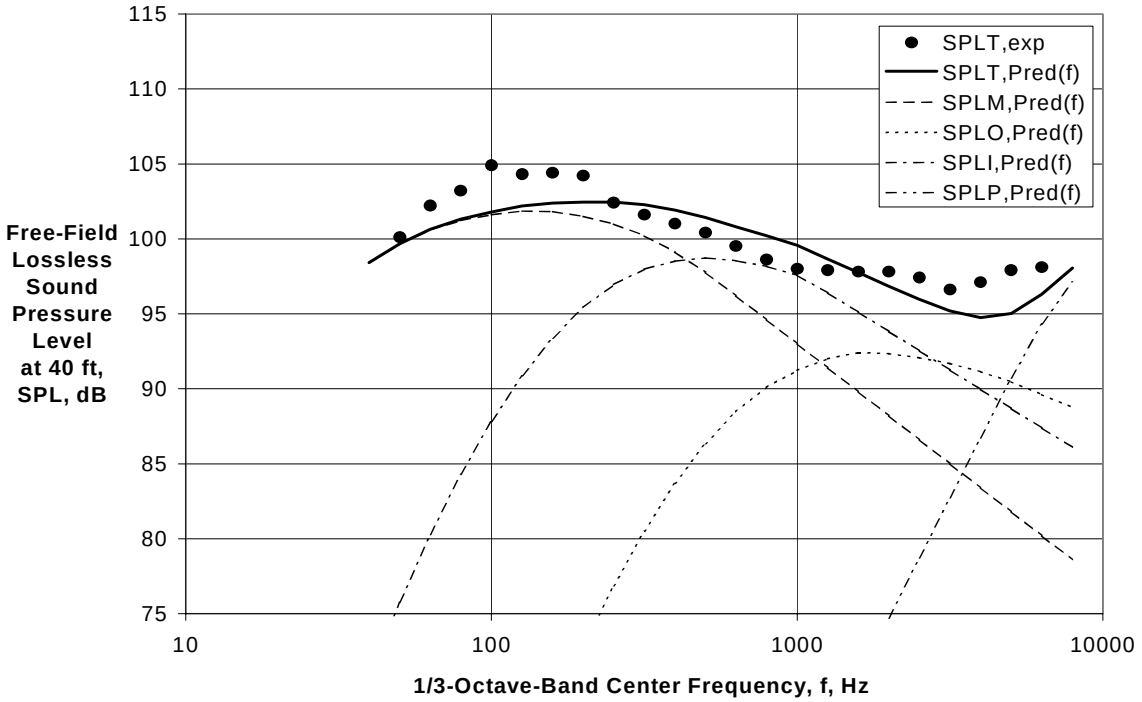

(a) Directivity Angle θ = 60 deg

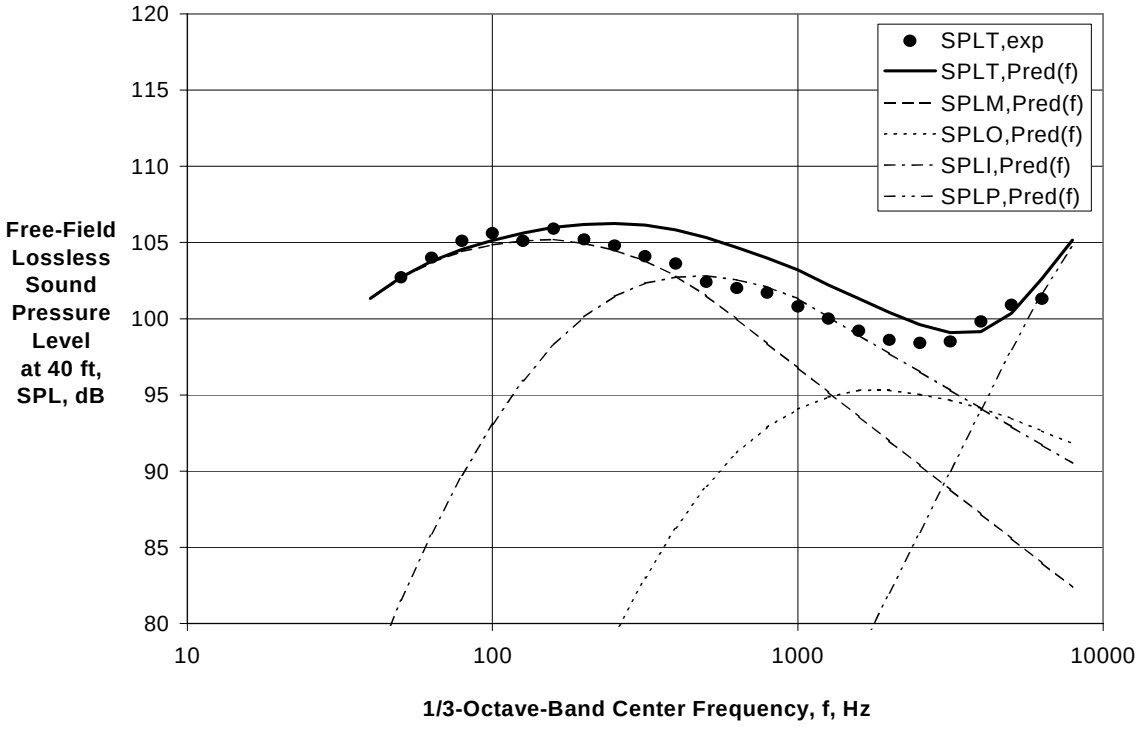

(b) Directivity Angle θ = 90 deg

Figure 30.—Experimental and Predicted Spectra for Baseline BPR ≅ 5 External Plug Nozzle at V_{mix}/c_{amb} = 1.06 and M_f = 0.28.

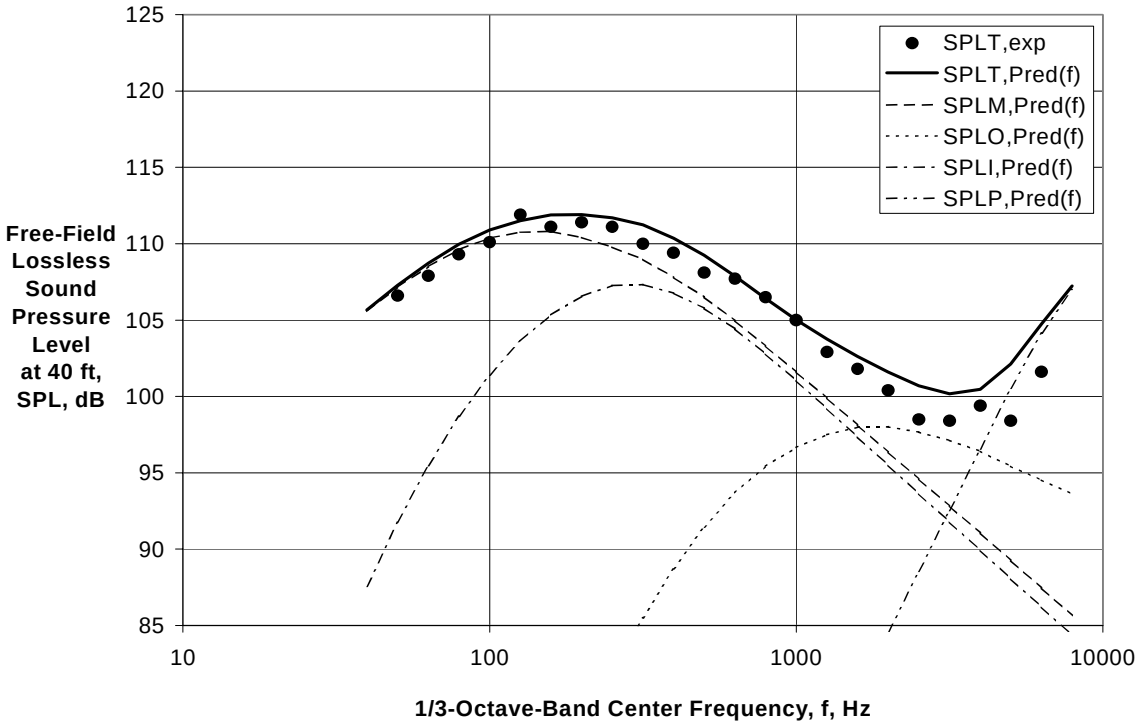

(c) Directivity Angle θ = 120 deg

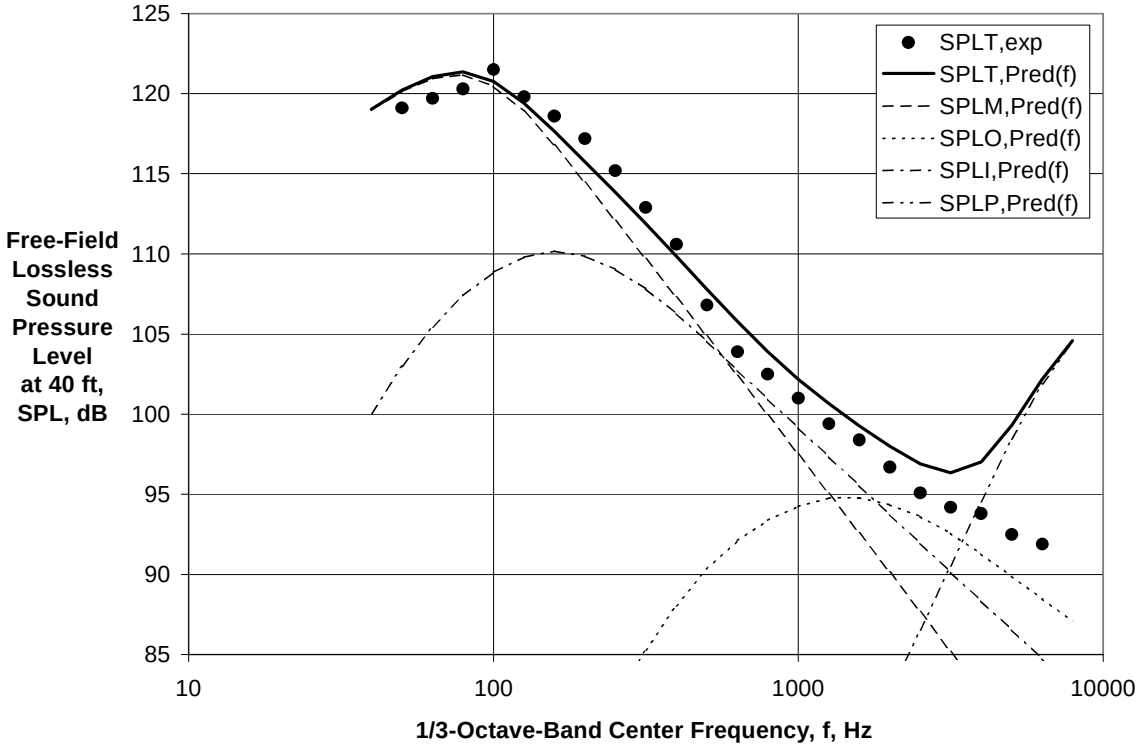

(d) Directivity Angle θ = 150 deg

Figure 30.—(Concluded) Experimental and Predicted Spectra for Baseline BPR ≅ 5 External Plug Nozzle at V_{mix}/c_{amb} = 1.06 and M_f = 0.28.

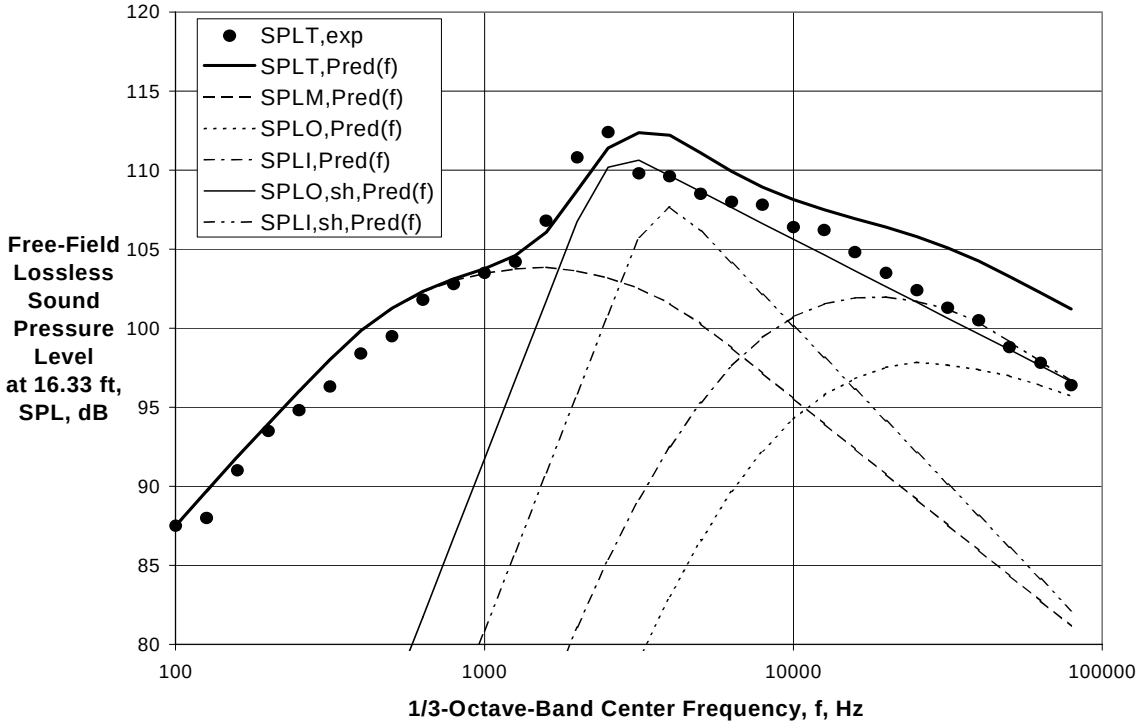

(a) Directivity Angle θ = 46 deg

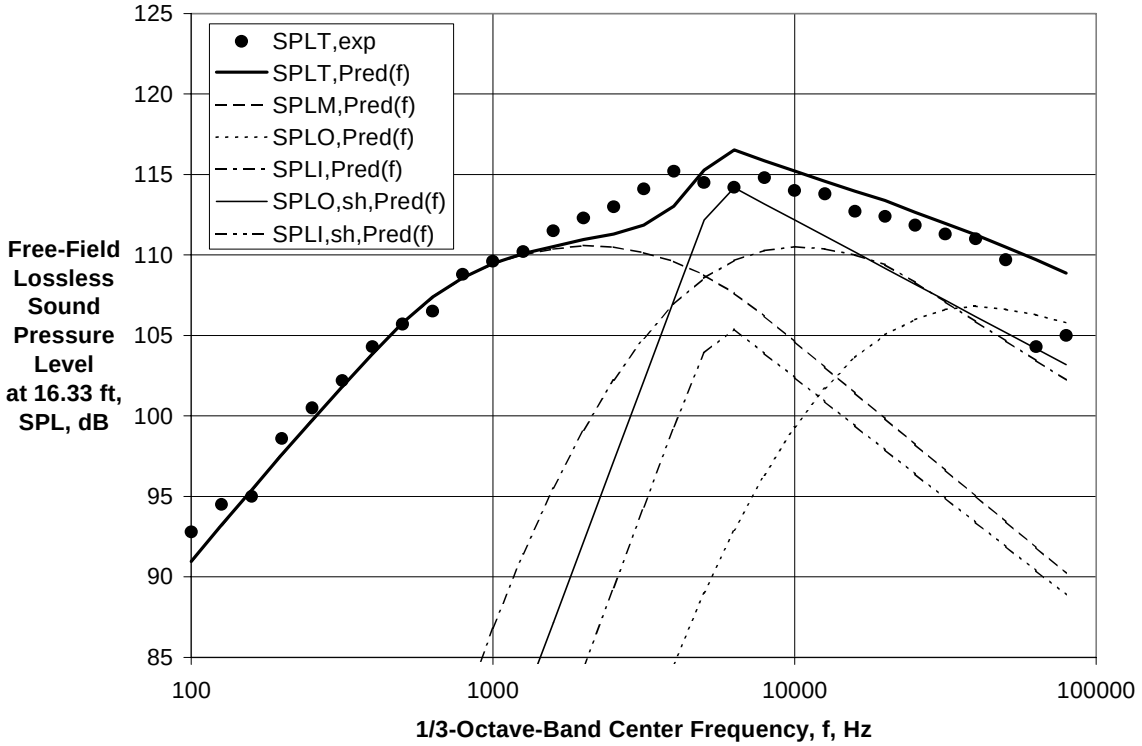

(b) Directivity Angle θ = 95 deg

Figure 31.—Experimental and Predicted Spectra for Baseline BPR ≅ 1 Coplanar Nozzle at V_{mix}/c_{amb} = 2.04 and M_f = 0.0.

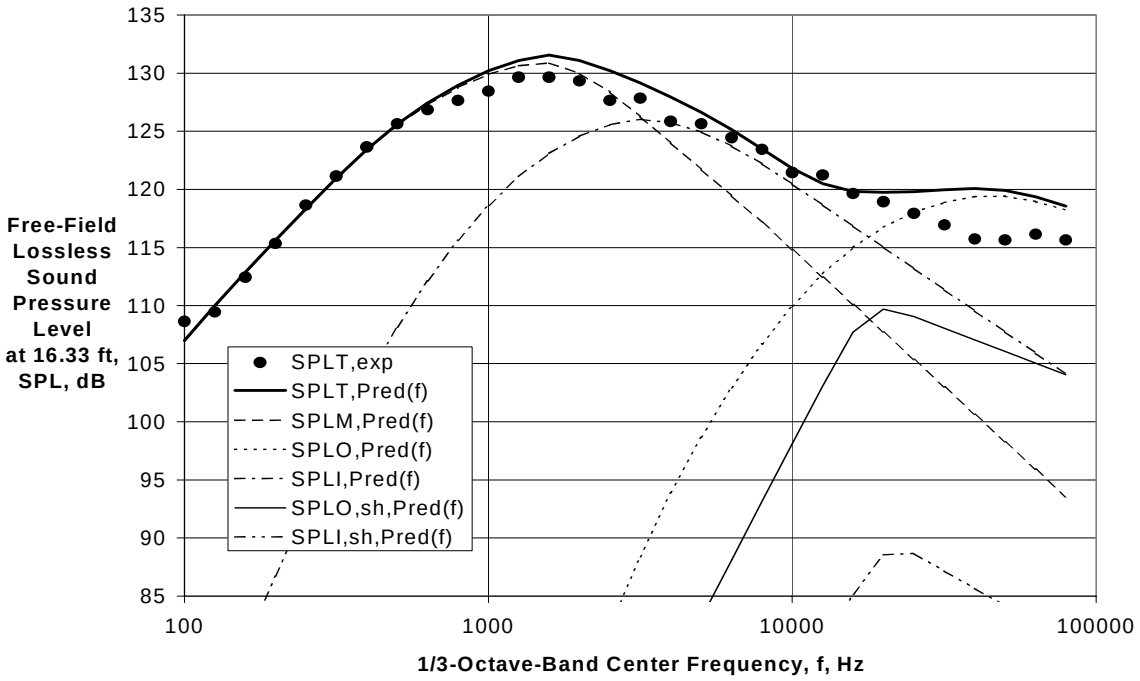

(c) Directivity Angle θ = 139 deg

Figure 31.—(Concluded) Experimental and Predicted Spectra for Baseline BPR ≅ 1 Coplanar Nozzle at V_{mix}/c_{amb} = 2.04 and M_f = 0.0.

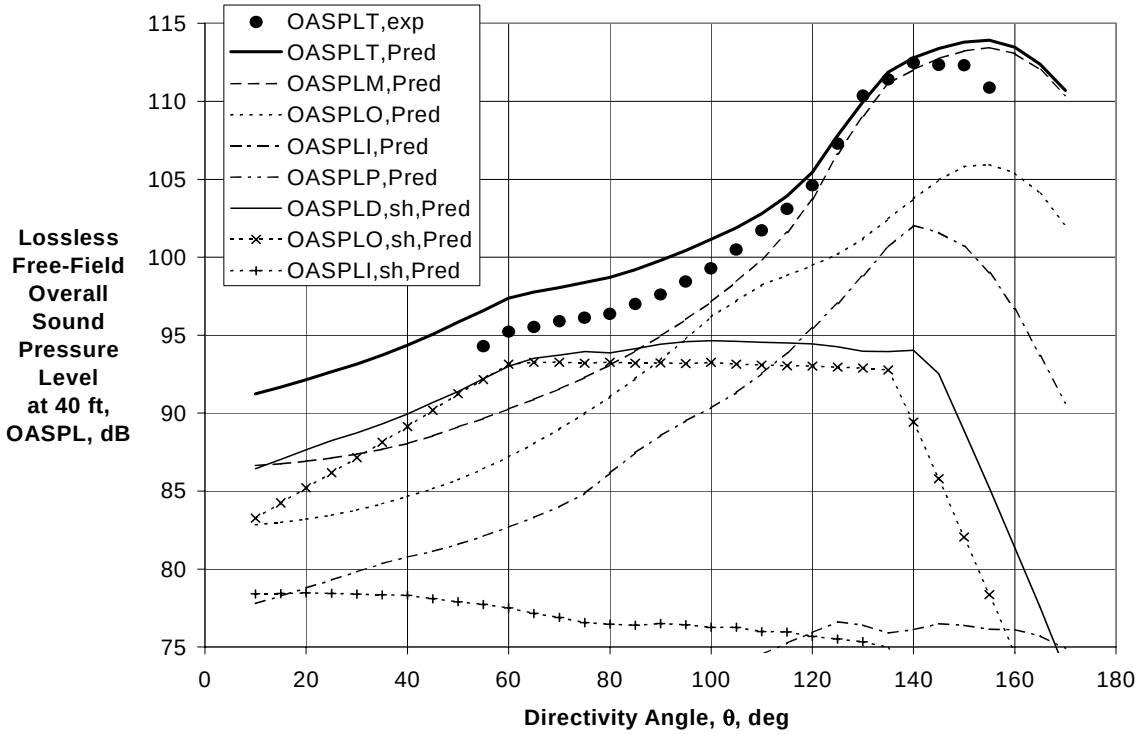

Figure 32.—Experimental and Predicted Directivities for Unsuppressed IVP Coannular External Plug Nozzle at V_{mix}/c_{amb} = 2.02 and M_f = 0.0.

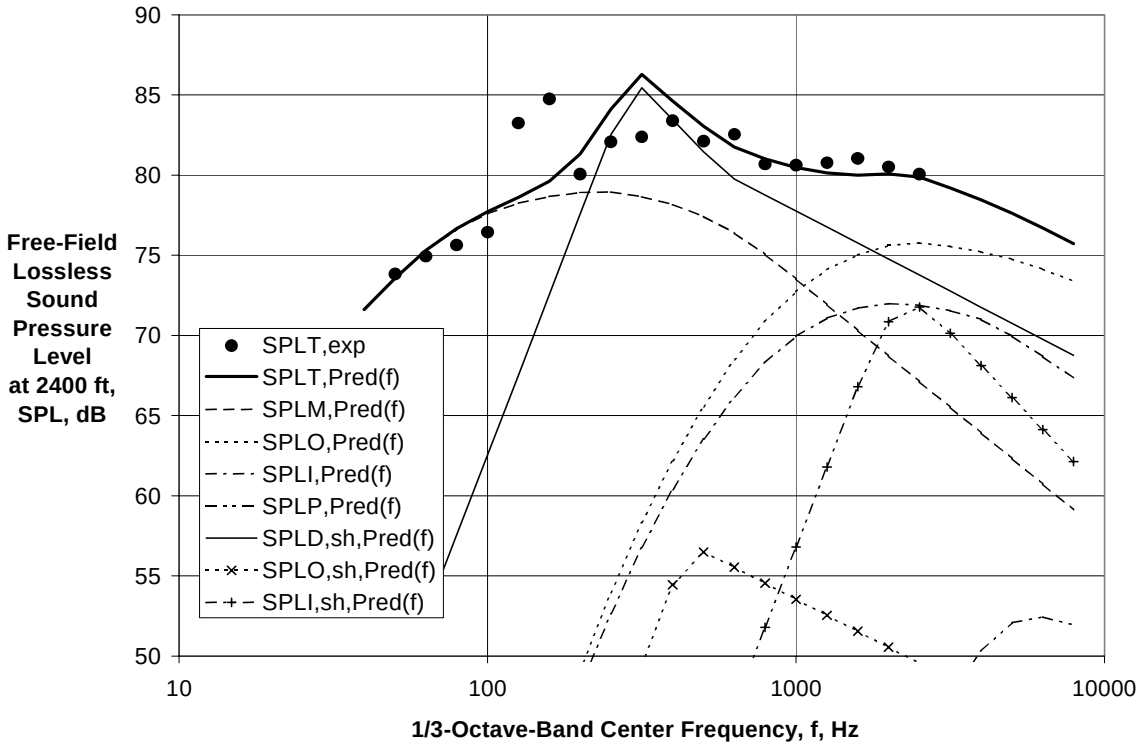

(a) Directivity Angle θ = 50 deg

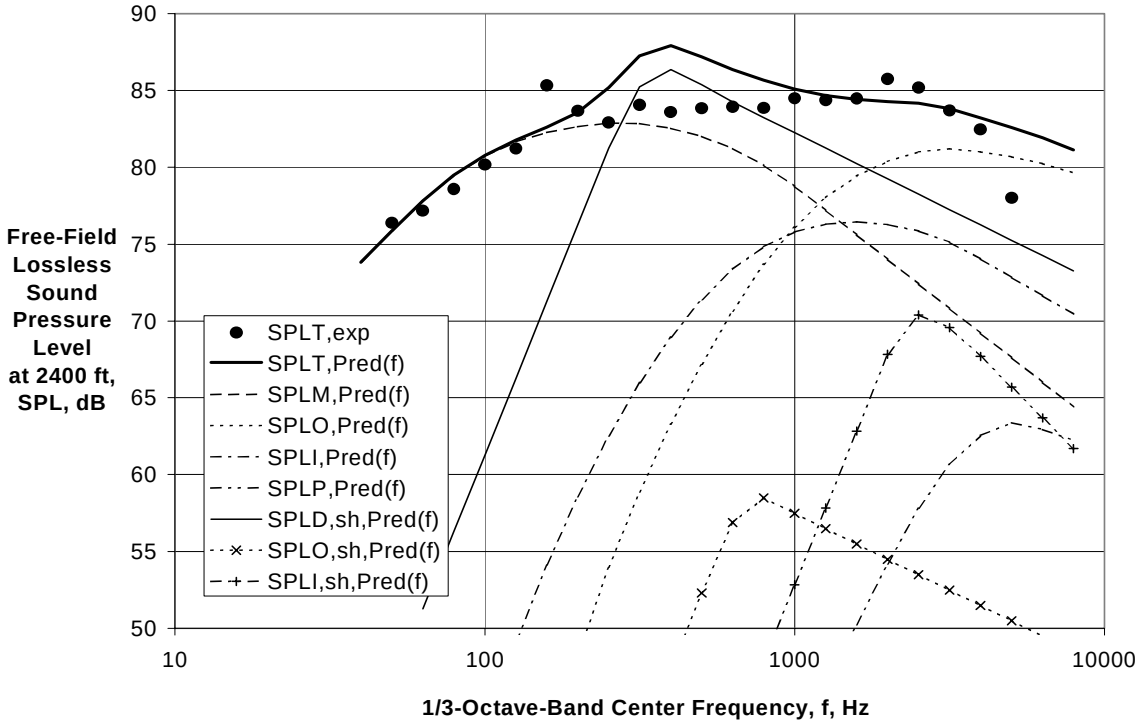

(b) Directivity Angle θ = 80 deg

Figure 33.—Experimental and Predicted Spectra for Unsuppressed IVP Coannular External Plug Nozzle at V_{mix}/c_{amb} = 2.02 and M_f = 0.0.

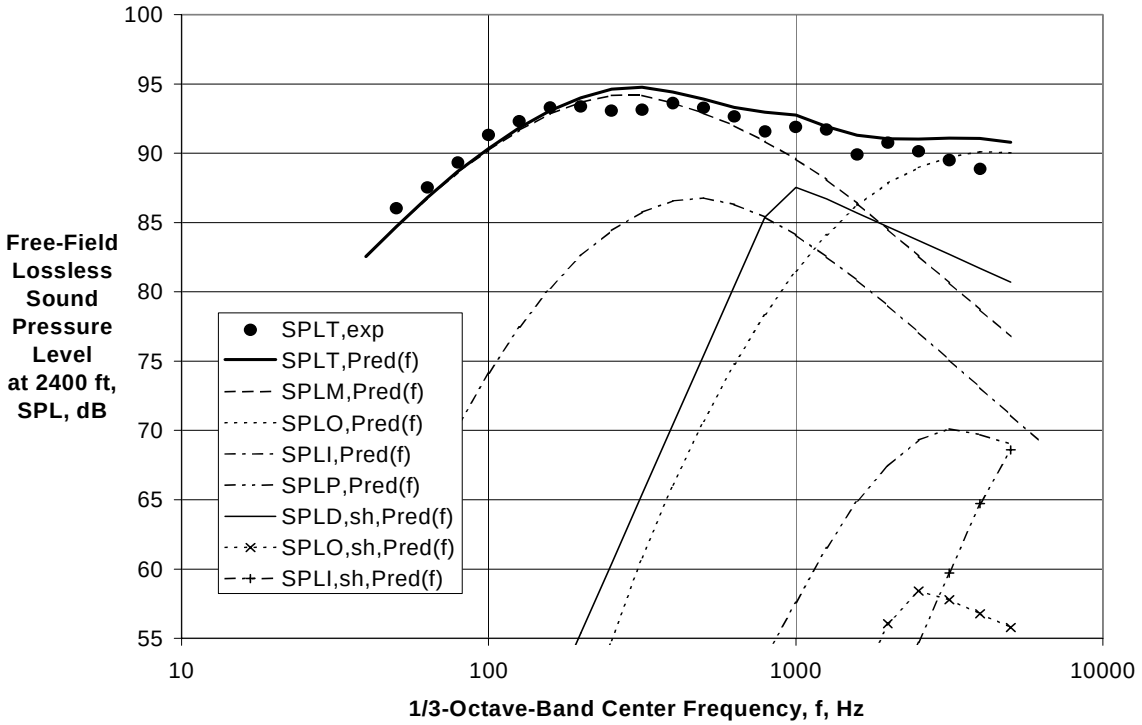

(c) Directivity Angle θ = 120 deg

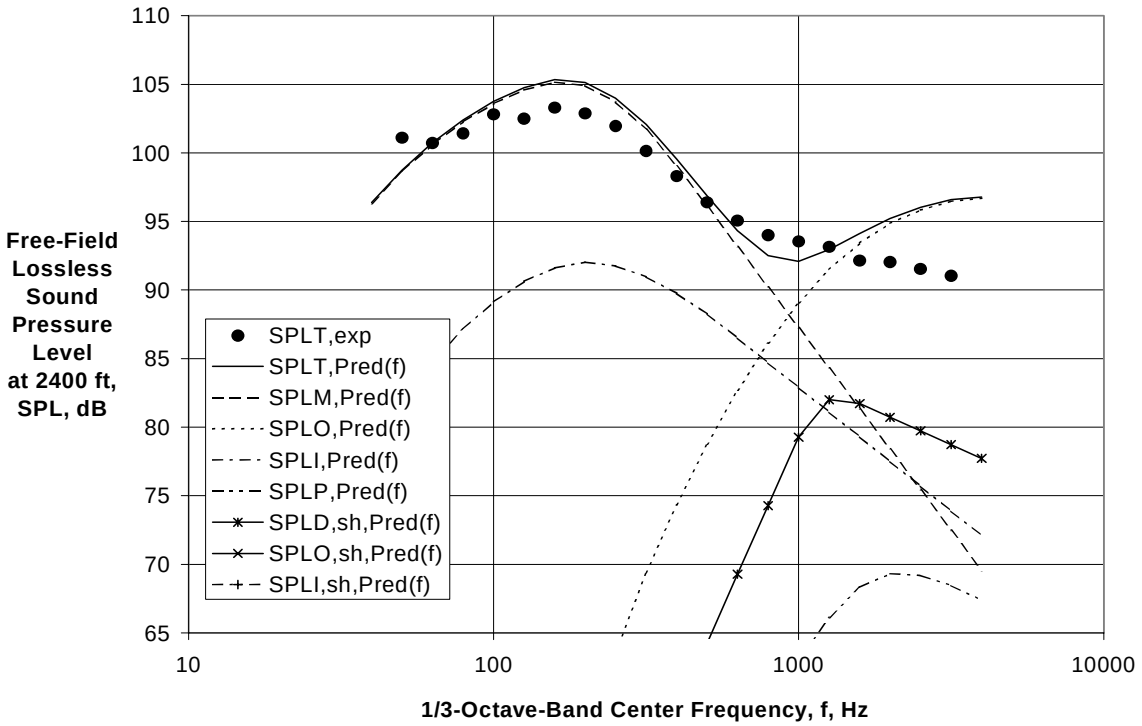

(d) Directivity Angle θ = 150 deg

Figure 33.—(Concluded) Experimental and Predicted Spectra for Unsuppressed IVP Coannular External Plug Nozzle at V_{mix}/c_{amb} = 2.02 and M_f = 0.0.

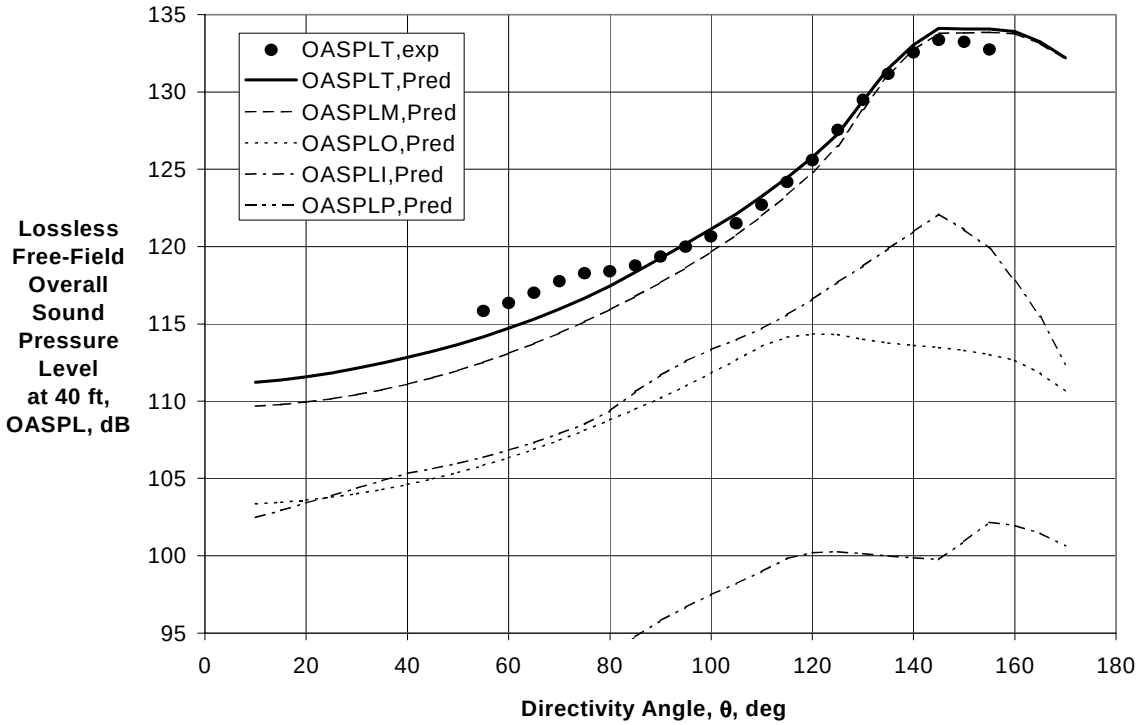

Figure 34.—Experimental and Predicted Directivities for BPR ≅ 5 External Plug Nozzle with Core Chevrons at V_{mix}/c_{amb} = 1.04 and M_f = 0.0.

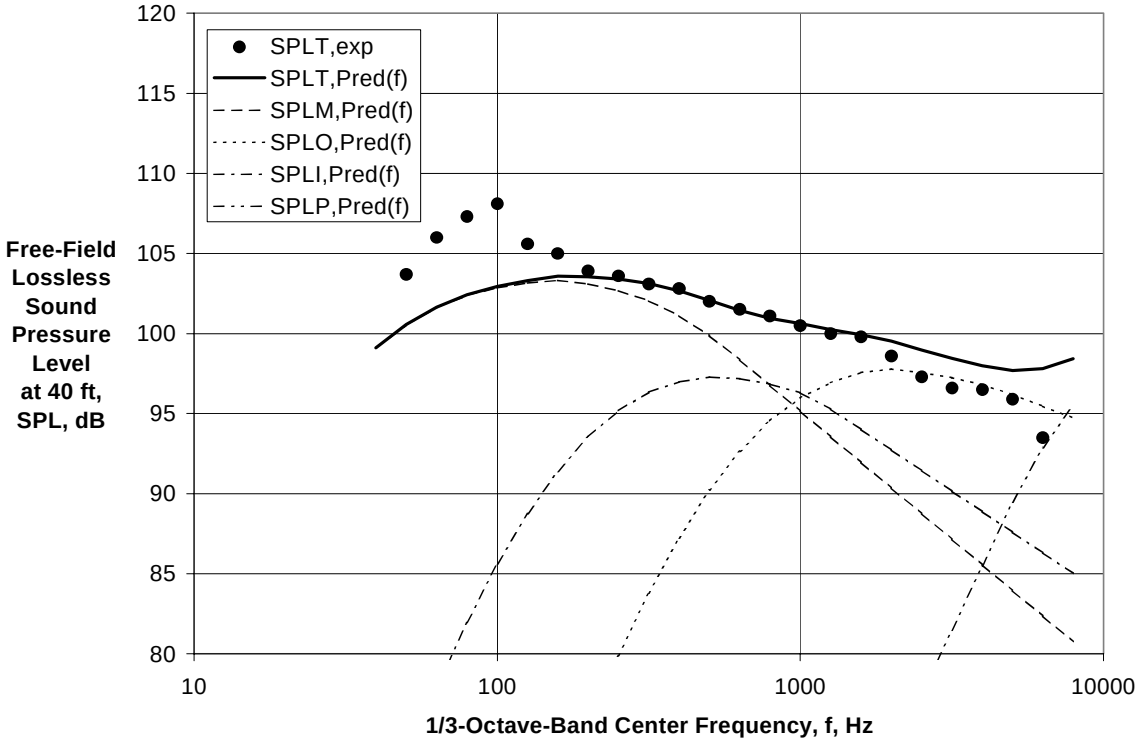

(a) Directivity Angle θ = 60 deg

Figure 35.—Experimental and Predicted Spectra for BPR ≅ 5 External Plug Nozzle with Core Chevrons at V_{mix}/c_{amb} = 1.04 and M_f = 0.0.

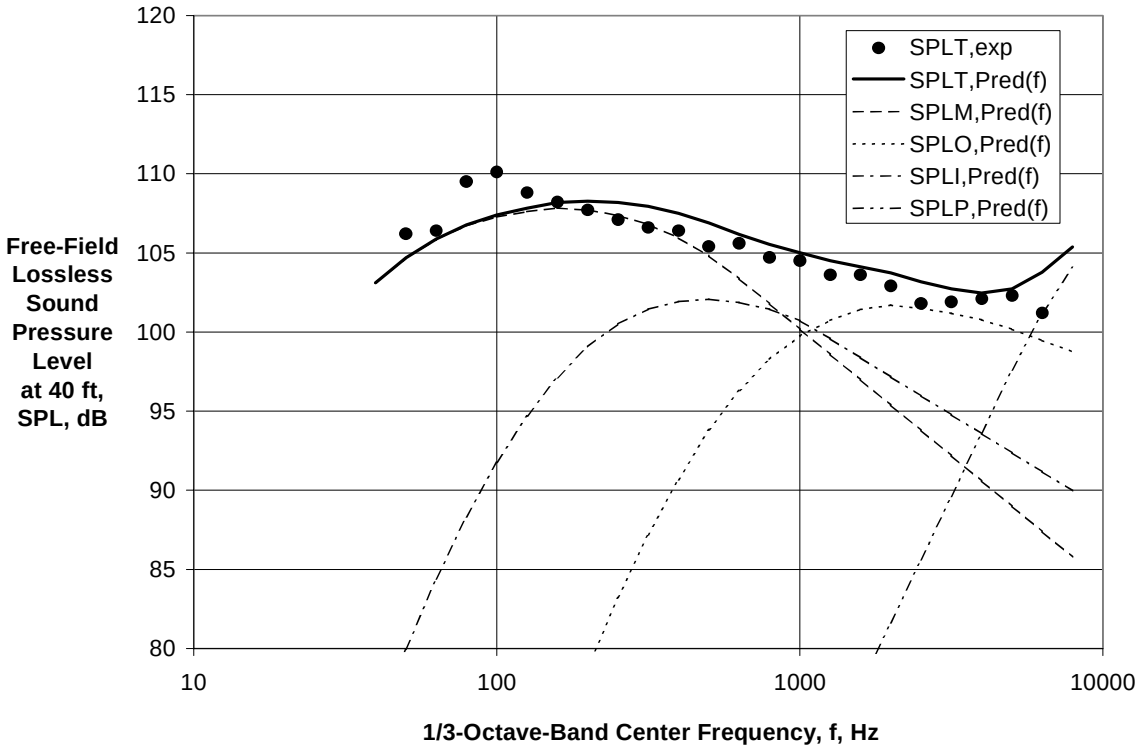

(b) Directivity Angle θ = 90 deg

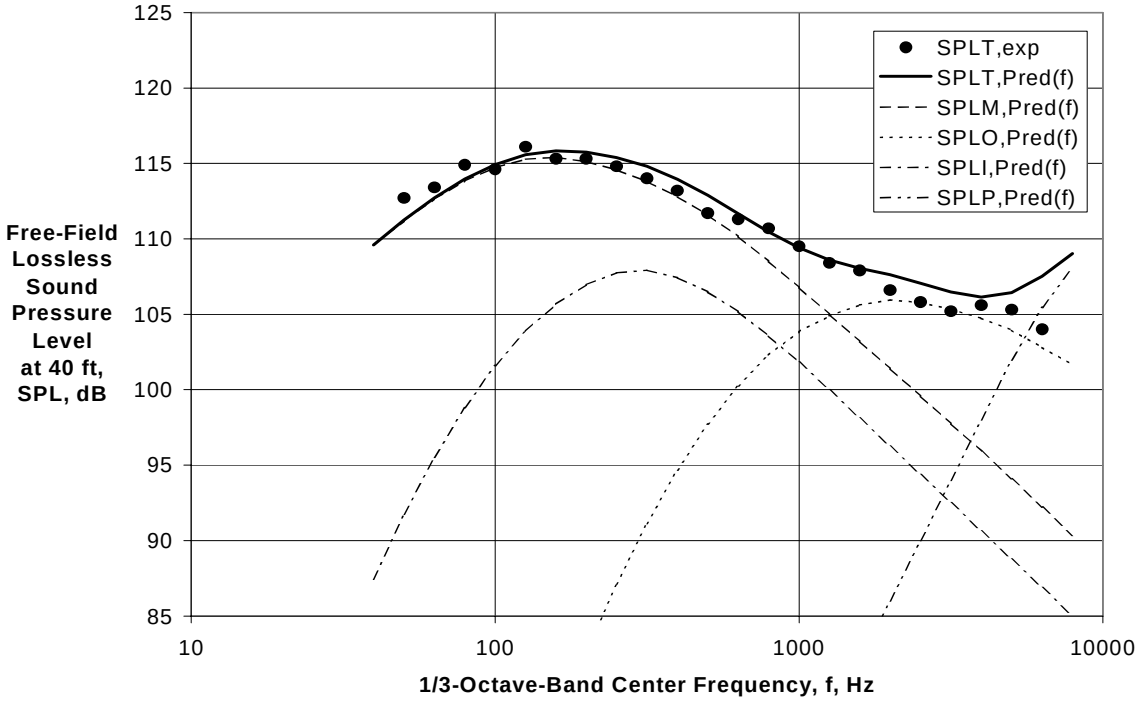

(c) Directivity Angle θ = 120 deg

Figure 35.—(Continued) Experimental and Predicted Spectra for BPR ≅ 5 External Plug Nozzle with Core Chevrons at V_{mix}/c_{amb} = 1.04 and M_f = 0.0.

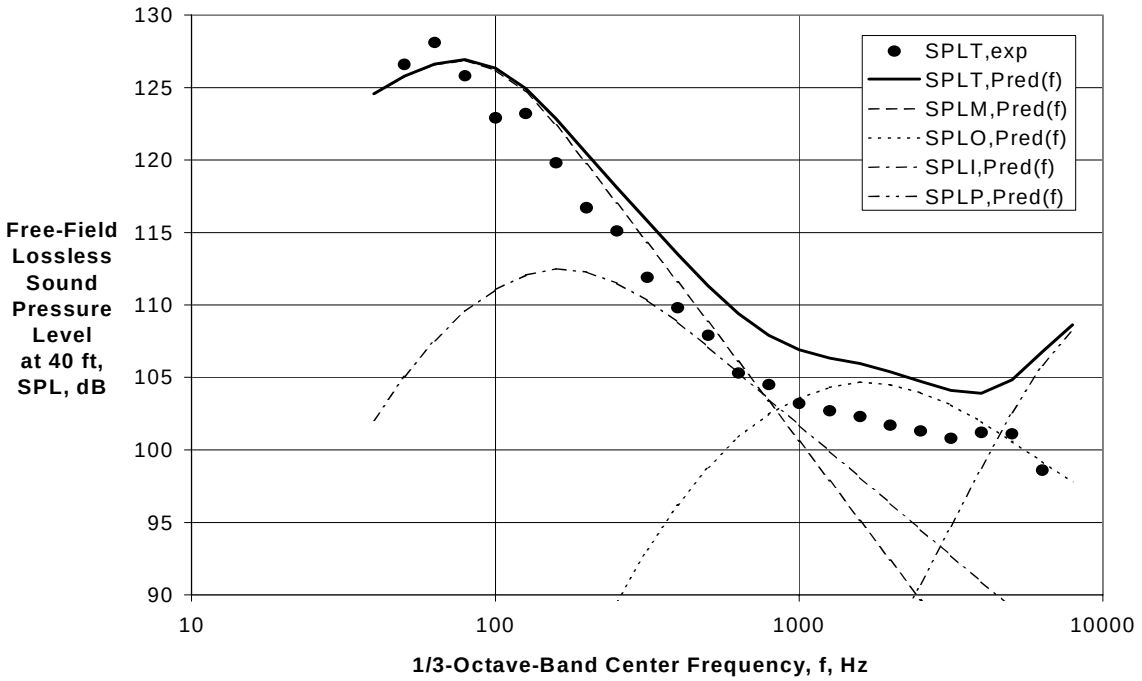

(d) Directivity Angle θ = 150 deg

Figure 35.—(Concluded) Experimental and Predicted Spectra for BPR ≅ 5 External Plug Nozzle with Core Chevrons at V_{mix}/c_{amb} = 1.04 and M_f = 0.0.

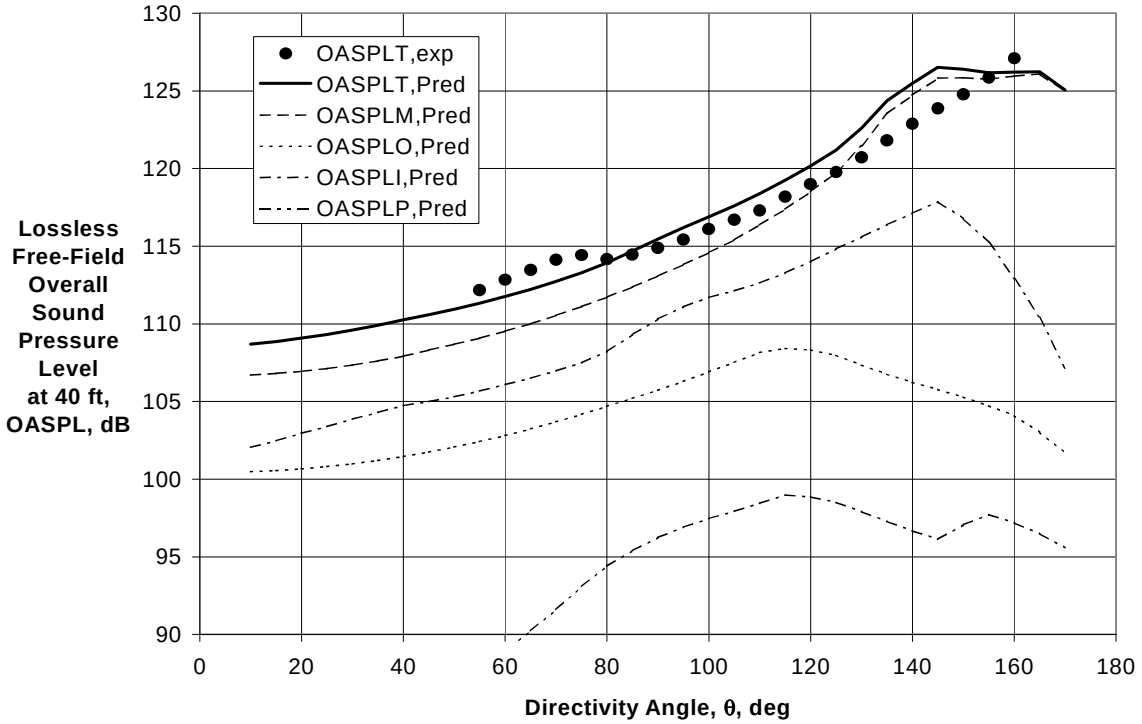

Figure 36.—Experimental and Predicted Directivities for BPR ≅ 5 External Plug Nozzle with Core Chevrons at V_{mix}/c_{amb} = 1.07 and M_f = 0.28.

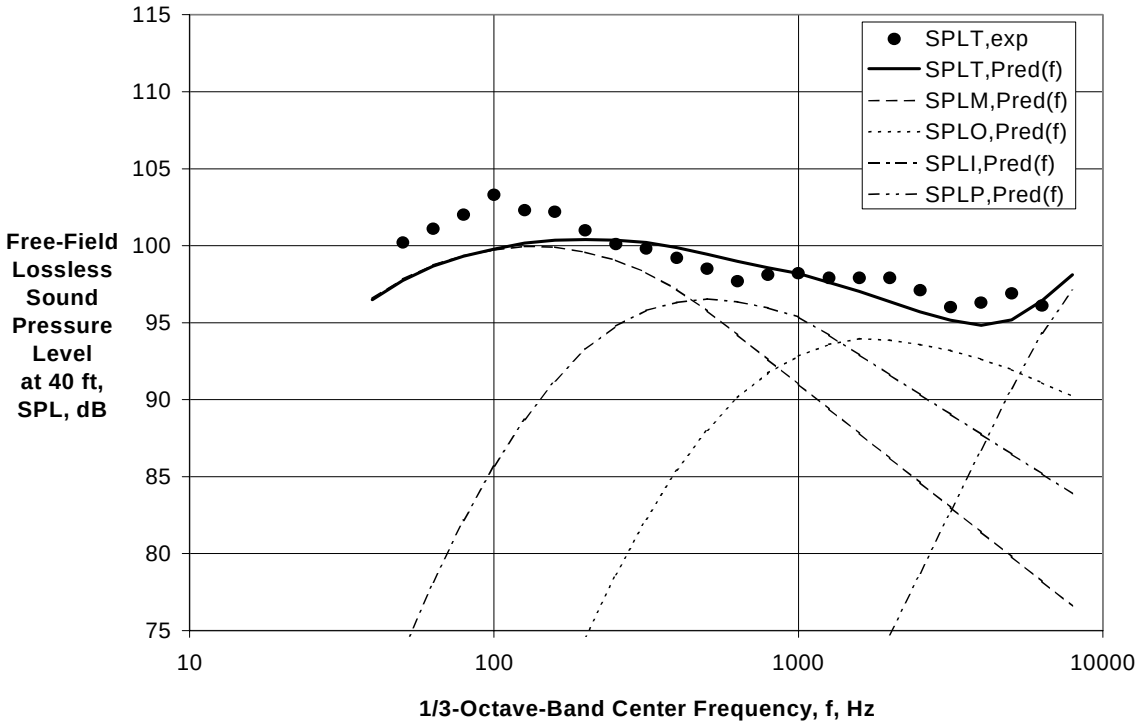

(a) Directivity Angle θ = 60 deg

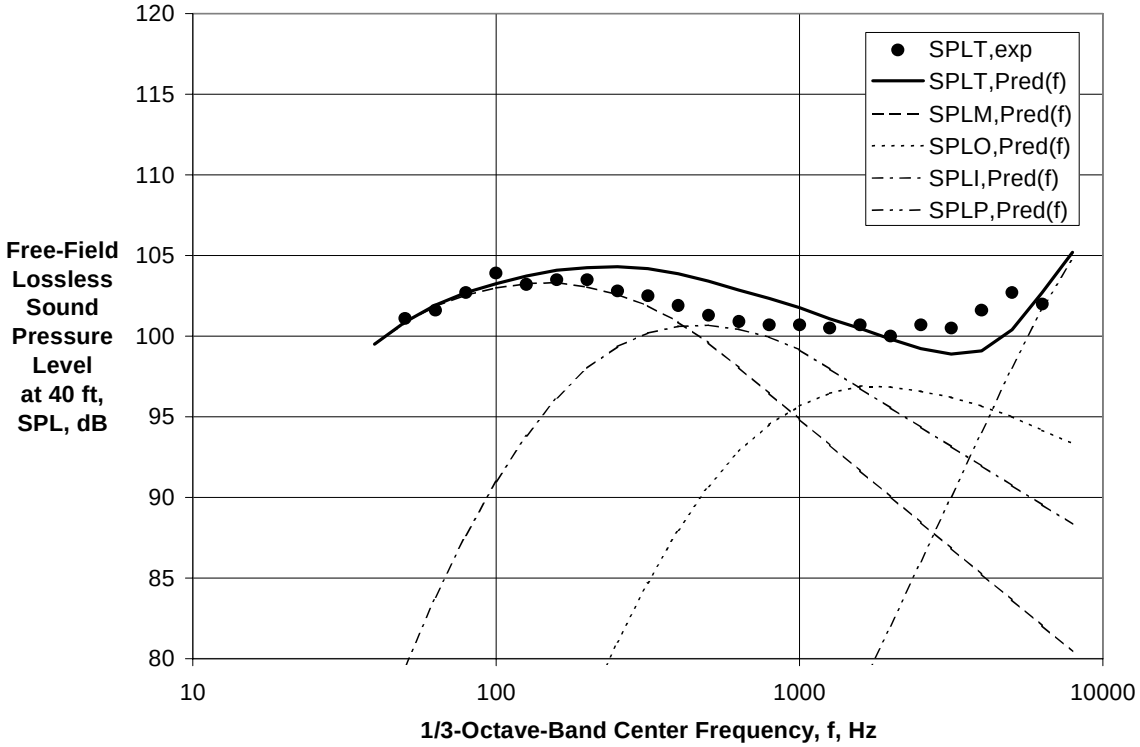

(b) Directivity Angle θ = 90 deg

Figure 37.—Experimental and Predicted Spectra for BPR ≅ 5 External Plug Nozzle with Core Chevrons at V_{mix}/c_{amb} = 1.07 and M_f = 0.28.

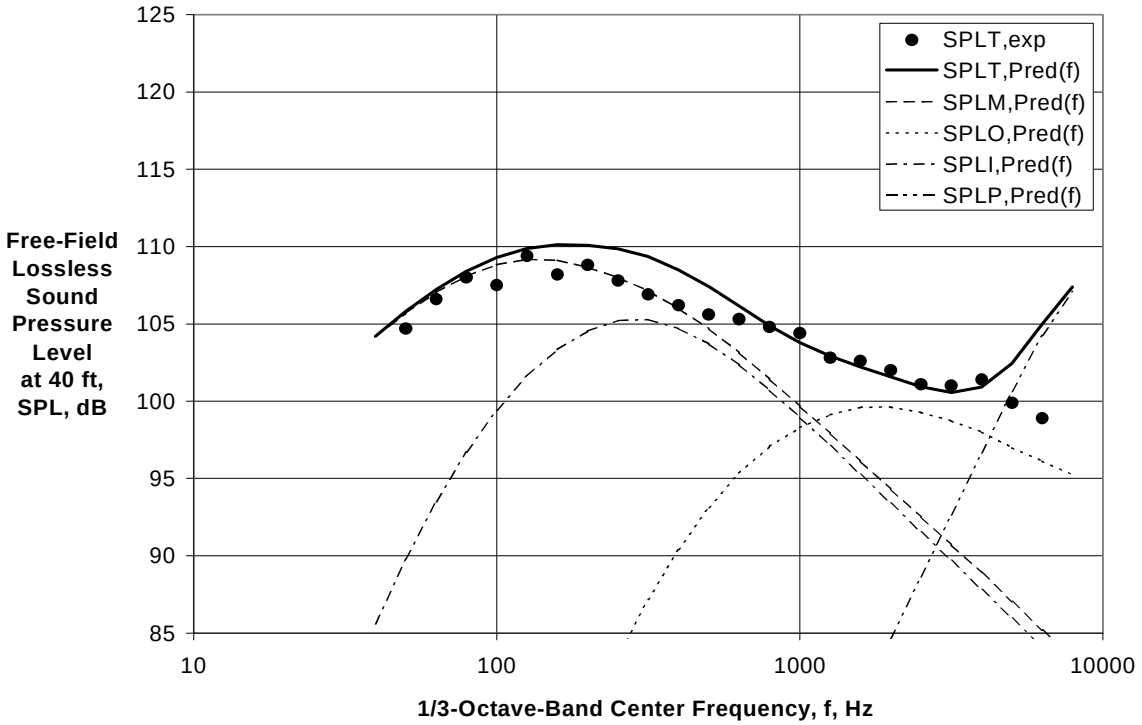

(c) Directivity Angle θ = 120 deg

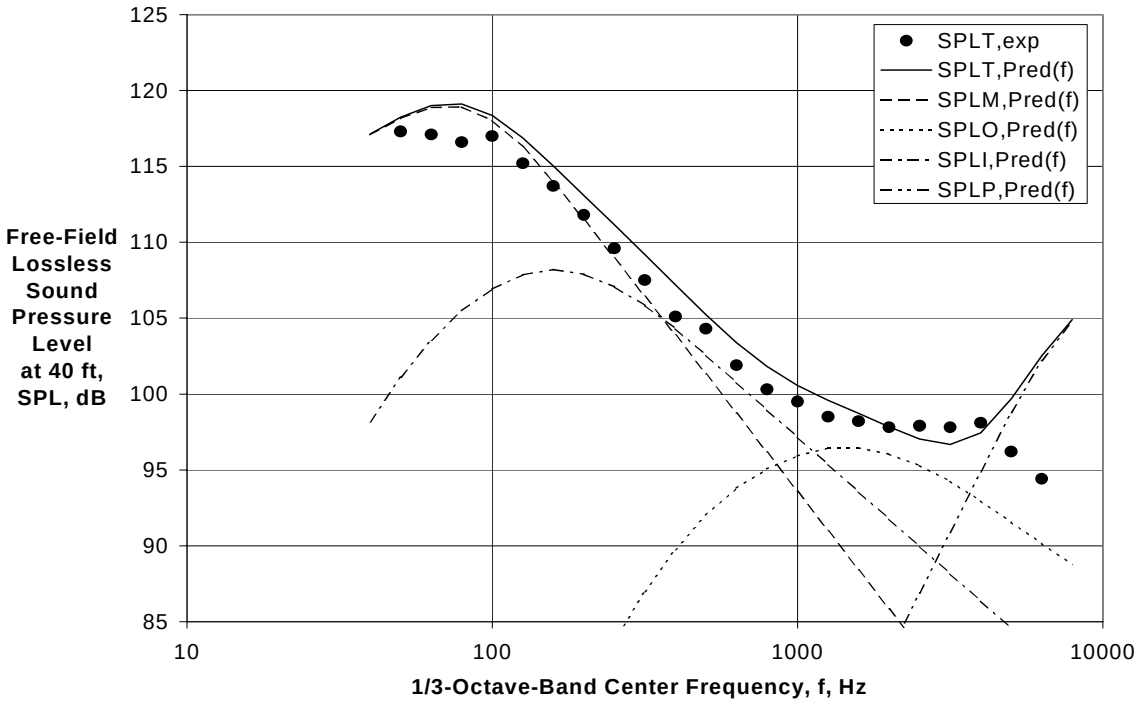

(d) Directivity Angle θ = 150 deg

Figure 37.—(Concluded) Experimental and Predicted Spectra for BPR ≅ 5 External Plug Nozzle with Core Chevrons at V_{mix}/c_{amb} = 1.07 and M_f = 0.28.

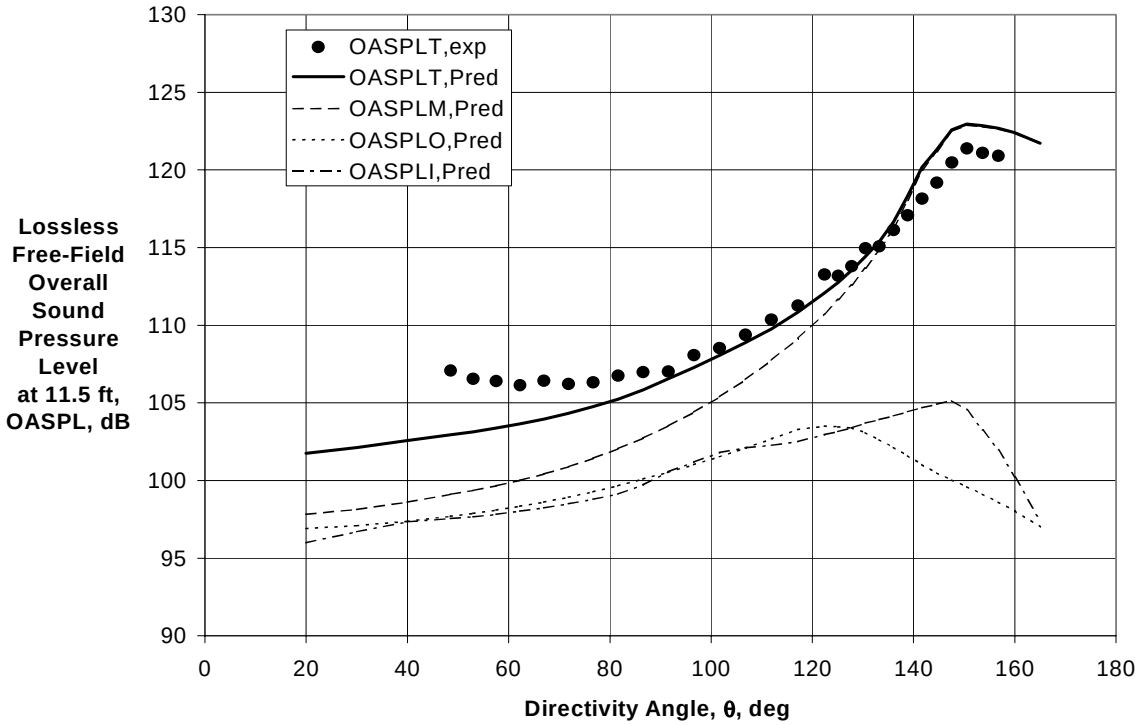

Figure 38.—Experimental and Predicted Directivity for BPR ≅ 5 Internal Plug Nozzle with Core Petals at V_{mix}/c_{amb} = 0.975 and M_f = 0.10.

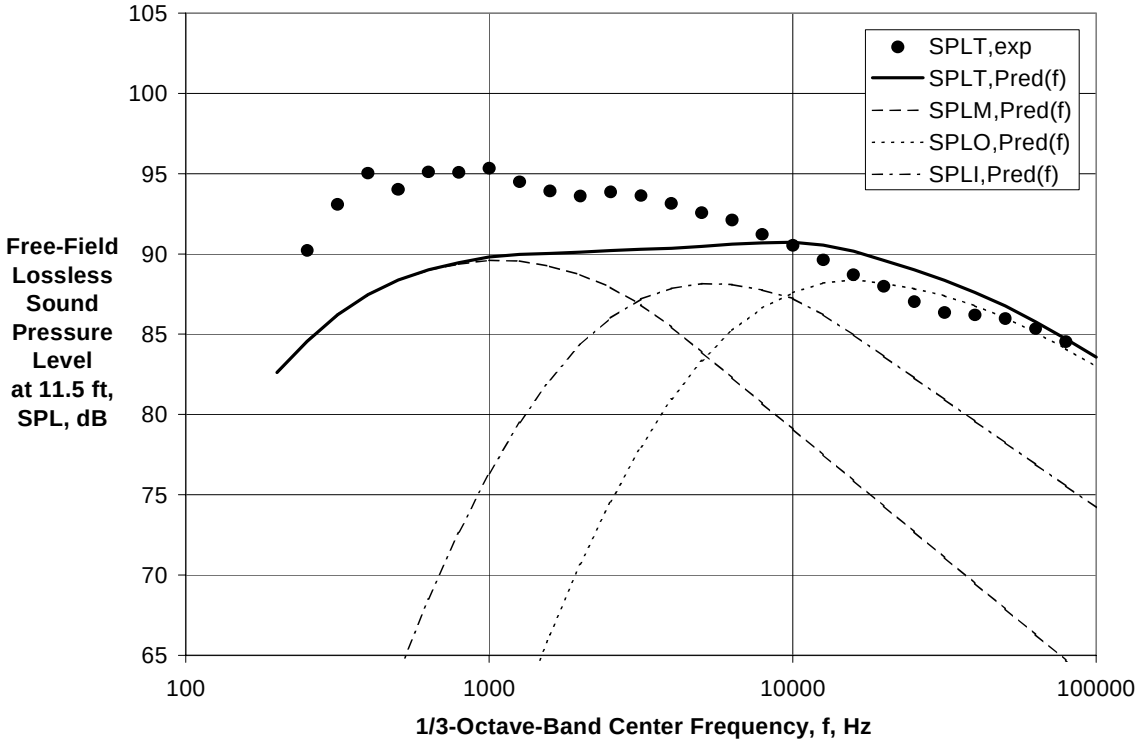

(a) Directivity Angle θ = 58 deg

Figure 39.—Experimental and Predicted Spectra for BPR ≅ 5 Internal Plug Nozzle with Core Petals at V_{mix}/c_{amb} = 0.975 and M_f = 0.10.

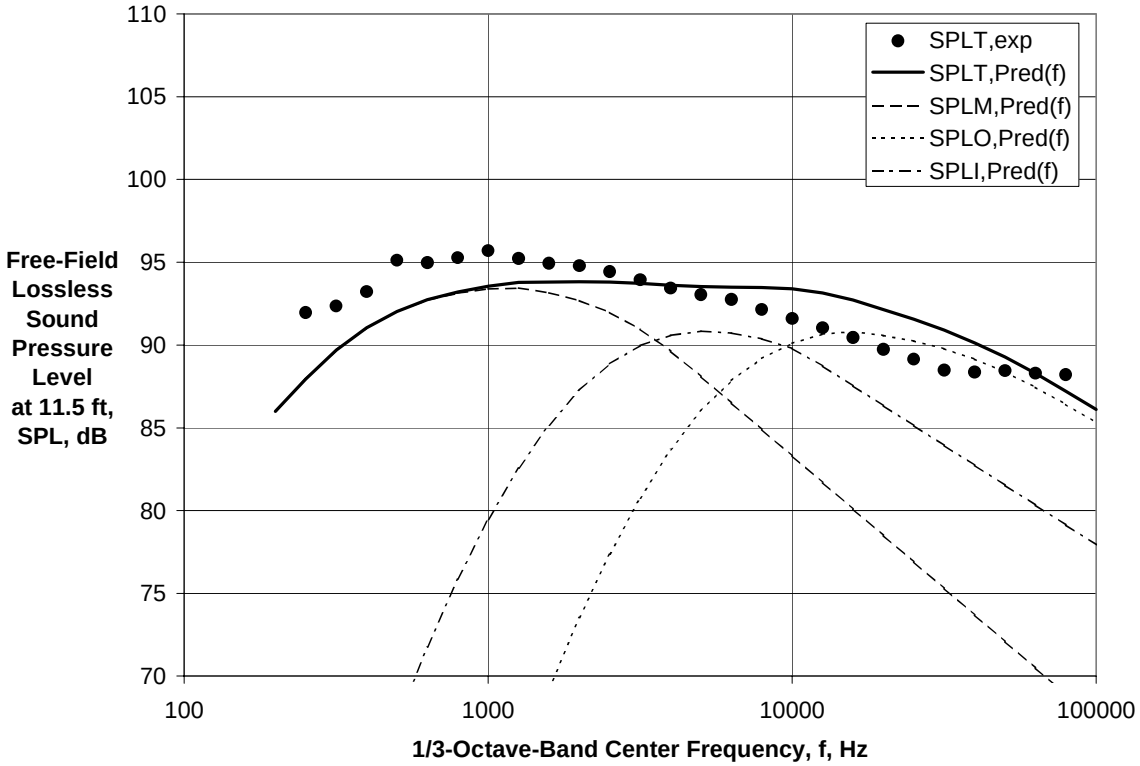

(b) Directivity Angle θ = 92 deg

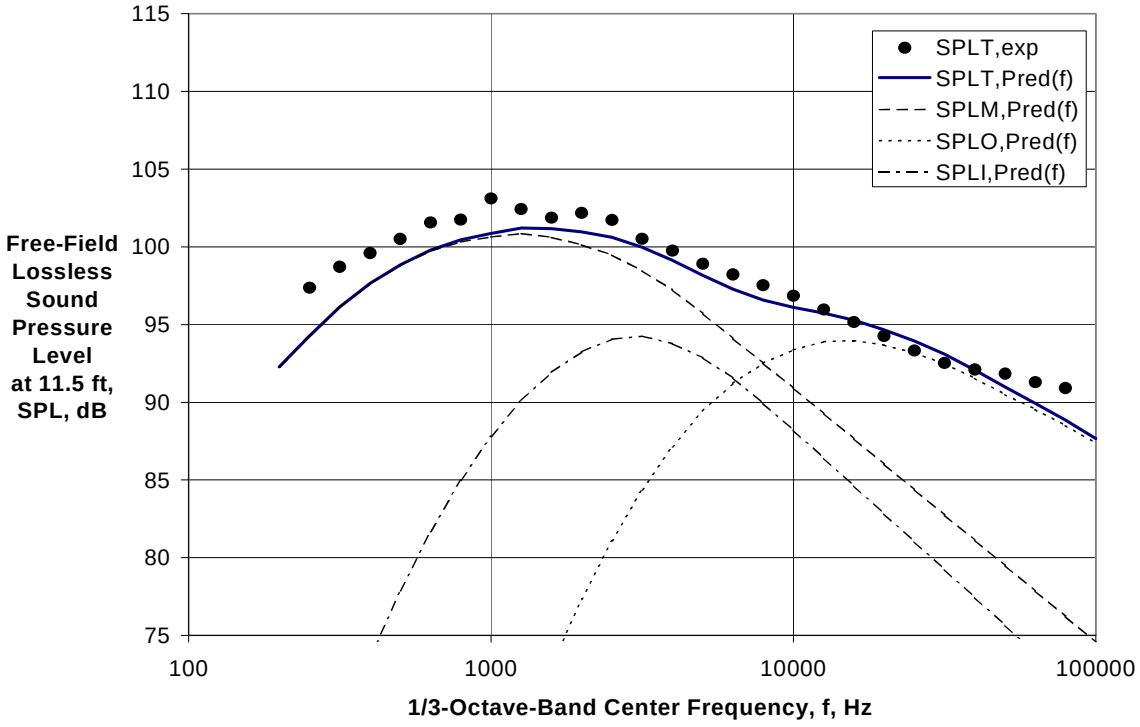

(c) Directivity Angle θ = 122 deg

Figure 39.—(Continued) Experimental and Predicted Spectra for BPR ≅ 5 Internal Plug Nozzle with Core Petals at V_{mix}/c_{amb} = 0.975 and M_f = 0.10.

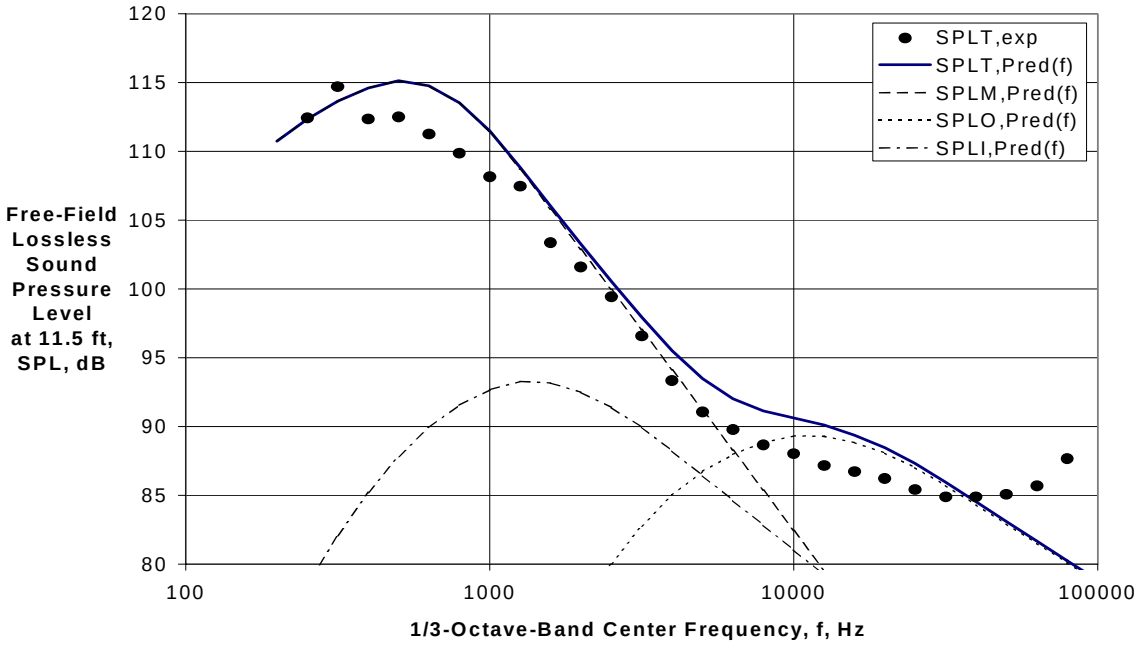

(d) Directivity Angle θ = 157 deg

Figure 39.— (Concluded) Experimental and Predicted Spectra for BPR ≅ 5 Internal Plug Nozzle with Core Petals at V_{mix}/c_{amb} = 0.975 and M_f = 0.10.

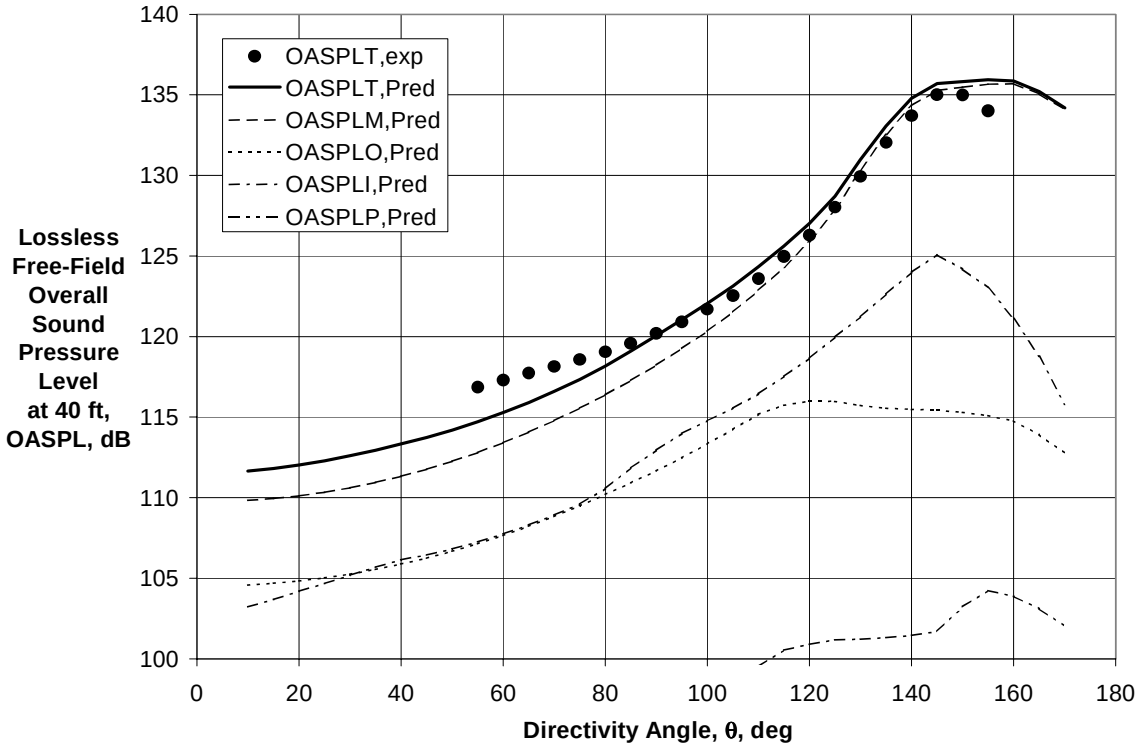

Figure 40.—Experimental and Predicted Directivity for BPR ≅ 5 External Plug Nozzle with Core and Fan Chevrons at V_{mix}/c_{amb} = 1.09 and M_f = 0.0.

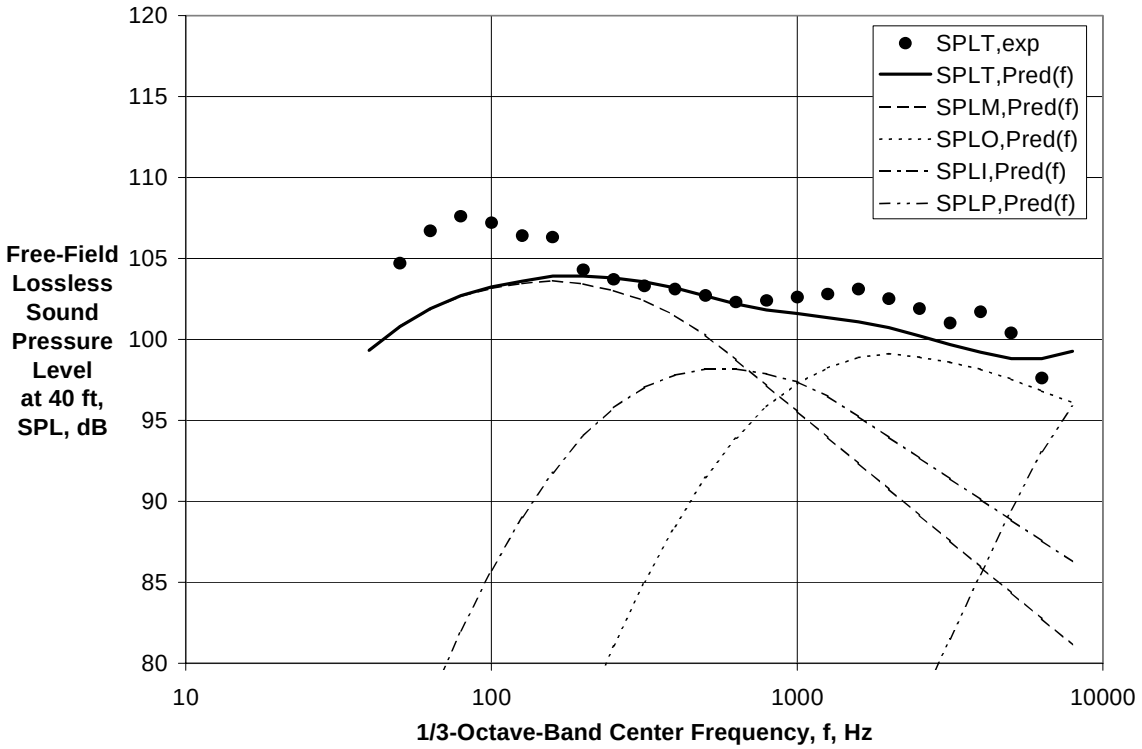

(a) Directivity Angle θ = 60 deg

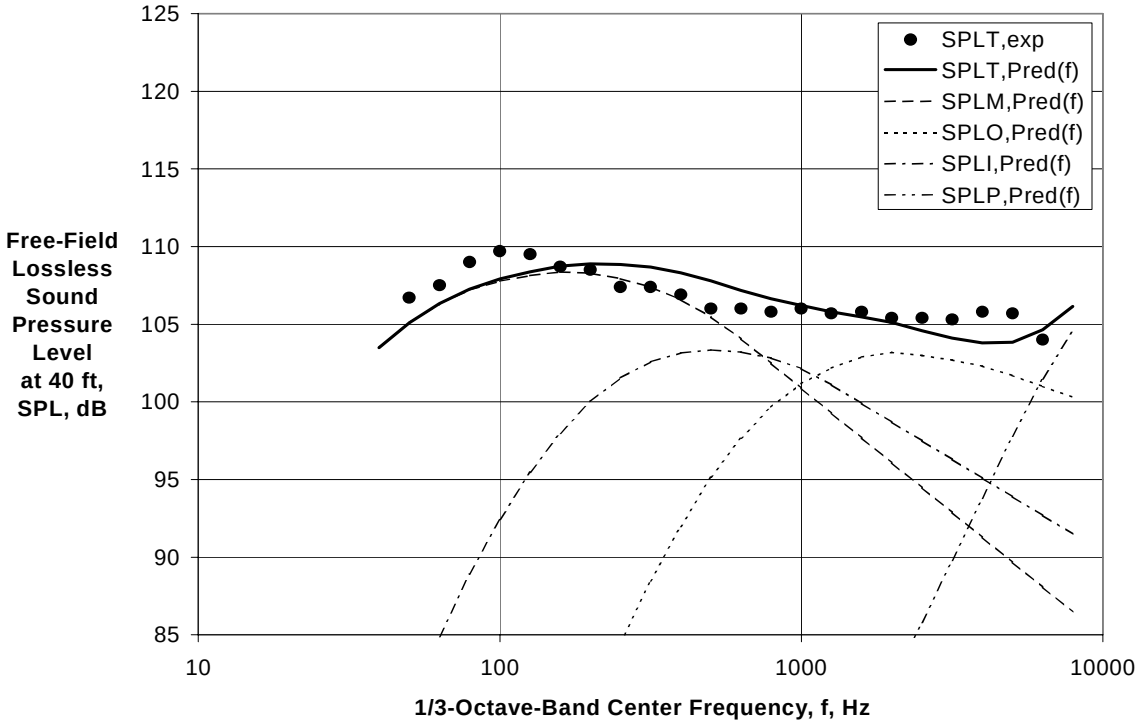

(b) Directivity Angle θ = 90 deg

Figure 41.—Experimental and Predicted Spectra for BPR ≅ 5 External Plug Nozzle with Core and Fan Chevrons at V_{mix}/c_{amb} = 1.09 and M_f = 0.0.

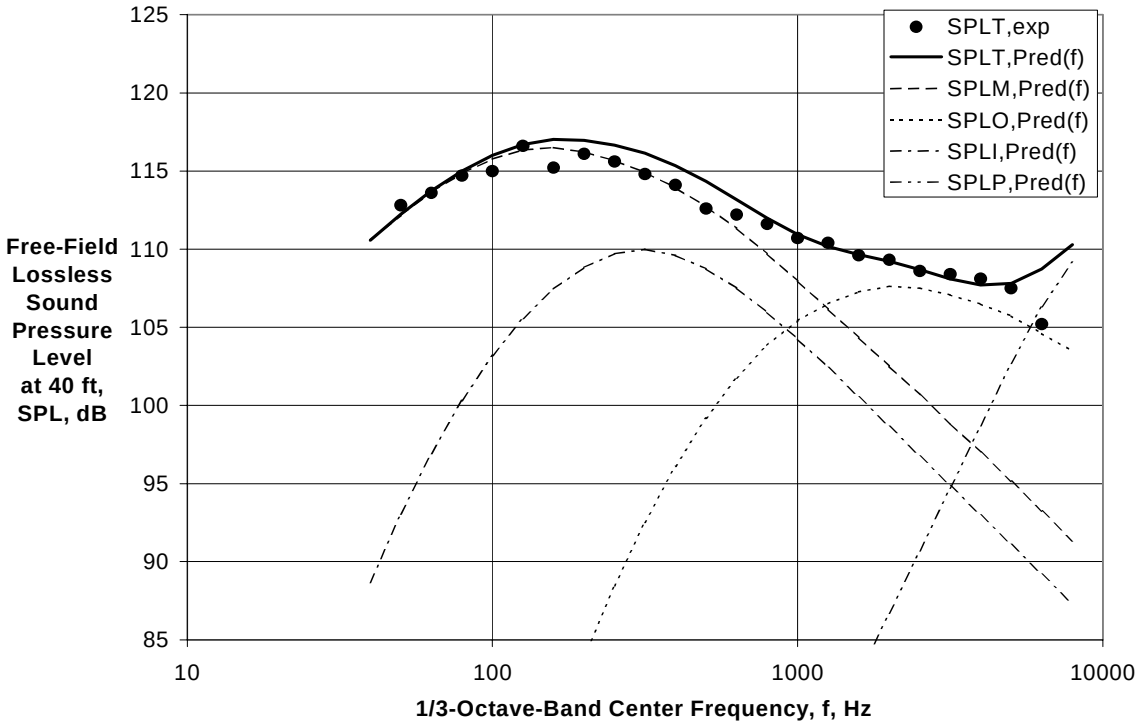

(c) Directivity Angle θ = 120 deg

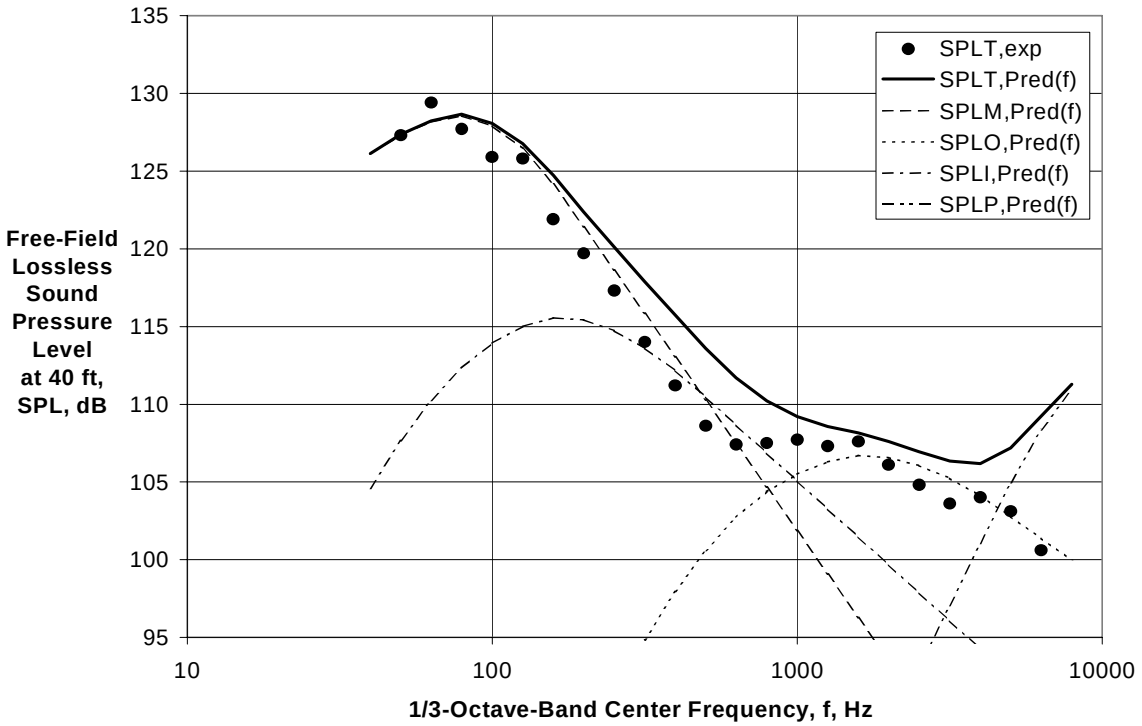

(d) Directivity Angle θ = 150 deg

Figure 41.—(Concluded) Experimental and Predicted Spectra for BPR ≅ 5 External Plug Nozzle with Core and Fan Chevrons at V_{mix}/c_{amb} = 1.09 and M_f = 0.0.

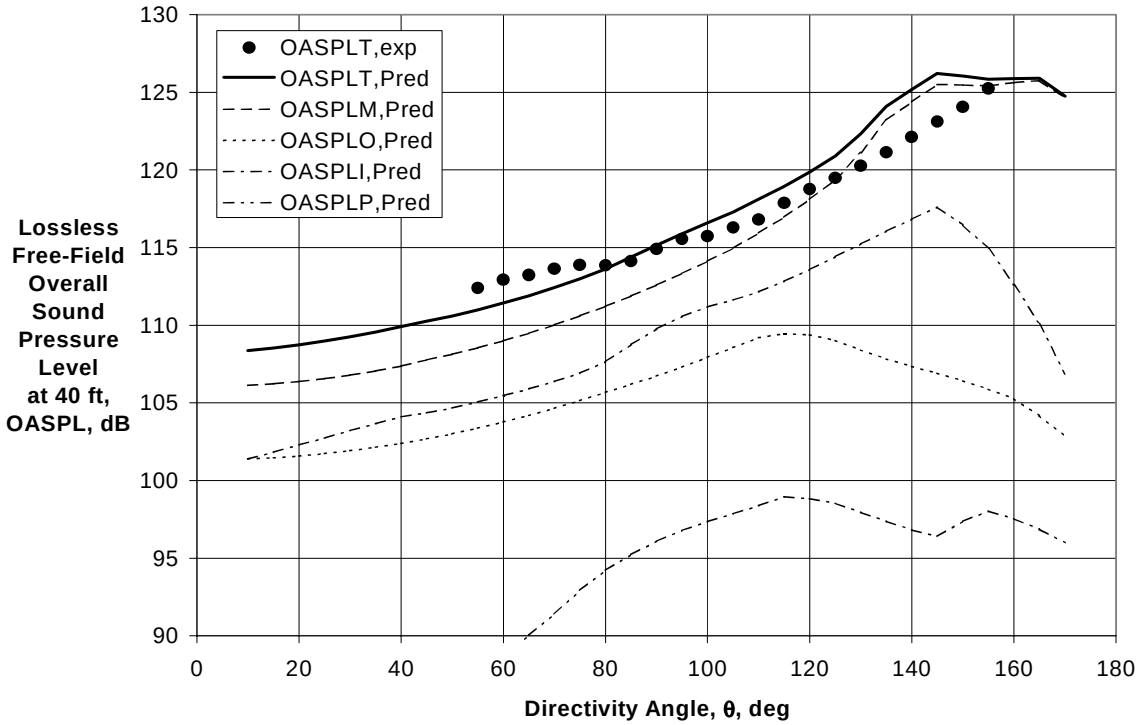

Figure 42.—Experimental and Predicted Directivities for BPR ≅ 5 External Plug Nozzle with Core and Fan Chevrons at V_{mix}/c_{amb} = 1.09 and M_f = 0.28.

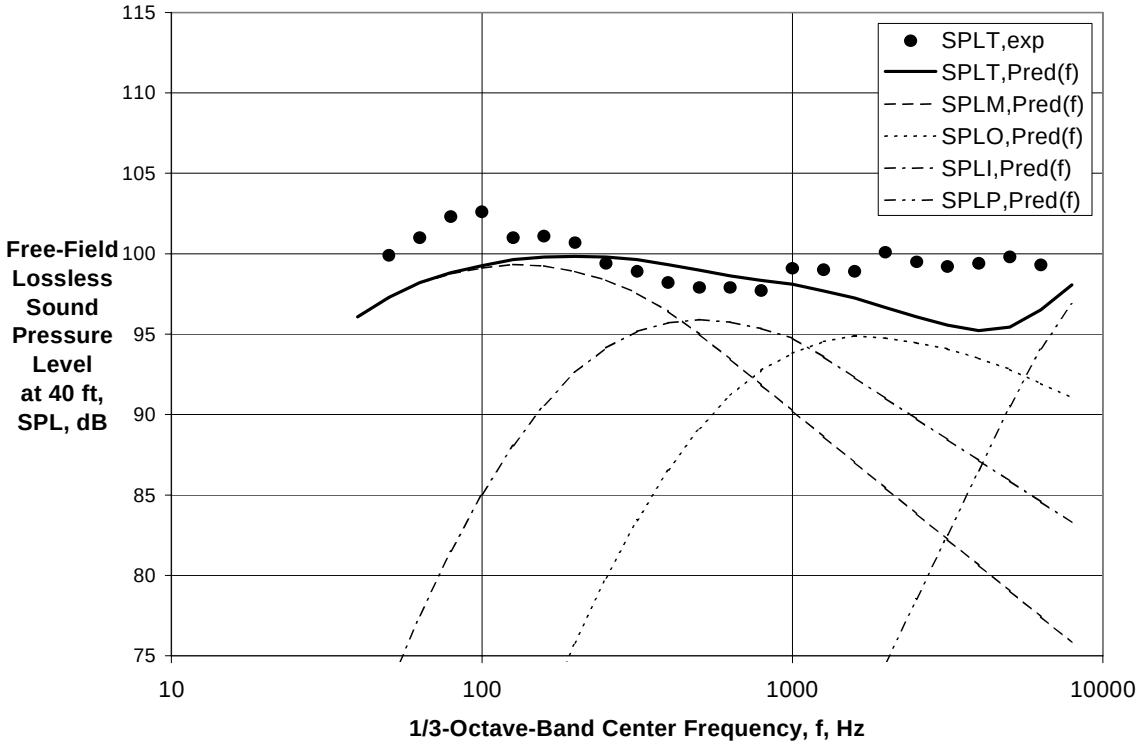

(a) Directivity Angle θ = 60 deg

Figure 43.—Experimental and Predicted Spectra for BPR ≅ 5 External Plug Nozzle with Core and Fan Chevrons at V_{mix}/c_{amb} = 1.09 and M_f = 0.28.

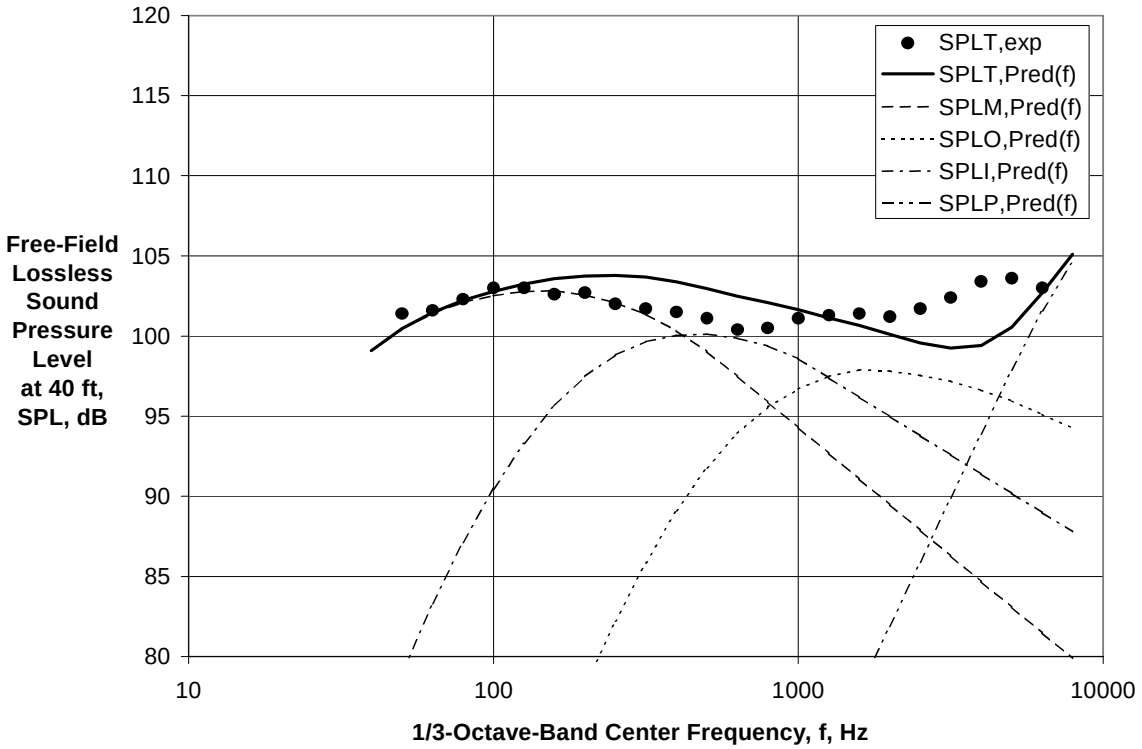

(b) Directivity Angle θ = 90 deg

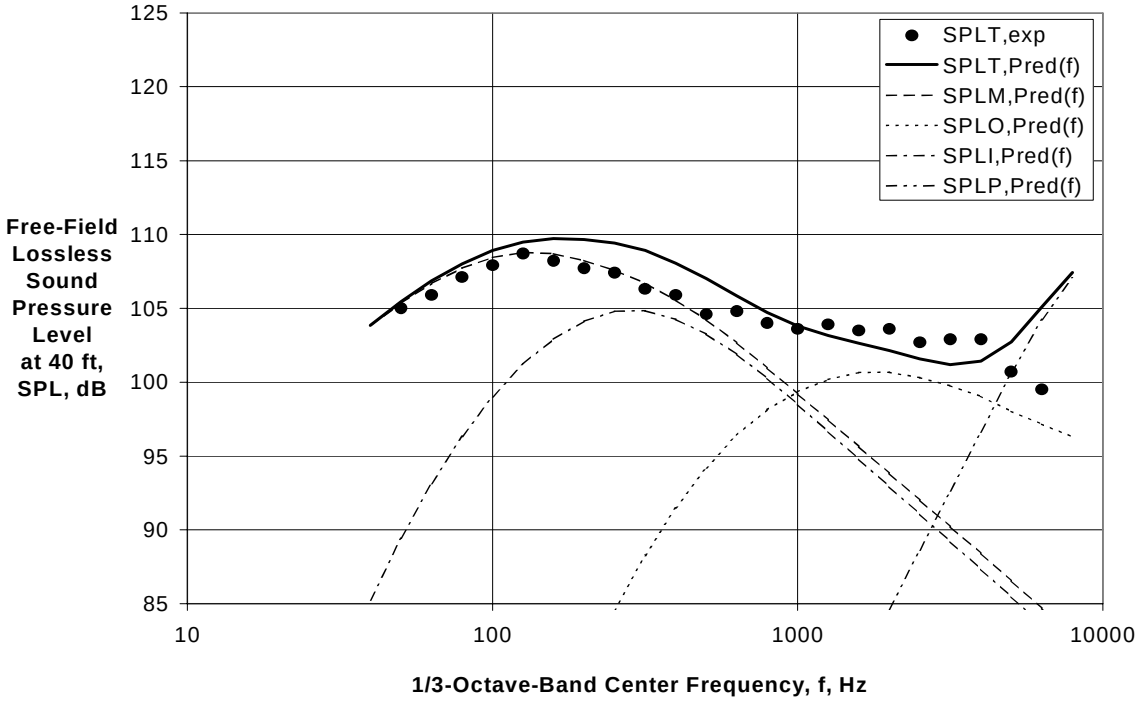

(c) Directivity Angle θ = 120 deg

Figure 43.—(Continued) Experimental and Predicted Spectra for BPR ≅ 5 External Plug Nozzle with Core and Fan Chevrons at V_{mix}/c_{amb} = 1.09 and M_f = 0.28.

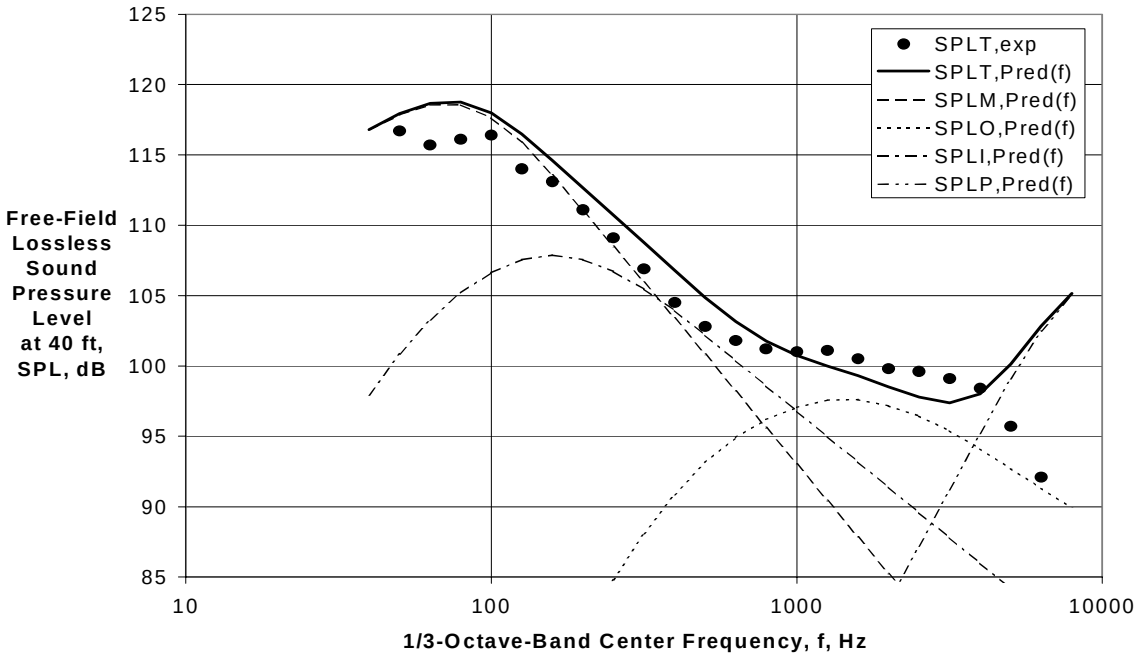

(d) Directivity Angle θ = 150 deg

Figure 43.—(Concluded) Experimental and Predicted Spectra for BPR ≅ 5 External Plug Nozzle with Core and Fan Chevrons at V_{mix}/c_{amb} = 1.09 and M_f = 0.28.

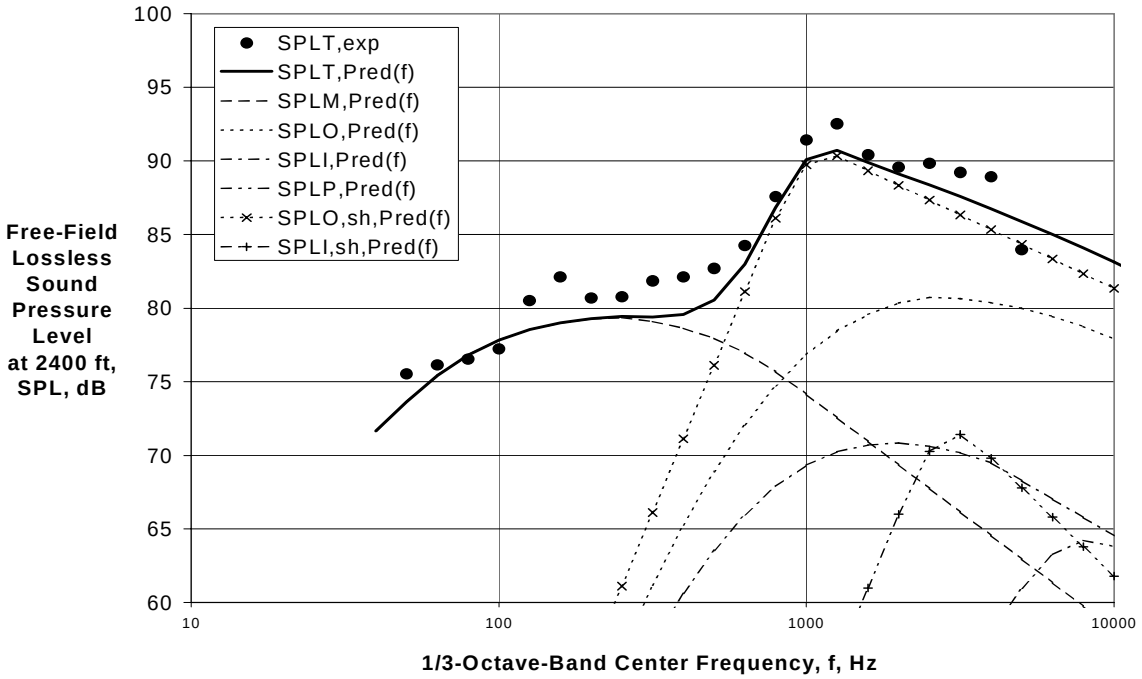

(a) Directivity Angle θ = 60 deg

Figure 44.—Experimental and Predicted Spectra for BPR ≅ 4 IVP External Plug Nozzle with 20-Chute Outer Stream Suppressor at V_{mix}/c_{amb} = 2.19 and M_f = 0.0.

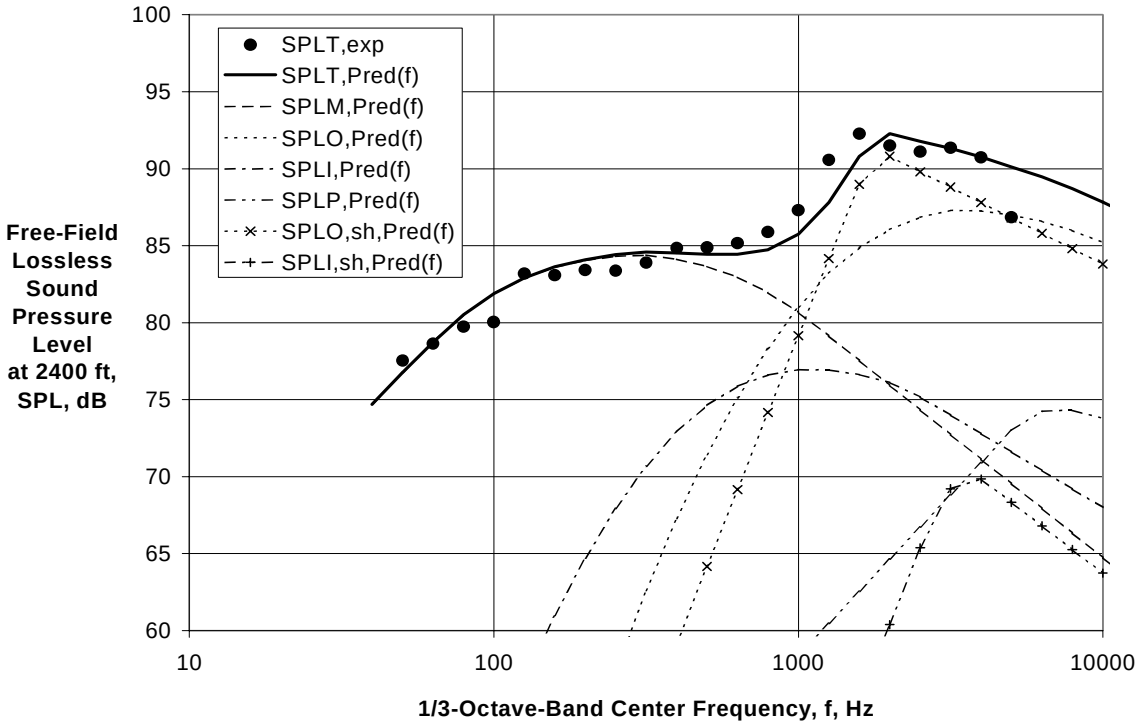

(b) Directivity Angle θ = 90 deg

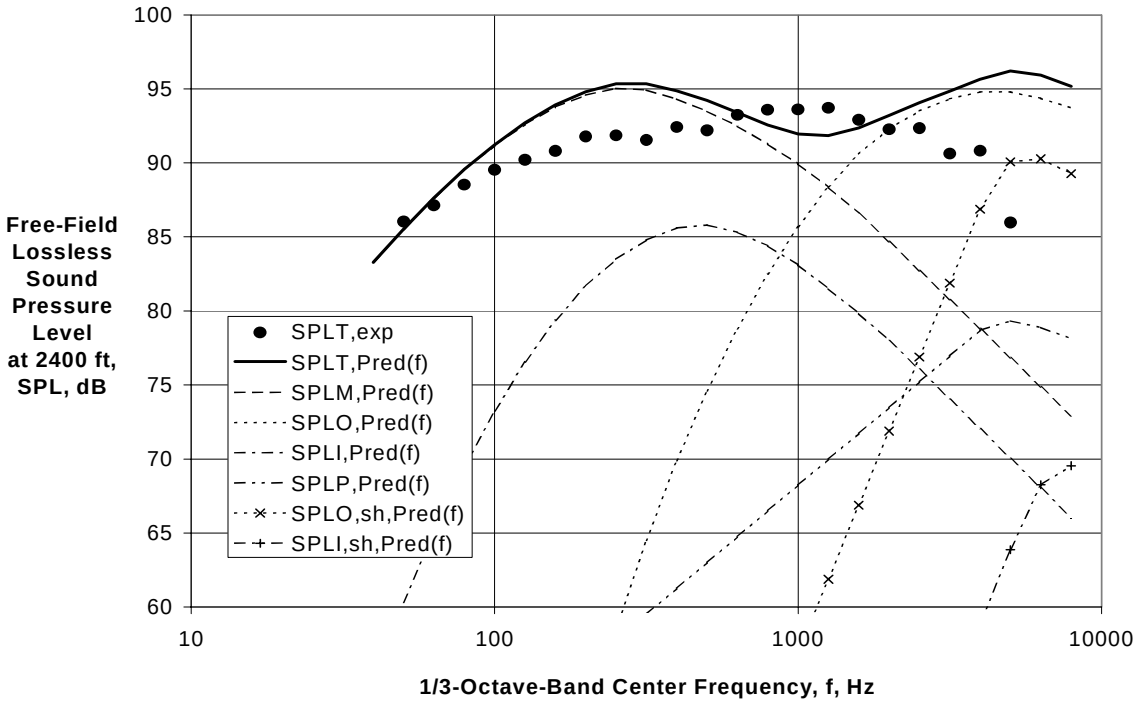

(c) Directivity Angle θ = 120 deg

Figure 44.—(Concluded) Experimental and Predicted Spectra for BPR ≅ 4 IVP External Plug Nozzle with 20-Chute Outer Stream Suppressor at V_{mix}/c_{amb} = 2.19 and M_f = 0.0.

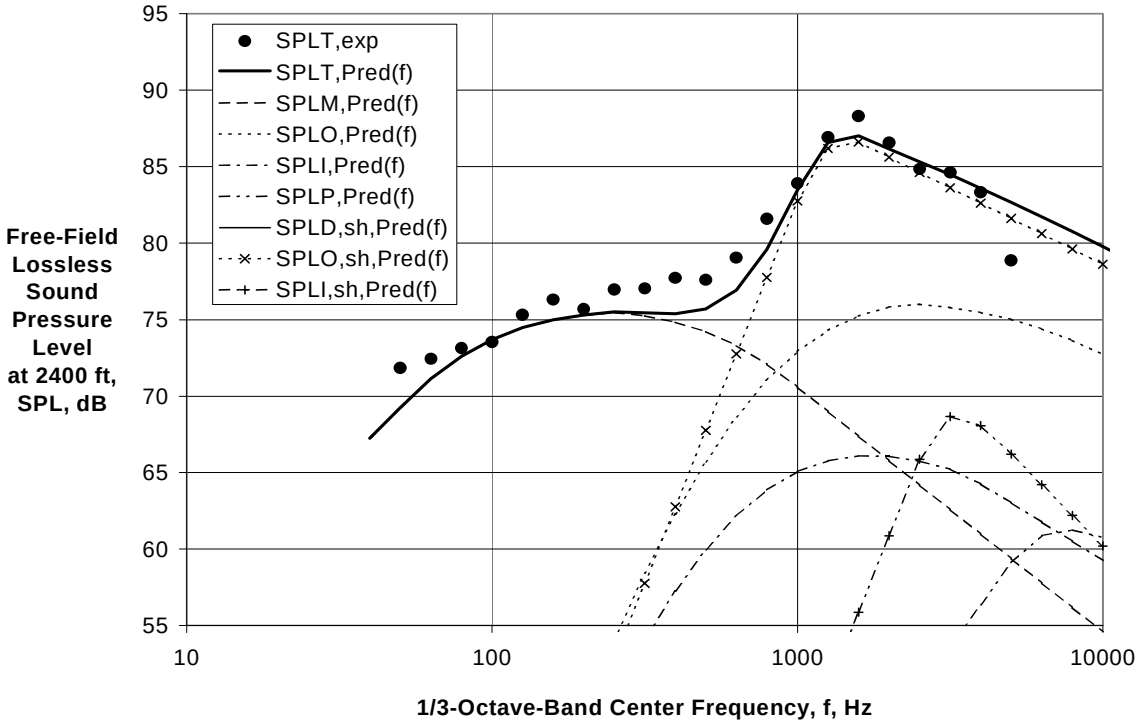

(a) Directivity Angle θ = 60 deg

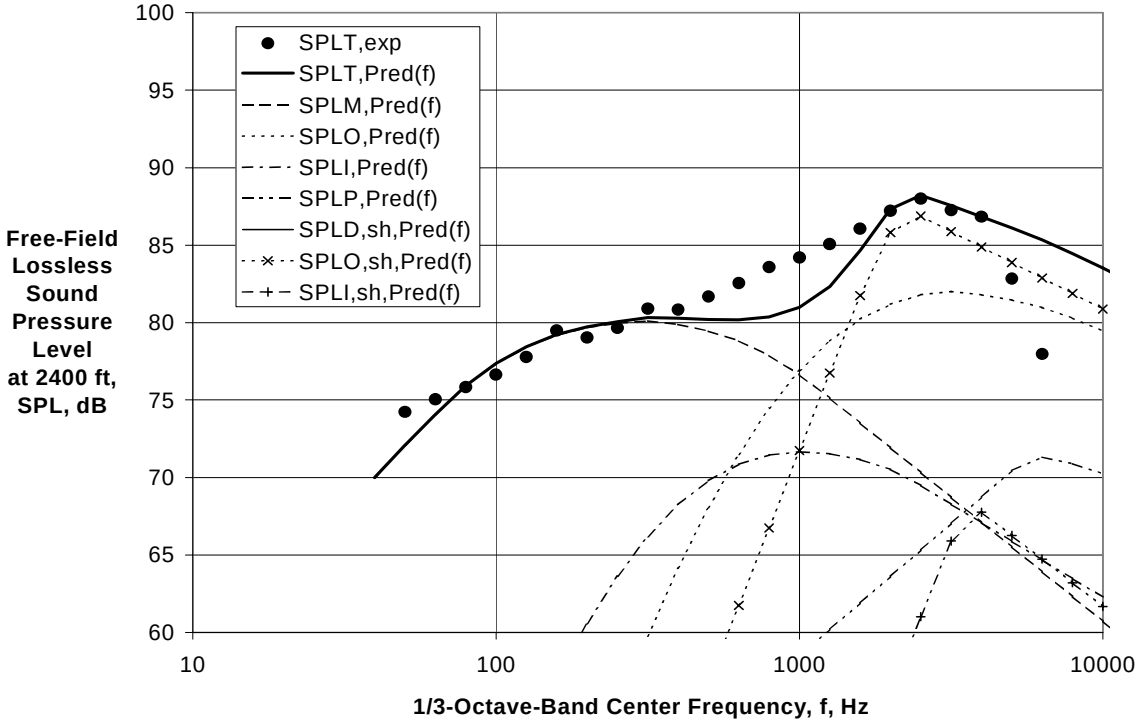

(b) Directivity Angle θ = 90 deg

Figure 45.—Experimental and Predicted Spectra for BPR ≅ 4 IVP External Plug Nozzle with 20-Chute Outer Stream Suppressor at V_{mix}/c_{amb} = 1.92 and M_f = 0.0.

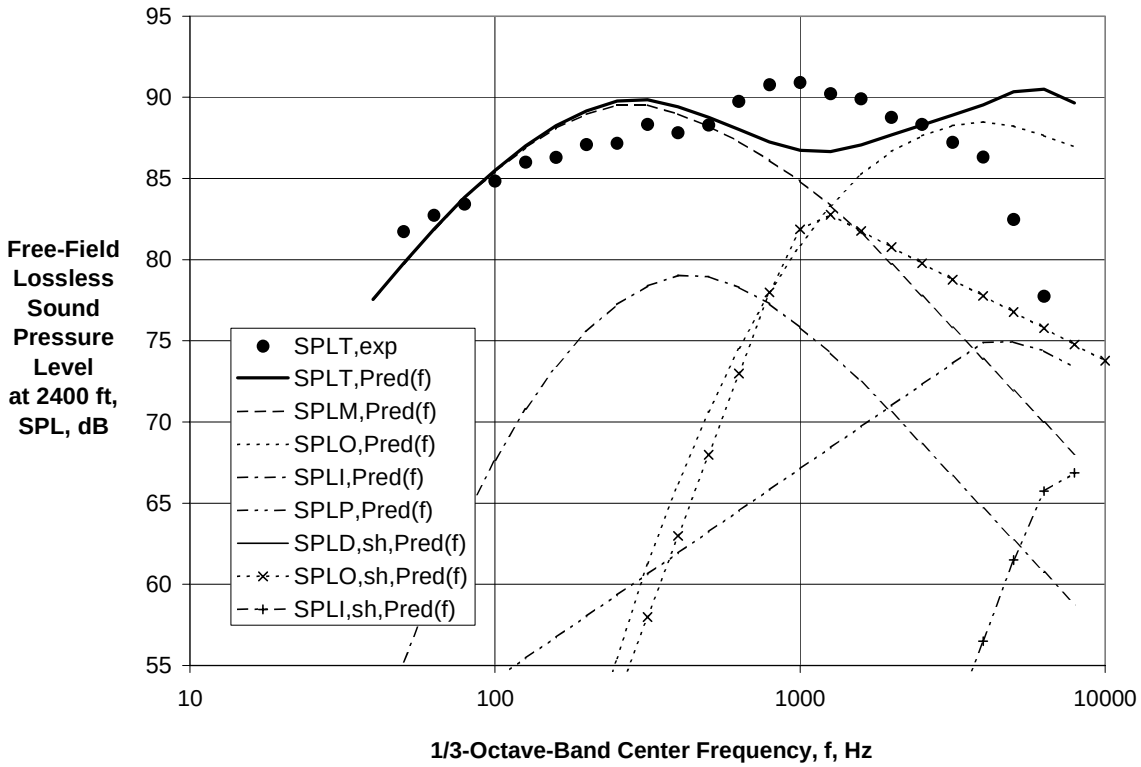

(c) Directivity Angle θ = 120 deg

Figure 45.—(Concluded) Experimental and Predicted Spectra for BPR ≅ 4 IVP External Plug Nozzle with 20-Chute Outer Stream Suppressor at V_{mix}/c_{amb} = 1.92 and M_f = 0.0.

REPORT DOCUMENTATION PAGE

Form Approved
OMB No. 0704-0188

1. AGENCY USE ONLY (*Leave blank*)	2. REPORT DATE	3. REPORT TYPE AND DATES COVERED
	March 2004	Final Contractor Report

4. TITLE AND SUBTITLE

Jet Noise Modeling for Supersonic Business Jet Application

5. FUNDING NUMBERS

WBS–22–781–30–12
NAS3–00178, Task Order 9

6. AUTHOR(S)

James R. Stone, Eugene A. Krejsa, and Bruce J. Clark

7. PERFORMING ORGANIZATION NAME(S) AND ADDRESS(ES)

Modern Technologies Corporation
Propulsion Systems Group
7530 Lucerne Drive, Suite 206
Middleburg Heights, Ohio 44130

8. PERFORMING ORGANIZATION REPORT NUMBER

E–14458

9. SPONSORING/MONITORING AGENCY NAME(S) AND ADDRESS(ES)

National Aeronautics and Space Administration
Washington, DC 20546–0001

10. SPONSORING/MONITORING AGENCY REPORT NUMBER

NASA CR—2004-212984

11. SUPPLEMENTARY NOTES

Project Manager, Jeffrey J. Berton, Aeronautics Directorate, NASA Glenn Research Center, organization code 2400, 216–977–7031.

12a. DISTRIBUTION/AVAILABILITY STATEMENT

Unclassified - Unlimited
Subject Categories: 05, 07, 71, and 45 Distribution: Nonstandard

Available electronically at http://gltrs.grc.nasa.gov

This publication is available from the NASA Center for AeroSpace Information, 301–621–0390.

12b. DISTRIBUTION CODE

13. ABSTRACT ***(Maximum 200 words)***

This document describes the development of an improved predictive model for coannular jet noise, including noise suppression modifications applicable to small supersonic-cruise aircraft such as the Supersonic Business Jet (SBJ), for NASA Langley Research Center (LaRC). For such aircraft a wide range of propulsion and integration options are under consideration. Thus there is a need for very versatile design tools, including a noise prediction model. The approach used is similar to that used with great success by the Modern Technologies Corporation (MTC) in developing a noise prediction model for two-dimensional mixer ejector (2DME) nozzles under the High Speed Research Program and in developing a more recent model for coannular nozzles over a wide range of conditions. If highly suppressed configurations are ultimately required, the 2DME model is expected to provide reasonable prediction for these smaller scales, although this has not been demonstrated. It is considered likely that more modest suppression approaches, such as dual stream nozzles featuring chevron or chute suppressors, perhaps in conjunction with inverted velocity profiles (IVP), will be sufficient for the SBJ.

14. SUBJECT TERMS

Noise prediction (aircraft); Noise reduction; Coaxial nozzles; Noise measurement; Jet aircraft noise

15. NUMBER OF PAGES

106

16. PRICE CODE

17. SECURITY CLASSIFICATION OF REPORT	18. SECURITY CLASSIFICATION OF THIS PAGE	19. SECURITY CLASSIFICATION OF ABSTRACT	20. LIMITATION OF ABSTRACT
Unclassified	Unclassified	Unclassified	